December 2018

Surface Functionalized Gold Nanoparticle Applications in Catalysis and Lipid-Nanoparticle Assemblies

Saptarshi Chakraborty
Clemson University, saptarc@g.clemson.edu

SURFACE FUNCTIONALIZED GOLD NANOPARTICLE APPLICATIONS IN
CATALYSIS AND LIPID-NANOPARTICLE ASSEMBLIES

A Dissertation
Presented to
the Graduate School of
Clemson University

In Partial Fulfillment
of the Requirements for the Degree
Doctor of Philosophy
Chemical Engineering

by
Saptarshi Chakraborty
December 2018

Accepted by:
Dr. Christopher L. Kitchens, Committee Chair
Dr. Mark Blenner
Dr. Sapna Sarupria
Dr. Frank Alexis

ABSTRACT

The general objectives of my dissertation are to devise strategies to impart unique functionality to gold nanoparticles (AuNPs) through surface modification and utilizing such surface-functionalized AuNP systems to 1) facilitate colloidal catalyst recovery and reuse while maintaining activity and 2) measure the interactions of engineered AuNPs with biological membranes as related to stimuli-responsive liposomal therapeutics.

AuNP surface functionalization is an essential step in the synthesis, stability and functionality-specific applications of AuNPs. Due to the ability to control AuNP shape, size and surface properties, AuNP applications have seen an exponential growth in various sectors that include catalysis, biomedicine, drug-delivery, sensing, imaging, energy applications, etc. Solution-based synthesis of surface functionalized AuNPs through the Turkevich and Brust synthesis methods produce reproducible narrow size-distribution colloidal AuNPs and provides a reliable platform to investigate effects of surface functionality on various applications.

Chapters 1 and 2 introduces the concept of AuNP as catalyst and experimentally compares the two major categories of catalyst; colloidal versus supported catalyst). Chapters 3-4 shows the successful development of a platform of colloidal AuNPs which are recovered from an aqueous medium through pH manipulation and illustrates how ligand structure on the AuNP surface is a primary factor determining catalytic activity, stability and recoverability. Chapter 5 is aimed at investigating interactions of engineered AuNP with the lipid membranes of small unilamellar vesicles (SUV) and depicts substantial membrane softening from AuNP inclusions.

The colloidal systems were investigated through various characterization tools such as calorimetry, light scattering, spectroscopy and advanced electron microscopy. Additionally, this work has employed elastic and inelastic neutron scattering techniques heavily as a result of extensive collaboration with government user facilities such as National Institute of Standards and Technology and Oak Ridge National Laboratory.

Overall, in my doctoral research, I have successfully manipulated AuNP properties through surface functionalization and assessed AuNP applications in two major areas: (1) sustainable catalysis and (2) lipid-nanoparticle assemblies as a platform to quantify membrane biomechanical properties. The current work sets the groundwork for expansion of such functionalized nanoparticle systems (including other metal NPs such as Pt, Pd, Ag, etc.) to a much larger application base in catalysis, nano-bio interactions, nanomedicine, drug delivery, and sensors to name a few.

DEDICATION

This dissertation is dedicated to my loving and supportive parents (Amrita and Somenath). Their scientific upbringing and encouragement to 'do whatever the heart wants', is the reason for my success as a researcher. Thank you to my grandfather (Dr. U. Mukhopadhyay) for introducing me to his dissertation when I was 10 years old and the endless talks about X-ray diffraction in my teens, which in some part, made a research career sound cooler.

microscope facilities at URI. Special thanks to Junhuan Ding and Mark Thies for the collaboration on the lignin characterization project.

TABLE OF CONTENTS

LIST OF TABLES

LIST OF FIGURES

xiii

xxi

CHAPTER ONE

INTRODUCTION AND BACKGROUND

1.1 Introduction.

The National Nanotechnology Initiative has established a generalized description which defines nanotechnology as the understanding and control of matter with at least one dimension of size 1 to 100 nanometers.[1] The unique properties of nano-materials arise from quantum and physical effects exhibited in the nano-scale. Quantum-mechanical rules predict that nanoparticles in the diameter range of 1-10 nm display electronic band structures that result in properties that are different than the bulk material counterparts. Nanoparticle properties strongly depends on the material, particle size and shape. The NP behavior and surface properties are heavily dependent on the nanoparticle surface chemistry.[2] This dissertation is primarily focused on intentionally manipulating nanoparticle surface chemistry for applications in catalysis, as well as, the biomechanical effects of nanoparticle inclusions on lipid bilayers in phospholipid nanoparticle assemblies.

Today, transition metal nanoparticles have found applications in photochemistry, nano-electronics and optics[3-13], but the essential application still remains in catalysis. Currently, more than 60% of all chemical products and 90% industrial chemical processes involves catalysis.[14] The importance of catalysis is reiterated by the fact that more than 35% of the global GDP is related to catalysis.[15] The fundamentals behind nano-catalysts are to utilize material reactivity at the nanoscale which is vastly different than the bulk material. These nano-catalysts possess large surface to volume ratios and the catalytic activity arises from the greater ratio of atoms that reside on the surface. Consequently,

highly active surface atoms that lead to activity, can also lead to nanoparticles instability. A relevant example of catalysis at nano-scale is the fact that bulk gold has historically been considered an inert metal, but at the nanoscale it becomes catalytically active, as shown by the pioneering work of Haruta et al. in low temperature CO oxidation.[16-18] Nanoparticle catalysis has been in use since the 19th century (before the development of technology to characterize nano-scale phenomena) with the advent of photography coincidentally employing silver nanoparticles (AgNPs) and decomposition of peroxides using platinum nanoparticles (PtNPs).[19] Nanoparticles of noble metals that include ruthenium, rhodium, palladium, platinum, gold and their oxides have been studied extensively. Pioneering work in the field of nitrobenzene reduction by NP catalysts were reported as far back as 1940[20-21]. Parravano reported hydrogen atom transfer between benzene and cyclohexane and oxygen atom transfer between CO and CO_2 using AuNPs.[22-23] The early work of Nord in the 1940s and Turkevich in the 1950s chose Pd as the metal of choice for NP. After Haruta's findings, Bond and Sermon[24] and Hirai et al.[25-26] investigated AuNP-catalyzed olefin hydrogenation. Extensive systematic studies were conducted on NP catalysis in the field of redox catalysis, photo-catalysis,[27-33] hydrogenation of unsaturated substrates and oxidation.[34-35] During the 1990s, applications of PdNPs catalysis in the Heck C-C coupling (reaction between butyl acrylate and iodobenzene, etc.) were reported by Reetz. [36-39] In addition, numerous reaction systems have also been catalyzed by colloidal and supported metal nanocatalysts such as oxidations[40-42], cross coupling reactions[43-53], electron transfer reactions[48, 54-56], hydrogenations[57-62], fuel cell reactions[63-65] and various others.

1.2. Colloidal (Quasi-Homogeneous or Soluble-Heterogeneous) Nanoparticle Catalysts: A Bridge between Homogeneous and Heterogeneous Catalysts

Catalysts are traditionally categorized into two classifications: homogeneous or heterogeneous catalysts (see Figure 1.1). In homogeneous catalysis, catalysts are present in the same phase as the reactant and product. Homogenous catalysts generally offer access to all catalytic sites as they are essentially soluble metal complexes. Metal ions in such systems can catalyze reactions due to their variable oxidation states. Tuning of chemo-, regio- and enantioselectivity are advantages offered because these metal ions are surrounded by organic ligands which provide a very specific steric environment (Figure 1.1). Homogeneous catalysts are generally very selective but the primary barrier to homogeneous catalyst utilization is the difficulty of catalyst separation from final products for reuse.

In heterogeneous catalysis, the catalyst is in a different phase than the reactant and/or product. Heterogeneous catalysts are essentially nanoparticles or ionic species adsorbed or covalently bonded to a solid support (silica, metal oxides, carbonaceous supports, etc). Primarily, industrial heterogeneous catalysts are high-surface area solids with the active component attached to it. Catalytically active sites in this case reside only on the available material surface, thus support attachment decreases the overall activity. Although, catalytic activity is not generally an issue for heterogeneous catalysts, selectivity and conversion is often limited and presents a major problem in fine chemical synthesis. Metal leaching into products from the supports and growth of the active phase on the supports are other major challenges faced by heterogeneous catalysts. However, the

economies offered by the ease of catalyst recovery has led to the vast commercialization of heterogeneous catalyst industrially over the homogeneous counterpart.
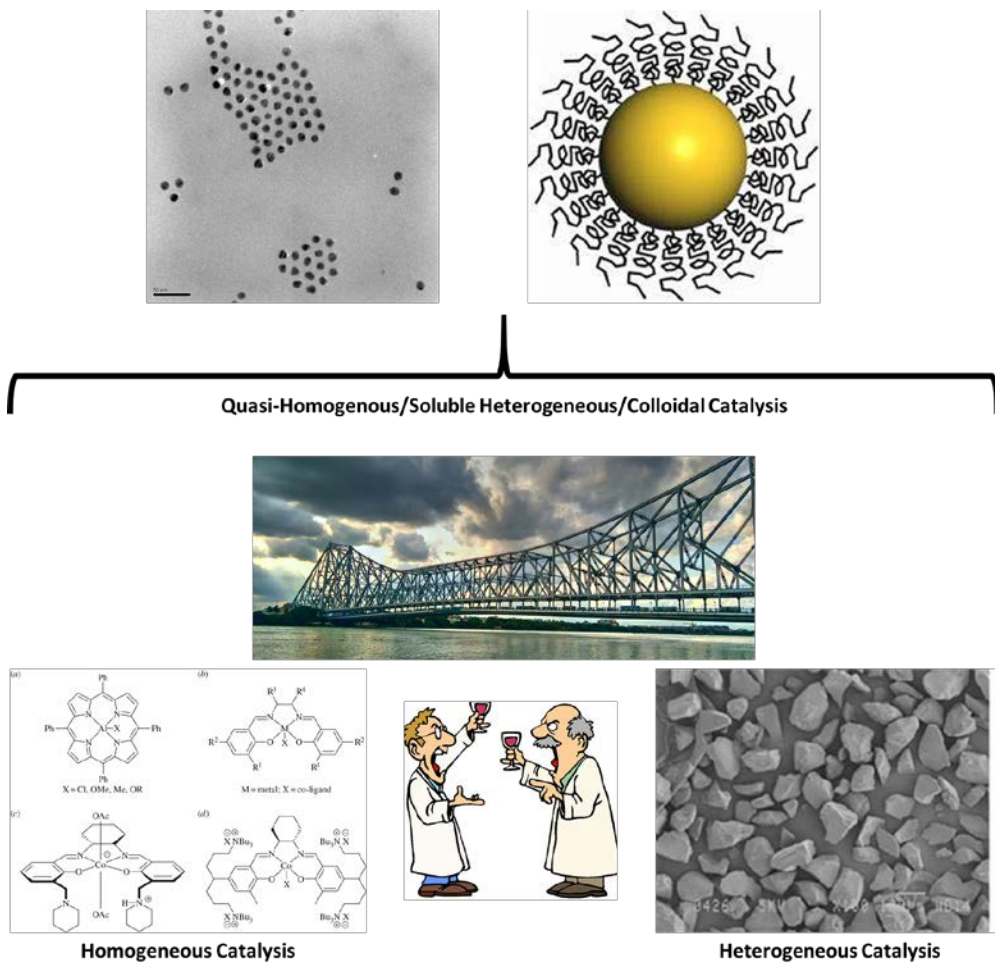
Figure 1.1. Major categories of metal catalysts (does not include enzymatic catalysts)

'They don't talk to each other because they were developed as totally separate fields' said Gabor Somorjai at the UC Berkeley about homogeneous and heterogeneous catalyst researchers. 'Until recently they were taught separately, used separately and they are served by different literatures.' Recently researchers have shown great interest in combining the properties of homogenous and heterogeneous catalysts. From the

perspective of heterogeneous catalyst researchers, the goal has been to create smaller and more finely dispersed catalysts particles and preventing aggregation on the supports with the ultimate goal of creating atomically dispersed catalysts on supports.

On the other hand, homogeneous catalyst researchers have focused on developing quasi-homogeneous catalysts where active catalysts are essentially nanoparticles with various surface functionality designed to impart specific properties like stability under heat and pH, chirality, recoverability, etc. This quasi-homogeneous system (colloidal catalysts) offers various approaches towards catalyst recovery and acts as a bridge between homo- and heterogeneous catalysts.[6, 66-69] However, there are many issues such as stability, recyclability and selectivity which are still in the nascent phase of research and requires systematic research.

1.3. Gold Nanoparticles (Colloids) as Catalysts

Gold in the nano regime (AuNP) is surprisingly active and an effective green catalyst, although bulk gold is generally inert.[70-71] The large surface area of metal nanoparticles, qualifies them to act either as heterogeneous promoters for catalytic reactions or as supports for homogeneous catalysts. From the perspective of nanoparticle catalysis, AuNP catalysts can be discriminated in terms of the role of the metal. Figure 1.2 (i)-(iii) depicts cases where the metal nanoparticle is the dominating influence on catalytic activity. Here, the catalytic reaction takes place on the surface of the nanoparticles. Figure 1.2 (iii) depicts a system where the metal capping ligand also influences the catalytic activity of the metal actively. Various reactions have been conducted using AuNP in one of the forms mentioned in Figure 1.2 and can be found in numerous reviews.[71-79]. In this

dissertation, we have focused primarily colloidal catalyst design of the kind depicted in Figure 1.2 (ii). Ligands used in this work do not participate in the catalytic activity and serve as stabilizers with specific functions such as enhanced stability and recoverability.
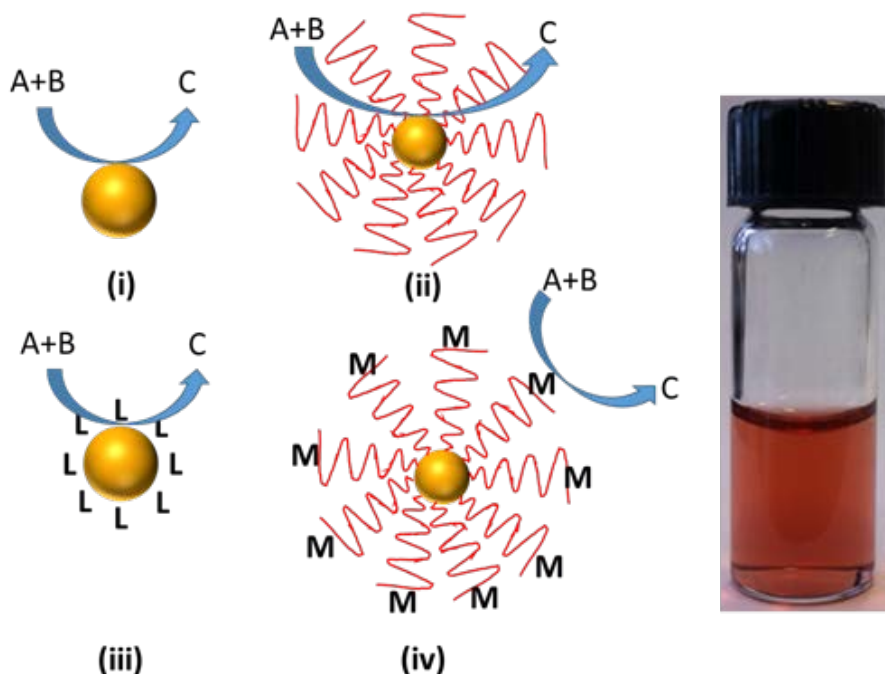
Figure 1.2. Typical AuNP catalysts (i) metal nanoparticles, (ii) metal nanoparticle capped with protective shell, (iii) metal nanoparticle capped with ligand participating in the catalysis and (iv) metal nanoparticles with active catalysts supported on protective shells. Only in case (iv), core material does not promote the reaction.

1.4 Colloidal AuNP synthesis and Surface Chemistry

The two most common synthesis techniques for AuNPs involve wet chemical synthesis which gives enhanced control over size, shape and surface chemistry. Hydrophilic catalysts used in this work have been synthesized through the Turkevich method[80] where gold precursor is reduced in presence of a reducing agent (trisodium citrate or sodium borohydride). This method yields relatively monodisperse particle size

distributions and ease of surface functionalization. On reducing Au precursors (such as gold chloride, HAuCl$_4$) in the presence of trisodium citrate (TSC), TSC acts both as a reducing agent and provides colloidal stabilization. AuNPs of size ranges greater than 10 nm can be easily be synthesized by this technique by altering the precursor to TSC ratio or by seeded-growth methods.[81] Modifying Turkevich method with stronger reducing agents such as sodium borohydride, leads to formation of smaller 4-5 nm AuNPs. The Turkevich method has been exclusively used in Chapters 2-4 and AuNPs were subsequently functionalized by appropriate ligands.

Brust synthesis[82] is another technique utilized to directly synthesize hydrophobic AuNPs. Particle size distribution in these cases can be easily controlled by altering the precursor to hydrophobic ligand ratio. AuNPs with diameters of 2-10 nm are easily synthesized with sufficient size distribution control and AuNP with high concentrations (milligram of gold) can be produced. Size distribution can be enhanced by employing various post-synthesis fractionation techniques such as anti-solvent fractionation, etc. AuNPs produced through Brust synthesis has been extensively used in the lipid nanoparticle assemblies work in Chapter 5.

1.5. 4-Nitrophenol Reduction as Model Reaction for Kinetic Analysis

Nitrophenol and its derivatives are significant by-products produced from pesticides, herbicides and synthetic dyes.[83-84] 4-Nitrophenol has been shown to cause central nervous system, liver and kidney damage in both humans and animals. Removal of these compounds from the environment is thus paramount. In addition, reduction of 4-Nitrophenol is an essential transformation in the pharmaceutical industry for development

of analgesics, antipyretic drugs, photographic development, corrosion inhibitors, anti-corrosion lubricant, etc.[85-86]
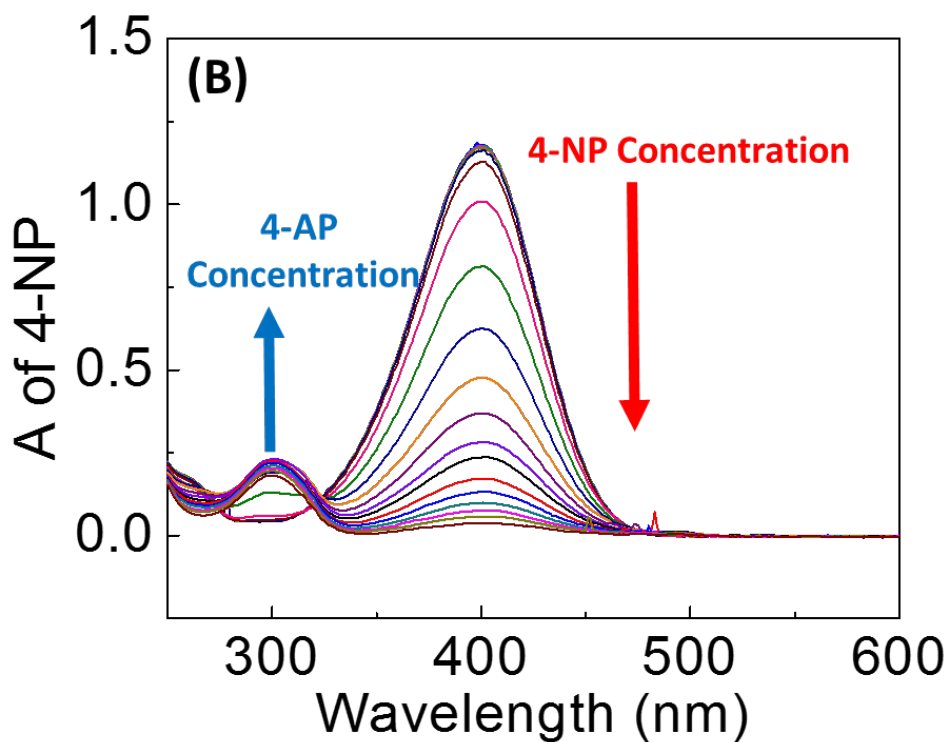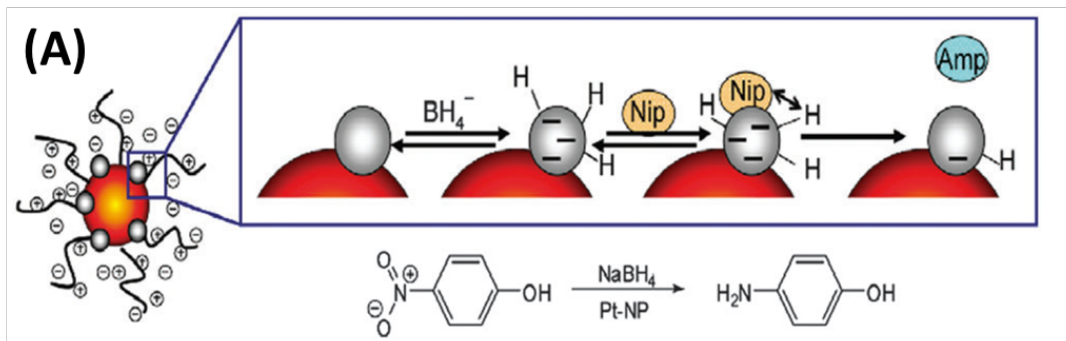
Figure 1.3. (A) Schematic depicts the 4-NP reduction reaction following a Langmuir-Hinshelwood mechanism. Reproduced with permission from J. Phys. Chem. C, 2010, 114 (19), pp 8814–8820. (B) Simple colorimetric tracking of reaction progress via time-resolved UV-Vis spectroscopy provides a simple way to quantify reaction kinetics.

Metal nanoparticle catalytic efficacy can be studied by comparing catalysts through a model reaction. The reaction should be mechanistically simple, well researched and can be studied with repeatability with simple bench-scale setup. The metal nanoparticle catalyzed, aqueous reduction of 4-Nitrophenol to 4-Aminophenol is one such reaction which has been considered a model reaction in different laboratories around the world. Most common metal nanoparticles can catalyze this reaction and involves a simple electron transfer process in presence of reducing agent such as sodium borohydride and 4-Aminophenol is the sole product. The primary advantage of using this reaction is the simple time-resolved UV-Vis spectrophotometric measurement and tracking of the reactants and products (4-NP at λ_{max} = 400 nm and 4-AP at λ_{max} = 300 nm under alkaline conditions in presence of sodium borohydride).

The 4-NP reduction has been explained by numerous mechanism based on the particular systems investigated: Langmuir-Hinshelwood[87] mechanism (Figure 1.3A), Eley-Rideal[88-89] mechanism, Semiconductor[90] mechanism, defect-mediated[91] mechanism and photo-catalytic mechanism. Langmuir-Hinshelwood (LH) mechanism involves the surface adsorption of reducing agent and 4-Nitrophenol on catalyst followed by a hydrogen transfer.[92] This mechanism applies to all catalysts systems studied in this work and the other mechanism are out of scope for this dissertation. In presence of excess reducing agent, the reaction essentially follows pseudo-first order reaction kinetics. The pseudo-first order reaction rate constant can be directly obtained from the time-resolved spectrophotometric data by plotting *ln (C_0/C_t) vs. Time* (Figure 1.3B).

1.6 Applications of Neutron Scattering

This dissertation involves extensive static and dynamic characterization of soft matter systems such as ligands on AuNP surface, lipid bilayer thickness measurements, bending dynamics in lipid bilayers and lignin structural and molecular weight analysis (Appendix A) using neutron scattering techniques. A common theme between all of the above characterized systems is the prevalence of hydrogen in their structures which makes neutrons the probe of choice for characterization of these systems. In addition, the structural length scale and the time scale of dynamics of the studied systems falls in the time and length scales accessed by cold neutrons (longer wavelength). The major advantages of using neutrons as probes are:

1. Neutron scattering lengths vary wildly with atomic number (especially for light atoms and unlike X-ray which increase with atomic number) (Figure 1.4A). This allows for the use of isotopic substitution to enhance contrast between specific parts of a structure. Deuterium labeling or using deuterated solvents (scattering length densities of hydrogen and deuterium are vastly different) to achieve enhanced contrast between background and the studied entity, has been extensively used in this work.

2. Neutrons interacts with matter through nuclear interactions. Thus, neutrons have high penetration (low absorption) for most elements and makes neutron scattering a bulk probe.

3. Wide range of neutrons momentum transfer and energy transfer allows probing both static structures and dynamics in condensed matter at various time and length scales. Near angstrom to near micron length scales and time scale from femto second to second are easily accessed through neutron scattering techniques (Figure 1.4B). Length scales and

time scales relevant for the soft matter systems studied in Chapters 4-5 and Appendix A coincide with the neutron probes time and length scale, making neutron scattering a potential tool to apply in this work.

Major disadvantages of neutron scattering include cost of neutron production, low fluxes relative to other techniques and the requirement of relatively large sample amounts. In this work, all neutron experiments were conducted at NIST Center for Neutron Research at Gaithersburg, MD. Neutron beam times were accessed through peer-review based proposals. The limited amount of experimental data from neutron scattering shows the major disadvantage of this technique, such as low neutron flux, long measurement times and concentrated sample requirement.
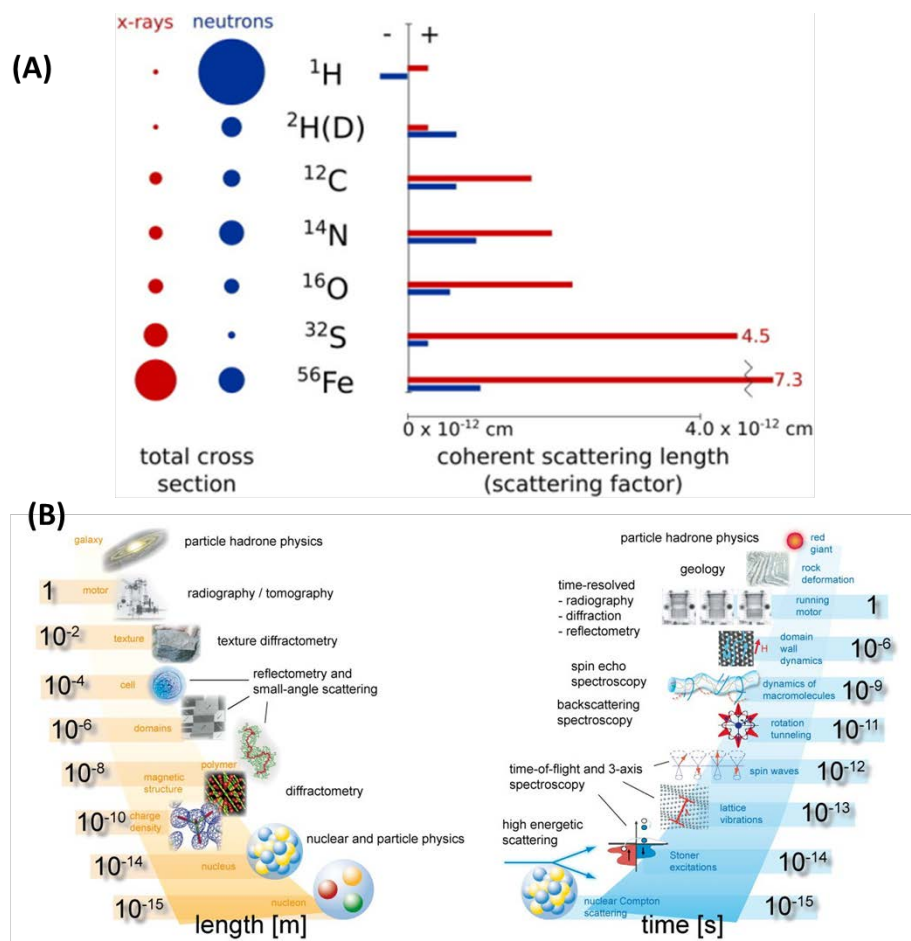
Figure 1.4. (A) Dependence of scattering cross section for X-ray and neutron for common elements. (B) Time and length scale investigated through neutron scattering. Picture: Karin Griewatsch, Kiel University, KFN.

There are 4 main types of neutron scattering measurements:

1. Transmission measurements: This is the simplest form of measurement and requires monochromatic beam, collimation and a simple neutron detector. Transmission measurements contains information about sample content and relative fraction of various elements. For example, relative ratio of carbon to hydrogen in crude oils could be measured through this measurement. In this work, transmission measurements were carried out for

12

all small angle neutron scattering (SANS) and neutron spin echo (NSE) measurements to normalize scattering data.

      2. Elastic Scattering: This measurement consists of recording scattered intensities with varying scattering angle. This resolves the momentum transfer vector $q = 4\pi/\lambda \sin\left(\frac{\theta}{2}\right)$ where λ is the neutron wavelength and θ is the scattering angle. Intensities at various scattering angles are generally measured using a position-sensitive detector and then averaged radially or otherwise (Figure 1.5 A). Main elastic scattering instruments include: diffractometers (high scattering angle, measures small length scales), reflectometers and small angle neutron scattering instruments (SANS, low scattering angle, measures larger length scales) (length scale and scattering angles are summarized schematically in Figure 1.5B).
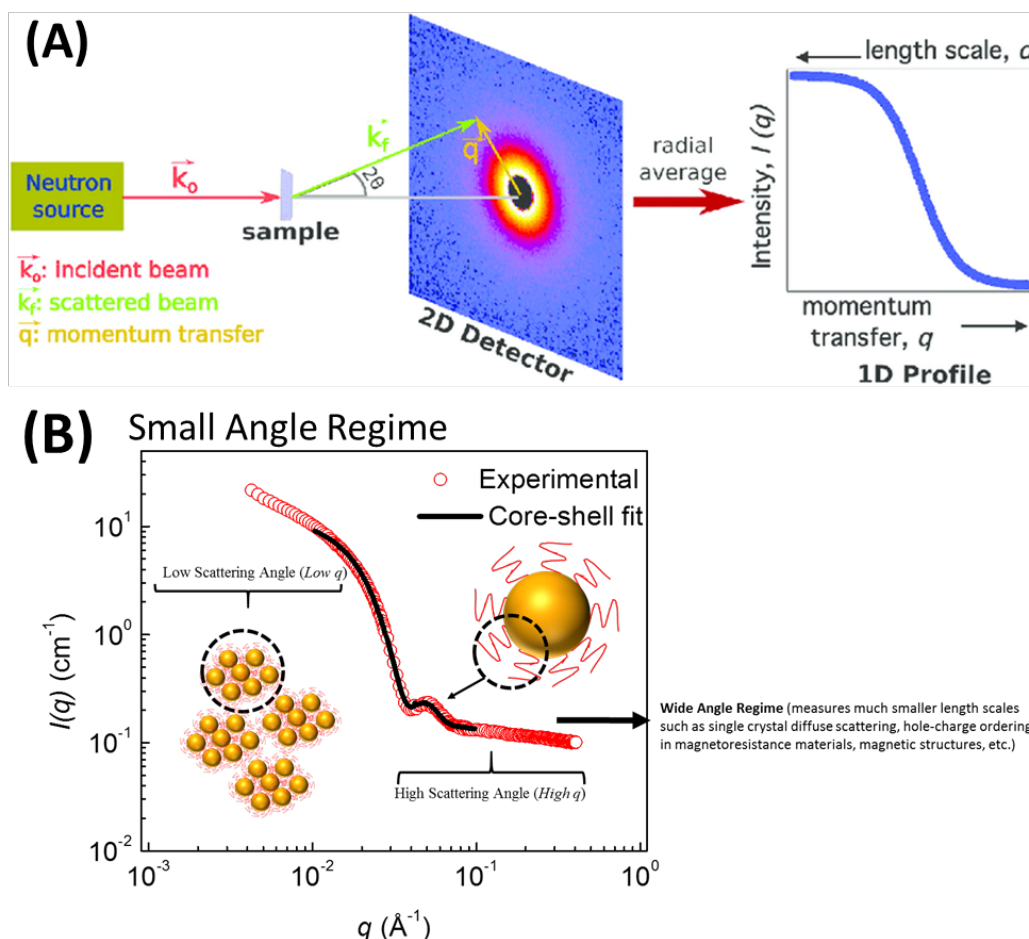
Figure 1.5. (A) Small Angle Neutron Scattering (SANS) schematic depicting scattering profile on a position-sensitive detector and radial averaging leading to a 1-D spectra. (B) Typical SANS scattering profile for a core-shell nanoparticle depicting smaller length scales (for example, shell thickness) measured at high-q region, whereas larger repeating structures such as core-shell nanoparticle clustering can be probed at the low-q region. Solid black line shows a representative data fit to the core-shell model to calculate the shell thickness.

SANS has been heavily used in Chapter 4-5 and Appendix A to characterize ligand polymer structure, lipid bilayer and lignin macromolecular structure. In Chapter 4, SANS was used to characterize polymer ligand shell thickness and shell solvation. SANS is able to probe the length scale of interest for AuNP-polymer shell (sub-nanometer to

nanometers) with enhanced contrast between hydrogenated ligand and deuterated solvents. In Chapter 5, lipid bilayer thickness was probed through SANS as SANS covers the length scale of interest (~5 nm bilayer thickness) and offers similar contrast enhancement between hydrogenated bilayer and deuterated solvent. Lignin in solution exhibits structures in the nanometer scale as well as aggregates in the micron length scale. SANS can probe both these length scales in solution simultaneously with contrast between hydrogenated lignin macromolecules and deuterated solvents. Useful information from SANS data can extracted by fitting the reduced and normalized SANS scattering profiles to SANS models (such as, spherical models such as sphere, core-shell, micelle, vesicle; cylindrical models, ellipsoidal models, shape independent power law models in the low q region, etc.). Data fitting has to be carried out with extreme caution as models can be forcefully made to fit to most scattering data. Supporting evidences such as TEM images, light or X-Ray scattering profiles, thorough understanding of the probed system through experiments or intelligent deduction and detailed mathematical behavior of the model functions leads to accurate determination of parameters from a SANS data fit. More details related to various models used in this work and data fitting consideration can be found in Supplementary Information of the respective published articles.

     3. Quasi-elastic/Inelastic Neutron scattering: QENS refers to inelastic energy transfers around zero energy transfer, whereas inelastic scattering corresponds to finite energy changes. In addition to neutron detection, neutron energies are resolved by using time-of-flight methods. Main instruments to measure energy changes includes: triple axis,

TOF and backscattering spectrometers. Energy ranges from μeV to meV are covered by these instruments. QENS instruments are largely used to investigate diffusive modes.

4. **Neutron Spin-Echo spectrometer:** NSE is another type of QENS instrument but has been singled-out because it measures correlations in the time domain instead of the energy domain. It uses polarized neutrons that are made to precess in the pre-sample flight path, get quasi-elastically scattered from sample and are made to precess again in the opposite direction in the post-sample flight path (Figure 1.6C). The difference in number of spin precessions before and after the sample is proportional to the neutron velocity change during scattering and therefore measures energy transfer. This instrument can probe time scale in the nano-second range and q range from 0.01 $Å^{-1}$ and 0.5 $Å^{-1}$. NSE has been heavily used in Chapter 5 of this dissertation. In Chapter 5, we have measured the bending dynamics of pure lipid bilayers and lipid bilayers with AuNP inclusions. The time and length scales of lipid membrane dynamics for small unilamellar vesicles is completely accessed by NSE. In addition, using hydrogenated lipids in deuterated solvent allows for enhanced contrast between the bilayer and bulk solvent thus making NSE an ideal probe to conduct bending dynamics measurements.
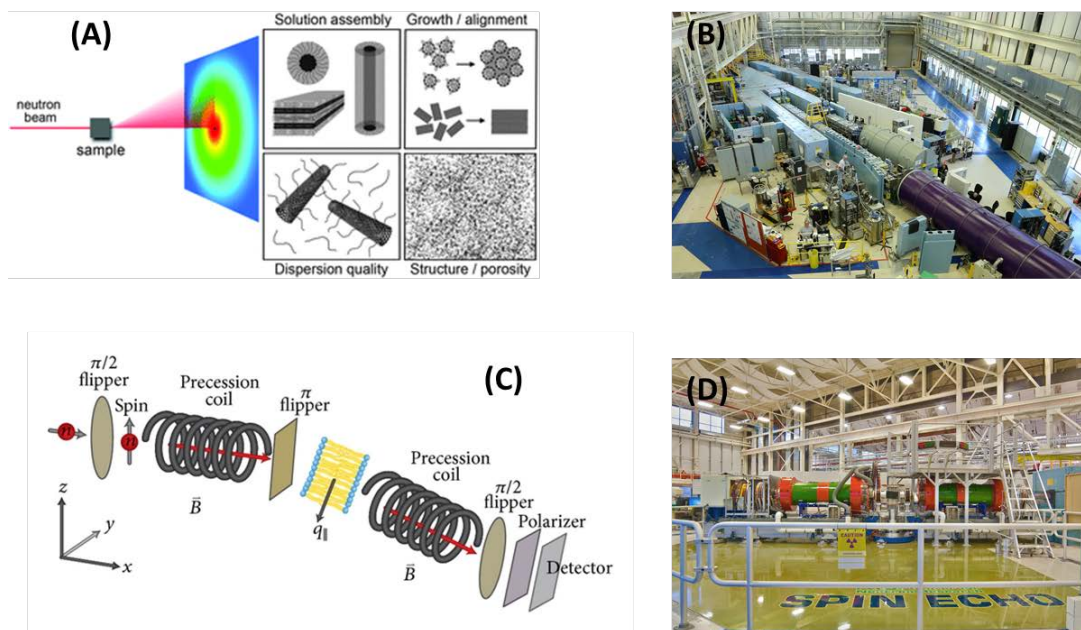
Figure 1.6. (A) and (B) illustrates use of SANS to characterize various systems. (C) and (D) depicts the schematic and the NSE instrument at NCNR, Gaithersburg, MD.

1.7 Dissertation Structure

The primary goal of this dissertation is the intentional manipulation of AuNP surface chemistry to harness certain properties which allows the application as catalysts and bilayer inclusions for biophysical systems.

Chapter 2 discusses the comparison of supported and colloidal gold nanoparticles as catalysts using a common experimental tool kit. We demonstrate the advantages of using colloidal AuNPs in comparison to supported AuNPs in terms of greater available surface area and enhanced catalytic activity. We have additionally been able to qualitatively measure the synergistic effect of support towards AuNP catalytic activity. Experimental evidences to explain the rise of induction time has also been provided in

this work. ***(Publication: J. Phys. Chem. C, 2018, 122 (14), pp 7749–7758,***

DOI:10.1021/acs.jpcc.8b00664)

Chapter 3 focuses on developing a colloidal AuNP catalyst which can be successfully recovered, thus taking a step towards ameliorating the major recovery challenge faced by colloidal catalyst. We demonstrate successful AuNP functionalization with pH responsive small molecule to facilitate pH triggered AuNP recovery. However, we found that achieving recovery, catalytic activity and colloidal stability was a very delicate balance. ***(Publication: Nanomaterials 2018, 8(5), 339; https://doi.org/10.3390/nano8050339)***

Chapter 4 focuses on removing the problems faced in Chapter 3 namely, maintaining colloidal stability and recoverability without compromising catalytic activity. To achieve this goal, we have used lessons from our group's previous work,[93] which showed direct correlation between catalytic activity and ligand packing density on AuNP surface. Thus the solution to retaining AuNP catalytic activity lied in functionalizing AuNP surfaces with large MW polymers. However, there were no existing polymers which could satisfy all the following conditions: (1) have high affinity to AuNP surface and maintain colloidal stability, and (2) be pH responsive simultaneously to facilitate pH triggered recovery and reuse. Thus, we synthesized a new polymer by introducing thiol groups on a pH responsive polymer backbone through EDC/NHS chemistry. Here primary amines are conjugated to carboxylic acids via an amide linkage, thereby introducing any group (thiol in our case) which terminates the amine molecule. This synthesis can lead to development of a platform ligand for AuNP functionalization whereby any thiol containing compound

with an amine/carboxylic acid group can be coupled on another molecule which contains a carboxylic acid/amine group. Various quantities of thiol groups were introduced on a polyacrylic acid backbone to result in a thiolated pH responsive polymer which leads to different degree of binding on AuNP surface. This novel ligand successfully attached to AuNP surface, AuNPs showed enhanced colloidal stability in general and during reactions and demonstrated ease of pH triggered recovery and phase transfer recovery. We explore various factors affecting catalytic activity including ligand structure, softness and chemistry. *(Publication: manuscript submitted to ACS Applied Materials and Interfaces)*

Chapter 5 investigates a different application of surface-functionalized hydrophobic AuNPs and the inclusion into lipid bilayers for modification of the membrane biomechanical properties. AuNPs were intentionally functionalized with short chain hydrophobic thiols to render them colloidally stable in hydrophobic environments. The goal of this functionalization was to successfully incorporate AuNPs inside the hydrophobic core of a lipid bilayer system. The purpose of this study was two-folds: (a) developing and characterizing liposome-nanoparticle assemblies as a novel stimuli-responsive drug delivery vehicle and (c) to study the potentially toxic effects of hydrophobic AuNPs by quantifying changes in lipid bilayer biophysical properties. We demonstrate membrane softening due to nanoparticle inclusion as one of the major findings of this study. *(Publication: DOI: 10.1021/acs.langmuir.8b02553)*

Chapter 6 discusses the scope and recommendations for future work and summarizes the major findings of this dissertation.

1.8 References

1.   National Nanotechnology Initiative. **2014**.

2.   Brust, M.; Kiely, C. J., Some Recent Advances in Nanostructure Preparation from Gold and Silver Particles: A Short Topical Review. *Colloids and Surfaces A: Physicochemical and Engineering Aspects* **2002,** *202*, 175-186.

3.   Schmid, G.; Chi, L. F., Metal Clusters and Colloids. *Advanced Materials* **1998,** *10*, 515-526.

4.   Rao, C. Y.; Burge, H. A.; Brain, J. D., The Time Course of Responses to Intratracheally Instilled Toxic Stachybotrys Chartarum Spores in Rats. *Mycopathologia* **2000,** *149*, 27-34.

5.   Aiken, J. D.; Finke, R. G., A Review of Modern Transition-Metal Nanoclusters: Their Synthesis, Characterization, and Applications in Catalysis. *J Mol Catal a-Chem* **1999,** *145*, 1-44.

6.   Lewis, L. N., Chemical Catalysis by Colloids and Clusters. *Chemical Reviews* **1993,** *93*, 2693-2730.

7.   Schmid, G., Large Clusters and Colloids. Metals in the Embryonic State. *Chemical Reviews* **1992,** *92*, 1709-1727.

8.   Henglein, A., Small-Particle Research: Physicochemical Properties of Extremely Small Colloidal Metal and Semiconductor Particles. *Chemical Reviews* **1989,** *89*, 1861-1873.

9.   V. Goia, D.; Matijevic, E., Preparation of Monodispersed Metal Particles. *New Journal of Chemistry* **1998,** *22*, 1203-1215.

10.   Ghavidast, A.; Mahmoodi, N. O., A Comparative Study of the Photochromic Compounds Incorporated on the Surface of Nanoparticles. *Journal of Molecular Liquids* **2016,** *216*, 552-564.

11.   Feng, Z.; Yu, J.; Kong, J.; Wang, T., A Novel Porous Al2o3 Layer/Agnps–Hemin Composite for Degradation of Azo Dyes under Visible and Uv Irradiation. *Chemical Engineering Journal* **2016,** *294*, 236-245.

12.   Loh, G. C., Electronic and Magnetic Properties of Encapsulated Mos2 Quantum Dots: The Case of Noble Metal Nanoparticle Dopants. *ChemPhysChem* **2016,** *17*, 1180-1194.

13.   Astafyeva, L. G.; Pustovalov, V. K., Efficiency of Absorption of Solar Radiation by Liquids Containing Metallic Nanoparticles. *Journal of Applied Spectroscopy* **2016,** *83*, 218-224.

14.   Kandepi, V. V. K. M.; Narender, N., Synthesis of N-Heterocyclic Compounds over Zeolite Molecular Sieve Catalysts: An Approach Towards Green Chemistry. *Catal Sci Technol* **2012,** *2*, 471-487.

15.   Zaera, F., New Challenges in Heterogeneous Catalysis for the 21st Century. *Catal Lett* **2012,** *142*, 501-516.

16.   Haruta, M.; Kobayashi, T.; Sano, H.; Yamada, N., Novel Gold Catalysts for the Oxidation of Carbon-Monoxide at a Temperature Far Below 0-Degrees-C. *Chem Lett* **1987**, 405-408.

17.   Haruta, M.; Yamada, N.; Kobayashi, T.; Iijima, S., Gold Catalysts Prepared by Coprecipitation for Low-Temperature Oxidation of Hydrogen and of Carbon-Monoxide. *J Catal* **1989,** *115*, 301-309.

18.   Haruta, M., Catalysis of Gold Nanoparticles Deposited on Metal Oxides. *Cattech* **2002,** *6*, 102-115.

19.   Bradley, J. S., The Chemistry of Transition Metal Colloids. In *Clusters and Colloids*, Wiley-VCH Verlag GmbH: 2007; pp 459-544.

20.   Rampino, L. D.; Nord, F. F., Preparation of Palladium and Platinum Synthetic High Polymer Catalysts and the Relationship between Particle Size and Rate of Hydrogenation. *J Am Chem Soc* **1941,** *63*, 2745-2749.

21.   Rampino, L. D.; Nord, F. F., Applicability of Palladium Synthetic High Polymer Catalysts. *J Am Chem Soc* **1941,** *63*, 3268-3268.

22.   Cha, D. Y.; Parravan.G, Surface Reactivity of Supported Gold .1. Oxygen Transfer between Co and Co2. *J Catal* **1970,** *18*, 200-&.

23.   Parravan.G, Surface Reactivity of Supported Gold .2. Hydrogen Transfer between Benzene and Cyclohexane. *J Catal* **1970,** *18*, 320-&.

24.   Bond, G. C.; Sermon, P. A.; Webb, G.; Buchanan, D. A.; Wells, P. B., Hydrogenation over Supported Gold Catalysts. *J Chem Soc Chem Comm* **1973**, 444-445.

25.   Hirai, H.; Nakao, Y.; Toshima, N., Preparation of Colloidal Rhodium in Polyvinyl-Alcohol) by Reduction with Methanol. *J Macromol Sci Chem* **1978,** *A12*, 1117-1141.

26.   Hirai, H.; Nakao, Y.; Toshima, N., Colloidal Rhodium in Poly(Vinylpyrrolidone) as Hydrogenation Catalyst for Internal Olefins. *Chem Lett* **1978**, 545-548.

27.   Moradpour, A.; Amouyal, E.; Keller, P.; Kagan, H., Hydrogen Production by Visible-Light Irradiation of Aqueous-Solutions of Ru (Bipy)23+. *Nouv J Chim* **1978,** *2*, 547-549.

28.   Henglein, A.; Lilie, J., Storage of Electrons in Aqueous-Solution - the Rates of Chemical Charging and Discharging the Colloidal Silver Microelectrode. *J Am Chem Soc* **1981,** *103*, 1059-1066.

29.   Henglein, A., Catalysis of the Reduction of Tl+ and of Ch2cl2 by Colloidal Silver in Aqueous-Solution. *J Phys Chem-Us* **1979,** *83*, 2858-2862.

30.   Kurihara, K.; Fendler, J. H.; Ravet, I.; Nagy, J. B., Hydrogenation of Ethylene and Cyclohexene Catalyzed by Colloidal Platinum Particles Obtained in Polymerized Vesicles. *J Mol Catal* **1986,** *34*, 325-335.

31.   Boutonnet, M.; Kizling, J.; Touroude, R.; Maire, G.; Stenius, P., Monodispersed Colloidal Metal Particles from Nonaqueous Solutions - Catalytic Behavior for the Hydrogenation of but-1-Ene of Platinum Particles in Solution. *Appl Catal* **1986,** *20*, 163-177.

32.   Degani, Y.; Willner, I., Photoinduced Hydrogenation of Ethylene and Acetylene in Aqueous-Media - the Functions of Palladium and Platinum Colloids as Catalytic Charge Relays. *J Chem Soc Perk T 2* **1986**, 37-41.

33.   Willner, I.; Maidan, R.; Mandler, D.; Durr, H.; Dorr, G.; Zengerle, K., Photosensitized Reduction of Co2 to Ch4 and H-2 Evolution in the Presence of

Ruthenium and Osmium Colloids - Strategies to Design Selectivity of Products Distribution. *J Am Chem Soc* **1987,** *109*, 6080-6086.

34.   Bradley, J. S.; Hill, E.; Leonowicz, M. E.; Witzke, H., Clusters, Colloids and Catalysis. *J Mol Catal* **1987,** *41*, 59-74.

35.   Larpent, C.; Patin, H., Catalytic Hydrogenations in Biphasic Liquid Liquid-Systems .2. Utilization of Sulfonated Tripod Ligands for the Stabilization of Colloidal Rhodium Dispersions. *J Mol Catal* **1988,** *44*, 191-195.

36.   Reetz, M. T.; Breinbauer, R.; Wanninger, K., Suzuki and Heck Reactions Catalyzed by Preformed Palladium Clusters and Palladium/Nickel Bimetallic Clusters. *Tetrahedron Lett* **1996,** *37*, 4499-4502.

37.   Reetz, M. T.; Helbig, W., Size-Selective Synthesis of Nanostructured Transition-Metal Clusters. *J Am Chem Soc* **1994,** *116*, 7401-7402.

38.   Reetz, M. T.; Quaiser, S. A., A New Method for the Preparation of Nanostructured Metal-Clusters. *Angew Chem Int Edit* **1995,** *34*, 2240-2241.

39.   Reetz, M. T.; Lohmer, G., Propylene Carbonate Stabilized Nanostructured Palladium Clusters as Catalysts in Heck Reactions. *Chem Commun* **1996**, 1921-1922.

40.   Spiro, M.; de Jesus, D. M., Nanoparticle Catalysis in Microemulsions: Oxidation of N,N-Dimethyl-P-Phenylenediamine by Cobalt(Iii) Pentaammine Chloride Catalyzed by Colloidal Palladium in Water/Aot/N-Heptane Microemulsions. *Langmuir* **2000,** *16*, 2464-2468.

41.   Shiraishi, Y.; Toshima, N., Colloidal Silver Catalysts for Oxidation of Ethylene. *J Mol Catal a-Chem* **1999,** *141*, 187-192.

42.   Launay, F.; Roucoux, A.; Patin, H., Ruthenium Colloids: A New Catalyst for Alkane Oxidation by Tbhp in a Biphasic Water-Organic Phase System. *Tetrahedron Lett* **1998,** *39*, 1353-1356.

43.   Li, Y.; Hong, X. M.; Collard, D. M.; El-Sayed, M. A., Suzuki Cross-Coupling Reactions Catalyzed by Palladium Nanoparticles in Aqueous Solution. *Org Lett* **2000,** *2*, 2385-2388.

44.   Li, Y.; Boone, E.; El-Sayed, M. A., Size Effects of Pvp-Pd Nanoparticles on the Catalytic Suzuki Reactions in Aqueous Solution. *Langmuir* **2002,** *18*, 4921-4925.

45.   Li, Y.; El-Sayed, M. A., The Effect of Stabilizers on the Catalytic Activity and Stability of Pd Colloidal Nanoparticles in the Suzuki Reactions in Aqueous Solution. *J Phys Chem B* **2001,** *105*, 8938-8943.

46.   Narayanan, R.; El-Sayed, M. A., Effect of Catalysis on the Stability of Metallic Nanoparticles: Suzuki Reaction Catalyzed by Pvp-Palladium Nanoparticles. *J Am Chem Soc* **2003,** *125*, 8340-8347.

47.   Narayanan, R.; El-Sayed, M. A., Effect of Colloidal Nanocatalysis on the Metallic Nanoparticle Shape: The Suzuki Reaction. *Langmuir* **2005,** *21*, 2027-2033.

48.   Narayanan, R.; El-Sayed, M. A., Effect of Nanocatalysis in Colloidal Solution on the Tetrahedral and Cubic Nanoparticle Shape: Electron-Transfer Reaction Catalyzed by Platinum Nanoparticles. *J Phys Chem B* **2004,** *108*, 5726-5733.

49.   Kogan, V.; Aizenshtat, Z.; Popovitz-Biro, R.; Neumann, R., Carbon−Carbon and Carbon−Nitrogen Coupling Reactions Catalyzed by Palladium Nanoparticles Derived

from a Palladium Substituted Keggin-Type Polyoxometalate. *Org Lett* **2002,** *4*, 3529-3532.

50.   Gopidas, K. R.; Whitesell, J. K.; Fox, M. A., Synthesis, Characterization, and Catalytic Applications of a Palladium-Nanoparticle-Cored Dendrimer. *Nano Letters* **2003,** *3*, 1757-1760.

51.   Na, Y.; Park, S.; Han, S. B.; Han, H.; Ko, S.; Chang, S., Ruthenium-Catalyzed Heck-Type Olefination and Suzuki Coupling Reactions: Studies on the Nature of Catalytic Species. *J Am Chem Soc* **2004,** *126*, 250-258.

52.   Yeung, L. K.; Crooks, R. M., Heck Heterocoupling within a Dendritic Nanoreactor. *Nano Letters* **2001,** *1*, 14-17.

53.   Caló, V.; Nacci, A.; Monopoli, A.; Laera, S.; Cioffi, N., Pd Nanoparticles Catalyzed Stereospecific Synthesis of B-Aryl Cinnamic Esters in Ionic Liquids. *The Journal of Organic Chemistry* **2003,** *68*, 2929-2933.

54.   Narayanan, R.; El-Sayed, M. A., Effect of Catalytic Activity on the Metallic Nanoparticle Size Distribution: Electron-Transfer Reaction between Fe(Cn)(6) and Thiosulfate Ions Catalyzed by Pvp-Platinum Nanoparticles. *J Phys Chem B* **2003,** *107*, 12416-12424.

55.   Narayanan, R.; El-Sayed, M. A., Shape-Dependent Catalytic Activity of Platinum Nanoparticles in Colloidal Solution. *Nano Letters* **2004,** *4*, 1343-1348.

56.   Narayanan, R.; El-Sayed, M. A., Changing Catalytic Activity During Colloidal Platinum Nanocatalysis Due to Shape Changes: Electron-Transfer Reaction. *J Am Chem Soc* **2004,** *126*, 7194-7195.

57.   Yoo, J. W.; Hathcock, D. J.; El-Sayed, M. A., Propene Hydrogenation over Truncated Octahedral Pt Nanoparticles Supported on Alumina. *J Catal* **2003,** *214*, 1-7.

58.   Yoo, J. W.; Hathcock, D.; El-Sayed, M. A., Characterization of Pt Nanoparticles Encapsulated in Al2o3 and Their Catalytic Efficiency in Propene Hydrogenation. *J Phys Chem A* **2002,** *106*, 2049-2054.

59.   Ohde, H.; Ohde, M.; Wai, C. M., Swelled Plastics in Supercritical Co2 as Media for Stabilization of Metal Nanoparticles and for Catalytic Hydrogenation. *Chem Commun* **2004**, 930-931.

60.   Adlim, M.; Abu Bakar, M.; Liew, K. Y.; Ismail, J., Synthesis of Chitosan-Stabilized Platinum and Palladium Nanoparticles and Their Hydrogenation Activity. *J Mol Catal a-Chem* **2004,** *212*, 141-149.

61.   Boudjahem, A. G.; Monteverdi, S.; Mercy, M.; Bettahar, M. M., Study of Nickel Catalysts Supported on Silica of Low Surface Area and Prepared by Reduction of Nickel Acetate in Aqueous Hydrazine. *J Catal* **2004,** *221*, 325-334.

62.   Claus, P.; Hofmeister, H., Electron Microscopy and Catalytic Study of Silver Catalysts: Structure Sensitivity of the Hydrogenation of Crotonaldehyde. *J Phys Chem B* **1999,** *103*, 2766-2775.

63.   Anderson, M. L.; Stroud, R. M.; Rolison, D. R., Enhancing the Activity of Fuel-Cell Reactions by Designing Three-Dimensional Nanostructured Architectures: Catalyst-Modified Carbon-Silica Composite Aerogels. *Nano Letters* **2002,** *2*, 235-240.

64.   Long, J. W.; Stroud, R. M.; Swider-Lyons, K. E.; Rolison, D. R., How to Make Electrocatalysts More Active for Direct Methanol Oxidation - Avoid Ptru Bimetallic Alloys! *J Phys Chem B* **2000,** *104*, 9772-9776.

65.   Moore, J. T.; Corn, J. D.; Chu, D.; Jiang, R. Z.; Boxall, D. L.; Kenik, E. A.; Lukehart, C. M., Synthesis and Characterization of a Pt3ru1/Vulcan Carbon Powder Nanocomposite and Reactivity as a Methanol Electrooxidation Catalyst. *Chem Mater* **2003,** *15*, 3320-3325.

66.   Front Matter. In *Nanoparticles and Catalysis*, Wiley-VCH Verlag GmbH & Co. KGaA: 2008; pp I-XXIII.

67.   Bonnemann, H.; Brijoux, W.; Brinkmann, R.; Dinjus, E.; Joussen, T.; Korall, B., Formation of Colloidal Transition-Metals in Organic Phases and Their Application in Catalysis. *Angew Chem Int Edit* **1991,** *30*, 1312-1314.

68.   Narayanan, R.; El-Sayed, M. A., Catalysis with Transition Metal Nanoparticles in Colloidal Solution: Nanoparticle Shape Dependence and Stability. *J Phys Chem B* **2005,** *109*, 12663-12676.

69.   Schmid, G., Large Clusters and Colloids - Metals in the Embryonic State. *Chemical Reviews* **1992,** *92*, 1709-1727.

70.   Daniel, M.-C.; Astruc, D., Gold Nanoparticles: Assembly, Supramolecular Chemistry, Quantum-Size-Related Properties, and Applications toward Biology, Catalysis, and Nanotechnology. *Chemical Reviews* **2004,** *104*, 293-346.

71.   Astruc, D.; Lu, F.; Aranzaes, J. R., Nanoparticles as Recyclable Catalysts: The Frontier between Homogeneous and Heterogeneous Catalysis. *Angewandte Chemie International Edition* **2005,** *44*, 7852-7872.

72.   Lu, A.-H.; Salabas, E. L.; Schüth, F., Magnetic Nanoparticles: Synthesis, Protection, Functionalization, and Application. *Angewandte Chemie International Edition* **2007,** *46*, 1222-1244.

73.   Fernández-García, M.; Martínez-Arias, A.; Hanson, J. C.; Rodriguez, J. A., Nanostructured Oxides in Chemistry: Characterization and Properties. *Chemical Reviews* **2004,** *104*, 4063-4104.

74.   Roucoux, A.; Schulz, J.; Patin, H., Reduced Transition Metal Colloids: A Novel Family of Reusable Catalysts? *Chemical Reviews* **2002,** *102*, 3757-3778.

75.   Crooks, R. M.; Zhao, M.; Sun, L.; Chechik, V.; Yeung, L. K., Dendrimer-Encapsulated Metal Nanoparticles: Synthesis, Characterization, and Applications to Catalysis. *Accounts of Chemical Research* **2001,** *34*, 181-190.

76.   Roy, S.; Pericàs, M. A., Functionalized Nanoparticles as Catalysts for Enantioselective Processes. *Organic & Biomolecular Chemistry* **2009,** *7*, 2669-2677.

77.   Buchmeiser, M. R., Homogeneous Metathesis Polymerization by Well-Defined Group Vi and Group Viii Transition-Metal Alkylidenes: Fundamentals and Applications in the Preparation of Advanced Materials. *Chemical Reviews* **2000,** *100*, 1565-1604.

78.   Wang, Z.; Chen, G.; Ding, K., Self-Supported Catalysts. *Chemical Reviews* **2009,** *109*, 322-359.

79.   Trindade, A. F.; Gois, P. M. P.; Afonso, C. A. M., Recyclable Stereoselective Catalysts. *Chemical Reviews* **2009,** *109*, 418-514.

80.   Turkevich, J.; Stevenson, P. C.; Hillier, J., A Study of the Nucleation and Growth Processes in the Synthesis of Colloidal Gold. *Discussions of the Faraday Society* **1951,** *11*, 55-75.

81.   Jana, N. R.; Gearheart, L.; Murphy, C. J., Seed-Mediated Growth Approach for Shape-Controlled Synthesis of Spheroidal and Rod-Like Gold Nanoparticles Using a Surfactant Template. *Advanced Materials* **2001,** *13*, 1389-1393.

82.   Brust, M.; Walker, M.; Bethell, D.; Schiffrin, D. J.; Whyman, R., Synthesis of Thiol-Derivatised Gold Nanoparticles in a Two-Phase Liquid–Liquid System. *Journal of the Chemical Society, Chemical Communications* **1994**, 801-802.

83.   Panigrahi, S.; Basu, S.; Praharaj, S.; Pande, S.; Jana, S.; Pal, A.; Ghosh, S. K.; Pal, T., Synthesis and Size-Selective Catalysis by Supported Gold Nanoparticles: Study on Heterogeneous and Homogeneous Catalytic Process. *The Journal of Physical Chemistry C* **2007,** *111*, 4596-4605.

84.   Rode, C. V.; Vaidya, M. J.; Chaudhari, R. V., Synthesis of P-Aminophenol by Catalytic Hydrogenation of Nitrobenzene. *Organic Process Research & Development* **1999,** *3*, 465-470.

85.   Lai, T.-L.; Yong, K.-F.; Yu, J.-W.; Chen, J.-H.; Shu, Y.-Y.; Wang, C.-B., High Efficiency Degradation of 4-Nitrophenol by Microwave-Enhanced Catalytic Method. *Journal of Hazardous Materials* **2011,** *185*, 366-372.

86.   Narayanan, K. B.; Sakthivel, N., Synthesis and Characterization of Nano-Gold Composite Using Cylindrocladium Floridanum and Its Heterogeneous Catalysis in the Degradation of 4-Nitrophenol. *Journal of Hazardous Materials* **2011,** *189*, 519-525.

87.   Wunder, S.; Polzer, F.; Lu, Y.; Mei, Y.; Ballauff, M., Kinetic Analysis of Catalytic Reduction of 4-Nitrophenol by Metallic Nanoparticles Immobilized in Spherical Polyelectrolyte Brushes. *The Journal of Physical Chemistry C* **2010,** *114*, 8814-8820.

88.   Khalavka, Y.; Becker, J.; Sönnichsen, C., Synthesis of Rod-Shaped Gold Nanorattles with Improved Plasmon Sensitivity and Catalytic Activity. *J Am Chem Soc* **2009,** *131*, 1871-1875.

89.   Eley, D. D.; Rideal, E. K., Parahydrogen Conversion on Tungsten. *Nature* **1940,** *146*, 401.

90.   Sarkar, S.; Guria, A. K.; Pradhan, N., Influence of Doping on Semiconductor Nanocrystals Mediated Charge Transfer and Photocatalytic Organic Reaction. *Chem Commun* **2013,** *49*, 6018-6020.

91.   Schaub, R.; Wahlström, E.; Rønnau, A.; Lægsgaard, E.; Stensgaard, I.; Besenbacher, F., Oxygen-Mediated Diffusion of Oxygen Vacancies on the Tio₂(110) Surface. *Science* **2003,** *299*, 377-379.

92.   Langmuir, I., The Mechanism of the Catalytic Action of Platinum in the Reactions 2co + O2= 2co2 and 2h2+ O2= 2h2o. *Transactions of the Faraday Society* **1922,** *17*, 621-654.

93.   Ansar, S. M.; Kitchens, C. L., Impact of Gold Nanoparticle Stabilizing Ligands on the Colloidal Catalytic Reduction of 4-Nitrophenol. *ACS Catalysis* **2016,** *6*, 5553-5560.

CHAPTER TWO

COMPARISON OF COLLOIDAL VERSUS SUPPORTED GOLD NANOPARTICLE
CATALYSIS
[As published in *J. Phys. Chem. C 122, 14, 7749-7758 (2018)* with minor revisions]

2.1 Introduction

Gold was once considered an inert metal, but gold nanoparticles (AuNPs) have been

established as a very effective and widely used catalyst since the seminal works of Haruta[1]

in the late 1990s. Numerous studies since then have explored various AuNPs in catalyzing

reactions that include CO oxidation,[2] propylene epoxidation,[3] low temperature water gas

shift reactions,[4-5] alcohol oxidation,[6] nitroarene reduction [7] and carbon-carbon cross

coupling[8] to name a few. For industrial production of fine chemicals, AuNP and other

colloidal nanoparticle catalysts are immobilized on different supports, primarily due to the

advantage of catalyst recovery using simple mechanical methods like centrifugation,

filtration or sedimentation.[9] Supported catalysts are also effectively implemented in

continuous reactor systems with a stationary support for large scale chemical reactions.[10-11] Colloidal AuNPs have been theorized to be more catalytically active, have greater

selectivity and have greater opportunity in chiral catalysis than supported NPs.[11] Due to

difficulties in colloidal NP recovery, the application of colloidal catalysis is limited.[12-14]

Although there have been various studies on colloidal NPs and supported NPs

independently, there has been little systematic comparisons of the catalytic activity and

surface properties of the same colloidal NP system and the supported counterpart.

The main technique used to characterize NP catalyst surface area is through chemisorption

of small gas molecules like CO and H_2 on the catalyst particle surface. Unfortunately, gold

is not amenable to chemisorption of many molecules and thus few studies have characterized supported AuNPs with chemisorption.[15-19] Recently, Menegazzo and co-workers[20] performed CO chemisorption by a pulse flow technique and Fourier Transform Infrared (FTIR) measurements of adsorbed CO under strict control of temperature (140-180 K) effectively determining gold catalytic sites in the Au/TiO_2, Au/Fe_2O_3 and Au/ZrO_2 systems.[21] Although effective, these methods are specific to solid catalysts and cannot be applied to analogous colloidal catalyst systems. Other researchers have used transmission electron microscope (TEM) to quantify the available surface area which assumes shape and size monodispersity and is limited by small sample sizes.[22] However, TEM analysis does not provide any information about attached surface ligands or presence of surface roughness, which subsequently introduces inaccuracies in quantification of available surface area. Use of small molecular probes like organothiols is an effective tool to quantify catalyst surface area accurately for both supported and colloidal catalysts.

In this work, the catalytic activity of colloidal AuNP and supported AuNP catalysts is compared for the AuNP catalyzed reduction of 4-nitrophenol (4-NP) to 4-aminophenol (4-AP) by sodium borohydride. Citrate-stabilized AuNPs with a core diameter 5.6 ± 1.4 nm were investigated as colloidal AuNPs ($AuNP_{col}$). Subsequent immobilization of the colloidal AuNP on titania (80% anatase, 15% rutile and 5% amorphous phases with average particle diameter of 21 nm) yielded the supported AuNP catalyst ($AuNP_{sup}$). The advantage of using colloidal AuNPs on supports is greater control of particle size and removing support effects on the synthesized AuNP size, polydispersity and morphology in order to better elucidate size effects on catalysis. Citrate was intentionally chosen as the

stabilizing ligand because citrate binds weakly to AuNP surface and AuNP$_{col}$ and AuNP$_{sup}$ can be both considered 'naked'. The reactants and organothiol probe used in this study readily displace citrate from the AuNP surface during kinetic and adsorption measurements. High temperature annealing of supported catalysts is a preferred method to remove surface-bound ligands. Supported AuNP catalysts used in this study were separately annealed (AuNP$_{ann}$) to study effects of annealing on catalytic activity of AuNPs. Pal,[23] Esumi[24] and others have demonstrated 4-NP reduction reaction as a model reaction with no side reactions and ability for real-time in-situ monitoring using UV-Vis spectroscopy. The reaction conversion is determined from the change in intensity of the nitrophenolate ion peak at 400 nm. The reaction is conducted with excess NaBH$_4$ and treated as a pseudo first order reaction.[23-25] In this study, the pseudo first order rate constant is used for comparing the activity of AuNP$_{col}$ and AuNP$_{sup}$ catalysts.

AuNPs possess corners, edges and surface Au atoms which are reported to be the active sites for AuNP catalyzed reactions and deposition of colloidal AuNPs on a support results in a loss of available surface area and thus a reduction in available active sites.[26-29] Conversely, AuNP immobilization on supports can create special sites at the AuNP-support interfaces. Corners and edge sites at the metal-metal oxide support interface have been shown to be unique reaction sites with greater activity due to the low coordination of the Au atoms.[1, 30-31] Charge transfer between AuNP and support can also alter the electronic structure of the AuNP leading to enhanced catalytic activity for CO oxidation reactions, demonstrated both experimentally and computationally.[32-36]

In this work, UV-Vis absorption spectroscopy of 2-mercaptobenzimidazole (2-MBI) was used to quantify the available surface area on the colloidal AuNPs and supported AuNPs. Zhang[37] and Ansar[38] demonstrated the applicability of this technique to determine free surface area in thiolated polyethylene glycol (PEG-SH) stabilized AuNPs. We have quantified and contrasted catalytic activity of colloidal and supported AuNP in this treatise and subsequently measured the contribution of the support towards catalytic activity of the AuNP for the reduction of 4-NP. Induction time observed during 4-NP reduction reaction has also been examined and effect of reactant addition sequence and reactant concentration has been investigated in detail.[7, 22]

2.2 Methods

2.2.1. Chemicals and Instrumentation.

All reagents were purchased from Sigma Aldrich, except the P25 Aeroxide[39] titania support (80% anatase, 15% rutile and 5% amorphous phases with average particle diameter of 21 nm) which was purchased from Acros Organics. Aqua Regia was prepared at a 3:1 molar ratio of hydrochloric acid (37 %, 12 M extra pure) to nitric acid (69-71% extra pure) for Au digestion for ICP-OES (Inductively Coupled Plasma- Optical Emission Spectroscopy) analysis. 25mm cellulose acetate (CA) syringe filters (0.45 µm) were purchased from VWR International. Milli-Q water (resistivity > 18.2 MΩ.cm) was used for synthesis and reactions. UV-Vis spectra was acquired using a Varian Cary 50 UV-Vis-NIR spectrophotometer. ICP-OES data was acquired on a Perkin Elmer Optima 3100RL ICP-OES. TEM imaging was conducted on a Hitachi H9500 HRTEM (accelerating voltage of 300 kV) and Hitachi H7600 (accelerating voltage of 120 kV). STEM imaging was

conducted on a Hitachi HD2000 STEM. Formvar coated 300 mesh Cu grids were purchased from Electron Microscopy Sciences (EMS). Energy Dispersive Spectroscopy (EDS) analysis for elements was conducted on the HD2000.

2.2.2. AuNP synthesis.

Citrate-stabilized colloidal AuNPs were synthesized using a classic sodium borohydride reduction of gold precursor in presence of trisodium citrate.[40] Briefly, 125 µL of 0.1 M $HAuCl_4$ and 125 µL 0.1 M trisodium citrate solution was added to 50 mL deionized water and stirred with a magnetic stir bar. Drop wise addition of 500 µL of a solution of 38 mg of sodium borohydride in 20 mL of ice cold deionized water led to a color change of the solution from colorless to ruby red rapidly indicating the formation of colloidal citrate-stabilized AuNP. The UV-Vis maximum peak absorbance was at wavelength of 511 nm and size analysis using TEM of more than 1000 AuNPs using ImageJ[41] revealed a mean diameter of 5.6 ± 1.4 nm (Figure 2.1).
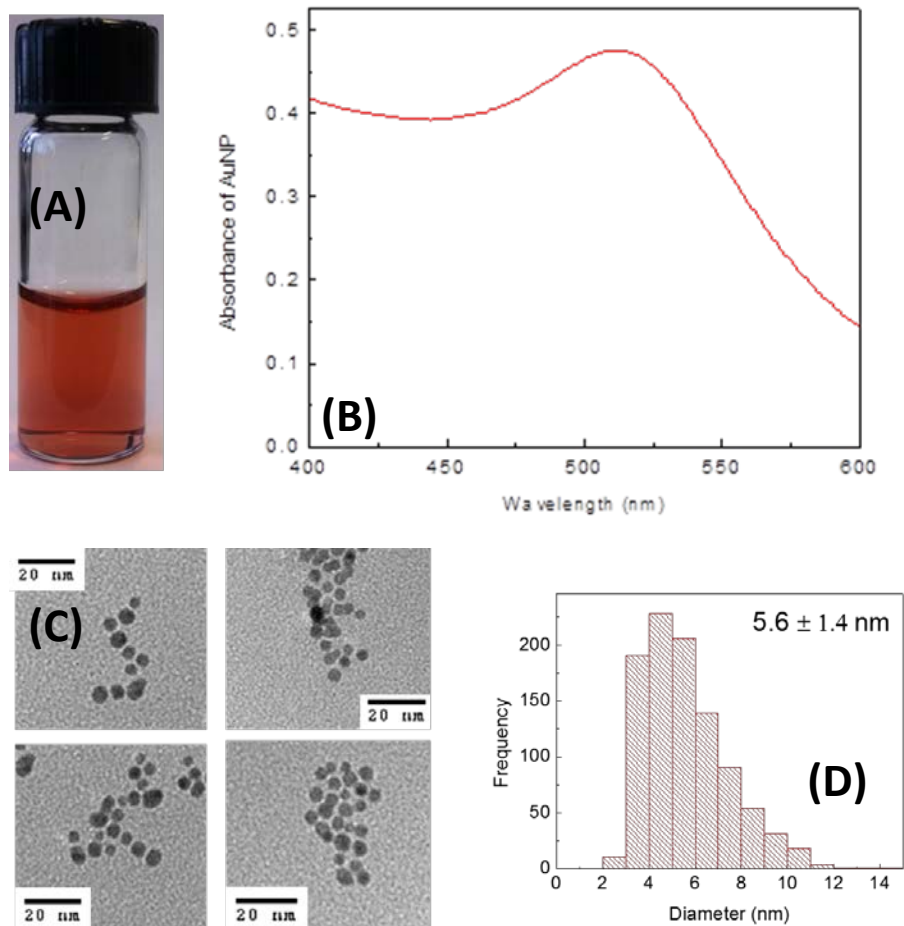
Figure 2.1. (A) AuNP-Cit colloidal catalyst. (B) LSPR peak (obtained from UV-Vis spectroscopy), (C) and (D) AuNP colloidal size analysis (obtained from transmission electron microscopy).

2.2.3. Deposition of colloidal AuNP on titanium dioxide.

Colloidal AuNP was immobilized on titania by adjusting pH of the mixture to the point of zero charge (PZC). Colloidal AuNP stability with pH was examined by UV-Vis spectroscopy by systematically changing the pH from 5.6 to 2.7 and particle aggregation was observed below pH 4. Colloidal AuNP and titania dispersion were mixed physically for 24 hours at pH 4. UV-Vis absorbance spectra of aqueous phase after gravity separation

of titania/AuNP indicated complete AuNP deposition at pH 4. AuNPs were immobilized on the titania support at Au loading (Au basis) of 1, 5 and 10 wt% (hereafter referred to as 1AuNP$_{sup}$, 5AuNP$_{sup}$ and 10AuNP$_{sup}$). For the 10AuNP$_{sup}$, 900 mg of titania was dispersed in 20 mL of deionized water and sonicated by a tip sonicator (Fisher Scientific 550 Sonic Dismembrator) for 10 min at 30% power and then pH adjusted to pH = 4. The pH of colloidal AuNP containing 100 mg Au was adjusted to pH = 4 and mixed with the titania dispersion overnight with magnetic stirring. Successful deposition of AuNPs on the support was indicated by a color change of titania from white to pink and the supernatant becoming a colorless solution. The supported AuNP was centrifuged and subsequently dried using a vacuum dryer to obtain dry supported catalyst. Annealing of dry supported catalyst (hereafter referred to as 10AuNP$_{ann}$, 5AuNP$_{ann}$ and 1AuNP$_{ann}$) were carried out at 400 °C in silica crucibles in oxygen for an hour using a muffle furnace with an electric heating coil. (Figure 2.2)

Figure 2.2. Immobilization of colloidal citrate-AuNP on titania and subsequent annealing at 400 °C. The growth of AuNP on titania during the annealing process is evident because of the color change from dark pink to purple.

2.2.4. Determination of Au concentration.

Concentration of Au in colloidal AuNP and Au loading on supported catalyst was determined using ICP-OES on a Perkin Elmer Optima 3100RL ICP-OES. Known mass of

supported catalysts were digested in concentrated freshly prepared aqua regia for 12 hours under constant stirring and diluted 20 fold in deionized water to obtain 5% (v/v %) aqua regia. Standards in the range of 0.1-100 ppm Au were prepared in 5% aqua regia.

2.2.5. Size Analysis using Electron Microscopy.

TEM grids of catalysts were prepared by drop casting 5 µL of the as-prepared supported AuNP suspension and resting for 1 minute. The excess liquid sample was wicked away using a Whatman filter paper. The particle size distribution of AuNP on the surface of titania and morphology were examined by high resolution transmission electron microscopy (HR-TEM). Scanning Transmission Electron Microscopy (STEM) analysis with Energy Dispersive Spectroscopy (EDS) was performed to confirm presence of AuNP on the support via Z-contrast images. Size analysis was conducted on ImageJ[41] software (Figure 2.3 and 2.4) and two tailed t-test (exceeding 95% confidence level) statistical analysis was conducted.
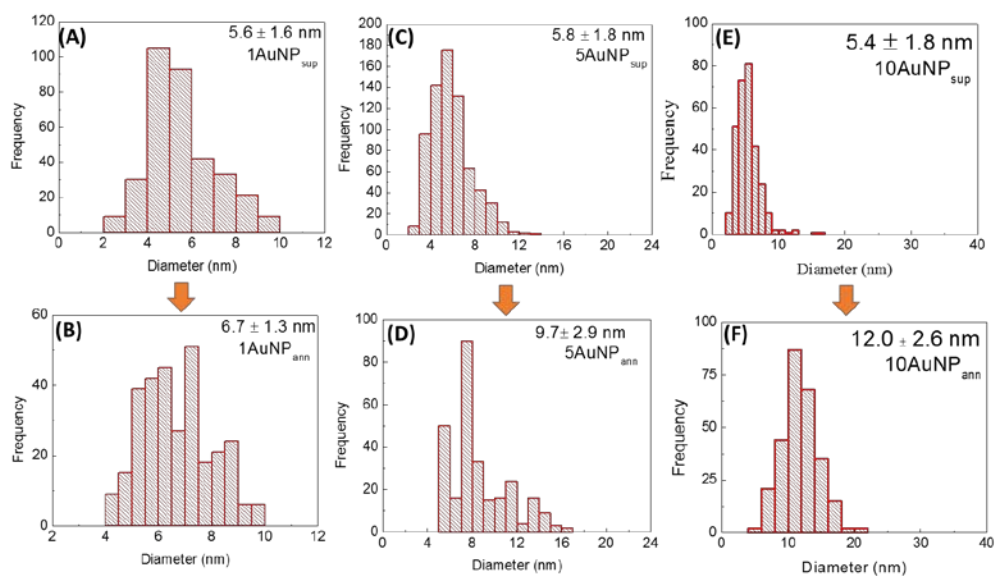
Figure 2.3. Size analysis of catalyst (A) 1AuNP$_{sup}$ & (B) 1AuNP$_{ann}$; (C) 5AuNP$_{sup}$ & (D) 5AuNP$_{ann}$ and (E) 10AuNP$_{sup}$ & (F) 10AuNP$_{ann}$. Increase in size of AuNP due to annealing can be clearly observed.
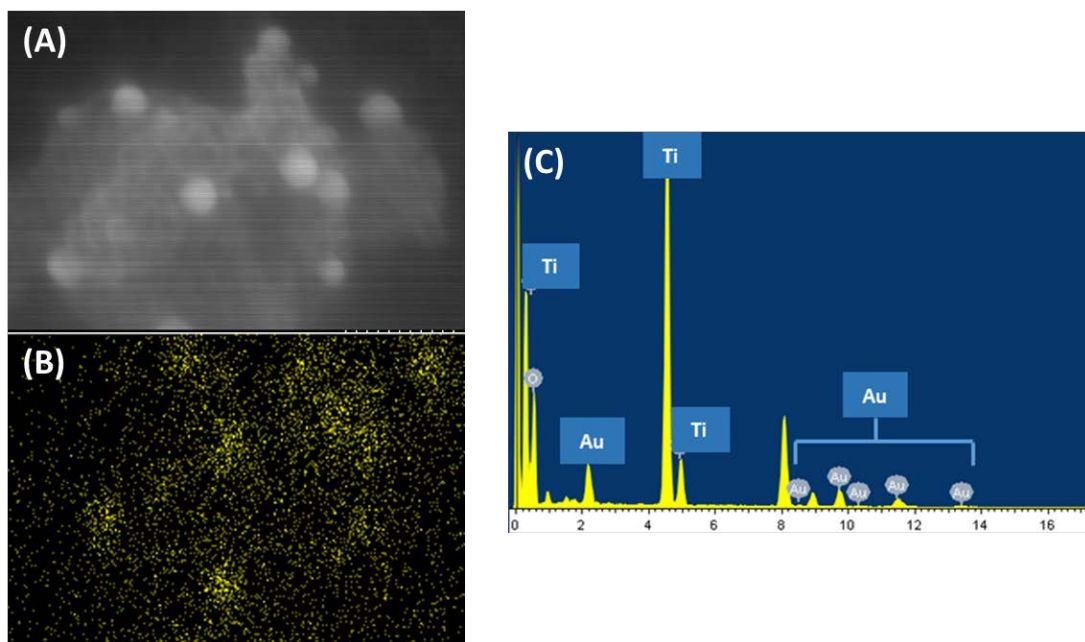
Figure 2.4. STEM images of immobilized AuNP on titania (A) AuNP on titania in scanning electron microscopy mode, (B) EDS image where concentrated yellow scatter points represent AuNP corresponding to Figure 1.4A and (C) corresponding EDS spectra.

2.2.6. 4-Nitrophenol Reduction Catalysis for Kinetics.

For AuNP$_{sup}$ catalysts, the 4-NP reduction reaction was carried out in a 4 mL stirred quartz cell and monitored by UV-Vis absorbance spectroscopy. All reactions with supported catalysts contained a supported catalyst mass of 0.1 mg (AuNP + TiO$_2$) and total volume of 3 mL. For example, the 10AuNP$_{sup}$ reaction used 1 mL of 0.2 mM 4-NP, 900 µL DI water and 800 µL of 10AuNP$_{sup}$ suspension (0.125 mg/mL catalyst) in a 4 mL stirred quartz cell. 300 µL of NaBH$_4$ in deionized water (5 mg/mL) was added to the quartz cell and time-resolved UV-Vis spectra were acquired for 60 mins. The intensity of the 4-NP peak at 400 nm was used to track reaction progress. Amount of annealed supported catalysts (10AuNP-$_{ann}$) was similarly used which contained same amounts of Au as 10AuNP$_{sup}$. For equivalent

colloidal AuNP catalyst 10AuNP$_{col}$, 1 mL of 0.2 mM 4-NP was mixed with 1516 µL of DI water and 184 µL of AuNP colloid (0.05 mg Au/mL concentration). 300 µL of NaBH$_4$ freshly prepared solution (5 mg/mL) was added and time-resolved spectra were acquired for 60 min. Induction time experiments were conducted in a similar manner using the 1AuNP$_{col}$ and 1AuNP$_{sup}$ catalysts where induction times were observed. Mixing sequences, 4-NP concentrations and NaBH$_4$ concentrations were varied as detailed in the discussion section. N$_2$ purging was carried out by bubbling reactants with N$_2$ gas for 2 hours. Purged reactants were mixed under a N$_2$ environment and sealed with a PTFE cuvette cap and parafilm under nitrogen.

2.2.7. 2-MBI Adsorption to quantify available surface area.

To quantify the available surface area on AuNP, 2-MBI adsorption method was used. The kinetics of 2-MBI adsorption was measured to determine the time required for complete saturation of the Au surface. For the supported catalysts, 0.2 mg of Au (17.5 mg, 4.3 mg and 2.2 mg for 1AuNP$_{sup}$, 5AuNP$_{sup}$ and 10AuNP$_{sup}$, respectively) was mixed with 30 µM solution of 2-MBI under constant stirring. 20 mg of pure titania was also used in a similar manner as control. Aliquots were drawn at regular intervals from the mixture and filtered through a 0.45 µm cellulose acetate syringe filter to remove the supported catalyst. The absorbance intensity at 300 nm was used to quantify 2-MBI adsorption rate and total time for 2-MBI saturation on the AuNP surface. The total adsorbed moles of 2-MBI was confirmed with a 24 hour room temperature incubation. Colloidal AuNP and annealed AuNP catalysts were examined in a similar manner. All surface area measurements are in

terms of number of molecules of 2-MBI adsorbed thus yielding a relative measure of surface area.

2.3 Results and Discussion

UV-Vis analysis of the as-prepared colloidal AuNPs had a maximum absorption at 511 nm which is a characteristic localized surface plasmon resonance (LSPR) absorption for 5 nm colloidal AuNP in water (Figure 2.1). TEM images of the colloidal citrate-stabilized AuNPs revealed the mean diameter to be 5.6 ± 1.4 nm (Figure 2.1). AuNPs deposited on titania was imaged by HRTEM and STEM (Figure 2.5). STEM and EDS analysis confirmed the successful immobilization of AuNP on titania and Figure 2.5 C shows various facets, edges and vertices of the embedded AuNP.
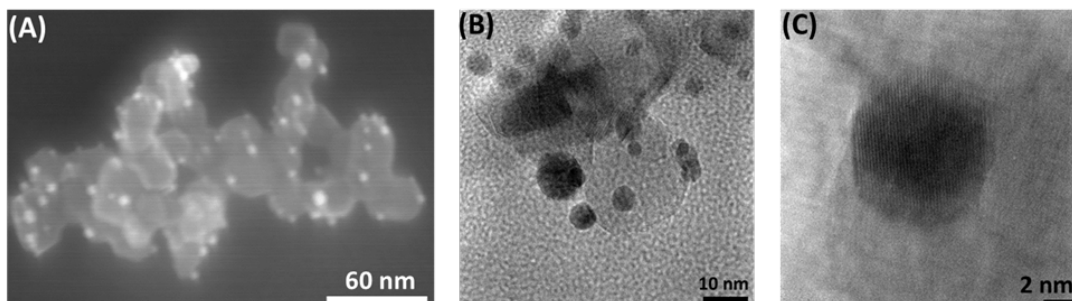
Figure 2.5. (A) STEM image of typical 5AuNP$_{sup}$ catalyst under scanning mode. (B) and (C) HR-TEM image of a typical 5AuNP$_{sup}$ catalyst depicting various facets, edges and vertices of AuNP on titania.

Figure 2.6 shows example TEM images and particle size distribution for 10AuNP$_{sup}$ and 10AuNP$_{ann}$. The size distributions of AuNP for all catalyst systems have been summarized in Figure 2.6. High resolution d-spacing of the support and AuNPs immobilized on the support before and after annealing obtained from HRTEM images showed no observable change in lattice structure due to annealing.

44

(E) AuNP Catalyst	Mean Diameter (nm)	Actual Au loading (%wt)
AuNP$_{col}$	5.6± 1.4	NA
1AuNP$_{sup}$	5.6 ± 1.6	1.14 ± 0.02
1AuNP$_{ann}$	6.7 ± 1.3	1.13 ± 0.03
5AuNP$_{sup}$	5.8 ± 1.8	4.69 ± 0.03
5AuNP$_{ann}$	9.7 ± 2.9	5.44 ± 0.14
10AuNP$_{sup}$	5.4 ± 1.8	9.20 ± 0.09
10AuNP$_{ann}$	12.0 ± 2.6	9.15 ± 0.03
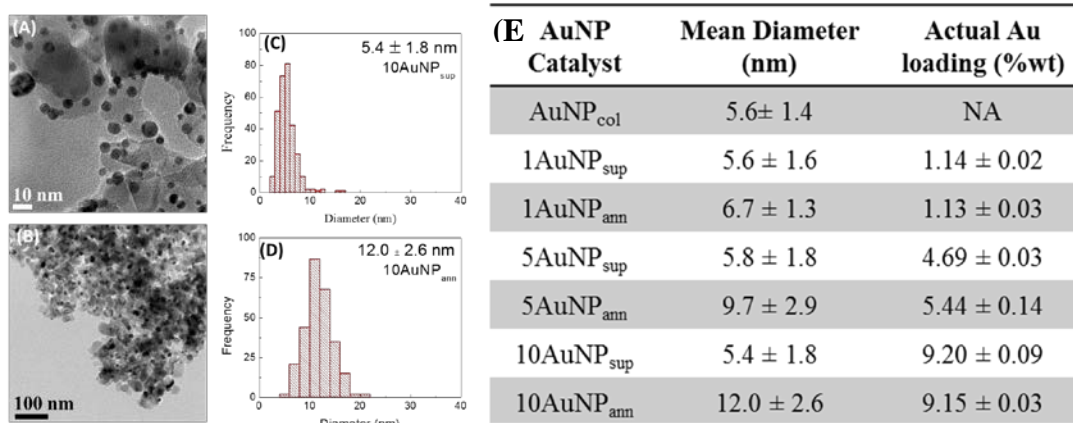
Figure 2.6. TEM images and size distribution of the AuNP on titania support for (A) and (C) 10AuNP$_{sup}$; (B) and (D) 10AuNP$_{ann.}$ (E) Size distributions of the colloidal and titania supported AuNP catalysts and Au loading (wt %). Size distribution histograms are shown in (Figure 2.3)

From Figure 2.6, the size distribution of AuNP$_{sup}$ are statistically equivalent to the AuNP$_{col}$ demonstrating that pH adjustment and immobilization process has no effect on the AuNP diameter. A statistically significant increase in the mean diameter is observed for the 5AuNP$_{ann}$ and 10AuNP$_{ann}$ catalysts where extent of particle size growth increases with increased AuNP loading. The 1AuNP$_{ann}$ size distribution, despite having a nominally larger average diameter, was not statistically different from the AuNP$_{col}$ catalyst. Gold clusters are known to sinter due to a low Tammann temperature (395 $^{\circ}$C), making them unsuitable for high temperature reactions[42-43] and size growth via. an Ostwald ripening.[44] The extent of particle coalescence is dependent upon Au mobility and thus decreased particle separation distances with higher loading results in increase particle size growth. This also explains the lack of sintering effects in 1AuNP$_{ann}$ catalysts resulting in no statistical change in the mean diameter from the colloidal AuNP. AuNP crystal structure remained unaltered during annealing as evidenced by similar d-spacing of AuNP.
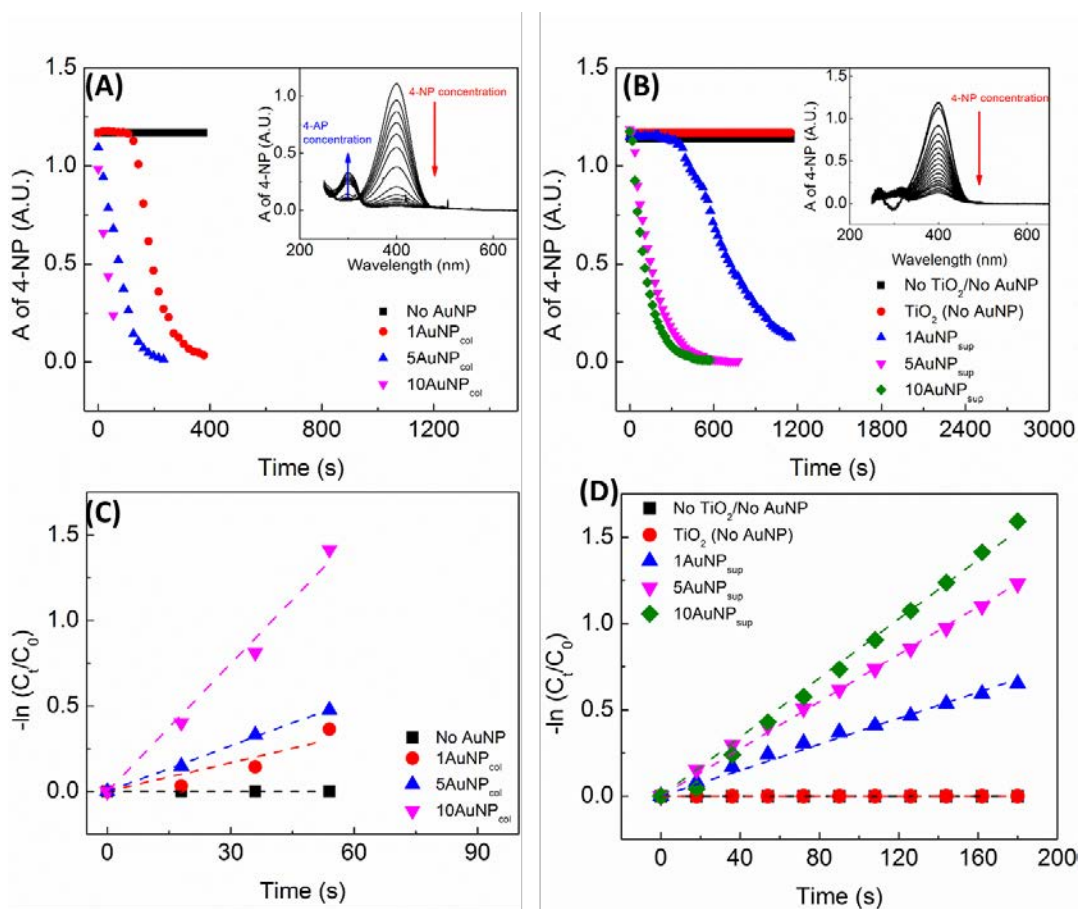
Figure 2.7. Comparison of catalytic activity for colloidal and supported AuNP catalyst with Au loading. (A), (B) In situ 4-NP peak intensity at 400 nm as a function of time, tracking the reaction progress for colloidal and supported catalyst respectively. Insets show typical spectra of 4-NP with time as reaction progresses (5AuNP$_{col}$ for 1.7A inset; 1AuNP$_{sup}$ for 1.7B inset). Negative intensity at 300 nm from 4-aminophenol peak in 1.7B (inset) is due to corrections to account for scattering from larger AuNP$_{sup}$ catalyst. Corresponding spectra for products at t = 12 hours was subtracted as background for all AuNP$_{sup}$/AuNP$_{ann}$ catalysts. (C) and (D) Absorbance data fit to pseudo first-order kinetics with respect to 4-NP to determine the rate constants.

Figure 2.7A and B present the 4-NP absorbance intensity at 400 nm, which demonstrates

the effect of AuNP concentration on the catalytic reduction of 4-NP to 4-AP for AuNP$_{col}$

and AuNP$_{sup}$ respectively. The absorbance decrease following the induction time was fit to

a pseudo first order rate equation (Figure 2.7C and 2.7D) and the slope of the linear fits

yield pseudo first order rate constants shown in Figure 2.8. It is important to note that 4-NP photo-catalytic reduction does not take place on titania (in presence of $NaBH_4$ and without AuNP) under reaction conditions.

(B) AuNP catalyst	Rate (min^{-1})	Induction Time (s)
$1AuNP_{col}$	0.34 ± 0.09	108 ± 18
$1AuNP_{sup}$	0.23 ± 0.03	486 ± 90
$1AuNP_{ann}$	0.04 ± 0.01	459 ± 99
$5AuNP_{col}$	0.53 ± 0.06	0
$5AuNP_{sup}$	0.41 ± 0.02	0
$5AuNP_{ann}$	0.14 ± 0.08	108 ± 18
$10AuNP_{col}$	1.10 ± 0.01	0
$10AuNP_{sup}$	0.51 ± 0.06	0
$10AuNP_{ann}$	0.28 ± 0.01	0
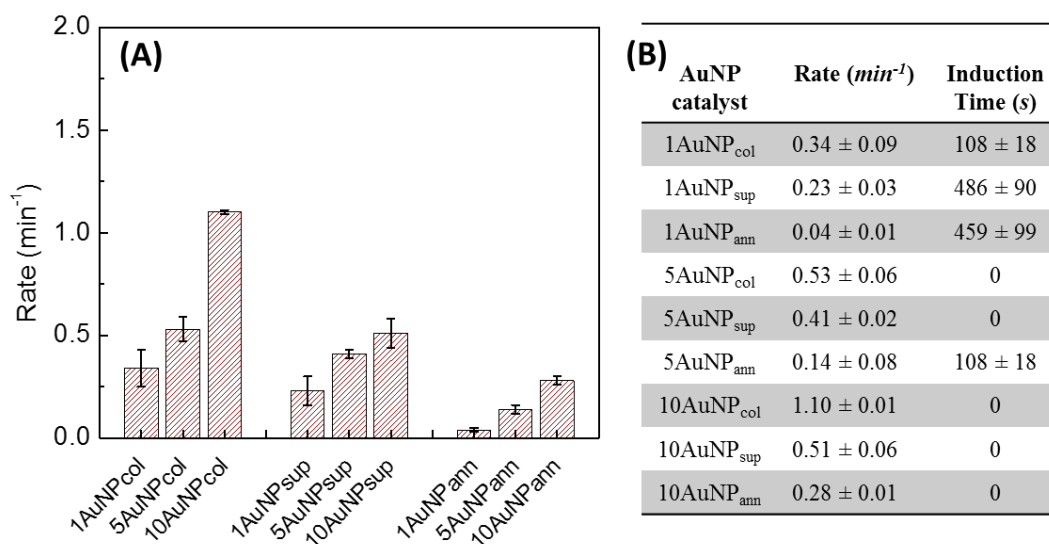
Figure 2.8. Summary of the reaction rate constants and induction times observed for each catalyst system. Measurements are averaged over three independent runs with one standard deviation reported as the error.

Rate constants increased with Au loading for each catalyst showing the kinetic dependence on AuNP concentration and intuitively on the Au available surface area. Rate constants decrease from colloidal AuNP to supported AuNP for all Au loadings (for example, 54% decrease in rate constant from $10AuNP_{col}$ to $10AuNP_{sup}$). Annealing resulted in further decrease in rate constant (for example, 75% reduction in rate constant from $10AuNP_{col}$ to $10AuNP_{ann}$). Changes in rate constant can be attributed to a combination of opposing effects, available surface area loss during immobilization, particle size change, surface restructuring, and synergistic support effects including generation of unique active site at

the AuNP-titania interfaces and charge transfer between support and AuNP. AuNPs mean diameter for $AuNP_{col}$ and $AuNP_{sup}$ does not change on immobilization. Decrease in activity of $10AuNP_{ann}$ and $5AuNP_{ann}$ can be explained by a combination of surface area loss due to immobilization and AuNP size growth. $1AuNP_{ann}$ does not show a statistically different size change on immobilization but a change in catalytic activity is observed from Figure 2.8B.

In order to directly measure the loss of available surface area with immobilization, we employed 2-MBI adsorption technique used in previous studies.[37-38, 45] Total number of molecules of 2-MBI adsorbed can be correlated to the available surface area and number of active sites available for the 4-NP reduction reaction, although 2-MBI does not differentiate between sites with different activities. The kinetics of 2-MBI adsorption on AuNP catalysts were examined and time required for complete saturation of AuNP surface with 2-MBI was found to be less than a minute due to the strong thiol-Au bond, ensuring complete saturation after 24 hours of incubation. This also shows that diffusion barriers are not present for 2-MBI adsorption on the 'naked' AuNPs in the absence of reactants.
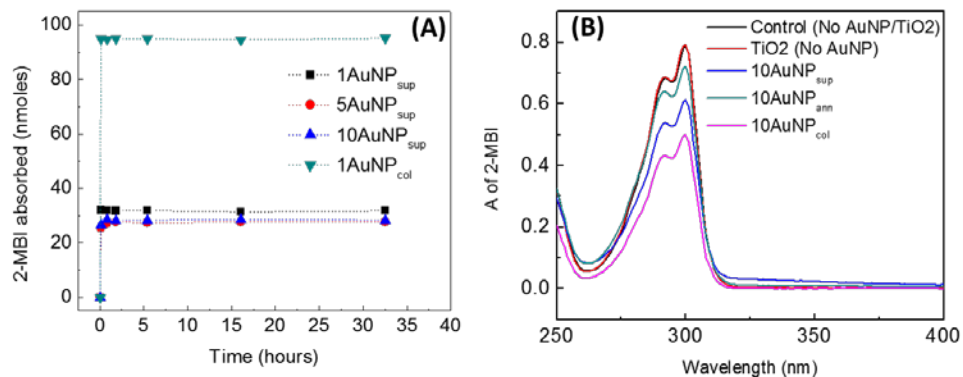
Figure 2.9. 2-MBI adsorption, (A) Adsorption kinetics of 2-MBI on AuNP$_{sup}$ and AuNP$_{col}$ systems (the dashed lines are for visual aid only) and (B) typical UV-Vis spectra of 2-MBI after incubation with various 10AuNP system for 24 hours showing decrease in intensity of 2-MBI absorbance.

Figure 2.9 shows that 2-MBI does not adsorb onto the TiO$_2$ support but selectively adsorbs to AuNP surface. Selectivity is a major advantage of this method to characterize available surface area of Au supported catalyst over other chemisorption methods. Furthermore, this method can be extended to colloidal systems and measured in the same media as the catalytic reaction.

AuNP catalyst	Specific available surface area x 10^{17} (*available surface area. mg^{-1} Au*)	% available surface area loss
$1AuNP_{col}$	2.51 ± 0.04	NA
$1AuNP_{sup}$	1.09 ± 0.03	56.6 ± 0.9
$1AuNP_{ann}$	1.05 ± 0.02	58.1 ± 0.5
$5AuNP_{col}$	2.59 ± 0.05	NA
$5AuNP_{sup}$	0.95 ± 0.02	63.3 ± 0.7
$5AuNP_{ann}$	0.74 ± 0.01	71.2 ± 0.9
$10AuNP_{col}$	2.55 ± 0.04	NA
$10AuNP_{sup}$	0.98 ± 0.05	61.3 ± 1.1
$10AuNP_{ann}$	0.68 ± 0.01	81.1 ± 0.6
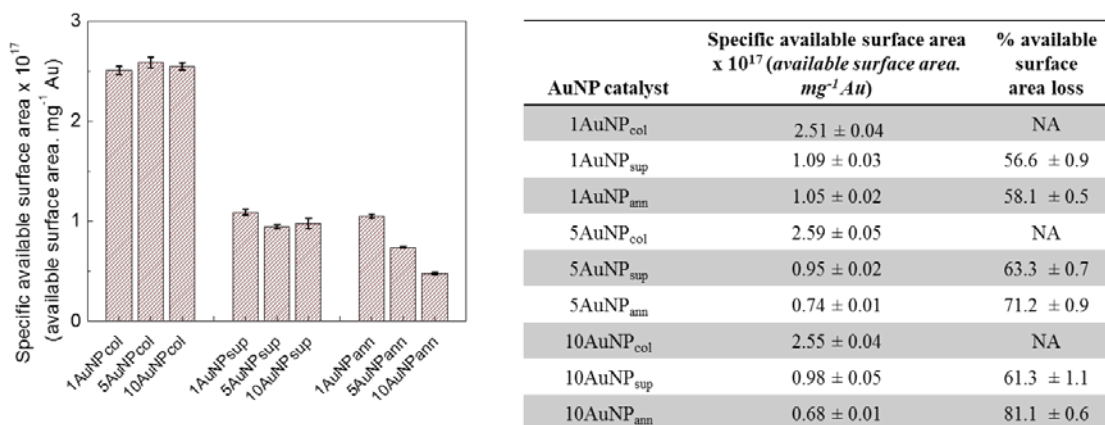
Figure 2.10. Specific available surface area measured from 2-MBI adsorption experiments. Available surface area is denoted in terms of molecules of 2-MBI adsorbed and depicts a relative measure of surface area.

Figure 2.10 presents the compiled 2-MBI adsorption results and demonstrates an average reduction in available surface area ca. 60% due to the $AuNP_{col}$ immobilization on the titania support. Annealed catalysts show a loss of surface area dependent on the Au loading (58%, 71% and 81% for $1AuNP_{ann}$, $5AuNP_{ann}$ and $10AuNP_{ann}$). Specific available surface area for all Au loadings of $AuNP_{sup}$ catalysts were statistically not different (two tailed t-test exceeding 95% confidence level) which is consistent with the similar AuNP size distribution on the support. We observe reduced specific available surface area for $5AuNP_{ann}$ and $10AuNP_{ann}$ catalysts, which is consistent with the increase in AuNP diameter. Figure 2.10 also shows no statistical difference in specific available surface area for the $1AuNP_{sup}$ and $1AuNP_{ann}$ catalyst, which is consistent with mean diameter measurements.
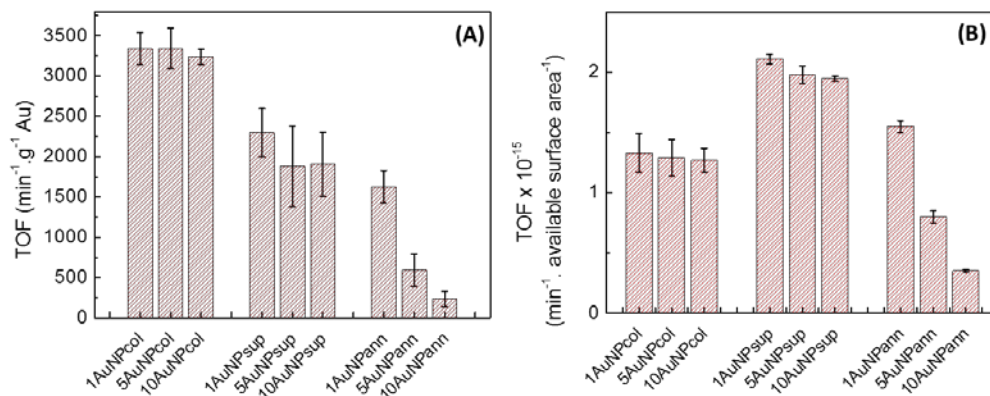
Figure 2.11. Turnover Frequency normalized to (A) mass of Au and (B) available surface area (in terms of adsorbed 2-MBI molecules). Results are averaged over three independent runs with one standard deviation reported as the error.

In order to directly compare catalytic activity of $AuNP_{col}$ to $AuNP_{sup}$ and $AuNP_{ann}$ catalyst, Turnover Frequency (TOF) normalized to the gold mass (TOF_M) and available surface area (TOF_{SA}) in each catalyst was examined. TOF is an important metric to compare different catalyst systems[46] and is used here to contrast the colloidal and supported AuNP catalyst and quantify the metal oxide support effect on catalytic activity in the 4-NP reduction reaction. On a gold mass basis, TOF_M for $AuNP_{sup}$ was ca.40% lower compared to $AuNP_{col}$ (Figure 2.11A). It is interesting to note that despite the surface area reduction of ca. 60% in case of $AuNP_{sup}$ compared to $AuNP_{col}$ (Figure 2.10A), the reduction in TOF_M is only ca. 40%. This suggests that new sites with greater catalytic activity are generated at the AuNP-TiO_2 interfaces and contribute to the $AuNP_{sup}$ less than proportionate decrease in TOF_M. TOF_M of $1AuNP_{ann}$ was found to be significantly lower than $1AuNP_{sup}$ although no statistically significant change in shape or size was observed on annealing. TOF_M for $5AuNP_{ann}$ and $10AuNP_{ann}$ were even more significantly decreased compared to $5AuNP_{sup}$ and $10AuNP_{sup}$ (68% and 87% reduction respectively) due to the change in size and

51

decreased surface area available per mass of Au. It is interesting to note that the change in TOF_M is much higher than the change in surface area (22% and 31% for $5AuNP_{ann}$ and $10AuNP_{sup}$). This can be explained by changes in electronic properties due to ripening and loss in surface features like vertices and edges due to the high temperature annealing.

To demonstrate the enhancement of catalytic activity of AuNP due to titania support, TOF_{SA} were compared for the colloidal and supported catalysts. TOF_{SA} accounts for the loss in surface area and normalizes the catalytic activity of the AuNP by the available surface area providing a good metric to judge the contribution of support. TOF_{SA} for $AuNP_{sup}$ was consistently higher than $AuNP_{col}$ for all Au loadings (Figure 2.11B), which can be attributed to the synergistic effect of the support towards AuNP catalytic activity for the 4-NP reduction reaction. Prior research has demonstrated that metal oxide supports stabilize and alter electronic properties of AuNPs.[35, 47] It has been proposed that contact edges between AuNPs and support are unique active sites with low coordinated Au atoms.[48] Theoretical calculations have shown that supports can play a crucial role in the activation of reactants bound to AuNP surface.[26] $1AuNP_{ann}$ shows a statistically significant increase in TOF_{SA} compared to colloidal AuNP but to a much lesser degree than $1AuNP_{sup}$ although no significant difference in AuNP diameters and surface area measured through 2-MBI adsorption was observed. This may be attributed to morphological changes on the surface of AuNP during annealing resulting in loss of edges and vertices which results in the loss of catalytic active sites. 2-MBI does not differentiate between sites with different activities, where similar available surface areas possess different rates of reaction and lower TOF_{SA} for $1AuNP_{ann}$ compared to $1AuNP_{sup}$. $5AuNP_{ann}$ and $10AuNP_{ann}$ show a substantial

decrease in TOF_{SA} compared to the colloidal AuNP and supported AuNP, also attributed to loss of vertices and edges as well as decreased activity due to increased AuNP size.[49-50] An induction time was observed for only the 1AuNP system. This phenomena has been proposed to be due to different mechanisms: a) diffusion time for substrate adsorption on the AuNP surface,[51-52] b) the presence of dissolved oxygen that reacts with $NaBH_4$ rather than 4-NP ,[53] c) oxide layer on the metal NP surface[54] and d) surface restructuring to render the AuNP surface active.[55] 4-NP reduction reactions were conducted in N_2 environment with all reactants purged with N_2, as well as in atmospheric conditions. No significant changes were observed in the induction time for both scenarios, which diminishes the dissolved oxygen argument for this work. Induction time has also been linked to ligand desorption/migration phenomena induced by $NaBH_4$.[38, 56] Catalysts used in this study did not have any protective ligands, except loosely bound citrate that is easily displaced by 4-NP and BH_4^- ions. Furthermore, the lack of induction time for the 2-MBI adsorption diminishes the desorption/migration explanation. In this work, the induction time is dependent on the concentration of AuNP present in the reaction media with all other factors remaining constant, suggesting a dependence on the relative amounts of reactant to the AuNP available surface area or active sites. All Au loadings show similar quantities of 2-MBI adsorbed and TEM analysis show that all AuNPs are present on the surface of titania. This suggests that AuNP available surface area are equally accessible to reactants and mass transfer resistances due to the heterogeneous nature of the catalyst is not a factor.

To examine the impact of reactants to the induction time, systematic experiments were conducted (with $1AuNP_{col}$ and $1AuNP_{sup}$) where the mixing sequence of reactants and

catalysts were altered. Control experiments were conducted following the same mixing sequence as the kinetic studies where 4-NP and catalysts were incubated before addition of $NaBH_4$. An induction time of 108 ± 18 s for the $1AuNP_{col}$ catalyst (Figure 2.12A) and 360 ± 36 s for the $1AuNP_{sup}$ catalyst (Figure 2.12B) was observed. These reactions contained the same AuNP concentration and hence $1AuNP_{col}$ possesses larger available surface area compared to $1AuNP_{sup}$ and decreased induction time. Incubation of 4-NP and catalyst in the control experiments for shorter or prolonged time periods did not change the induction time. This suggests rapid saturation of the surface of AuNP by 4-NP and does not suggest slow surface modification by 4-NP. In Figure 2.12A, the reactants in the parenthesis were mixed and incubated for 108 s (equal to the induction time observed for $1AuNP_{col}$ catalyst). An incubation time of 240 s was used for (4-NP/$NaBH_4$) + $1AuNP_{sup}$ catalyst addition sequence whereas an incubation time of 120 s was used for ($1AuNP_{sup}$/$NaBH_4$) + 4-NP addition sequence. Time resolved UV-Vis spectra was acquired as soon as the third component (outside parenthesis in Figure 2.12A and B) was added.
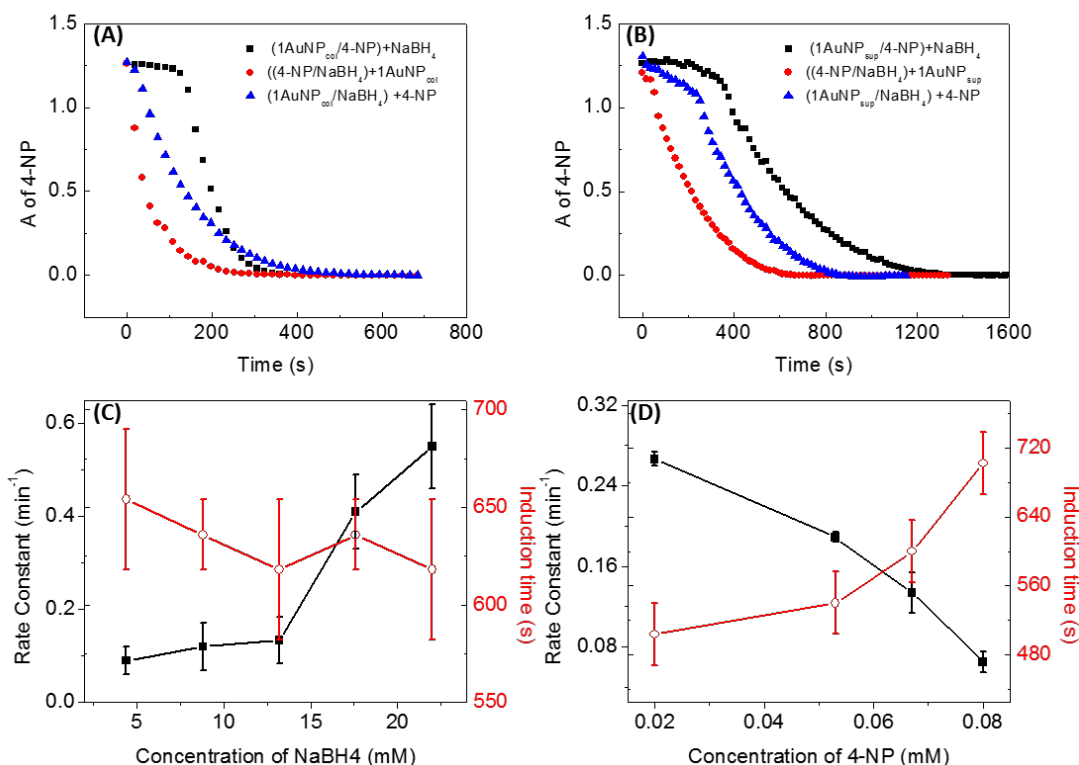
Figure 2.12. Mixing sequence kinetics (reactants in the parenthesis were incubated for specific amount of time and then the third component was added); (A) mixing sequences for $1AuNP_{col}$ system, (B) mixing sequence for $1AuNP_{sup}$ system; (C) Dependence of rate constant and induction time on the concentration of $NaBH_4$ for $1AuNP_{sup}$ catalyst and (D) Dependence of rate constant and induction time on the concentration of 4-NP for $1AuNP_{sup}$ catalyst. Red and black solid lines in (C) and (D) are for visual aid only.

Figure 2.12A shows that the induction time is completely removed after incubating (4-NP/$NaBH_4$) and ($1AuNP_{col}$/$NaBH_4$) for 108 s. Few researchers have attributed the induction time to a slow surface restructuring of the AuNP by the substrates.[7, 57] Slow surface restructuring can be ruled out as the explanation for induction time based on complete disappearance of induction time in case of (4-NP/$NaBH_4$) + $1AuNP_{col}$ and ($1AuNP_{col}$/$NaBH_4$) + 4-NP. Similarly, in Figure 2.12B, incubating (4-NP/$NaBH_4$) for 240

s followed by $1AuNP_{sup}$ addition, the induction time (360 ± 18 s for control) is completely removed. When ($1AuNP_{sup}/NaBH_4$) was incubated for 120 s with subsequent addition of 4-NP, the induction time was also removed but an initial reaction rate (0.05 ± 0.02 min^{-1}) was curiously slower resulting in a 'delay time' followed by an increased rate constant of 0.26 ± 0.05 min^{-1} (Figure 2.12B). This rate constant after the delay time was similar to that for (4-NP/NaBH$_4$) + $1AuNP_{sup}$ (0.28 ± 0.05 min^{-1}). The delay time (240 ± 18 s) was equal to the difference between the induction time observed in Figure 2.12B (360 ± 18 s) and incubation time (120 s). In addition to this observation, rate constants for addition sequence (4-NP/NaBH$_4$) + $1AuNP_{sup}$ (0.28 ± 0.05 min^{-1}) and (4-NP/NaBH$_4$) + $1AuNP_{col}$ (0.75 ± 0.07 min^{-1}) were both higher than rate constants for the control reactions; 0.20 ± 0.03 min^{-1} and 0.34 ± 0.05 min^{-1} respectively. This suggests that the induction time is dependent on relative surface coverage of 4-NP and NaBH$_4$ adsorbed on the AuNP surface.

To gather further evidence for this theory, 4-NP and NaBH$_4$ concentrations were varied systematically to examine the effect of reactant concentration on induction time for $1AuNP_{sup}$ catalyst. The NaBH$_4$ concentration was changed with constant 0.067 mM 4-NP concentration (Figure 2.12C) and the 4-NP concentration was changed with constant 13.2 mM NaBH$_4$ concentration (Figure 2.12D). NaBH$_4$ was added as the last step in all reactions with constant concentrations equivalent to the previous results. Increasing 4-NP concentration caused a reduction in rate constant which is similar to results obtained in previous works[22, 55] and justified by Langmuir-Hinshelwood mechanism for this reaction. An increase in the induction time was observed with increasing 4-NP concentration. At a high 4-NP concentration of 0.1 mM, the reaction induction time was greater than the time

frame studied (2 h). Increased BH_4^- ion concentration led to an increase in the rate constant, which is corroborated by previous studies[22, 55], but showed no strong correlation with induction time. Measuring change in induction time above 22 mM BH_4^- was not undertaken due to rapid evolution of H_2 bubbles in the cuvette.
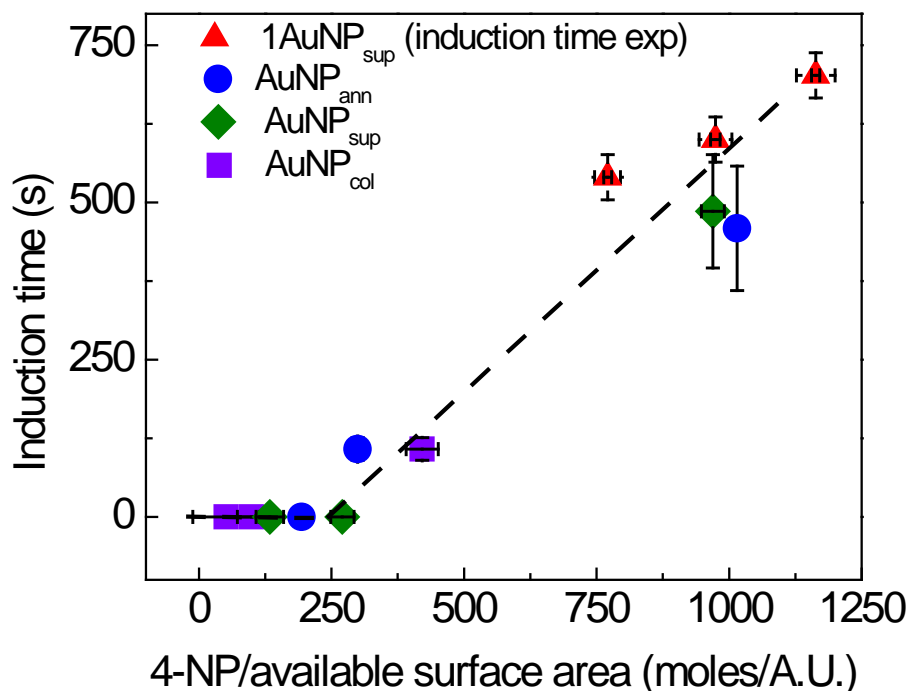
Figure 2.13. Induction time for various catalyst normalized to available surface area (as measured from 2-MBI adsorption experiments).

Based on these results, we can hypothesize that the induction time is directly related to the available surface area saturation by 4-NP and higher adsorption constant for 4-NP than NaBH$_4$ (5500 ± 1000 L/mol and 58 ± 5 L/mol respectively) as calculated by Wunder et al.[55] 1AuNP$_{sup}$ catalyst has minimum relative surface area available compared to 5AuNP$_{sup}$ and 10AuNP$_{sup}$ leading to maximum blocking of its available surface area. Figure 2.13

suggests a relationship between induction time and 4-NP concentration normalized to available surface area. This clearly elucidates the above hypothesis of available surface area blocking by 4-NP where higher 4-NP/available surface area results in higher induction time and vice versa. Figure 2.13 suggests a threshold ratio of 4-NP per available surface area above which the induction time emerges. According to the Langmuir-Hinshelwood model[7] for this reaction, a borohydride ion has to react with the AuNP surface and provide a surface hydrogen species. Depending on the AuNP surface saturation by 4-NP, BH_4^- ion (having an adsorption constant 100 times lower than 4-NP) has to compete for available surface area on the AuNP surface. The $5AuNP_{sup}$ and $10AuNP_{sup}$ catalysts have relatively higher available surface area compared to $1AuNP_{sup}$ catalyst and hence no induction time was observed. We observe from Figure 2.12A and B that induction time is completely removed for the (4-NP/NaBH$_4$) + $1AuNP_{sup}$ catalyst. When $1AuNP_{sup}$ is added last, it is figuratively "bare" and not saturated by 4-NP, thus BH_4^- does not compete with 4-NP for available surface area and can simultaneously adsorb onto the AuNP surface to initiate the reaction thus demonstrating no induction time. Slower reaction rates for (1AuNP/NaBH$_4$) + 4-NP addition sequence and a delay time for the $1AuNP_{sup}$ catalyst can be explained by similar arguments. BH_4^- saturates the AuNP surface and 4-NP (100 times higher adsorption constant than NaBH$_4$) has to compete for available surface area on the surface. This results in removal of induction time completely but initial reaction rate is slower when 4-NP replaces adsorbed NaBH$_4$ from the surface and simultaneously causes reaction. Pseudo first order reaction kinetics initiates when 4-NP reaches a threshold relative concentration to NaBH$_4$ on AuNP surface. These observations are also supported by the decrease in rate

constant and increase in induction time due to increase in 4-NP concentration. No reaction was observed for 4-NP concentration above 0.1 mM, because 4-NP desorption and $NaBH_4$ adsorption is a reversible process and excess of 4-NP inhibits the adsorption of $NaBH_4$ on the surface of AuNP. Incubation time was the same as the induction time for $1AuNP_{col}$ catalyst and thus no separate delay time could be observed. Lower reaction rates (0.30 ± 0.02 min^{-1}) for the ($1AuNP_{col}/NaBH_4$) + 4-NP addition sequence was observed compared to ($4\text{-}NP/NaBH_4$) + $1AuNP_{col}$ (0.75 ± 0.02 min^{-1}) but reaction reached near completion before any increase in rate constant could be observed similar to ($1AuNP_{sup}/NaBH_4$) + 4-NP addition sequence. Similar arguments of weaker adsorption constant of BH_4^- compared to 4-NP can be given for slower rate of reaction for this observation.

2.4 Conclusion

Successful comparison of the catalytic activity of colloidal AuNP to supported AuNP catalyst was conducted. A facile UV-Vis spectroscopy based organothiol adsorption technique has been used to quantify the AuNP available surface area for both colloidal and supported AuNP catalysts. Subsequently TOF analysis was used to quantify and contrast the catalytic activity of colloidal and supported AuNPs based on mass and available surface area. Our observations show significantly lower reaction rates for supported-AuNP catalysts compared to colloidal AuNP catalysts per Au mass basis, which is attributed to ca. 60% loss of available surface area during the immobilization process. Annealing, which is a preferred method of removal of stabilizing ligand from AuNP surface causes further loss in catalytic activity resulting from the growth of AuNPs on support surface and loss of surface features like edges and vertices. Higher TOF_{SA} values for supported AuNP

catalyst compared to the colloidal AuNP catalysts suggests that the titania support enhances AuNP catalytic activity in the 4-NP reduction reaction due to the formation of active sites at the AuNP-support interfaces which are more active than face, corner or edge sites. Induction time was attributed to AuNP surface saturation by 4-NP and accessibility of available surface area on AuNP surface by BH_4^- in presence of 4-NP. Our results show a threshold 4-NP to available surface area ratio at which induction time emerges suggesting competitive adsorption between 4-NP and BH_4^- for available surface area. Induction time can be removed completely by altering the addition sequence to (4-NP/NaBH$_4$) + AuNP where AuNP surface area is essentially 'bare' and available for adsorption of both reactants simultaneously resulting in instantaneous reaction.

2.5 Acknowledgements

2.6. References

1.   Haruta, M.; Yamada, N.; Kobayashi, T.; Iijima, S., Gold Catalysts Prepared by Coprecipitation for Low-Temperature Oxidation of Hydrogen and of Carbon Monoxide. *Journal of Catalysis* **1989,** *115*, 301-309.

2.   Ansar, S. M.; Haputhanthri, R.; Edmonds, B.; Liu, D.; Yu, L. Y.; Sygula, A.; Zhang, D. M., Determination of the Binding Affinity, Packing, and Conformation of Thiolate and Thione Ligands on Gold Nanoparticles. *J Phys Chem C* **2011,** *115*, 653-660.

3.   Sinha, A. K.; Seelan, S.; Tsubota, S.; Haruta, M., A Three-Dimensional Mesoporous Titanosilicate Support for Gold Nanoparticles: Vapor-Phase Epoxidation of

Propene with High Conversion. *Angewandte Chemie International Edition* **2004,** *43*, 1546-1548.

4.   Haruta, M., Size- and Support-Dependency in the Catalysis of Gold. *Catalysis Today* **1997,** *36*, 153-166.

5.   Bond, G. C.; Thompson, D. T., Catalysis by Gold. *Catalysis Reviews* **1999,** *41*, 319-388.

6.   Tsunoyama, H.; Ichikuni, N.; Sakurai, H.; Tsukuda, T., Effect of Electronic Structures of Au Clusters Stabilized by Poly(N-Vinyl-2-Pyrrolidone) on Aerobic Oxidation Catalysis. *J Am Chem Soc* **2009,** *131*, 7086-7093.

7.   Wunder, S.; Polzer, F.; Lu, Y.; Mei, Y.; Ballauff, M., Kinetic Analysis of Catalytic Reduction of 4-Nitrophenol by Metallic Nanoparticles Immobilized in Spherical Polyelectrolyte Brushes. *J Phys Chem C* **2010,** *114*, 8814-8820.

8.   Tsunoyama, H.; Sakurai, H.; Ichikuni, N.; Negishi, Y.; Tsukuda, T., Colloidal Gold Nanoparticles as Catalyst for Carbon-Carbon Bond Formation: Application to Aerobic Homocoupling of Phenylboronic Acid in Water. *Langmuir* **2004,** *20*, 11293-11296.

9.   Shylesh, S.; Schünemann, V.; Thiel, W. R., Magnetically Separable Nanocatalysts: Bridges between Homogeneous and Heterogeneous Catalysis. *Angewandte Chemie International Edition* **2010,** *49*, 3428-3459.

10.   Polshettiwar, V.; Luque, R.; Fihri, A.; Zhu, H.; Bouhrara, M.; Basset, J.-M., Magnetically Recoverable Nanocatalysts. *Chemical Reviews* **2011,** *111*, 3036-3075.

11.   Stratakis, M.; Garcia, H., Catalysis by Supported Gold Nanoparticles: Beyond Aerobic Oxidative Processes. *Chemical Reviews* **2012,** *112*, 4469-4506.

12.   Grunes, J.; Zhu, A.; Somorjai, G. A., Catalysis and Nanoscience. *Chem Commun* **2003**, 2257-2260.

13.   Bell, A. T., The Impact of Nanoscience on Heterogeneous Catalysis. *Science* **2003,** *299*, 1688-1691.

14.   Sheldon, R. A., E Factors, Green Chemistry and Catalysis: An Odyssey. *Chem Commun* **2008**, 3352-3365.

15.   Fukushima, T.; Galvagno, S.; Parravano, G., Oxygen-Chemisorption on Supported Gold. *Journal of Catalysis* **1979,** *57*, 177-182.

16.   Shastri, A. G.; Datye, A. K.; Schwank, J., Gold Titania Interactions - Temperature-Dependence of Surface-Area and Crystallinity of Tio2 and Gold Dispersion. *Journal of Catalysis* **1984,** *87*, 265-275.

17.   Iizuka, Y.; Fujiki, H.; Yamauchi, N.; Chijiiwa, T.; Arai, S.; Tsubota, S.; Haruta, M., Adsorption of Co on Gold Supported on Tio2. *Catalysis Today* **1997,** *36*, 115-123.

18.   Berndt, H.; Pitsch, I.; Evert, S.; Struve, K.; Pohl, M. M.; Radnik, J.; Martin, A., Oxygen Adsorption on Au/Al2o3 Catalysts and Relation to the Catalytic Oxidation of Ethylene Glycol to Glycolic Acid. *Appl Catal a-Gen* **2003,** *244*, 169-179.

19.   Margitfalvi, J. L.; Fasi, A.; Hegedus, M.; Lonyi, F.; Gobolos, S.; Bogdanchikova, N., Au/Mgo Catalysts Modified with Ascorbic Acid for Low Temperature Co Oxidation. *Catalysis Today* **2002,** *72*, 157-169.

20.   Menegazzo, F.; Manzoli, M.; Chiorino, A.; Boccuzzi, F.; Tabakova, T.; Signoretto, M.; Pinna, F.; Pernicone, N., Quantitative Determination of Gold Active Sites by Chemisorption and by Infrared Measurements of Adsorbed Co. *Journal of Catalysis* **2006,** *237*, 431-434.

21.   Menegazzo, F.; Pinna, F.; Signoretto, M.; Trevisan, V.; Boccuzzi, F.; Chiorino, A.; Manzoli, M., Quantitative Determination of Sites Able to Chemisorb Co on Au/Zro2 Catalysts. *Applied Catalysis A: General* **2009,** *356*, 31-35.

22.   Wunder, S.; Lu, Y.; Albrecht, M.; Ballauff, M., Catalytic Activity of Faceted Gold Nanoparticles Studied by a Model Reaction: Evidence for Substrate-Induced Surface Restructuring. *ACS Catalysis* **2011,** *1*, 908-916.

23.   Pradhan, N.; Pal, A.; Pal, T., Silver Nanoparticle Catalyzed Reduction of Aromatic Nitro Compounds. *Colloids and Surfaces A: Physicochemical and Engineering Aspects* **2002,** *196*, 247-257.

24.   Esumi, K.; Miyamoto, K.; Yoshimura, T., Comparison of Pamam–Au and Ppi–Au Nanocomposites and Their Catalytic Activity for Reduction of 4-Nitrophenol. *Journal of Colloid and Interface Science* **2002,** *254*, 402-405.

25.   Panigrahi, S.; Basu, S.; Praharaj, S.; Pande, S.; Jana, S.; Pal, A.; Ghosh, S. K.; Pal, T., Synthesis and Size-Selective Catalysis by Supported Gold Nanoparticles: Study on Heterogeneous and Homogeneous Catalytic Process. *The Journal of Physical Chemistry C* **2007,** *111*, 4596-4605.

26.   Lopez, N.; Janssens, T. V. W.; Clausen, B. S.; Xu, Y.; Mavrikakis, M.; Bligaard, T.; Nørskov, J. K., On the Origin of the Catalytic Activity of Gold Nanoparticles for Low-Temperature Co Oxidation. *Journal of Catalysis* **2004,** *223*, 232-235.

27.   Lopez, N.; Nørskov, J. K.; Janssens, T. V. W.; Carlsson, A.; Puig-Molina, A.; Clausen, B. S.; Grunwaldt, J. D., The Adhesion and Shape of Nanosized Au Particles in a Au/Tio2 Catalyst. *Journal of Catalysis* **2004,** *225*, 86-94.

28.   Remediakis, I. N.; Lopez, N.; Nørskov, J. K., Co Oxidation on Rutile-Supported Au Nanoparticles. *Angewandte Chemie International Edition* **2005,** *44*, 1824-1826.

29.   Lopez, N.; Nørskov, J. K., Catalytic Co Oxidation by a Gold Nanoparticle: A Density Functional Study. *J Am Chem Soc* **2002,** *124*, 11262-11263.

30.   Mills, G.; Gordon, M. S.; Metiu, H., Oxygen Adsorption on Au Clusters and a Rough Au(111) Surface: The Role of Surface Flatness, Electron Confinement, Excess Electrons, and Band Gap. *The Journal of Chemical Physics* **2003,** *118*, 4198-4205.

31.   Pietron, J. J.; Stroud, R. M.; Rolison, D. R., Using Three Dimensions in Catalytic Mesoporous Nanoarchitectures. *Nano Letters* **2002,** *2*, 545-549.

32.   Vijay, A.; Mills, G.; Metiu, H., Adsorption of Gold on Stoichiometric and Reduced Rutile Tio2 (110) Surfaces. *The Journal of Chemical Physics* **2003,** *118*, 6536-6551.

33.   Parker, S. C.; Grant, A. W.; Bondzie, V. A.; Campbell, C. T., Island Growth Kinetics During the Vapor Deposition of Gold onto Tio2(110). *Surface Science* **1999,** *441*, 10-20.

34. Chen, M. S.; Goodman, D. W., The Structure of Catalytically Active Au on Titania. *Science* **2004**.

35. Chen, M. S.; Goodman, D. W., Structure–Activity Relationships in Supported Au Catalysts. *Catalysis Today* **2006,** *111*, 22-33.

36. Valden, M.; Lai, X.; Goodman, D. W., Onset of Catalytic Activity of Gold Clusters on Titania with the Appearance of Nonmetallic Properties. *Science* **1998,** *281*, 1647-1650.

37. Siriwardana, K.; Gadogbe, M.; Ansar, S. M.; Vasquez, E. S.; Collier, W. E.; Zou, S.; Walters, K. B.; Zhang, D., Ligand Adsorption and Exchange on Pegylated Gold Nanoparticles. *The Journal of Physical Chemistry C* **2014,** *118*, 11111-11119.

38. Ansar, S. M.; Kitchens, C. L., Impact of Gold Nanoparticle Stabilizing Ligands on the Colloidal Catalytic Reduction of 4-Nitrophenol. *Acs Catalysis* **2016,** *6*, 5553-5560.

39. Ohtani, B.; Prieto-Mahaney, O. O.; Li, D.; Abe, R., What Is Degussa (Evonik) P25? Crystalline Composition Analysis, Reconstruction from Isolated Pure Particles and Photocatalytic Activity Test. *Journal of Photochemistry and Photobiology A: Chemistry* **2010,** *216*, 179-182.

40. Frens, G., Controlled Nucleation for Regulation of Particle-Size in Monodisperse Gold Suspensions. *Nature-Phys Sci* **1973,** *241*, 20-22.

41. Schneider, C. A.; Rasband, W. S.; Eliceiri, K. W., Nih Image to Imagej: 25 Years of Image Analysis. *Nature methods* **2012,** *9*, 671-675.

42. Haruta, M., Catalysis of Gold Nanoparticles Deposited on Metal Oxides. *CATTECH* **2002,** *6*, 102-115.

43.   Golunski, S., Why Use Platinum in Catalytic Converters? *Tc* **2007,** *975*, 44.

44.   Parker, S. C.; Campbell, C. T., Reactivity and Sintering Kinetics of Au/Tio2(110) Model Catalysts: Particle Size Effects. *Topics in Catalysis* **2007,** *44*, 3-13.

45.   Vangala, K.; Ameer, F.; Salomon, G.; Le, V.; Lewis, E.; Yu, L.; Liu, D.; Zhang, D., Studying Protein and Gold Nanoparticle Interaction Using Organothiols as Molecular Probes. *The Journal of Physical Chemistry C* **2012,** *116*, 3645-3652.

46.   Boudart, M., Turnover Rates in Heterogeneous Catalysis. *Chemical Reviews* **1995,** *95*, 661-666.

47.   Chen, M.; Goodman, D. W., Catalytically Active Gold: From Nanoparticles to Ultrathin Films. *Accounts of Chemical Research* **2006,** *39*, 739-746.

48.   Molina, L. M.; Hammer, B., Active Role of Oxide Support During Co Oxidation at $\mathrm{a}\mathrm{U}/\mathrm{M}\mathrm{G}\mathrm{O}$. *Physical Review Letters* **2003,** *90*, 206102.

49.   Laoufi, I.; Saint-Lager, M. C.; Lazzari, R.; Jupille, J.; Robach, O.; Garaudée, S.; Cabailh, G.; Dolle, P.; Cruguel, H.; Bailly, A., Size and Catalytic Activity of Supported Gold Nanoparticles: An in Operando Study During Co Oxidation. *The Journal of Physical Chemistry C* **2011,** *115*, 4673-4679.

50.   Haruta, M., When Gold Is Not Noble: Catalysis by Nanoparticles. *The Chemical Record* **2003,** *3*, 75-87.

51.   Kuroda, K.; Ishida, T.; Haruta, M., Reduction of 4-Nitrophenol to 4-Aminophenol over Au Nanoparticles Deposited on Pmma. *Journal of Molecular Catalysis A: Chemical* **2009,** *298*, 7-11.

52.   Zeng, J.; Zhang, Q.; Chen, J.; Xia, Y., A Comparison Study of the Catalytic Properties of Au-Based Nanocages, Nanoboxes, and Nanoparticles. *Nano Letters* **2010,** *10*, 30-35.

53.   Sharma, G.; Ballauff, M., Cationic Spherical Polyelectrolyte Brushes as Nanoreactors for the Generation of Gold Particles. *Macromol Rapid Comm* **2004,** *25*, 547-552.

54.   Pal, T.; Sau, T. K.; Jana, N. R., Reversible Formation and Dissolution of Silver Nanoparticles in Aqueous Surfactant Media. *Langmuir* **1997,** *13*, 1481-1485.

55.   Wunder, S.; Polzer, F.; Lu, Y.; Mei, Y.; Ballauff, M., Kinetic Analysis of Catalytic Reduction of 4-Nitrophenol by Metallic Nanoparticles Immobilized in Spherical Polyelectrolyte Brushes. *J. Phys. Chem. C* **2010,** *114*, 8814-8820.

56.   Ansar, S. M.; Ameer, F. S.; Hu, W.; Zou, S.; Pittman, C. U.; Zhang, D., Removal of Molecular Adsorbates on Gold Nanoparticles Using Sodium Borohydride in Water. *Nano Letters* **2013,** *13*, 1226-1229.

57.   Zhou, X.; Xu, W.; Liu, G.; Panda, D.; Chen, P., Size-Dependent Catalytic Activity and Dynamics of Gold Nanoparticles at the Single-Molecule Level. *J Am Chem Soc* **2010,** *132*, 138-146.

CHAPTER THREE

pH-RESPONSIVE MERCAPTOUNDECANOIC ACID FUNCTIONALIZED GOLD

NANOPARTICLES AND APPLICATIONS IN CATALYSIS

[As published in *Nanomaterials 2018, 8(5), 339* with minor revisions]

3.1 Introduction

Gold nanoparticles (AuNPs) have attracted significant interest due to their optical, electronic, and chemical properties, which have demonstrated potential applicability in a variety of fields, including chemical catalysis[1-3]. While AuNPs possess inherent properties, surface functionalization with a variety of ligands affords the enhancement of existing properties or the introduction of additional capabilities that make the functionalized AuNPs suitable for novel applications. For example, AuNPs functionalized with external stimuli-responsive molecules possess chemical or physical properties that are triggered by light, pH, temperature, ions, or other stimuli, which have a significant potential for applications in reusable catalysis, sensory devises, biomedical applications, etc. [4-8]

AuNP functionalized with pH-responsive groups, such as carboxylic acids, sulfonates, and amines, have been synthesized and possess pH-responsive behaviors in solution.[4, 9-11] For example, 11-mercaptoundecanoic acid (MUA) is a pH-responsive ligand that binds strongly to AuNPs through the thiol group and effectively disperses nanoparticles in water at neutral and basic pH levels. MUA-stabilized AuNPs (AuNP-MUA) have been synthesized, and their colloidal behavior has been studied as a function of pH, ionic strength, and amine-induced AuNP-MUA aggregation in water.[12-14] Su et al. synthesized the MUA-functionalized 13 nm AuNPs via ligand exchange between citrate and MUA, and

studied the colloidal stability and phase behavior [15]. They believed that the aggregation of AuNP-MUA at pH 3 is governed by hydrogen-bonding forces between the surface adsorbed MUA molecules. At pH 11, the AuNP-MUA are colloidally stable in solution but form three-dimensional close-packed aggregates on TEM grids, due to decreased electrostatic repulsion interactions between deprotonated MUA and counter-ions (Na^+) during the sample drying process. Recently, Pillai et al. studied the nanoparticle size effect on the precipitation pH (pH^{prec}) for AuNPs functionalized with a mixed monolayer of MUA and N,N,N-trimethyl (11-mercaptoundecyl) ammonium ion [12]. They found that the pH^{prec} increased from pH = 5.3 to pH = 7.3 when increasing the nanoparticle size from 4.2 to 11.5 nm. Laaksonen et al. studied the stability of 2.3 nm AuNP-MUA at a set pH, using the hydroxide as base and varying the size of counter-ions, and showed that AuNP-MUA aggregation occurred at 70–90 mM for Na^+, and at greater than 1 M for the quaternary ammonium cation [13]. The steric hindrance caused by the quaternary ammonium adsorbed in the Stern layer stabilized the AuNP-MUA against aggregation. Recently, Wang et al. studied the stability of 4–6 nm AuNP-MUA to different monovalent cations that have different propensities for bridging interactions, as well as for concomitant AuNP-MUA aggregation [14]. The authors showed that the order of salt concentrations needed for AuNP-MUA aggregation is CsCl >> KCl > LiCl > NaCl > RbCl, which does not correlate with the size of the hydrated cations.

Though AuNP-MUA aggregation and redispersion in water has been explored before, the pH-triggered AuNP-MUA phase transfer between the water and organic phases (without aggregation) and reuse in catalysis has been not reported. While understood

phenomenologically, there is a fundamental tradeoff between colloidal stability and catalytic activity, which is driven by nanoparticle ligand surface passivation. This understanding is integral to the design of colloidal catalysts with sufficient activity and the ability to be recovered and reused in subsequent reactions. Our approach is to use stimuli-responsive surface functional groups for the catalyst recovery and reuse; however, the challenge is to balance the degree of surface coverage where higher passivation promotes colloidal stability and preservation of the nanoparticle catalyst, but also inhibits activity. Recently, we studied the catalytic activity of thiolated polyethylene glycol (PEG) ligands with varying chain lengths and surface coverage for the catalytic 4-nitrophenol reduction reaction [16]. Our results demonstrated an inverse correlation between catalytic activity and PEG surface coverage on the AuNPs.

In this work, we perform an in-depth study of pH-triggered AuNP-MUA aggregation and redispersion, as well as AuNP phase transfer between water and organic phases. This phase behavior is then coupled with application as a recoverable and reusable colloidal catalyst. Our results show that MUA provides pH-responsive dispersibility and phase transferability between aqueous and organic media, with the addition of a pH-responsive phase transfer facilitator. The activity of AuNP-MUA in the catalyzed reduction of 4-nitrophenol (4-NP) to 4-aminophenol (4-AP) by sodium borohydride ($NaBH_4$) was explored. AuNP-MUA are catalytically active towards the reduction of 4-NP to 4-AP at lower MUA surface coverage; however, low surface coverage also results in decreased recovery and reusability. We have explored this tradeoff for AuNP-MUA and demonstrated the ability to achieve pH-

triggered AuNP-MUA phase transfer between the water and organic phase (without aggregation) and reuse, without loss in catalytic activity.

3.2 Materials and Methods

3.2.1. Chemicals and Equipment

Toluene was purchased from Alfa Aesar (Tewksbury, MA, USA). All other chemicals were acquired from Sigma Aldrich (St. Louis, MO, USA). No further purification was conducted on the chemicals. Ultra-pure Milli-Q water (resistivity 18.2 MΩ.cm) was used for all synthesis and reactions. A pH meter (sympHony SB90M5, VWR International, Radnor, PA, USA) was used to measure pH. UV-VIS spectra were acquired on a UV-VIS Spectrometer (Varian Cary 50,Agilent Technologies, Santa Clara, CA, USA).

3.2.2 Mercaptoundecanoic Acid (MUA) Functionalized AuNP Synthesis and pH triggered Recovery

Borohydride reduction was employed to synthesize citrate-stabilized 5 nm diameter AuNPs. The citrate reduction method was used for synthesizing 13 and 45 nm diameter AuNPs [17-19]. A mixture of 0.5 mM $HAuCl_4$ (50 mL) and 0.5 mM trisodium citrate was made in a conical flask. A solution of 0.1 M sodium borohydride (1.5 mL of ice-cold, freshly prepared) was subsequently added dropwise under constant stirring. Stirring was continued for an additional hour. For 13-nm AuNPs, 150 mL of 1 mM $HAuCl_4$ aqueous solution was heated while gently stirring. When the solution begins to boil, 5.0 mL of 120-mM citrate in H_2O was added, and the resulting solution was stirred at 400 rpm for 15 min

71

as the color of the solution changed from colorless to red. Two-step nanoparticle seeded growth method was used to synthesize the citrate-capped 45-nm AuNPs [19]. In brief, 10 mL of as-synthesized 13 AuNP was added to 150 mL of boiling solution containing 0.6 mM $HAuCl_4$, followed by addition of 1% w/w aqueous trisodium citrate (21.7 µmol, 1.3 mL). The mixture was heated for 30 min under vigorous stirring.

Citrate-stabilized AuNPs were ligand exchanged with thiolated MUA to generate AuNP-MUA. A total of 1.3 mM MUA (30 mL, dilute NaOH) and 10 mL of as-synthesized citrate-AuNP were incubated for 24 h. AuNP-MUA was washed by repeated centrifugal precipitation and re-dispersion three times with H_2O, to remove excess MUA. Typical UV-Vis spectrum depicting LSPR peaks of AuNP-MUAs and AuNP-Cit are shown in Figure 3.1.
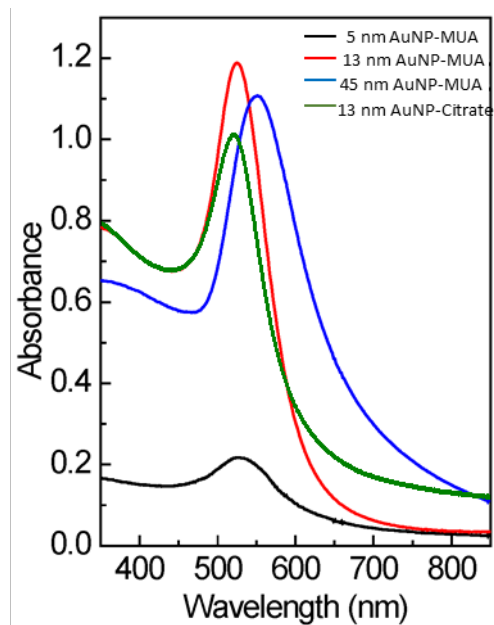
Figure 3.1. UV-Vis spectra of MUA functionalization AuNPs with diameter of 5 nm, 13 nm, and 45 nm. Green spectra represent 13 nm citrate stabilized AuNP.

3.2.3 Thermogravimetric (TGA) Analysis

The quantity of MUA grafted to AuNP was measured through TGA (SDT Q600,TA Instruments, New Castle, DE, USA). On a TGA pan (alumina), 50 mL purified AuNP-MUA was reduced down to 60 µL by repeated centrifugation (14,500 rpm, 1 h) and deposited. Water was removed initially by holding the TGA temperature at 100 °C for 15 min. A temperature ramp of 10 °C/min was applied till a final temperature of 600 °C was achieved and the temperature was held for 15 min (N_2 purge, 20 mL/min). Typical TGA curve for pure MUA and MUA functionalized AuNP are shown in Figure 3.2.
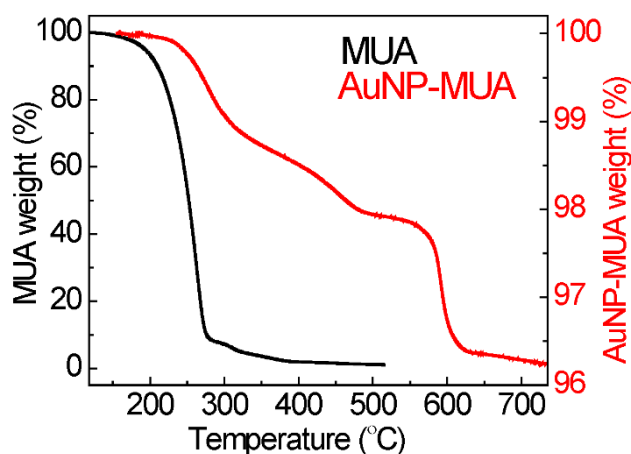
Figure 3.2. TGA curves of neat MUA (black curve) and MUA functionalized AuNPs (red curve).

3.2.4 4-Nitrophenol Reduction Catalysis

Time-resolved UV-VIS spectra was acquired in a 4 mL quartz cell (Varian Cary 50 spectrophotometer). AuNP-MUA (1 mL), H_2O (0.9 mL), and 0.2 mM 4-NP (1 mL) were mixed in the quartz cell. Change in intensity of 4-NP peak at 400 nm as function of time (individual spectra were acquired every 0.2 min) was used to track reaction progress.

3.2.5. Transmission Electron Microscopy (TEM) Analysis

Hitachi 9500 (300 kV, Hitachi, Schaumburg, IL, USA) was used to acquire high-resolution TEM images of AuNPs, and ImageJ size analysis was conducted on the images. Then 10 uL of AuNP was drop cast on a 300 mesh Cu grids (Formvar coated) and allowed to dry. TEM grids were subsequently stored in a desiccator for complete removal of solvent. TEM size analysis are summarized in Figure 3.3.

74
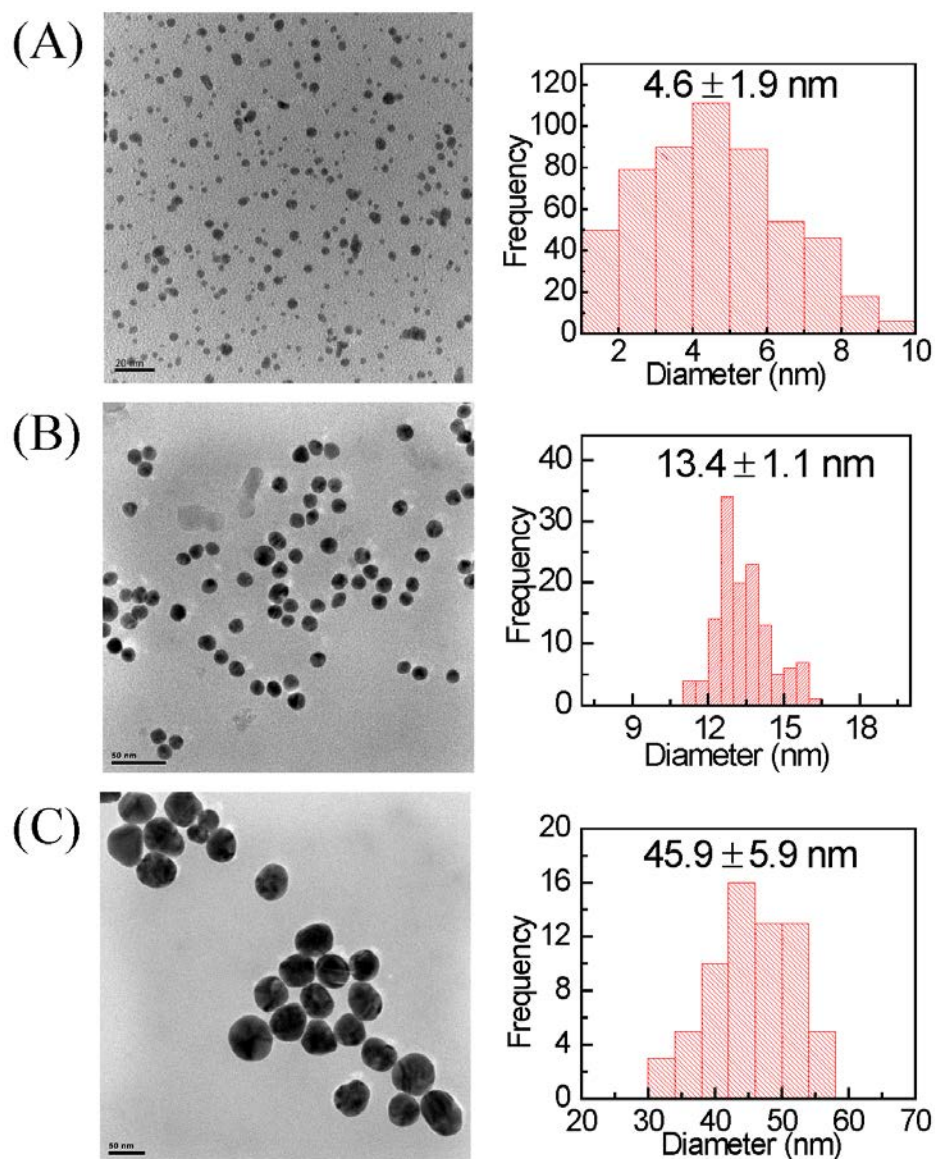
Figure 3.3. TEM images and histograms of distribution of sizes of AuNPs with diameter of (A) 5 nm, (B) 13 nm, and (C) 45 nm. The scale bars in the images (A), (B), and (C) are 20 nm, 50 nm, and 50 nm, respectively.

3.2.6. Dynamic Light Scattering (DLS) Measurements

DLS measurements were made on five-times-diluted as-prepared AuNPs at 25 °C (Malvern instrument Zeta sizer Nano series, Westborough, MA, USA). The solutions were

adjusted to the desired pH with either 0.1 M HCl or 0.1 M NaOH solutions, and their hydrodynamic diameters (number averaged) and ζ potentials were measured. Results are summarized in Table 3.1.

Nominal particle size /nm	Hydrodynamic diameter (nm)		Zeta potential (mV)	
	Before	After	Before	After
5	6.5 (±2.1)	11.1(±3.5)	-63.1(±1.9)	-42.6(±9.0)
13	16.3(±2.7)	18.3(±1.8)	-32.3(±1.0)	-39.8(±1.0)
45	48.4(±5.3)	49.2(±6.4)	-35.0(±1.8)	-41.6(±1.2)

Table 3.1. Hydrodynamic diameter and Zeta potential of AuNPs before and after MUA functionalization.

3.3 Results and Discussion

Citrate-capped AuNPs with three different sizes (5, 13, and 45 nm) were first synthesized by the borohydride and citrate reduction methods.[17-19] Transmission electron microscopy (TEM) shows that the average sizes of as-synthesized AuNPs are 4.6 ± 1.9, 13.4 ± 1.1, and 45.9 ± 5.9 nm in diameter (Figure 3.3). MUA-stabilized AuNPs were prepared by a ligand exchange reaction between citrate-stabilized AuNPs and the MUA in dilute KOH. Dynamic light scattering (DLS) data for AuNPs before and after MUA functionalization demonstrate the colloidal stability of nanoparticles in a dilute KOH solution (Table 3.1). The UV-VIS spectra of AuNPs-MUA exhibit a characteristic localized surface plasmon resonance (LSPR) absorption at 510–560 nm, confirming stability in basic medium (Figure

3.1). MUA strongly binds with AuNPs through covalent bonding of the thiol to the gold surface, yielding a pH-responsive –COOH group at the distal end. Figure 3.4 and 3.5 shows the pH-responsiveness of AuNP-MUA, undergoing reversible aggregation/precipitation and re-dispersion at an acidic and basic pH, respectively. Wine-red color solution (Figure 3.5A left vial) indicates well-dispersed nanoparticles in basic medium. In acidic medium (dilute HCl is used to adjust pH with mild stirring), the nanoparticles aggregate immediately and precipitate over an hour of incubation, leading to the complete settling of nanoparticles (right vial). The strong LSPR peak is used to monitor the aggregation and redispersion of AuNPs by UV-VIS spectroscopy (Figure 3.4). The complete disappearance of the peak at an acidic pH indicates that aggregated nanoparticles completely settled out. Complete re-dispersion of the precipitated AuNPs (dilute KOH is used for pH adjustment with mild stirring) is evident by the complete recovery of the LSPR peak at 526 nm and absorbance of approximately 1.1, accounting for dilution. Figure 3.4 shows the reversibility of the AuNP-MUA (13 nm particles) aggregation/re-dispersion process for several cycles. Other sizes of AuNP-MUA (5 and 45 nm particles) exhibit the same reversible aggregation and re-dispersion (data not shown).
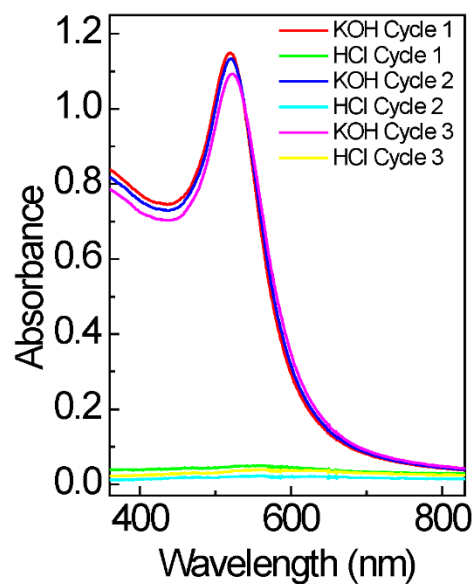
Figure 3.4. UV-Vis absorption spectra of AuNP-MUA recorded at acidic and basic pH values. The pH was varied by adding 10 µL of appropriate concentrations of HCl or KOH solutions. The aggregation/disaggregation of AuNP-MUA by changing pH were repeated up to 3 cycles.
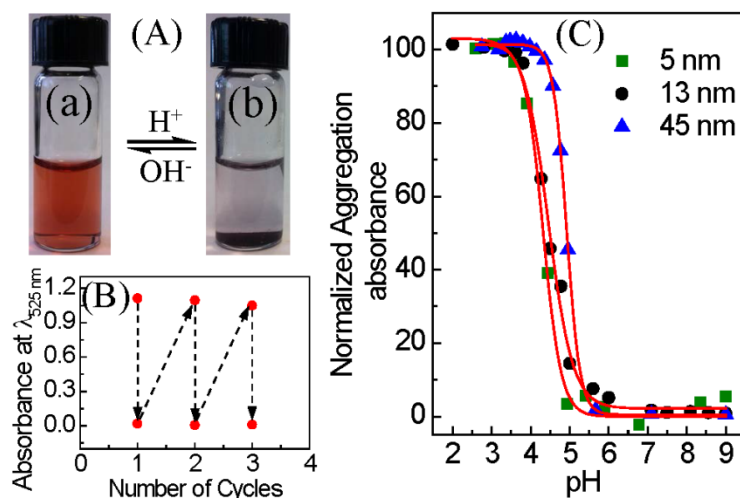
Figure 3.5. (**A**) Photographs showing the reversibility of 13-nm mercaptoundecanoic acid functionalized gold nanoparticles (AuNP-MUA) clustering/re-dispersion by changing the pH of the medium. The left vial (a) contains well-dispersed AuNP-MUA at a basic pH, and the right vial (b) contains aggregated and settled AuNP-MUA at an acidic pH; (**B**) Plot showing the pH-triggered reversibility of aggregation and re-dispersion monitored by the localized surface plasmon resonance (LSPR) peak intensity at 525 nm for 13-nm AuNP-MUA; and (**C**) normalized UV-VIS absorbance peak ratio of aggregated and unaggregated AuNP-MUA as a function of aqueous phase pH. The absorbance for un-aggregated 5, 13, and 45 nm diameter AuNPs were measured at wavelengths of 522, 525, and 551 nm, respectively, and the absorbance for aggregated 5, 13, and 45 AuNPs were measured at wavelengths of 562, 595, and 725 nm, respectively.
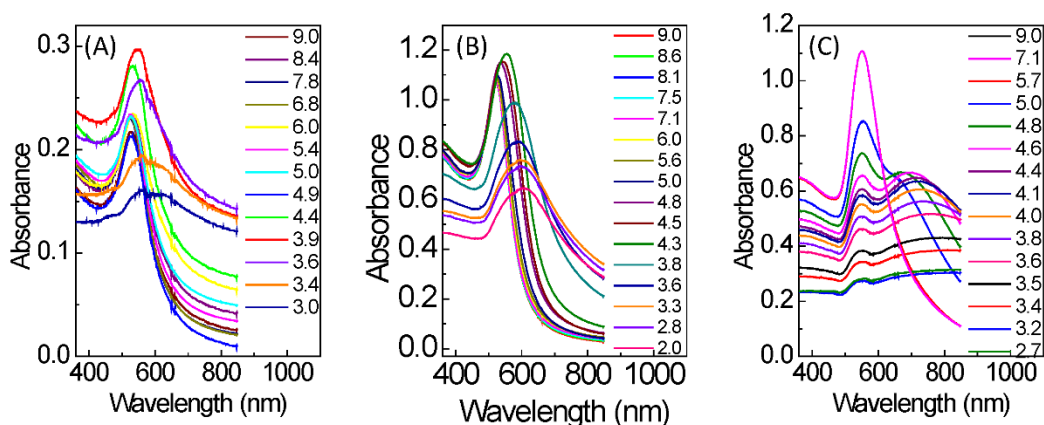
Figure 3.6. UV-Vis absorption spectra of AuNP-MUA recorded at different pH values varied from 9 to 3. (A), (B), and (C) are 5 nm, 13 nm, and 45 nm diameter AuNP functionalized with MUA, respectively.

The pH of AuNP-MUA aggregation was determined from a UV-VIS absorbance titration curve (Figure 3.6) obtained by monitoring the peak maximum absorbance for aggregated and un-aggregated peaks at different pH values. The LSPR peak at 510–560 nm for well-dispersed AuNPs peak shifts to a higher wavelength, and decreases in intensity as the AuNPs aggregate and settle [20-21]. The pH of AuNP-MUA aggregation (pH_{agg}) is determined from the inflection point of a sigmoidal fit of the absorbance, yielding pH values of 4.3, 4.5, and 4.9 for 5 nm, 13 nm, and 45 nm particles, respectively. Pillai et al. also observed similar trend for a MUA and N,N,N-trimethyl (11-mercaptoundecyl) ammonium ion mixed monolayer functionalized 4.2–11.5 nm AuNPs [12]. Also, Wang et al. reported that the pK_a value of MUA bound to AuNPs increases with increasing nanoparticle size from 4.1 to 7.2 nm [22]. Therefore, it is clear that as the particle size increases (nanoparticle curvature reduces), the deprotonation of the –COOH group on the nanoparticle surface is inhibited, due to the strong electrostatic repulsions between the carboxylate ions. In other words, at a given pH value, the fraction of –COO⁻ (compared to –COOH) on the AuNP surface

increases as the nanoparticle size decreases, which corresponds to the pH_{agg} increase with nanoparticle size. Furthermore, it should be noted that the wavelength and intensity of the LSPR peak of plasmonic nanoparticles is very sensitive to the dielectric properties of the local environment of the nanoparticles and the interparticle interaction (particle spacing) of nanoparticles [23-24]. Thus, to delineate these effects, measurement of the apparent diffusion coefficient and hydrodynamic diameter by DLS can complement the UV-VIS as an in situ measurement of nanoparticle aggregation as a function of pH.

The onset pH of AuNP-MUA aggregation determined by the DLS titration curve, as evidenced by increasing hydrodynamic diameter (Figure 3.7), commences at a pH of about 4.1 for all the three sizes of AuNPs-MUA. Our DLS results for pH at onset of AuNP-MUA aggregation are consistent (within the same pH units) with the data obtained from the UV-VIS titration method (Figure 3.6). As can be seen in Figure 3.7, at higher pH (>5), the ζ-potential is highly negative due to the deprotonated carboxylate group of MUA, which provides electrostatic repulsion between AuNP-MUA and thus colloidal stability. The magnitude of the ζ-potential is commonly used as the measure of colloidal stability, neglecting steric contributions[25-27]. Once the pH decreases below 5, the ζ-potential dramatically decreases, due to the protonation of the carboxylate groups over the pH range from 5 to 3. As a result, the electrostatic repulsion between nanoparticles decreases, eventually leading to nanoparticle aggregation. The decreasing magnitude of the AuNP-MUA ζ-potential as a function of pH indicates that the onset of aggregation, with an increased hydrodynamic diameter at pH 4.1, occurs at a ζ-potential of ~ −20 mV for all the sizes of particles. Thus, the ζ-potential data indicate that the AuNP-MUA aggregate with

an approximately 50% reduction of surface charge. Indeed, the ζ-potential is not quite equivalent to the surface charge on AuNPs; also, the ζ-potential of AuNP-MUA is dependent not only on the pK_a of surface-adsorbed MUA, but also on the MUA packing density and the surrounding environment.
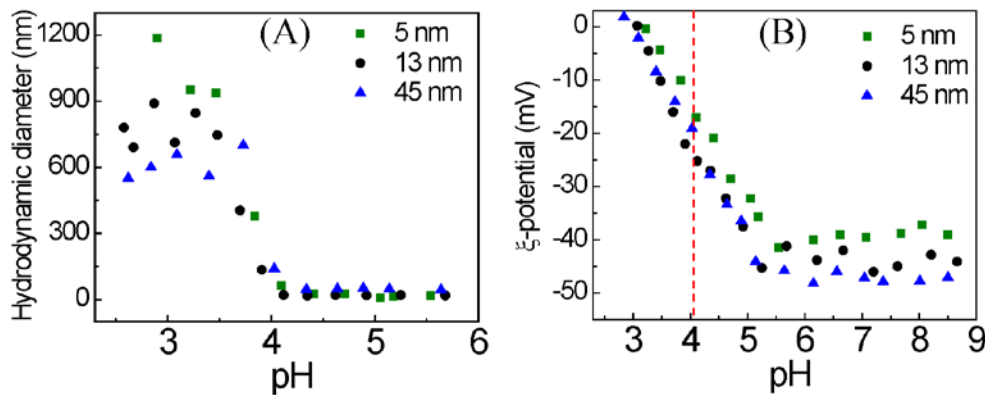
Figure 3.7. (**A**) Hydrodynamic diameter of the AuNP-MUA as a function of pH, and (**B**) ζ-potential of the AuNP-MUA as a function of pH. The red line indicates the onset of AuNP-MUA aggregation based on the hydrodynamic diameter data from figure A.

Therefore, the ζ-potential and hydrodynamic data also confirm that the pH_{agg} of AuNP-MUA is ~4.1, which is comparable with $pK_a \approx 4.8$ for MUA in solution [28]. However, the pH_{agg} for AuNP-MUA is about two pH unit smaller than the reported pK_a value for MUA adsorbed on AuNPs [22, 29]. Recently, Charron et al. reported the pK_a value of MUA adsorbed onto 5 nm AuNP by titrating with NaOH (acid-base titration method) [29]. They reported the pK_a value of MUA adsorbed on AuNP is around 7, which suggests a pK_a about two pH units higher than that of the unbound MUA. Wang et al. studied the dissociation behavior of AuNP-tethered MUA as a function of pH, using an acid-base (or potentiometric) titration method [22]. They also observed similar phenomena for the pK_a of MUA bound to 7.2 nm

AuNPs increased to ~8.3, which is significantly higher than that of MUA in solution (pK$_a$ ≈ 4.8) [22].

Figure 3.8. Control experiment to show that ODA facilitates the phase transfer of AuNP-MUA. (A) Without adding ODA, Photographs of glass vials containing aqueous solutions (top) of AuNP-MUA in contact with chloroform (bottom). The initial aqueous solution of the AuNP-MUA in the vial was red in colour with pH > 4.1 (left). By adding 0.1 M HCl, the pH of the AuNPs aqueous solution was gradually decreased below 4.1 (right). After vigorous shaking and storing for about 2 min, the thin film of aggregated AuNPs, formed at water/chloroform and chloroform/glass wall interfaces. Redispersion of the AuNPs back to the aqueous phase is observed by adjusting pH of aqueous medium > 4.1 by adding 0.1 M NaOH, and (B) With ODA, Photographs show the pH triggered reversible phase transfer of AuNP-MUA between water and CHCl$_3$ layers by switching the pH. The left side vial containing well dispersed AuNP-MUA in aqueous phase (top layer) at basic pH and right side vial containing AuNP-MUA transferred into CHCl$_3$ phase (bottom layer) after adding HCl and vigorous shaking and storing for about 2 min.

Direct transfer of nanoparticles from aqueous to organic phases is frequently employed in nanoparticle synthesis and purification applications[30-31]. In some colloidal nanoparticle catalytic applications, phase transfer of nanoparticles between two immiscible liquids is extremely advantageous for the recycling and reuse of catalysts, due to the avoidance of irreversible nanoparticle aggregation. To date, many methods used to modulate

nanoparticle phase transfer have been developed, such as host–guest interactions [32-33], electrostatic interactions [34-36], covalent modifications [37], and ligand exchanges [38-42]. It must be mentioned that with many of these methods, reversible phase transfer is not achieved; however, for certain applications, irreversible phase transfer is preferred. Here we demonstrate reversible pH-triggered phase transfer of 13 nm AuNP-MUA between the aqueous and organic phases. AuNP-MUA in an aqueous phase are transferred into a $CHCl_3$ layer, by reducing the aqueous layer pH from 11.0 to 8.0 with 0.1 M HCl and vigorous mixing for 2 min (Figure 3.8). The phase transfer occurs only in the presence of octadecylamine (ODA), which acts as the phase transferring agent when the ODA is protonated (charged) at pH below the pK_a and is deprotonated at pH above the pK_a. In short, a pH of 1.5 mL of AuNP-MUA (pH = 11) was adjusted to 8.0 with HCl, and subsequently vigorously agitated with 1.5 mL of chloroform containing ~ 1 mg ODA for 2 min. The necessity of ODA as a phase-transferring agent is demonstrated with a control experiment where AuNP-MUA aggregates on the vial surface and water-chloroform interface when acidic pH is employed without using ODA. (Figure 3.8). Phase transfer between aqueous and organic phases is reversible for at least four cycles (Figure 3.9), as indicated by monitoring the LSPR peak of AuNP-MUA in the aqueous layer (Figure 3.10). The pH for the phase transition (pH_{trans}) of 8.7 was determined from the inflection point of a sigmoidal fit of the percentage of AuNP-MUA transferred from aqueous to organic layers as a function of pH, determined from the LSPR peak absorbance in the aqueous layer (Figure 3.9 and 3.11). The transfer from aqueous to organic phase occurs when the pH of the aqueous layer is below the pK_a of the amine head group in ODA (~10.6) and above the

pK_a of MUA (~4.5) (Figure 3C). The phase transfer into the organic phase is due to the ion-pair formation between a negatively-charged carboxylate group (above pH ~4) and the positively-charged amine group of ODA (below pH 10.6). The long hydrophobic alkyl chain of ODA makes the AuNP-MUA more hydrophobic via its ion-pair formation. AuNP-MUA (1.8 nm diameter) phase transfer to organic phase by binding to highly-hydrophobic cationic molecules, such as tetraoctylammonium, has been reported previously [43]. Recently, Yuan et al. demonstrated a phase transfer cycle (aqueous → organic → aqueous) where glutathione functionalized Ag, Au, Cu, and Pt nanoparticles (<2 nm diameter) have been transferred into toluene or hexane via electrostatic interaction between negatively charged carboxylate groups on metal nanoparticles and positively charged cetyltrimethylammonium (CTA^+, hydrophobic) [34]. The removal of CTA^+ from the nanoparticle by forming a hydrophobic salt between tetramethylammonium decanoate and CTA^+ restores the negative charge on the nanoparticle surface, and returns the nanoparticles back to the aqueous phase. In this work, we have shown that the AuNP-MUA can easily and reversibly separate from an aqueous phase by either aggregation or phase separation methods.
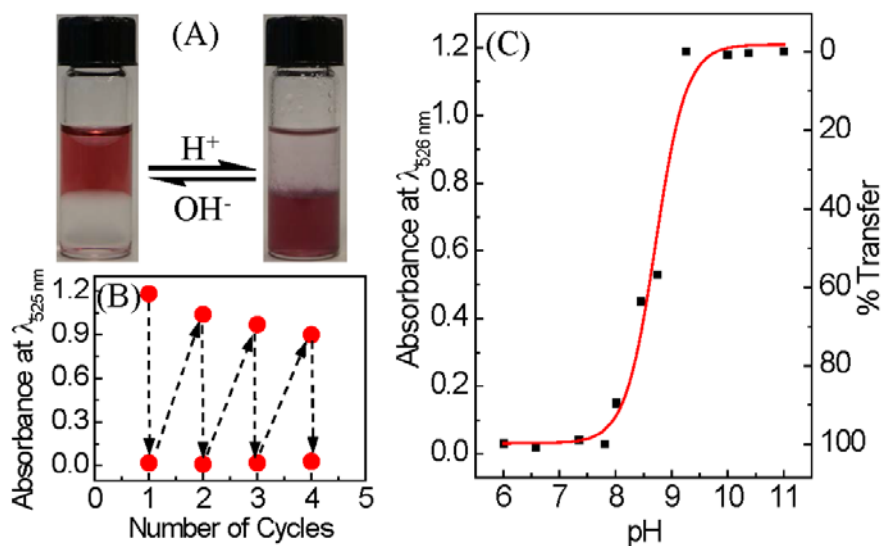
Figure 3.9 (**A**) Photographs of the pH-triggered reversible phase transfer of 13-nm AuNP-MUA between water and CHCl$_3$ layers, by switching the pH. The left side vial contains well-dispersed AuNP-MUA in the aqueous phase (top layer) at basic pH, and the right side vial contains AuNP-MUA transferred into the CHCl$_3$ phase (bottom) layer after adding HCl and vigorous shaking, (**B**) Plot showing pH-triggered reversible phase transfer of 13 nm AuNP-MUA between the water and organic phase, by monitoring the AuNP-MUA LSPR peak intensity at 525 nm wavelength in aqueous phase; and (**C**) absorbance of AuNP-MUA in aqueous phase at 525 nm (left scale) versus the pH and percentage transfer of AuNP-MUA from an aqueous to a CHCl$_3$ layer as a function of pH. The percentage of transfer was calculated by taking the absorbance of the AuNP-MUA (in aqueous medium) at pH 11.0 as 0%. The red color solid curve represents sigmoidal fitting of the experimental data.
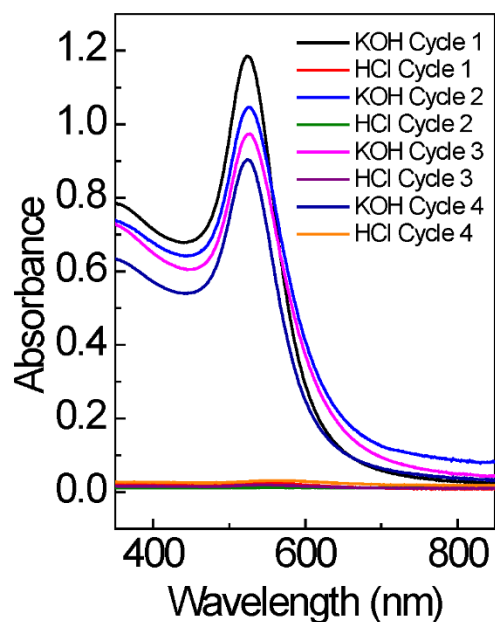
Figure 3.10. pH triggered reversible phase transfer of AuNP-MUA studied using UV-Vis spectroscopy**.** UV-Vis absorption spectra of AuNP-MUA recorded from aqueous layer. The pH was varied by adding appropriate concentrations of HCl or KOH solutions. The direct phase transfer of AuNP-MUA between aqueous and $CHCl_3$ phases were repeated up to 4 cycles by changing pH of aqueous medium.
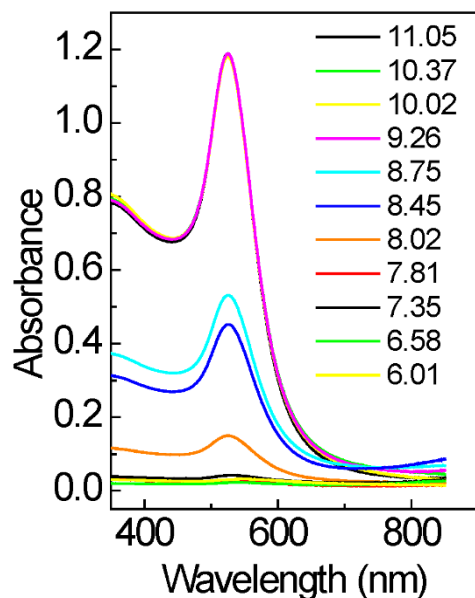
Figure 3.11. The onset of phase transfer of AuNP-MUA from aqueous to CHCl$_3$ phase was studied using the pH titration and monitored the LSPR peak of nanoparticles in aqueous phase over the pH 11 to pH 6 by using UV-Vis spectroscopy.

The ability to reversibly induce AuNP-MUA separation and re-dispersion is only half of the equation for colloidal catalysis; it must also possess catalytic activity. The catalytic activity of 13 nm AuNP-MUA was tested with the 4-nitrophenol (4-NP) reduction by borohydride, which is a common model reaction for ligand-modified AuNPs [44-47]. Figure 3.12 show the time-resolved UV-VIS spectra of a 4-NP reduction reaction catalyzed by AuNP, as a function of MUA surface coverage. The MUA surface coverage on the AuNPs was controlled by stoichiometry—mixing different concentrations of MUA with AuNPs during the ligand exchange process. MUA surface coverage on AuNP for 1 mM MUA with the AuNPs sample was determined by thermogravimetric analysis (TGA) (Figure 3.2). The

percentage weight loss of MUA adsorbed onto AuNPs is 3.7%, corresponding to the MUA monolayer packing density on AuNPs of 4.56 molecules/nm^2 (Figure 3.2), which is comparable to previously reported MUA packing density on AuNPs (5.70 molecules/nm^2) [48]. MUA surface coverage at different concentrations of MUA in an AuNP ligand exchange was determined using the 4.56 molecules/nm^2 monolayer packing density. The estimated surface coverage on AuNPs are 0%, 30%, 60%, 100%, and 100% for 0, 2.5, 5.0, 10.0, and 25.0 µM MUA in the ligand exchange reaction, respectively. Figure 3.12 shows the kinetics of the reaction monitored in situ using time-resolved UV-VIS spectroscopy, via changes in intensity of the 4-NP peak at 400 nm [44-47]. No reaction was observed for the 100% MUA surface coverage, which is expected due to complete thiol binding to all catalytic sites. At surface coverage below 100%, the AuNP-MUA are active in catalyzing the 4-NP reduction. Furthermore, an induction time was observed for 60% of the MUA surface coverage sample (Figure 3.12). Induction time is generally observed in ligand stabilized colloidal catalysts, and occurs due to mass transfer resistance offered by the ligand [46, 49] or slow surface restructure due to adsorbed reactants [50-52]. A similar phenomenon has been observed in our prior work for the catalytic activity of thiolated PEG functionalized AuNPs, where increased induction time coincided with increased surface coverage.
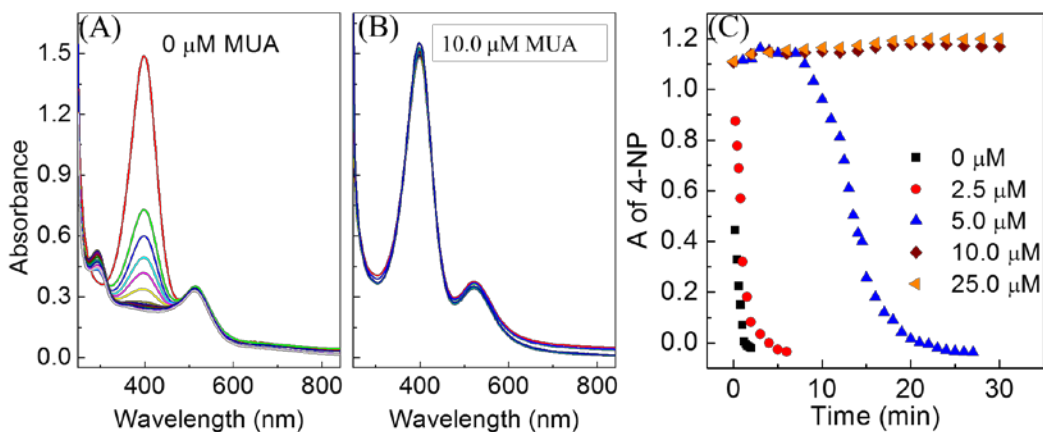
Figure 3.12. Catalytic activity of AuNP-MUA as function of MUA packing density on AuNPs. (**A**) Time-resolved UV-VIS spectra of 4-nitrophenol (4-NP) reduction reaction catalyzed by AuNPs functionalized with 0 µM MUA, (**B**) Time-resolved UV-VIS spectra of 4-nitrophenol reduction reaction catalyzed by AuNPs and functionalized with 10 µM MUA, and (**C**) The progress of the reaction tracked by the change in 4-NP absorbance peak at 400 nm over the time.

While catalytic activity was observed with 0%, 30%, and 60% MUA surface coverage, the decreased surface coverage did not provide sufficient colloidal stability. As such, the AuNPs could not be recovered and re-dispersed by aggregation/re-dispersion or phase transfer methods following the catalytic reaction. However, the pH-triggered reversible phase transfer and aggregation/re-dispersion of AuNP-MUA was achieved with 60% surface coverage in the absence of the reaction. In order to enhance the colloidal stability, the surface coverage was increased to 90% by increasing the MUA concentration to 7.5 µM. Ninety percent of surface coverage on AuNP is catalytically active, despite longer induction times on the order of 20 min (Figure 3.13). More importantly, 90% of surface coverage AuNP-MUA was successfully recovered after the first reaction cycle, and reused

in a second catalytic cycle by both aggregation/re-dispersion and phase transfer methods. In the second cycle, the catalytic induction times were increased, but 100% 4-nitrophenol conversation was maintained. The rate constant is obtained by fitting the data from Figure 3.13 to pseudo-first-order reaction kinetics with respect to 4-nitrophenol, and the rate constant is indicative of catalytic activity. The reaction rate constants for the catalysts recovered by aggregation/re-dispersion method are 0.29 ± 0.04 and 0.20 ± 0.06 min^{-1} for the first and second cycles, respectively, and the rate constants for the phase transfer method are 0.31 ± 0.03 and 0.23 ± 0.05 min^{-1} for the first and second cycles, respectively. Unfortunately, the catalytic activity was lost for the third catalytic cycle, due to the irreversible aggregation of AuNP-MUA during the recovery processes.
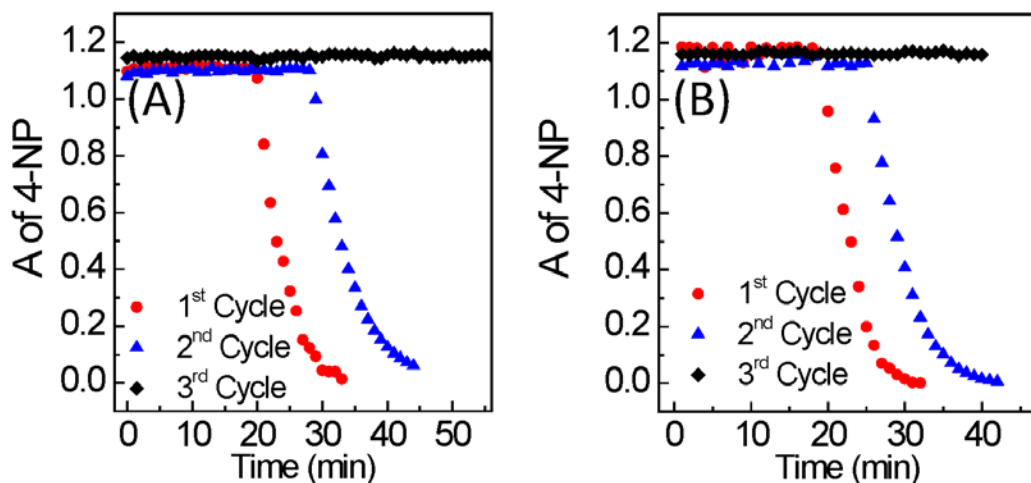
Figure 3.13. Recovery and reuse of AuNP-MUA with 90% surface coverage in catalysis by using (**A**) pH-triggered aggregation/redispersion method and (**B**) pH-triggered phase transformation method.

3.4 Conclusions

We have demonstrated that pH controls the dispersion of MUA-functionalized AuNPs where reversible aggregation and redispersion in an aqueous phase is achieved around pH 4.1 or the pK_a of MUA. Furthermore, reversible phase transfer between aqueous and organic phases (toluene or $CHCl_3$) can be achieved with the use of an amine-containing phase transfer agent (ODA) at pH 8.7 or the pK_a of the amine, where an ion pair formation induces phase transfer to chloroform. The catalytic activity of AuNPs functionalized with different surface coverages of MUA were studied. Complete inhibition of catalytic activity was observed at 100% surface coverage of MUA. AuNPs with 60% and less MUA surface coverage were colloidally stable and catalytically active, but possessed poor recoverability and reusability following the reactions. In this system, there is a tradeoff between colloidal stability and catalytic activity, which scale with surface coverage. Surface coverage of 90% MUA was found to be an optimal level of coverage where catalytic activity was observed, as well as the ability to recover and reuse for two catalytic cycles. The catalyst recovery by aggregation/re-dispersion and aqueous/organic phase transfer methods were achieved at pHs 4.1 and 8.7, respectively. The fundamental insight from this work allows for the understanding and designing the reusable colloidal metal nanoparticle catalysts with different surface functionalities and catalyzing the reaction at different pH conditions.

3.5 References

1.   Kang, B.; Mackey, M. A.; El-Sayed, M. A., Nuclear Targeting of Gold Nanoparticles in Cancer Cells Induces DNA Damage, Causing Cytokinesis Arrest and Apoptosis. *J. Am. Chem. Soc. 132*, 1517-1519.

2.   Shang, C.; Liu, Z.-P., Origin and Activity of Gold Nanoparticles as Aerobic Oxidation Catalysts in Aqueous Solution. *J. Am. Chem. Soc.* **2011,** *133*, 9938-9947.

3.   Abadeer, N. S.; Murphy, C. J., Recent Progress in Cancer Thermal Therapy Using Gold Nanoparticles. *J. Phys. Chem. C.* **2016,** *120*, 4691-4716.

4.   Yuan, Y.; Yan, N.; Dyson, P. J., Ph-Sensitive Gold Nanoparticle Catalysts for the Aerobic Oxidation of Alcohols. *Inorg. Chem.* **2011,** *50*, 11069-11074.

5.   Nam, J.; Won, N.; Jin, H.; Chung, H.; Kim, S., Ph-Induced Aggregation of Gold Nanoparticles for Photothermal Cancer Therapy. *J. Am. Chem. Soc.* **2009,** *131*, 13639-13645.

6.   Kanaoka, S.; Yagi, N.; Fukuyama, Y.; Aoshima, S.; Tsunoyama, H.; Tsukuda, T.; Sakurai, H., Thermosensitive Gold Nanoclusters Stabilized by Well-Defined Vinyl Ether Star Polymers: Reusable and Durable Catalysts for Aerobic Alcohol Oxidation. *J. Am. Chem. Soc.* **2007,** *129*, 12060-12061.

7.   Kim, Y.; Johnson, R. C.; Hupp, J. T., Gold Nanoparticle-Based Sensing of "Spectroscopically Silent" Heavy Metal Ions. *Nano Lett.* **2001,** *1*, 165-167.

8.   Wei, Y.; Han, S.; Kim, J.; Soh, S.; Grzybowski, B. A., Photoswitchable Catalysis Mediated by Dynamic Aggregation of Nanoparticles. *J. Am. Chem. Soc.* **2010,** *132*, 11018-11020.

9.   Yang, H.; Heng, X.; Hu, J., Salt- and Ph-Resistant Gold Nanoparticles Decorated with Mixed-Charge Zwitterionic Ligands, and Their Ph-Induced Concentration Behavior. *RSC Adv.* **2012,** *2*, 12648-12651.

10.   Kairdolf, B. A.; Nie, S., Multidentate-Protected Colloidal Gold Nanocrystals: Ph Control of Cooperative Precipitation and Surface Layer Shedding. *J. Am. Chem. Soc.* **2011,** *133*, 7268-7271.

11.   Kalsin, A. M.; Kowalczyk, B.; Smoukov, S. K.; Klajn, R.; Grzybowski, B. A., Ionic-Like Behavior of Oppositely Charged Nanoparticles. *J. Am. Chem. Soc.* **2006,** *128*, 15046-15047.

12.   Pillai, P. P.; Huda, S.; Kowalczyk, B.; Grzybowski, B. A., Controlled Ph Stability and Adjustable Cellular Uptake of Mixed-Charge Nanoparticles. *J. Am. Chem. Soc.* **2013,** *135*, 6392-6395.

13.   Laaksonen, T.; Ahonen, P.; Johans, C.; Kontturi, K., Stability and Electrostatics of Mercaptoundecanoic Acid-Capped Gold Nanoparticles with Varying Counterion Size. *ChemPhysChem* **2006,** *7*, 2143-2149.

14.   Wang, D.; Tejerina, B.; Lagzi, I.; Kowalczyk, B.; Grzybowski, B. A., Bridging Interactions and Selective Nanoparticle Aggregation Mediated by Monovalent Cations. *ACS Nano* **2011,** *5*, 530-536.

15.   Chia-Hao, S.; Pei-Lin, W.; Chen-Sheng, Y., Ph Dependence of Interparticle Coupling for Gold Nanoparticle Assemblies Formation: Electrostatic Attraction and Hydrogen Bonding. *Bull. Chem. Soc. Jpn.* **2004,** *77*, 189-193.

16.   Ansar, S. M.; Kitchens, C. L., Impact of Gold Nanoparticle Stabilizing Ligands on the Colloidal Catalytic Reduction of 4-Nitrophenol. *ACS Catal.* **2016,** *6*, 5553-5560.

17.	Freeman, R. G.; Hommer, M. B.; Grabar, K. C.; Jackson, M. A.; Natan, M. J., Ag-Clad Au Nanoparticles: Novel Aggregation, Optical, and Surface-Enhanced Raman Scattering Properties. *J. Phys. Chem.* **1996,** *100*, 718-724.

18.	Jana, N. R.; Gearheart, L.; Murphy, C. J., Seeding Growth for Size Control of 5-40 Nm Diameter Gold Nanoparticles. *Langmuir* **2001,** *17*, 6782-6786.

19.	Liu, S. H.; Han, M. Y., Synthesis, Functionalization, and Bioconjugation of Monodisperse, Silica-Coated Gold Nanoparticles: Robust Bioprobes. *Adv. Funct. Mater.* **2005,** *15*, 961-967.

20.	Siriwardana, K.; Gadogbe, M.; Ansar, S. M.; Vasquez, E. S.; Collier, W. E.; Zou, S.; Walters, K. B.; Zhang, D., Ligand Adsorption and Exchange on Pegylated Gold Nanoparticles. *J. Phys. Chem. C.* **2014,** *118*, 11111-11119.

21.	Wang, G.; Sun, W., Optical Limiting of Gold Nanoparticle Aggregates Induced by Electrolytes. *J. Phys. Chem. B.* **2006,** *110*, 20901-20905.

22.	Wang, D.; Nap, R. J.; Lagzi, I.; Kowalczyk, B.; Han, S.; Grzybowski, B. A.; Szleifer, I., How and Why Nanoparticle's Curvature Regulates the Apparent Pka of the Coating Ligands. *J. Am. Chem. Soc.* **2011,** *133*, 2192-2197.

23.	Mulvaney, P., Surface Plasmon Spectroscopy of Nanosized Metal Particles. *Langmuir* **1996,** *12*, 788-800.

24.	Kelly, K. L.; Coronado, E.; Zhao, L. L.; Schatz, G. C., The Optical Properties of Metal Nanoparticles: The Influence of Size, Shape, and Dielectric Environment. *J. Phys. Chem. B.* **2003,** *107*, 668-677.

25.   Parviz, D.; Das, S.; Ahmed, H. S. T.; Irin, F.; Bhattacharia, S.; Green, M. J., Dispersions of Non-Covalently Functionalized Graphene with Minimal Stabilizer. *ACS Nano* **2012,** *6*, 8857-8867.

26.   Mefford, O. T.; Vadala, M. L.; Goff, J. D.; Carroll, M. R. J.; Mejia-Ariza, R.; Caba, B. L.; St. Pierre, T. G.; Woodward, R. C.; Davis, R. M.; Riffle, J. S., Stability of Polydimethylsiloxane-Magnetite Nanoparticle Dispersions against Flocculation: Interparticle Interactions of Polydisperse Materials. *Langmuir* **2008,** *24*, 5060-5069.

27.   Kalliola, S.; Repo, E.; Sillanpää, M.; Singh Arora, J.; He, J.; John, V. T., The Stability of Green Nanoparticles in Increased Ph and Salinity for Applications in Oil Spill-Treatment. *Colloids and Surfaces A: Physicochem. Eng. Aspects.* **2016,** *493*, 99-107.

28.   Sugihara, K.; Teranishi, T.; Shimazu, K.; Uosaki, K., Structure Dependence of the Surface Pka of Mercaptoundecanoic Acid Sam on Gold. *Electrochemistry* **1999,** *67*, 1172-1174.

29.   Charron, G.; Hühn, D.; Perrier, A.; Cordier, L.; Pickett, C. J.; Nann, T.; Parak, W. J., On the Use of Ph Titration to Quantitatively Characterize Colloidal Nanoparticles. *Langmuir* **2012,** *28*, 15141-15149.

30.   Edwards, E. W.; Chanana, M.; Wang, D.; Möhwald, H., Stimuli-Responsive Reversible Transport of Nanoparticles across Water/Oil Interfaces. *Angew. Chem. Int. Ed.* **2008,** *47*, 320-323.

31.   Qin, B.; Zhao, Z.; Song, R.; Shanbhag, S.; Tang, Z., A Temperature-Driven Reversible Phase Transfer of 2-(Diethylamino)Ethanethiol-Stabilized Cdte Nanoparticles. *Angew. Chem. Int. Ed.* **2008,** *47*, 9875-9878.

32.   Peng, L.; You, M.; Wu, C.; Han, D.; Öçsoy, I.; Chen, T.; Chen, Z.; Tan, W., Reversible Phase Transfer of Nanoparticles Based on Photoswitchable Host–Guest Chemistry. *ACS Nano* **2014,** *8*, 2555-2561.

33.   Dorokhin, D.; Tomczak, N.; Han, M.; Reinhoudt, D. N.; Velders, A. H.; Vancso, G. J., Reversible Phase Transfer of (Cdse/Zns) Quantum Dots between Organic and Aqueous Solutions. *ACS Nano* **2009,** *3*, 661-667.

34.   Yuan, X.; Luo, Z.; Zhang, Q.; Zhang, X.; Zheng, Y.; Lee, J. Y.; Xie, J., Synthesis of Highly Fluorescent Metal (Ag, Au, Pt, and Cu) Nanoclusters by Electrostatically Induced Reversible Phase Transfer. *ACS Nano* **2011,** *5*, 8800-8808.

35.   Cheng, H.-W.; Schadt, M. J.; Young, K.; Luo, J.; Zhong, C.-J., Determination of Ion Pairing on Capping Structures of Gold Nanoparticles by Phase Extraction. *Analyst* **2015,** *140*, 6239-6244.

36.   Mayya, K. S.; Caruso, F., Phase Transfer of Surface-Modified Gold Nanoparticles by Hydrophobization with Alkylamines. *Langmuir* **2003,** *19*, 6987-6993.

37.   McMahon, J. M.; Emory, S. R., Phase Transfer of Large Gold Nanoparticles to Organic Solvents with Increased Stability. *Langmuir* **2007,** *23*, 1414-1418.

38.   Dong, A.; Ye, X.; Chen, J.; Kang, Y.; Gordon, T.; Kikkawa, J. M.; Murray, C. B., A Generalized Ligand-Exchange Strategy Enabling Sequential Surface Functionalization of Colloidal Nanocrystals. *J. Am. Chem. Soc.* **2011,** *133*, 998-1006.

39.   Dai, M.-Q.; Yung, L.-Y. L., Ethylenediamine-Assisted Ligand Exchange and Phase Transfer of Oleophilic Quantum Dots: Stripping of Original Ligands and Preservation of Photoluminescence. *Chem. Mater.* **2013,** *25*, 2193-2201.

40.   Frankamp, B. L.; Fischer, N. O.; Hong, R.; Srivastava, S.; Rotello, V. M., Surface Modification Using Cubic Silsesquioxane Ligands. Facile Synthesis of Water-Soluble Metal Oxide Nanoparticles. *Chem. Mater.* **2006,** *18*, 956-959.

41.   Wang, X.; Tilley, R. D.; Watkins, J. J., Simple Ligand Exchange Reactions Enabling Excellent Dispersibility and Stability of Magnetic Nanoparticles in Polar Organic, Aromatic, and Protic Solvents. *Langmuir* **2014,** *30*, 1514-1521.

42.   Woehrle, G. H.; Brown, L. O.; Hutchison, J. E., Thiol-Functionalized, 1.5-Nm Gold Nanoparticles through Ligand Exchange Reactions: Scope and Mechanism of Ligand Exchange. *J. Am. Chem. Soc.* **2005,** *127*, 2172-2183.

43.   Kim, K.-H.; Yamada, M.; Park, D.-W.; Miyake, M., Particle Size Control of 11-Mercaptoundecanoic Acid-Protected Au Nanoparticles by Using Heat-Treatment Method. *Chem. Lett.* **2004,** *33*, 344-345.

44.   Gangula, A.; Podila, R.; M, R.; Karanam, L.; Janardhana, C.; Rao, A. M., Catalytic Reduction of 4-Nitrophenol Using Biogenic Gold and Silver Nanoparticles Derived from Breynia Rhamnoides. *Langmuir* **2011,** *27*, 15268-15274.

45.   Wunder, S.; Polzer, F.; Lu, Y.; Mei, Y.; Ballauff, M., Kinetic Analysis of Catalytic Reduction of 4-Nitrophenol by Metallic Nanoparticles Immobilized in Spherical Polyelectrolyte Brushes. *J. Phys. Chem. C.* **2010,** *114*, 8814-8820.

46. Zeng, J.; Zhang, Q.; Chen, J.; Xia, Y., A Comparison Study of the Catalytic Properties of Au-Based Nanocages, Nanoboxes, and Nanoparticles. *Nano Lett.* **2010,** *10*, 30-35.

47. Johnson, J. A.; Makis, J. J.; Marvin, K. A.; Rodenbusch, S. E.; Stevenson, K. J., Size-Dependent Hydrogenation of P-Nitrophenol with Pd Nanoparticles Synthesized with Poly(Amido)Amine Dendrimer Templates. *J. Phys. Chem. C.* **2013,** *117*, 22644-22651.

48. Hinterwirth, H.; Kappel, S.; Waitz, T.; Prohaska, T.; Lindner, W.; Lämmerhofer, M., Quantifying Thiol Ligand Density of Self-Assembled Monolayers on Gold Nanoparticles by Inductively Coupled Plasma–Mass Spectrometry. *ACS Nano* **2013,** *7*, 1129-1136.

49. Kuroda, K.; Ishida, T.; Haruta, M., Reduction of 4-Nitrophenol to 4-Aminophenol over Au Nanoparticles Deposited on Pmma. *J. Mol. Catal. A: Chem.* **2009,** *298*, 7-11.

50. Xu, W.; Kong, J. S.; Yeh, Y.-T. E.; Chen, P., Single-Molecule Nanocatalysis Reveals Heterogeneous Reaction Pathways and Catalytic Dynamics. *Nat Mater* **2008,** *7*, 992-996.

51. Wunder, S.; Lu, Y.; Albrecht, M.; Ballauff, M., Catalytic Activity of Faceted Gold Nanoparticles Studied by a Model Reaction: Evidence for Substrate-Induced Surface Restructuring. *ACS Catal.* **2011,** *1*, 908-916.

52. Zhou, X.; Xu, W.; Liu, G.; Panda, D.; Chen, P., Size-Dependent Catalytic Activity and Dynamics of Gold Nanoparticles at the Single-Molecule Level. *J. Am. Chem. Soc.* **2010,** *132*, 138-146.

CHAPTER FOUR

LIGAND SOFTNESS AFFECTS CATALYTIC ACTIVITY AND REUSABILITY OF

pH-RESPONSIVE COLLOIDAL GOLD NANOPARTICLE

[As submitted to ACS Applied and Materials and Interfaces with minor revisions]

4.1 Introduction

Polymer functionalized nanoparticles have found applications in a variety of fields including targeted biomedicines,[1-4] catalysis,[5-7] sensors and electronics[8-11] and others. Gold nanoparticles (AuNPs) are particularly exciting as catalysts due to their ability to catalyze a wide variety of reaction at moderate temperatures (ambient and less), which include alcohol oxidation, nitroarene reduction, propylene epoxidation, low temperature water-gas shift reaction, carbon-carbon cross coupling, etc.[12-15] Supported AuNPs are used in a wide range of industrial applications and chemical synthesis due to the ease of recovery and applications in continuous reactors.[13, 16-17] However, supported AuNPs demonstrate extensive surface area loss (leading to lower turnover numbers) with respect to analogous colloidal AuNPs. Low chemo, regio and enantio-selectivity are some other shortcomings associated with supported AuNP catalysts.[13, 18] Colloidal catalysts circumvents these issues by providing greater catalytic surface area and potential enhanced selectivity.[13, 18] Conversely, colloidal AuNPs require stabilization in reaction media through stabilizing ligands which leads to a certain loss in available catalytic surface area.[12]

Colloidal AuNP catalysts have found applications in fine chemicals industries[19-20] and chiral catalysis,[13] however most colloidal catalysts systems are avoided in large scale application due to difficulties in catalyst recovery from reaction products. Common

product separation techniques such as distillation involves elevated temperatures and renders temperature-sensitive nano-catalysts inactive through degradation and/or irreversible aggregation. Unconventional colloidal AuNP catalyst recovery methods like ultrafiltration,[21-22] magnetic separation[23-24] and biphasic reaction[25-26] conditions usually suffer from drastic losses in catalytic activity or are inefficient. Colloidal AuNP recovery has seen some successes in the field of stimuli-responsive polymer functionalized AuNPs, where pH, light irradiation, temperature and solvent compositions have been varied to facilitate AuNP catalyst separation from products.[27-30] AuNPs functionalized with thermo-sensitive star polymers[27] and poly (N-isopropylacrylamide) stabilized Au nanorods[28] have been successfully recovered and reused through temperature variations. Double responsive (pH and solvent sensitive) polyampholyte functionalized AuNPs catalysts have been used successfully for six cycles without loss of activity, although using very harsh pH conditions (pH < 1).[31] Gold nanoparticles (NPs) stabilized by pH responsive carboxylate-modified polyvinylpyrrolidone were recycled up to 6 reaction cycles but involved similar harsh conditions (aggregation pH < 2.4).[30]

We have recently[32] used pH responsive mercaptoundecanoic acid (small chain length ligand, MUA) functionalized AuNP (AuNP-MUA) and demonstrated efficient pH-responsive recovery from aqueous media. AuNP-MUA was recovered multiple times through pH-triggered aggregation/redispersion and pH-triggered phase transfer to chloroform with octadecylamine (ODA) ion-pair transfer agent. However, high MUA packing density on AuNP surface rendered AuNPs non-catalytic at 100% MUA surface coverage in the 4-nitrophenol (4-NP) reduction reaction. Catalytic activity was retained for

partial surface coverage, which in turn reduced AuNP-MUA recovery and stability. Large chain length polymeric ligands have been shown to provide increased colloidal stability while also providing greater catalytic surface area on AuNP surface.[12] We have shown large chain length thiolated poly(ethylene)glycol functionalized AuNPs to be highly catalytic towards 4-NP reduction. Decreased packing density associated with increased PEG chain length, results in greater available AuNP catalytic surface area (increased reaction rates). Based on these results, we previously[33] designed a large molecular weight (MW) (~1.8 kDa) pH responsive thiolated poly(acrylic) acid polymer (AuNP-SPAA, 25 % of carboxylic acid moieties modified to thiol moieties) to stabilize AuNPs (AuNP-SPAA). AuNP-SPAA demonstrated strong catalytic activity (for 4-NP reduction) while simultaneously possessing successful pH triggered aggregation/redipsersion (at pH ~4) and ODA-mediated phase-transfer properties (at pH ~8). However, major catalytic activity losses were observed for both recovery processes, with phase transfer recovery demonstrating enhanced catalytic activity retention.

In the current work, we have improved the catalyst reusability by manipulating the ligand shell chemistry. Catalytic activity retention has been enhanced substantially and we have elucidated the causes of catalytic activity loss in AuNP-SPAA during the 4-NP reduction reaction. Polymer softness effects (conformation, MW, packing density and ligand shell hydration) on catalytic activity and catalyst recoverability were examined through kinetic studies, thermogravimetric analysis (TGA) and small angle neutron scattering (SANS). Enhanced catalyst reusability was achieved but with sacrificing catalytic activity on decreasing the polymer shell softness. We demonstrate that catalytic

102

activity loss is due to irreversible AuNP-SPAA aggregation as a result of polymer desorption from the AuNP surface.

4.2 Experimental Section

4.2.1 Chemicals and Instrumentation

Reagents 1-ethyl-3-(3-(dimethylamino) propyl)-carbodiimide) hydrochloride, cysteamine hydrochloride and toluene, were purchased from TCI, Chem-Impex, and Alfa Aesar, respectively. Deuterated water (D_2O, 99.9%) was purchased from Cambridge Isotope Laboratories. All other chemical were purchased from Sigma-Aldrich and used without further purification. Deionized Milli-Q water (resistivity 18.2 MΩ.cm) was used in all synthesis and dilutions. All glassware and stir bars were cleaned with freshly prepared aqua regia. Polymer synthesis was carried out under N_2 environment on a Schlenk line.

4.2.2 PAA-SH Synthesis

Synthesis of thiolated poly(acrylic) acid (PAA-SH) was conducted using carbodiimide (EDC) chemistry in presence of N-hydroxysuccinimide (NHS). For a typical synthesis of 2 kDa PAA-SH (25 % available carboxylic acid groups modified with cysteamine), 750 mg of PAA (2 kDa, Sigma-Aldrich) was dissolved in 50 mL dimethyl sulfoxide (DMSO, anhydrous, Sigma Aldrich) under a N_2 environment. After complete polymer dissolution, 1-ethyl-3-(3-(dimethylamino) propyl) carbodiimide) hydrochloride (EDC, 0.50 g, TCI, >98%, in 5 mL DMSO) and N-hydroxysuccinimide (0.60 g NHS, Sigma-Aldrich in 5 mL DMSO) were added and stirred for 30 mins. EDC was used stoichiometrically to result in a theoretical 25% modification, NHS was used at twice the stoichiometric amount for optimum conversion. Subsequently, 2-Aminoethanethiol

(Cysteamine, 0.60 g, Chem-Impex, 99.5 %, in 5mL in DMSO) was added and stirred overnight under N_2 environment. 1 mL of PAA-SH in DMSO was mixed in 19 mL Milli-Q water and dialyzed against 5 L of Milli-Q water with 5 water exchanges to remove excess DMSO and reactants. Aqueous polymer solutions were lyophilized and preserved at -20 °C. PAA-SH with higher thiol contents were similarly prepared by increasing reactants stoichiometrically. Polymer functionalization was confirmed by attenuated total reflectance-Fourier transform infrared (ATR-FTIR) and thiol content quantified through proton nuclear magnetic resonance (H-NMR).

4.2.3 AuNP-SPAA Synthesis

A modified citrate reduction method was used to synthesize 12 nm average diameter citrate-stabilized AuNPs.[34-35] Briefly, 250 µL 0.05 M $HAuCl_4.3H_2O$ was mixed with 49 mL milli-Q water and brought to a boil under reflux condition with mild magnetic stirring. 1 mL 0.05 M trisodium citrate (citrate:Au = 4:1) was added to this solution and boiled for 15 mins. Solution was removed from heat and mildly stirred for 3 hours. Citrate-stabilized AuNP formation was confirmed by the localized surface plasmon resonance (LSPR) peak at wavelength ~ 520 nm.

AuNP-SPAA was synthesized by a ligand exchange reaction with citrate-stabilized AuNP and PAA-SH. Ligand exchange was conducted at pH 10 to deprotonate the acidic groups on PAA-SH and the solution was incubated for 24 hours at room temperature. Excess PAA-SH was removed by repeated centrifugation (14000 rpm, 1 hour) and redispersion of AuNP-SPAA in fresh milli-Q water at pH 10 for 4 cycles. Excess polymer

removal was confirmed by H-NMR when no detectable traces of PAA-SH was found in the centrifugation supernatant.

Transmission electron microscopy (TEM, H9500 Hitachi, 300 kV) was used to examine AuNP particle size and structure (size distribution analysis using ImageJ). TEM grids were prepared by drying 10 µL of AuNP on a 300 mesh Cu grid (Formvar coated) and subsequently drying in a desiccator overnight. Hydrodynamic diameter (volume weighted) and zeta potential (ζ) of dilute aqueous dispersions of purified AuNP-SPAA were measured using a Malvern Zetasizer Nano ZS (Model ZEN3600). UV-Vis absorbance spectroscopy measurements were carried out in 4 mL quartz cells on a Varian Cary 50 UV-Vis spectrophotometer. Polymer packing density was measured by thermogravimetric analysis (TA Instruments SDT Q600) where 50 mL of AuNP-SPAA dispersion was repeatedly centrifuged (14000 rpm, 1 hour) to 50 µL AuNP-SPAA and deposited into an alumina pan. Solvent was evaporated in the Q600 by holding temperature at 120 ^{o}C for 15 mins and then the temperature was ramped to 550 ^{o}C at 10 ^{o}C/min and held for 30 mins (N$_2$ purge, 20 mL/min).

Concentration of Au in all AuNP-SPAA solutions were measured through inductively coupled plasma-optical emission spectroscopy (ICP-OES) post purification. AuNPs were digested in a freshly prepared aqua regia solution (HCl/HNO$_3$ 3:1 molar ratio) and subsequently diluted 20 times for ICP-OES measurements. TraceCERT (1 g/L Au in HCl) was used as ICP standard.

4.2.4 4-NP Reduction for Kinetic Measurements

Performance and efficiency of the AuNP-SPAA catalysts was characterized by the 4-nitrophenol (4-NP) reduction to 4-aminophenol (4-AP) in presence of sodium borohydride. Reaction kinetics were measured by time-resolved UV-Vis spectroscopy, tracking the change in 4-NP (nitrophenolate ion) peak intensity at 400 nm versus time. Briefly, 1 mL of 0.2 mM 4-NP, requisite AuNP-SPAA volume (0.05 mg Au) and remaining milli-Q water to yield a final volume of 2.7 mL were added to a 4 mL quartz cuvette. 0.3 mL of 0.1 M $NaBH_4$ (freshly prepared in ice cold milli-Q water) was added to this solution and time-resolved spectra were immediately acquired with magnetic stirring.

4.2.5 Small Angle Neutron Scattering (SANS)

SANS experiments were conducted on the NGB-30m SANS[36] instrument at the National Institute of Standards and Technology (NIST) Center for Neutron Research (NCNR, Gaithersburg, MD). All sample were prepared at a concentration of ~20 mg Au/mL which yielded a ~ 0.1 % volume % in solution and were considered in the core shell particle dilute regime to minimize inter-particle interactions. Purified AuNP-SPAA in H_2O (200 mL) was centrifuged (10000 rpm, 1 hour) and supernatant removed to yield a final concentrated AuNP-SPAA volume of 1 mL. The concentrated AuNP-SPAA was further centrifuged and redispersed with 1 ml of D_2O. The centrifugation and redispersion with D_2O was repeated two more times. This ensured < 1% (by volume) of H_2O in the final colloidal catalyst. AuNP-SPAA in D_2O was loaded on 1 mm path length titanium demountable cell with quartz windows, maintained at 25 °C (± 0.1 °C accuracy). Three sample to detector distances of 14, 4 and 1 m using neutron wavelength 6Å (wavelength resolution of 12 %, full width at half maximum) was used to probe q-range from 0.004-0.4

Å^{-1}. Empty beam, empty cell, neat D$_2$O backgrounds were acquired in addition to transmission measurements for individual samples for raw data background correction and normalization using IgorPro.[37]

4.2.6 Catalyst Reuse and Recovery

Two catalyst recovery schemes were examined: (a) pH triggered AuNP-SPAA aggregation/redispersion and (b) pH triggered AuNP-SPAA phase transfer into chloroform by octadecylamine (ODA). In the first, the reaction product phase (containing AuNP-SPAA) was adjusted to pH = 4 using 0.01 M HCl and incubated (1 hr) for complete catalyst precipitation. The product-containing supernatant was removed and the precipitated AuNP-SPAA catalyst was redispersed in pH 10 Milli-Q water (KOH adjusted) for reuse in a subsequent reaction as shown in Scheme 4A.

(A) pH aggregation/redispersion

Remove Solvent/Products

pH ~ 10 → Add H⁺ → pH ~ 4 → Precipitation 1 hour →

Add OH⁻

Add fresh Solvent/Reactants

(B) Phase Transfer

Remove aq phase

pH ~ 11 Aqueous → Add H⁺ / ODA + CHCl₃ → pH ~ 7.5 Aqueous → Vortex 2 mins / ODA + CHCl₃ + AuNP → Aqueous → Add fresh pH ~ 11 solvent / Vortex 2 mins → Aqueous

Remove and Reuse chloroform + ODA
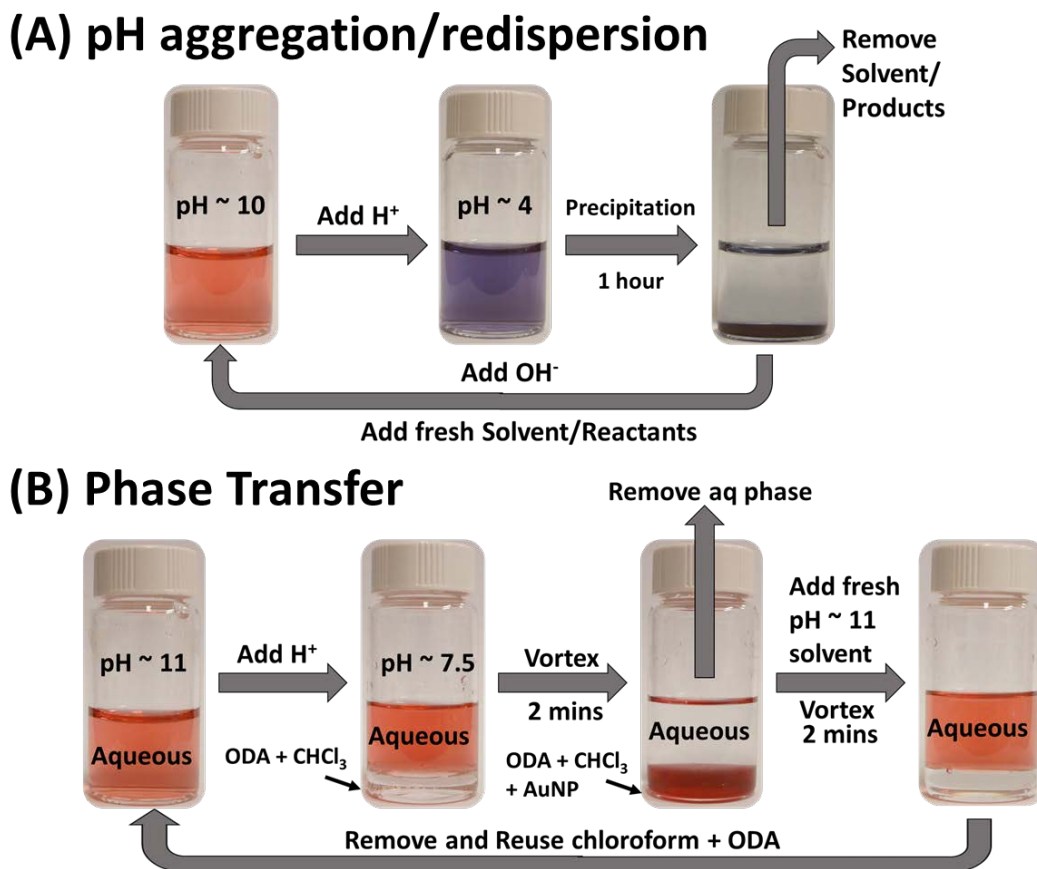
Scheme 4. (A) Depicts general catalyst recovery scheme using pH aggregation and redispersion and (B) depicts pH triggered phase transfer catalyst recovery scheme using chloroform and phase transfer agent octadecylamine. Fresh solvent can be replaced by reactants in these schemes for conducting multiple reaction cycles.

For the phase transfer recovery scheme, the pH of reaction products was modified to pH ~ 8 (below the pK_a of ODA) and 1 mL of chloroform containing 1 mg ODA was added and vigorously vortexed mixed for 2 mins. On protonation at pH ~ 7.5, ODA forms ion-pairs with the PAA carboxylic acid groups on the AuNP-SPAA rendering the catalysts hydrophobic. ODA acts as a phase transfer agent and facilitates complete phase transfer of aqueous AuNP-SPAA$_{2K}$ to chloroform. The aqueous phase containing products was removed and fresh Milli-Q water (pH ~11) was added and vigorously mixed for 2 mins. At

pH ~ 11, ion-pair dissociation leads to complete redispersion of AuNP-SPAA in alkaline aqueous medium and provides for catalyst recovery. Both schemes are shown pictorially in Scheme 4. AuNP-SPAA$_{30K}$ catalysts could not be completely recovered using Scheme 4B.

4.3 Results and Discussion

4.3.1 PAA-SH and AuNP-SPAA Synthesis.

Poly (acrylic acid), PAA is a resilient, pH sensitive polymer but lacks functionality that can bind strongly to gold surfaces, but it can be used as a platform polymer where the acidic groups can be easily and controllably modified to contain a diversity of functional moieties. Modification of the polymer backbone with thiol functionality provides strong binding to AuNP surfaces, enhanced colloidal stability and pH responsive properties to AuNPs. Thiolated-poly (acrylic acid), PAA-SH was synthesized by EDC-NHS mediated coupling of PAA (2 kDa and 30 kDa) with 2-aminoethanethiol (cysteamine). PAA thiolation was completed to varying extents (25, 50, 75 and 100%) to alter the polymer ligand softness on AuNP surface. ATR-FTIR of the functionalized PAA depicted two strong amide stretching vibrations and a weak N-H stretching vibration (Figure 4.1). Thiol content in PAA-SH was quantified through proton nuclear magnetic resonance (H-NMR) spectroscopy (Figure 4.2). The actual thiol contents (% carboxylic acid converted to thiol) measured through H-NMR are summarized in Table 4.1 in parenthesis adjacent to catalyst names. PAA-SH yield is explained through competitive side reactions and formation of anhydrides and N-acylurea.[38] Surprisingly, PAA-SH$_{2K}$ and PAA-SH$_{30K}$ yields were found

109

to be similar, thus they were treated as analogous polymers (e.g. PAA-SH$_{2K}$ (10%) and PAA-SH$_{30K}$ (12%)).
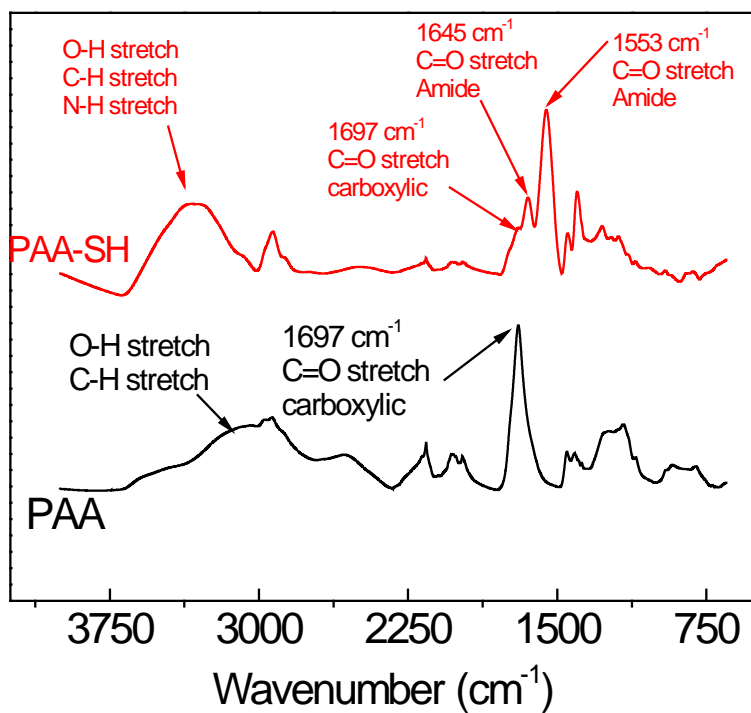
Figure 4.1. Typical ATR-FTIR of pure PAA$_{2K}$ and PAA-SH$_{2K}$ (22%)
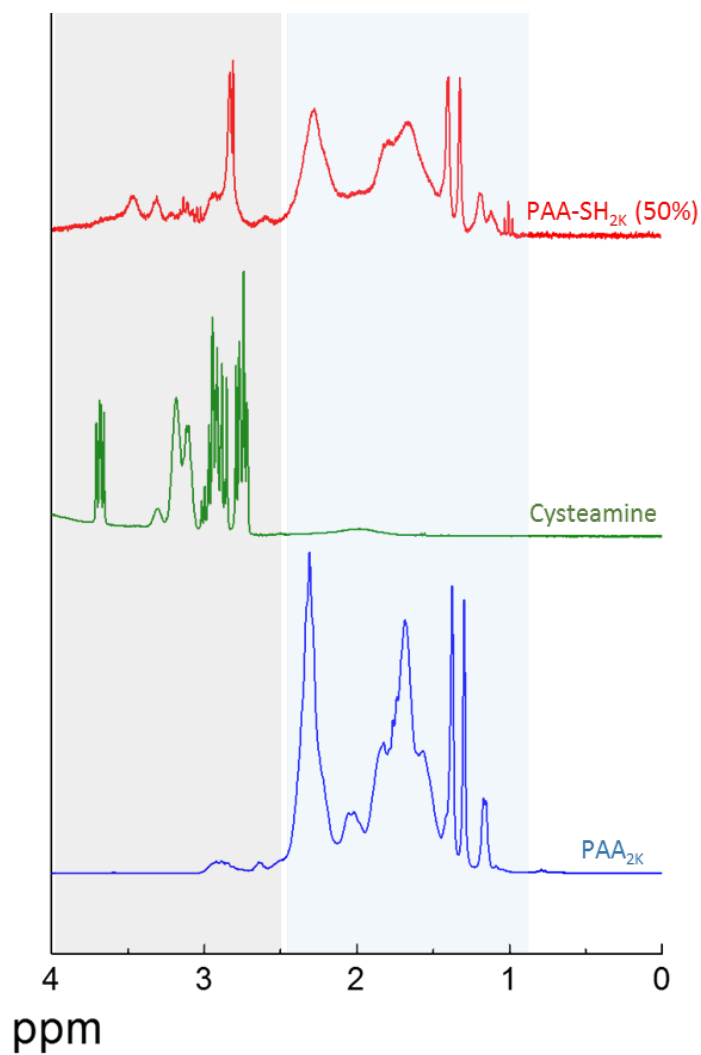
Figure 4.2. Typical H-NMR spectra of pure PAA$_{2K}$ in D$_2$O, pure cysteamine in D$_2$O and synthesized PAA-SH$_{2K}$ (50%) in D$_2$O. Thiol content was calculated based on ratio of protons from the polymer backbone (1-2.5 ppm) and protons from attached cysteamine (2.5-4 ppm).
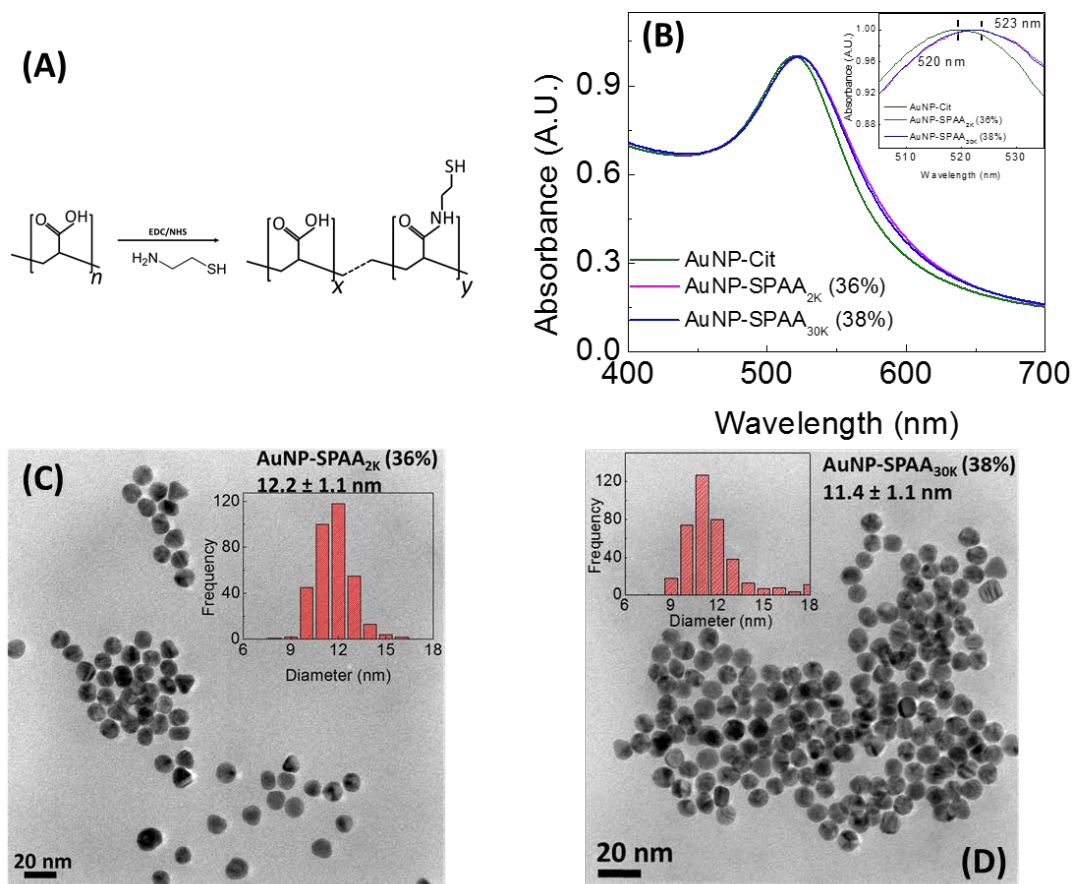
Figure 4.3. (A) Polymer synthesis scheme and structure of PAA-SH random copolymer with varying (x/y) ratios. (B) UV-Vis spectra showing the LSPR peak of AuNP-cit (~520 nm) and AuNP-SPAA$_{2K}$ (36%) and AuNP-SPAA$_{30K}$ (38%) (~523 nm) demonstrating red shift (inset) due to functionalization. Typical TEM and size distribution for (C) AuNP-SPAA$_{2K}$ (36%) and (D) AuNP-SPAA$_{30K}$ (38%).

Mean AuNP core diameters of AuNP-SPAA$_{2K}$ and AuNP-SPAA$_{30K}$ obtained through TEM image analysis (Figure 4.3B), zeta potentials and hydrodynamic diameter of AuNP-SPAA are summarized in Table 4.1. AuNP functionalization was confirmed by a red-shift in localized surface plasmon resonance (LSPR) peak from 520 nm (AuNP-Cit) to 523 nm for all colloidal AuNP-SPAA (Figure 4.3C). For a typical AuNP-SPAA$_{2K}$ (10%)

functionalization, increase in negative zeta (ζ) potential from -27.1 ± 1.5 mV to -38.1 ± 3.5 mV and hydrodynamic diameter (volume weighted) change from ≈ 20 nm (PDI = 0.21) to ≈ 39 nm (PDI = 0.3) also corroborates AuNP functionalization. A noticeable decrease in hydrodynamic diameter was observed on increasing thiol content in PAA-SH, which may be attributed to increased anchoring to the particle surface along the polymer backbone. AuNP-SPAA$_{30K}$ hydrodynamic diameters were consistently larger than analogous AuNP-SPAA$_{2K}$ catalysts owing to the increased MW. No significant change (2 tailed t-test with 95% confidence) in AuNP core diameter was observed on AuNP functionalization. A secondary test of functionalization was also conducted, where pH of AuNP-Cit and AuNP-SPAA was cycled from alkaline-acidic-alkaline (pH 10, pH 4 and pH 10 respectively). Permanent aggregation of AuNP-Cit was observed in acidic conditions whereas, all AuNP-SPAA samples aggregated in acidic media, but redispersed instantly under basic conditions.

Table 4.1. Catalyst characterization summary: AuNP core diameters by TEM, Hydrodynamic Diameter by DLS and Zeta (ζ) potential. Errors represent one standard deviation from the mean.

Catalyst	Core Diameter (nm)	Hydrodynamic Diameter (nm), (PDI)	Zeta (ζ) potential (mV)
AuNP-Cit	12.3 ± 1.2	20.1 (0.21)	-27.1 ± 1.5
AuNP-SPAA$_{2K}$(10%)	11.2 ± 1.1	39.2 (0.24)	-38.1 ± 3.5
AuNP-SPAA$_{2K}$(22%)	11.6 ± 1.5	37.1 (0.27)	-34.5 ± 1.5
AuNP-SPAA$_{2K}$(36%)	12.2 ± 1.1	35.4 (0.21)	-35.6 ± 3.1
AuNP-SPAA$_{2K}$(50%)	12.7 ± 1.1	36.1 (0.22)	-32.1 ± 3.2
AuNP-SPAA$_{30K}$(12%)	11.4 ± 0.9	51.4 (0.31)	-39.1 ± 1.6
AuNP-SPAA$_{30K}$(22%)	11.2 ± 1.0	49.1 (0.35)	-38.8 ± 1.1
AuNP-SPAA$_{30K}$(38%)	11.4 ± 1.1	47.2 (0.27)	-39.3 ± 2.2
AuNP-SPAA$_{30K}$(53%)	11.9 ± 1.1	43.1 (0.30)	-33.0 ± 2.0

4.3.2 Kinetics through Model 4-NP Reduction Reaction.

In this current work, the impact of ligand shell softness and ligand MW, on catalytic activity has been investigated through the reduction of 4-nitrophenol (4-NP) to 4-aminophenol (4-AP) by sodium borohydride in presence of AuNP catalysts.[7, 39] In-situ reaction progress was monitored with the 4-nitrophenolate absorbance peak intensity (400 nm) through time resolved UV-Vis spectroscopy (Figure 4.4A). Reaction rate constants were obtained through pseudo first order reaction kinetic analysis for 4-NP (-ln (C_t/C_0) vs. t) and demonstrates a linear relationship (Figure 4.4B). For most catalysts, an induction time was observed, consistent with previous studies (Figure 4.4A and D).[7, 12, 18] Rate constants and induction times for all catalysts are listed in Figure 4.4C and Figure 4.4D. All AuNP-SPAA rate constants were smaller (slower reaction rate) than 'bare' AuNP

citrate catalyst (0.66 ± 0.1 min^{-1}), suggesting partial surface passivation by PAA-SH ligands. A clear relation between the ligand MW and catalytic activity was observed, where all AuNP-SPAA$_{30K}$ exhibited faster reaction kinetics and smaller induction times with respect to analogous AuNP-SPAA$_{2K}$. Remarkable decreases in catalytic activity and increases in induction time were observed with increasing thiol content in the ligands for both AuNP-SPAA$_{2K}$ and AuNP-SPAA$_{30K}$.
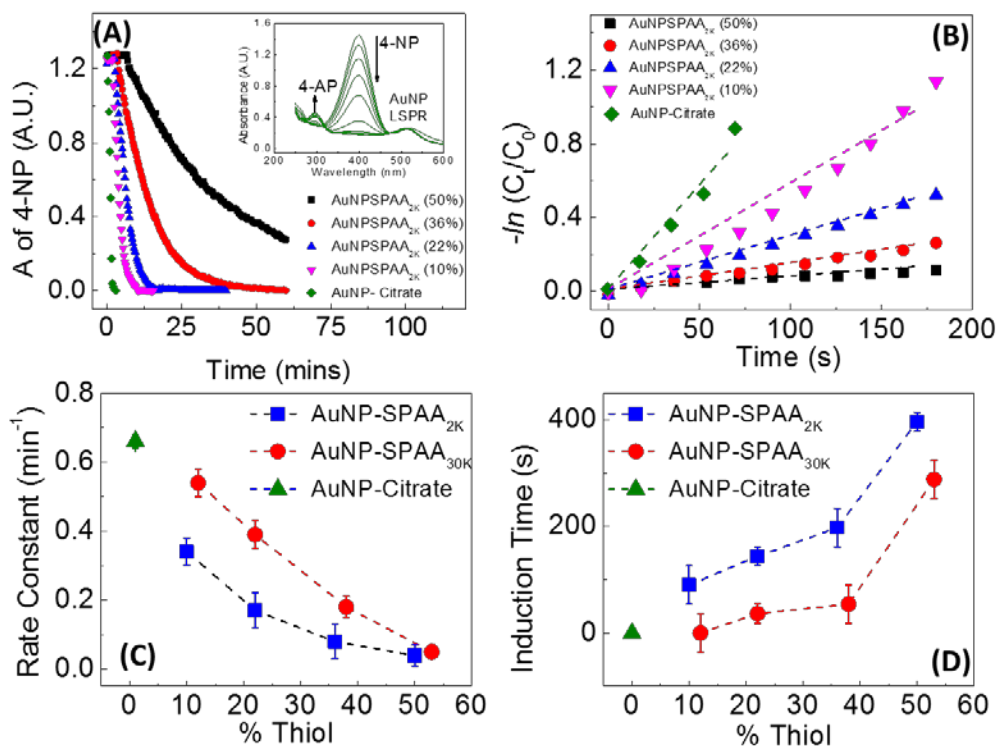
Figure 4.4 (A) Reaction progress tracked through change in 4-NP peak absorbance at 400 nm for AuNP-Cit and AuNP-SPAA$_{2K}$ catalyst (Inset shows typical time resolved UV-Vis spectra for AuNP-Cit). Error bars have been removed for clarity, (B) Dashed lines represent pseudo first order reaction data fit for first 3 mins of reaction, slope of linear fits yield rate constants. Summary of (C) Rate constants and (D) Induction time for AuNP-SPAA$_{2K}$ and AuNP-SPAA$_{30K}$ catalysts vs. thiol content. Error bars represent one standard deviation from mean of three separate reactions. Dashed lines are for visual aid only.

The model 4-NP reduction reaction follows a Langmuir-Hinshelwood mechanism where reaction occurs when both 4-NP and BH_4^- adsorb on AuNP available surface area.[7, 40] Reaction rate and induction time is thus controlled by AuNP surface accessibility by the reactants. For polymer ligand-stabilized AuNP catalysts, AuNP surface accessibility is directly related to polymer ligand packing density and available AuNP surface area.[12, 32] Reaction rate dependence on ligand MW and ligand softness can be elucidated by investigating the ligand packing density and polymer conformation on AuNP surface.

4.3.3 Ligand Packing Density on AuNP Surface.

Ligand packing density on AuNP surface was quantified from the ligand weight fraction obtained by TGA, assuming a mean nanoparticle diameter obtained by TEM. Figure 4.5 shows a drastic difference in ligand packing densities for analogous catalysts with 0.7 molecules/nm^2 for AuNP-SPAA$_{2K}$ (10%) and 0.01 molecules/nm^2 for AuNP-SPAA$_{30K}$ (12%) indicating increased softness for large MW PAA-SH. Remarkably, ligand packing density increased with increases in ligand thiol content for both AuNP-SPAA$_{2K}$ and AuNP-SPAA$_{30K}$ catalysts. We have previously measured packing densities of AuNPs functionalized with thiolated-polyethylene glycol (PEG-SH, one thiol moiety at PEG distal end) to be inversely related to PEG-SH MW.[12] PEG-SH (2 kDa) and PEG-SH (30 kDa) PEG-SH had packing densities of ~ 2.1 and ~ 0.47 molecules/nm^2 respectively. The 0.7 molecules/nm^2 packing density for AuNP-SPAA$_{2K}$(10%), which corresponds to ~ 3 thiol linkers randomly distributed per polymer, is roughly a third of the value observed in case of PEG-SH (2 kDa). PAA-SH in this work with multiple randomly distributed anchors can be envisioned in a 'carpet-like' conformation. The multiple anchor sites and carpet-like

conformation would lead to a larger molecular footprint and decreased packing density on the AuNP surface. Furthermore, low packing density of PAA-SH$_{30K}$ can be explained by carpet conformation of a much larger polymer compared to PAA-SH$_{2K}$. Increased thiol content led to increased packing density (~ 1.3 molecules/nm^2 for AuNP-SPAA$_{2K}$ (50%) with ~ 13 thiol groups per polymer). Ligand conformation on AuNP surface was subsequently investigated in detail through small angle neutron scattering (SANS).
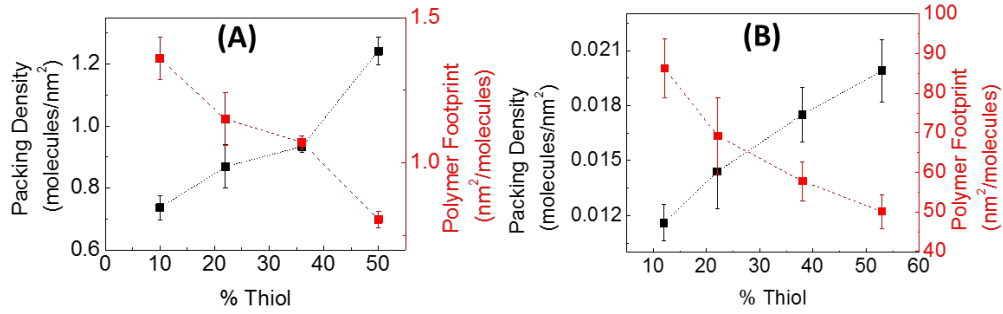
Figure 4.5. TGA curves of (A) AuNP-SPAA$_{2K}$ and (B) AuNP-SPAA$_{30K}$ with various thiol content. Error bars represent one standard deviation from the mean of three separate measurements. Dashed lines are for visual aid only.

4.3.4 Ligand Conformation, Shell Thickness and Solvation.

PAA-SH conformation on AuNP surface was investigated through small angle neutron scattering (SANS). SANS data were fitted with a spherical core-shell form factor:

$$P(q) = \frac{scale}{V_s}\left[\frac{3V_c(\rho_c - \rho_s)[\sin(qr_c) - qr_c\cos(qr_c)]}{(qr_c)^3} + \frac{3V_s(\rho_s - \rho_{solv})[\sin(qr_s) - qr\cos(qr_s)]}{(qr_s)^3}\right]^2 + bkg$$

(1)

where, outer shell volume (V_s); Core volume (V_c); shell radius (r_s); core radius (r_c); core scattering length density (SLD) core (ρ_c); shell SLD (ρ_s); solvent SLD (ρ_{solv}) and

background are included. Figure 4.6A depicts a typical SANS scattering pattern for AuNP-SPAA$_{2K}$ (10%) and AuNP-SPAA$_{30K}$ (12%) with spherical core-shell model fit (solid lines). Parameters such as volume fraction, ρ_c and ρ_{solv}, core diameter and polydispersity were fixed (obtained from TEM analysis), while shell thickness (r_s-r_c) and ρ_s were fit to the data. The low-q upturn and deviation from core-shell feature demonstrates the presence larger aggregates, potentially due to PAA-SH physical cross-linking at high concentrations used for SANS measurements.
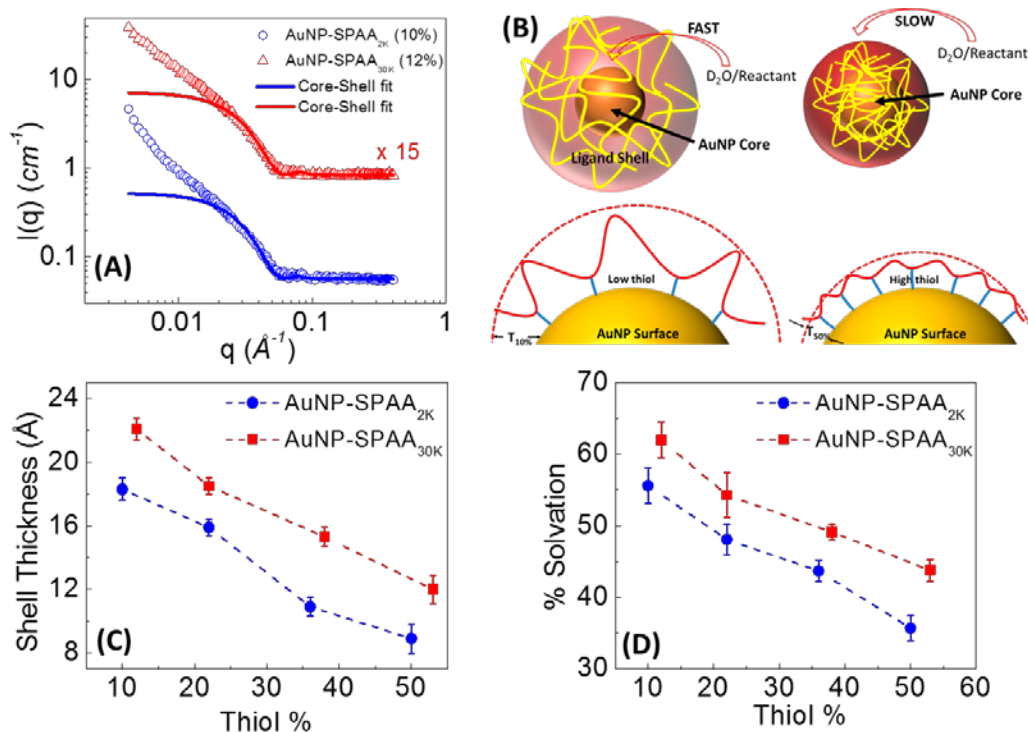
Figure 4.6 (A) Typical SANS scattering profile of AuNP-SPAA$_{2K}$ and AuNP-SPAA$_{30K}$ catalyst. Solid lines represent spherical core-shell fit to scattering data. Scattering profile of AuNP-SPAA$_{30K}$ and data fit has been vertically shifted by factor of 15 for visual clarity. (B) Schematic showing effect of thiol content on shell thickness, T (T$_{10\%}$>T$_{50\%}$) and conformation affecting AuNP available surface area and access of AuNP surface by solvent/reactant. (C) Shell thickness and (D) % shell solvation with thiol content for AuNP-SPAA$_{2K}$ and AuNP-SPAA$_{30K}$. Error bars represent one standard deviation from mean and dashed lines are visual aid only.

Previously[41-43] through SANS, a 1.2 nm shell thickness was measured for thiolated ligand dodecanethiol (DDT, 12 carbon) on AuNP surface. Larger chain length PEG-SH (end functionalized thiol) such as, 2 kDa PEG-SH and 5 kDa PEG-SH on 10 nm AuNP particles exhibited a shell thickness of 9.3 nm and 16.5 nm respectively.[44] AuNP-SPAA$_{2K}$ SANS spectra on the other hand, depicted a 0.9 nm (AuNP-SPAA$_{2K}$ (50%)) to 1.8 nm (AuNP-SPAA$_{2K}$ (10%)) shell thickness (Figure 4.6C). AuNP-SPAA$_{30K}$ shell thicknesses

(for example, 2.2 nm for AuNP-SPAA$_{30K}$ (12%)) was found to be marginally greater than all analogous AuNP-SPAA$_{2K}$ (for example, 1.8 nm for AuNP-SPAA$_{2K}$ (10%)) shell thickness (Figure 4.6C). These evidences confirm that the polymers are situated on AuNP surface in a 'carpet-like' conformation. The polymer backbone anchors to AuNP surfaces as depicted in Figure 4B through multiple attachment sites, leading to shell thicknesses comparable to small molecules like DDT (1.2 nm).

Figure 4.6C demonstrates a decrease in shell thickness with increasing thiol content for AuNP-SPAA$_{2K}$ (1.8 nm to 0.9 nm for increasing thiolation from 10 to 50 %) and AuNP-SPAA$_{30K}$ (2.2 nm to 1.2 nm for increasing thiolation from 12 to 53 %) depicting increase in shell hardness (schematically depicted in Figure 4.6B). TGA results supports the observation, where higher packing density coincides with increasing ligand thiol content. Ligand compactness on the AuNP surface can be measured by quantifying shell solvation by SANS. Solvent D$_2$O penetrates the hydrogenated shell and contributes towards the shell scattering length density (ρ_{shell}). Hence, ρ_{shell} has an intermediate value between ρ_{ligand} and ρ_{solv}, denoting the extent of shell solvation, calculated by eq. 2[41-42, 45]:

$$\% \ shell \ solvation = (\rho_{shell} - \rho_{ligand})/(\rho_{solv} - \rho_{ligand}) * 100 \qquad (2)$$

The AuNP-SPAA$_{30K}$ ligand shell consistently demonstrated higher percent solvation than the AuNP-SPAA$_{2K}$ ligand shells with equivalent thiolation (Figure 4.6D). Shell solvation measurements are consistent with the lower packing density and larger shell thickness measurements for AuNP-SPAA$_{30K}$ and supports AuNP-SPAA$_{30K}$ having a softer ligand shell on AuNP surface. Shell hardening was observed (shell solvation decrease) with increased thiolation (Figure 4.6D).

4-NP reduction reaction kinetics analysis revealed slower kinetics for catalysts with PAA-SH$_{2K}$ compared to PAA-SH$_{30K}$, as shell solvation directly relates to AuNP surface accessibility by solvent and reactants. Catalyst stabilized by ligands with greater thiol content (for example, AuNP-SPAA$_{2K}$ (50%) and AuNP-SPAA$_{30K}$ (53%)) demonstrated slower kinetics compared to catalysts stabilized by softer ligand shells (low thiol content). Highly solvated ligand shells (for example, AuNP-SPAA$_{30K}$ (12%), low thiol content and large MW ligand) allows 4-NP and BH$_4^-$ to readily access AuNP surface and 4-AP to rapidly exit the ligand shell, facilitating the Langmuir-Hinshelwood reaction mechanism.

4.3.5 Recovery and Reuse of AuNP-SPAA catalyst. To investigate ligand shell softness impacts on catalyst recoverability and reusability, the catalysts underwent pH-induced recovery and reuse cycles in presence of reactants 4-NP and NaBH$_4$ according to the Scheme 4A and 4B (discussed in the experimental section and pictorially in Scheme 4A and 4B). Reaction rate constants were obtained after each reuse cycle by conducting fresh 4-NP reduction reactions with recovered catalysts. Catalytic activity retention was ~ 2% for both AuNP-SPAA$_{2K}$ (10%) and AuNP-SPAA$_{30K}$ (12%) after five reaction cycles using Scheme 4A as depicted in Figure 4.7C and 4.7D. While a soft ligand shell is favorable for higher reaction rate constants, it is not robust against recycle and reuse over multiple cycles. On employing catalysts with harder shell (higher thiol content, for example, AuNP-SPAA$_{2K}$ (50%)), a slower reaction rate was obtained (Figure 4.7B), however catalytic activity retention ~75% was observed after 5 reaction cycles (Figure 4.7C). Similar enhancement in reusability was observed for AuNP-SPAA$_{30K}$ catalyst with high thiol content ligands (~48 % catalytic activity retention for AuNP-SPAA$_{30K}$ (53%) after five

reaction cycles). Overall, AuNP-SPAA$_{2K}$ performed better (more cycles with greater activity retention) than AuNP-SPAA$_{30K}$ catalysts for equivalent thiolations (Figure 4.7D).
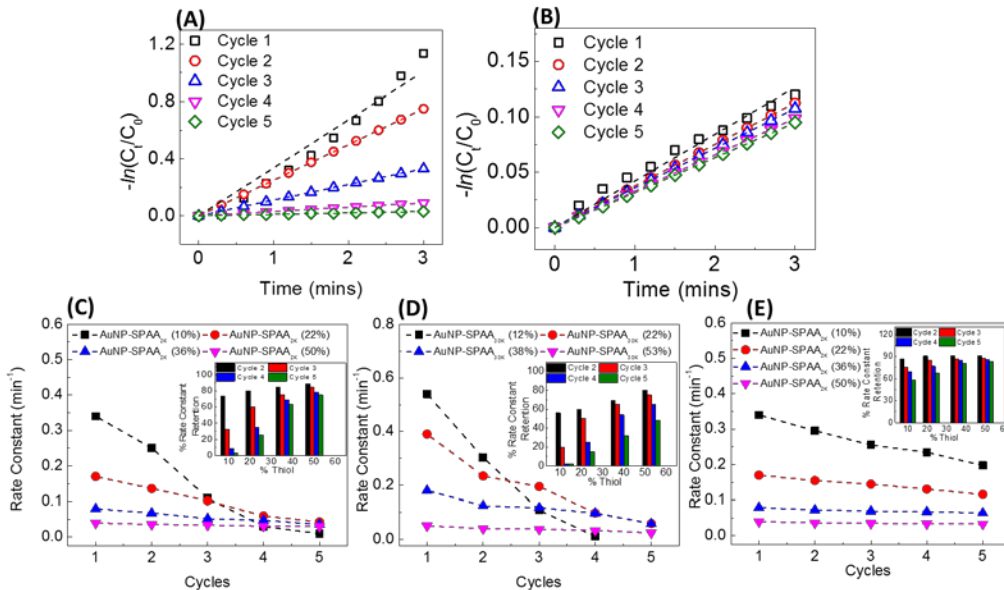
Figure 4.7. Pseudo-first order fits (dashed lines) to kinetic data with each cycle of aggregation/redispersion for (A) AuNP-SPAA$_{2K}$(10%) and (B) AuNP-SPAA$_{2K}$ (50%). Plot demonstrates low rate of reaction for AuNP-SPAA$_{2K}$ (50%) but demonstrates enhanced catalytic activity retention with each cycle. (C) and (D) summarizes rate constants for AuNP-SPAA$_{2K}$ and AuNP-SPAA$_{30K}$ respectively, with various thiol contents, for each cycle of aggregation/redispersion. Insets depict rate constant retention with each cycle. (E) Rate constants for AuNP-SPAA$_{2K}$ using recovery scheme 1B (phase transfer). Catalytic activity retention is greatly enhanced in scheme 1B compared to scheme 1A for AuNP-SPAA$_{2K}$ catalysts as depicted in the inset.

Figure 4.7E depicts AuNP-SPAA$_{2K}$ performance using phase transfer recovery scheme (Scheme 4B). Catalytic activity retention was greatly increased for Scheme 4B (~ 58 % activity retention for AuNP-SPAA$_{2K}$ (10%) after 5 reaction cycles) compared to Scheme 4A (~ 2% for AuNP-SPAA$_{2K}$ (10%)). Catalytic activity on recovery was further enhanced using catalyst with higher thiol content ligand such as AuNP-SPAA$_{2K}$ (50%) (~ 83% activity retention) compared to AuNP-SPAA$_{2K}$ (10%) (~ 58% retention) after 5

reaction cycles. Surprisingly, AuNP-SPAA$_{30K}$ could not be recovered by Scheme 4B when subjected to reaction conditions. Attempted phase transfer after reaction resulted in catalyst aggregation at the chloroform-water interface (Figure 4.8).
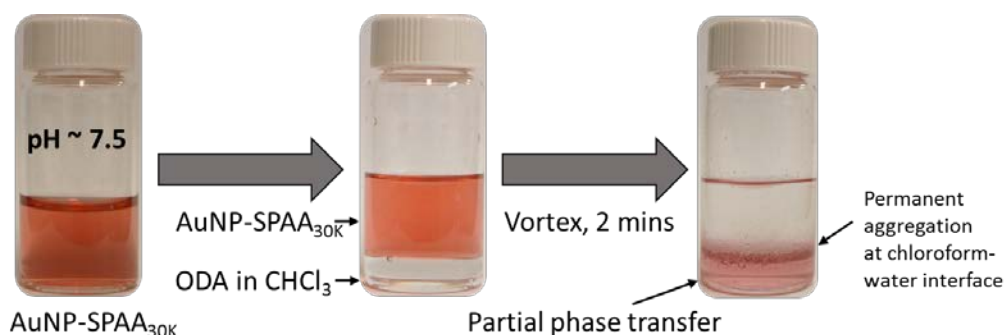
Figure 4.8. Pictures depicting catalyst aggregation at chloroform-water interface on attempting to recover AuNP-SPAA$_{30K}$ catalyst through phase transfer recovery (Scheme 4B)

To isolate the factors affecting catalytic activity retention with reaction cycles for both recovery schemes, the catalyst with the least activity retention with cycling (AuNP-SPAA$_{2K}$ (10%) for recovery Scheme 4A) was selected for detailed analysis. The effect of the recovery process on reusability was investigated in the absence of reactants (4-NP and NaBH$_4$). Figure 4.9A and B show significant reduction in rate constant for both schemes in the absence of reactants intermittent of the recovery cycles. Scheme 4B maintained catalytic activity more so than Scheme 4A. Surprisingly, no significant difference was observed on repeating the same experiments with 4-NP in the media. Greater losses during recovery process Scheme 4A vs. 4B can potentially be attributed to pH changes during complete aggregation/redispersion vs. phase transfer. Colloidal pH alteration includes ligand shell collapse (acidic) and swelling (alkaline) leading to AuNP aggregation and

redispersion respectively. Recovery Scheme 4A requires a pH change from pH 10 to pH 4, whereas recovery Scheme 4B includes pH change from pH 11 to pH 8. Harsh pH environment for the catalysts leads to minor permanent AuNP aggregation and catalytic activity loss. A 13% drop in LSPR peak intensity was observed on pH triggered aggregation/redispersion cycling without reactants (Figure S7 A), which corresponds to the 9% catalytic activity loss observed in Figure 4.9A.
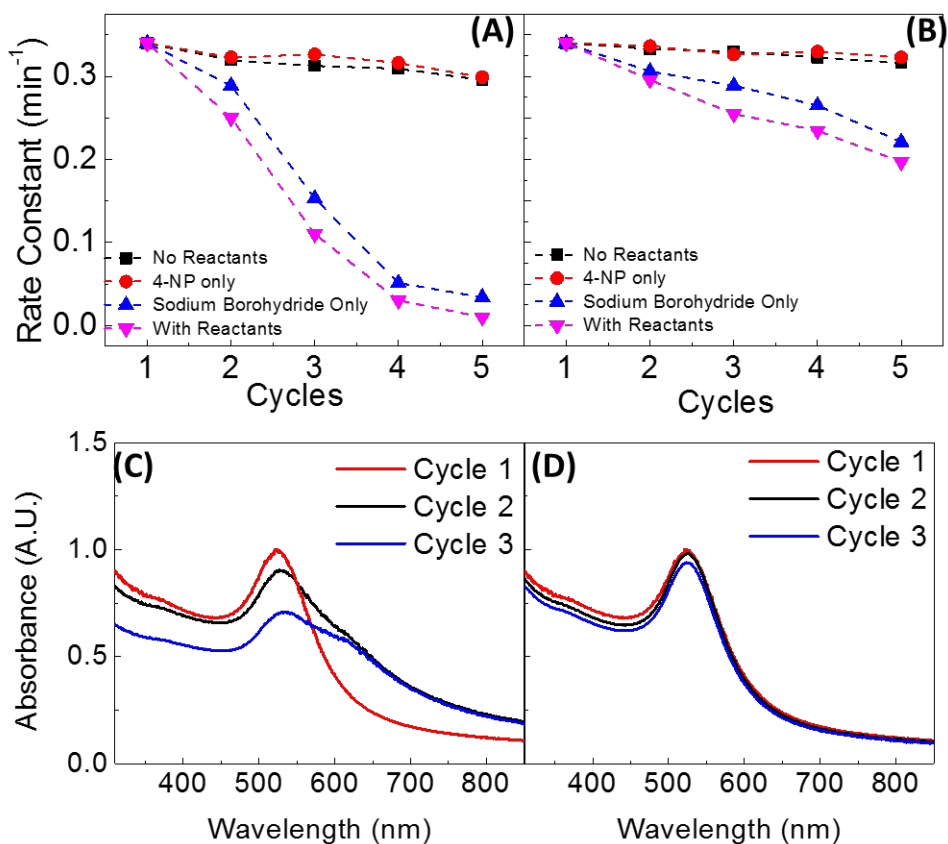
Figure 4.9. (A) Rate constants for AuNP-SPAA$_{2K}$ (10%) with recovery scheme 1A with no reactants, 4-NP only, sodium borohydride only, and with both reactants. (B) the same analysis for recovery scheme 1B. Dashed lines in (A) and (B) are for visual aid only. (C) UV-Vis spectra depicts the onset of aggregation with individual reaction cycles with AuNP-SPAA$_{2K}$ (10%) evidenced by LSPR peak intensity decrease and red-shift. (D) No measurable change in LSPR peak with AuNP-SPAA$_{2K}$ (50%) for 3 reaction cycles. Cycle 1 in (C) and (D) denotes fresh catalyst.
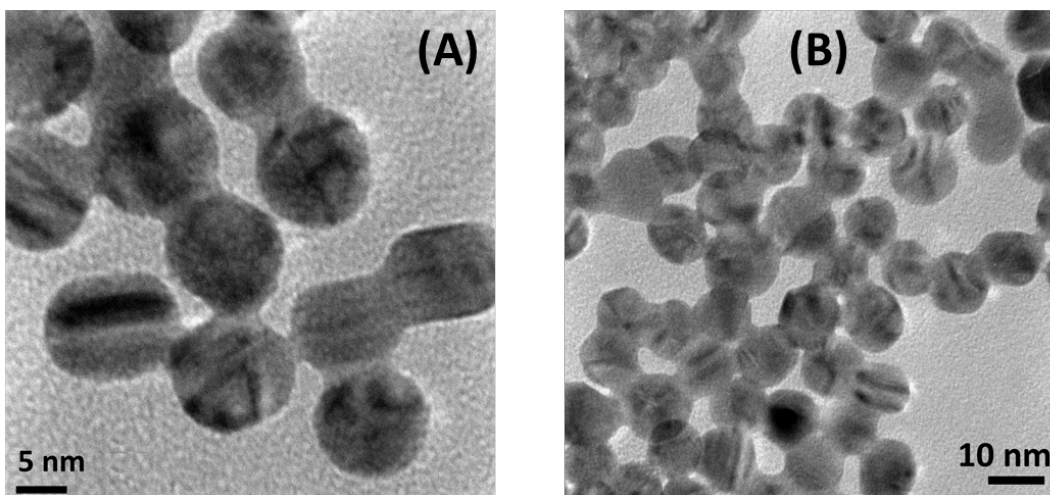
Figure 4.10. Presence of aggregates (fused AuNPs) of (A) AuNP-SPAA$_{2K}$ (10%) and (B) AuNP-SPAA$_{30K}$ (12%), post 2 recovery cycles. Available surface area loss due to AuNP aggregation leads to catalytic activity loss.

Recovery schemes 4A and 4B were also conducted in the presence of NaBH$_4$ only. Losses in catalytic activity were comparable to the losses during reaction (Figure 4.9A and 4.9B). Harsh reducing agents like NaBH$_4$ can lead to Au-sulfur bond cleavage leading to ligand desorption from AuNP surface causing permanent AuNP aggregation.[46-47] UV-Vis absorbance spectroscopy of spent catalyst was conducted for 3 reaction cycles (all reactant present) for AuNP-SPAA$_{2K}$ (10%) and AuNP-SPAA$_{2K}$ (50%). The AuNP-SPAA$_{2K}$ (10%) LSPR peak depicted intensity reduction and a red-shifted peak was generated (~630 nm) (Figure 4.9C) denoting catalyst aggregation with each cycle. However, insignificant LSPR peak intensity loss after three reaction cycles for AuNP-SPAA$_{2K}$ (50%) confirmed insignificant AuNP aggregation (Figure 4.9D). HRTEM images of AuNP-SPAA$_{2K}$ (10%) and AuNP-SPAA$_{30K}$ (12%) (Figure 4.10) clearly depicts AuNP catalyst fusion to form worm like aggregates after three reaction cycles (not observed in case of AuNP-SPAA$_{2K}$ (50%)). AuNP catalysts either aggregate by forming larger AuNP by complete ligand

desorption (surface area loss); or polymer shells interact forming cross-linked structures (also leading to surface passivation). Greater aggregation was observed for catalyst with softer polymers (low thiol content), whereas harder polymer shell catalysts (high thiol content polymer stabilized catalysts), consistently proved to be more robust by resisting $NaBH_4$ induced aggregation. Designing an effective pH responsive colloidal AuNP catalyst thus encompasses a balance between achieving high reaction rates and reusability by careful manipulation of polymer shell softness on AuNP surface.

4.4 Conclusion

We have demonstrated the synthesis and utilization of thiolated pH responsive PAA-SH ligand to functionalize colloidal AuNP catalysts. AuNP-SPAA catalysts can be efficiently recovered and reused for multiple 4-NP reduction reaction cycles by two different recovery schemes: pH triggered aggregation/redispersion and pH triggered phase transfer to chloroform using a phase transfer agent. pH triggered phase transfer was shown to be a more efficient catalyst recovery, however AuNP-SPAA$_{30K}$ could not be successfully recovered through this technique. PAA-SH$_{2K}$ and PAA-SH$_{30K}$ ligands were found to be attached to AuNP surface in a 'carpet-like' conformation due to the presence of multiple thiol anchors on the polymer backbone. We demonstrated that catalytic activity and catalyst recoverability strongly depends on the stabilizing ligand softness. Larger M.W. PAA-SH$_{30K}$ was shown to be softer than PAA-SH$_{2K}$ on AuNP surface resulting in faster reaction kinetics for AuNP-SPAA$_{30K}$ catalysts compared to analogous AuNP-SPAA$_{2K}$ catalysts. Low thiol content ligands (softer ligands) were found to be more solvated with larger shell thickness and AuNP catalysts demonstrated faster reaction kinetics. However, catalysts

with softer ligands demonstrated accelerated aggregation during reaction leading to greater catalytic activity loss with subsequent reaction cycles. Catalytic activity loss was attributed to ligand desorption mediated by sodium borohydride, leading to permanent catalyst aggregation. Catalytic activity loss and ligand desorption could be greatly reduced by using high thiol content PAA-SH stabilizer, although leading to slower reaction kinetics. These evidences provide means to design efficient and reusable colloidal AuNP catalysts by manipulating ligand shell softness and chemistry.

4.5 Acknowledgements

4.6. References

1.   Brown, S. D.; Nativo, P.; Smith, J.-A.; Stirling, D.; Edwards, P. R.; Venugopal, B.; Flint, D. J.; Plumb, J. A.; Graham, D.; Wheate, N. J., Gold Nanoparticles for the Improved Anticancer Drug Delivery of the Active Component of Oxaliplatin. *Journal of the American Chemical Society* **2010,** *132*, 4678-4684.

2.   Huo, S.; Jin, S.; Ma, X.; Xue, X.; Yang, K.; Kumar, A.; Wang, P. C.; Zhang, J.; Hu, Z.; Liang, X.-J., Ultrasmall Gold Nanoparticles as Carriers for Nucleus-Based Gene Therapy Due to Size-Dependent Nuclear Entry. *ACS Nano* **2014,** *8*, 5852-5862.

3.   Koch, A. M.; Reynolds, F.; Kircher, M. F.; Merkle, H. P.; Weissleder, R.; Josephson, L., Uptake and Metabolism of a Dual Fluorochrome Tat-Nanoparticle in Hela Cells. *Bioconjugate Chemistry* **2003,** *14*, 1115-1121.

4.   Kiyofumi, K.; Yuji, I.; Kunihito, K.; Tomohiro, K.; Kenji, K.; Sadahito, A., Magnetoresponsive on-Demand Release of Hybrid Liposomes Formed from Fe3o4 Nanoparticles and Thermosensitive Block Copolymers. *Small* **2011,** *7*, 1683-1689.

5.   Králik, M.; Biffis, A., Catalysis by Metal Nanoparticles Supported on Functional Organic Polymers. *Journal of Molecular Catalysis A: Chemical* **2001,** *177*, 113-138.

6.   Yan, N.; Zhang, J.; Yuan, Y.; Chen, G.-T.; Dyson, P. J.; Li, Z.-C.; Kou, Y., Thermoresponsive Polymers Based on Poly-Vinylpyrrolidone: Applications in Nanoparticle Catalysis. *Chemical Communications* **2010,** *46*, 1631-1633.

7.   Wunder, S.; Polzer, F.; Lu, Y.; Mei, Y.; Ballauff, M., Kinetic Analysis of Catalytic Reduction of 4-Nitrophenol by Metallic Nanoparticles Immobilized in Spherical Polyelectrolyte Brushes. *The Journal of Physical Chemistry C* **2010,** *114*, 8814-8820.

8.   Zamborini, F. P.; Leopold, M. C.; Hicks, J. F.; Kulesza, P. J.; Malik, M. A.; Murray, R. W., Electron Hopping Conductivity and Vapor Sensing Properties of Flexible Network Polymer Films of Metal Nanoparticles. *Journal of the American Chemical Society* **2002,** *124*, 8958-8964.

9.   Ofir, Y.; Samanta, B.; Rotello, V. M., Polymer and Biopolymer Mediated Self-Assembly of Gold Nanoparticles. *Chemical Society Reviews* **2008,** *37*, 1814-1825.

10.   Yu, A.; Liang, Z.; Cho, J.; Caruso, F., Nanostructured Electrochemical Sensor Based on Dense Gold Nanoparticle Films. *Nano Letters* **2003,** *3*, 1203-1207.

11.   Matsui, J.; Akamatsu, K.; Hara, N.; Miyoshi, D.; Nawafune, H.; Tamaki, K.; Sugimoto, N., Spr Sensor Chip for Detection of Small Molecules Using Molecularly Imprinted Polymer with Embedded Gold Nanoparticles. *Analytical Chemistry* **2005,** *77*, 4282-4285.

12.   Ansar, S. M.; Kitchens, C. L., Impact of Gold Nanoparticle Stabilizing Ligands on the Colloidal Catalytic Reduction of 4-Nitrophenol. *ACS Catalysis* **2016,** *6*, 5553-5560.

13.   Stratakis, M.; Garcia, H., Catalysis by Supported Gold Nanoparticles: Beyond Aerobic Oxidative Processes. *Chemical Reviews* **2012,** *112*, 4469-4506.

14.   Corma, A.; Garcia, H., Supported Gold Nanoparticles as Catalysts for Organic Reactions. *Chemical Society Reviews* **2008,** *37*, 2096-2126.

15.   Hui-Hui, C.; Fang, C.; Jian, Y.; Zhao-Xia, G., Gold-Nanoparticle-Decorated Thermoplastic Polyurethane Electrospun Fibers Prepared through a Chitosan Linkage for Catalytic Applications. *Journal of Applied Polymer Science* **2017,** *134*.

16.   Polshettiwar, V.; Luque, R.; Fihri, A.; Zhu, H.; Bouhrara, M.; Basset, J.-M., Magnetically Recoverable Nanocatalysts. *Chemical Reviews* **2011,** *111*, 3036-3075.

17.   Sankaranarayanapillai, S.; Volker, S.; R., T. W., Magnetically Separable Nanocatalysts: Bridges between Homogeneous and Heterogeneous Catalysis. *Angewandte Chemie International Edition* **2010,** *49*, 3428-3459.

18.   Chakraborty, S.; Ansar, S. M.; Stroud, J. G.; Kitchens, C. L., Comparison of Colloidal Versus Supported Gold Nanoparticle Catalysis. *The Journal of Physical Chemistry C* **2018,** *122*, 7749-7758.

19.   Tsunoyama, H.; Sakurai, H.; Ichikuni, N.; Negishi, Y.; Tsukuda, T., Colloidal Gold Nanoparticles as Catalyst for Carbon−Carbon Bond Formation: Application to Aerobic Homocoupling of Phenylboronic Acid in Water. *Langmuir* **2004,** *20*, 11293-11296.

20.   Zhang, Y.; Cui, X.; Shi, F.; Deng, Y., Nano-Gold Catalysis in Fine Chemical Synthesis. *Chemical Reviews* **2012,** *112*, 2467-2505.

21.   Wang, X.; Kawanami, H.; Islam, N. M.; Chattergee, M.; Yokoyama, T.; Ikushima, Y., Amphiphilic Block Copolymer-Stabilized Gold Nanoparticles for Aerobic Oxidation of Alcohols in Aqueous Solution. *Chemical Communications* **2008**, 4442-4444.

22.   Mertens, P. G. N.; Bulut, M.; Gevers, L. E. M.; Vankelecom, I. F. J.; Jacobs, P. A.; Vos, D. E. D., Catalytic Oxidation of 1,2-Diols to A-Hydroxy-Carboxylates with Stabilized Gold Nanocolloids Combined with a Membrane-Based Catalyst Separation. *Catalysis Letters* **2005,** *102*, 57-61.

23.   An, M.; Cui, J.; Wang, L., Magnetic Recyclable Nanocomposite Catalysts with Good Dispersibility and High Catalytic Activity. *The Journal of Physical Chemistry C* **2014,** *118*, 3062-3068.

24.   Shi, F.; Tse, M. K.; Zhou, S.; Pohl, M.-M.; Radnik, J.; Hübner, S.; Jähnisch, K.; Brückner, A.; Beller, M., Green and Efficient Synthesis of Sulfonamides Catalyzed by Nano-Ru/Fe3o4. *Journal of the American Chemical Society* **2009,** *131*, 1775-1779.

25.   Feng, X.; Zhang, J.; Cheng, S.; Zhang, C.; Li, W.; Han, B., A New Separation Method: Combination of Co2 and Surfactant Aqueous Solutions. *Green Chemistry* **2008,** *10*, 578-583.

26.   Scott, R. W. J.; Wilson, O. M.; Crooks, R. M., Synthesis, Characterization, and Applications of Dendrimer-Encapsulated Nanoparticles. *The Journal of Physical Chemistry B* **2005,** *109*, 692-704.

27.   Kanaoka, S.; Yagi, N.; Fukuyama, Y.; Aoshima, S.; Tsunoyama, H.; Tsukuda, T.; Sakurai, H., Thermosensitive Gold Nanoclusters Stabilized by Well-Defined Vinyl Ether Star Polymers: Reusable and Durable Catalysts for Aerobic Alcohol Oxidation. *Journal of the American Chemical Society* **2007,** *129*, 12060-12061.

28.   Li, D.; Liu, N.; Gao, Y.; Lin, W.; Li, C., Thermosensitive Polymer Stabilized Core-Shell Aunr@Ag Nanostructures as "Smart" Recyclable Catalyst. *Journal of Nanoparticle Research* **2017,** *19*, 377.

29.   Ohtani, B.; Prieto-Mahaney, O. O.; Li, D.; Abe, R., What Is Degussa (Evonik) P25? Crystalline Composition Analysis, Reconstruction from Isolated Pure Particles and Photocatalytic Activity Test. *Journal of Photochemistry and Photobiology A: Chemistry* **2010,** *216*, 179-182.

30.   Yuan, Y.; Yan, N.; Dyson, P. J., Ph-Sensitive Gold Nanoparticle Catalysts for the Aerobic Oxidation of Alcohols. *Inorganic Chemistry* **2011,** *50*, 11069-11074.

31.   Li, S.; Wu, Y.; Wang, J.; Zhang, Q.; Kou, Y.; Zhang, S., Double-Responsive Polyampholyte as a Nanoparticle Stabilizer: Application to Reversible Dispersion of Gold Nanoparticles. *Journal of Materials Chemistry* **2010,** *20*, 4379-4384.

32.   Ansar, S.; Chakraborty, S.; Kitchens, C., Ph-Responsive Mercaptoundecanoic Acid Functionalized Gold Nanoparticles and Applications in Catalysis. *Nanomaterials* **2018,** *8*, 339.

33.   Ansar, S. M.; Fellows, B.; Mispireta, P.; Mefford, O. T.; Kitchens, C. L., Ph Triggered Recovery and Reuse of Thiolated Poly(Acrylic Acid) Functionalized Gold Nanoparticles with Applications in Colloidal Catalysis. *Langmuir* **2017,** *33*, 7642-7648.

34.   Frens, G., Controlled Nucleation for the Regulation of the Particle Size in Monodisperse Gold Suspensions. *Nature Physical Science* **1973,** *241*, 20.

35.   Freeman, R. G.; Hommer, M. B.; Grabar, K. C.; Jackson, M. A.; Natan, M. J., Ag-Clad Au Nanoparticles: Novel Aggregation, Optical, and Surface-Enhanced Raman Scattering Properties. *The Journal of Physical Chemistry* **1996,** *100*, 718-724.

36.   Glinka, C. J.; Barker, J. G.; Hammouda, B.; Krueger, S.; Moyer, J. J.; Orts, W. J., The 30 M Small-Angle Neutron Scattering Instruments at the National Institute of Standards and Technology. *Journal of Applied Crystallography* **1998,** *31*, 430-445.

37.   Kline, S., Reduction and Analysis of Sans and Usans Data Using Igor Pro. *Journal of Applied Crystallography* **2006,** *39*, 895-900.

38.   Wang, C.; Yan, Q.; Liu, H.-B.; Zhou, X.-H.; Xiao, S.-J., Different Edc/Nhs Activation Mechanisms between Paa and Pmaa Brushes and the Following Amidation Reactions. *Langmuir* **2011,** *27*, 12058-12068.

39.   Kuroda, K.; Ishida, T.; Haruta, M., Reduction of 4-Nitrophenol to 4-Aminophenol over Au Nanoparticles Deposited on Pmma. *Journal of Molecular Catalysis A: Chemical* **2009,** *298*, 7-11.

40. Zhang, H.; Li, X.; Chen, G., Ionic Liquid-Facilitated Synthesis and Catalytic Activity of Highly Dispersed Ag Nanoclusters Supported on Tio2. *Journal of Materials Chemistry* **2009,** *19*, 8223-8231.

41. Von White, G.; Kitchens, C. L., Small-Angle Neutron Scattering of Silver Nanoparticles in Gas-Expanded Hexane. *The Journal of Physical Chemistry C* **2010,** *114*, 16285-16291.

42. Von White, G.; Mohammed, F. S.; Kitchens, C. L., Small-Angle Neutron Scattering Investigation of Gold Nanoparticle Clustering and Ligand Structure under Antisolvent Conditions. *The Journal of Physical Chemistry C* **2011,** *115*, 18397-18405.

43. Diroll, B. T.; Weigandt, K. M.; Jishkariani, D.; Cargnello, M.; Murphy, R. J.; Hough, L. A.; Murray, C. B.; Donnio, B., Quantifying "Softness" of Organic Coatings on Gold Nanoparticles Using Correlated Small-Angle X-Ray and Neutron Scattering. *Nano Letters* **2015,** *15*, 8008-8012.

44. Minelli, C.; Shard, A. G., Chemical Measurements of Polyethylene Glycol Shells on Gold Nanoparticles in the Presence of Aggregation. *Biointerphases* **2016,** *11*, 04B306.

45. Butter, K.; Hoell, A.; Wiedenmann, A.; Petukhov, A. V.; Vroege, G.-J., Small-Angle Neutron and X-Ray Scattering of Dispersions of Oleic-Acid-Coated Magnetic Iron Particles. *Journal of Applied Crystallography* **2004,** *37*, 847-856.

46. Perera, G. S.; Ansar, S. M.; Hu, S.; Chen, M.; Zou, S.; Pittman, C. U.; Zhang, D., Ligand Desorption and Desulfurization on Silver Nanoparticles Using Sodium Borohydride in Water. *The Journal of Physical Chemistry C* **2014,** *118*, 10509-10518.

47.   Ansar, S. M.; Ameer, F. S.; Hu, W.; Zou, S.; Pittman, C. U.; Zhang, D., Removal of Molecular Adsorbates on Gold Nanoparticles Using Sodium Borohydride in Water. *Nano Letters* **2013,** *13*, 1226-1229.

CHAPTER FIVE

PHOSPHOLIPID BILAYER SOFTENING DUE TO HYDROPHOBIC GOLD

NANOPARTICLE INCLUSIONS

[As published in *Langmuir, 2018, 34 (44), pp 13416–13425*) with minor revisions]

5.1 Introduction

Nanoparticle (NPs) applications in conjugation with biological entities has increased manifold with the advent of nanoparticle drug delivery systems and liposome-nanoparticle assemblies (LNAs) as stimuli responsive drug delivery vehicles.[1-4] From an environmental impact standpoint, increased exposure to NPs from consumer products has also led to increased nanoparticle-cell membrane interactions[5] resulting in NP uptake by endocytosis,[6] attachment,[7] cell membrane penetration and changes in cell membrane permeability.[8-9] Specifically, gold nanoparticles (AuNPs) have been extensively applied for gene therapy,[10] targeted drug delivery,[11-13] contrast agents in bioimaging,[14-15] biosensors,[16] hyperthermia agent[17-19] and other applications.

Cell membranes are in most cases, the first contact point between any engineered NP and a biological target. Cell membranes are complex systems containing a variety of lipids and embedded proteins which present difficulty in examining underlying biophysical properties. Single or multi-component lipid bilayers in the unilamellar liposomal form, provides a simple cell membrane model that can be used to examine NP-lipid bilayer interactions. Generally, NPs interact with liposomes in two ways: a) hydrophilic NPs adsorbed internally or externally to the bilayer inner or outer leaflet respectively,[3, 9, 20-24] or b) hydrophobic NP inclusions that reside inside the bilayer acyl core.[2, 25-28] In the current

136

work, we focus on the latter, where AuNP inclusions reside in the bilayer core. Prior studies involving LNAs have focused on formation, stability, structural changes, and phase behavior associated with AuNP incorporation.[25, 29, 30] Previously, we have demonstrated effects on structure and phase behavior of lipid bilayers with embedded stearylamine (SA) coated AuNPs.[31] Lipid bilayer thickening was observed in addition to increase in transition temperature on embedding SA-AuNPs in bilayer as shown by small angle neutron scattering (SANS) and differential scanning calorimetry (DSC) respectively.

From the perspective of designing efficient stimuli-responsive LNAs, it is essential to quantify the bio-mechanical effects brought about in the lipid bilayer due to AuNP inclusions. Similarly, in the context of AuNP toxicity, it is important to focus on lipid bilayer biomechanical parameters which dictate many biologically relevant processes. Membrane bending modulus is one of the most vital membrane property related to liposomal drug release characteristics and directly relates to permeability and bilayer phase behavior.[32] Bending fluctuations in lipid bilayers control biological phenomena such as budding[33], stalk formation[34] and gene delivery[35]. Bending modulus maintenance is thus directly linked to a cell's stability, proper functioning and its survival. Prior studies to quantify lipid bilayer bending modulus were limited to giant unilamellar vesicles (GUVs), when micropipette aspiration[36] or flickering spectroscopy[37] was utilized. Aforementioned methods are not feasible for measurements in the length scale of small unilamellar vesicles (SUVs) (< 100 nm diameter). Dynamic light scattering (DLS) can be used to study collective bilayer undulations and translational dynamics, however bending fluctuations of SUV bilayers are much smaller than length scales probed by light scattering and cannot be

isolated solely through DLS.[38-40] Nuclear magnetic resonance (NMR) probes much smaller length scales than bending dynamics length scale and is suited for vibrational, rotational and diffusion dynamics in lipid bilayers.[41-42] Solid-state NMR has been used to access the bending fluctuation domain, but suffers from sample geometry restrictions, sensitivity and lack of spatial correlations.[39, 43] Invasive techniques like atomic force microscopy (AFM) requires supported lipid bilayers which greatly differ in mechanical properties from liposomal/cellular bilayer structure in solution.[44]

Bending fluctuations in SUV bilayers have pico to nano second time scale and 0.1 nm to 10 nm length scale which overlaps the time and length regimes probed by neutron spin echo (NSE) spectroscopy.[20, 45-49] NSE is a non-invasive technique that can measure an ensemble average of bending dynamics providing greater statistical advantage over other methods. Neutrons as probes, provide greatly enhanced contrast between protonated lipids and deuterated solvent (D_2O) to directly measure bending fluctuations. NSE spectroscopy has been used previously to measure bending modulus for bilayers including multicomponent bilayers,[49-51] multi-bilayers,[47] stacked bilayers in complex fluids,[52] and mechanical properties of nanoscopic lipid domains.[53] NSE has been successfully utilized in investigating the effects of foreign molecules and inclusions like cholesterol,[54] local anesthetic,[55] non-steroidal anti-inflammatory drugs (NSAIDs),[56-57] and inorganic NPs attached to the outer leaflet of bilayers.[20] In this work, bending modulus of LNA bilayers composed of zwitterionic dipalmitoylphosphatidylcholine (DPPC) and dipalmitoylphosphatidylglycerol (DPPG) with dodecanethiol-functionalized AuNP (AuNP-DDT) inclusions, has been measured through a combination of DLS and NSE.

Effect of AuNP size and concentration has been examined at two different lipid to nanoparticle (L/N) ratios in the fluid phase. LNA structures were investigated extensively with cryo-transmission electron microscopy (cryo-TEM) and small angle neutron scattering (SANS).

5.2 Results and Discussion

5.2.1 AuNP Synthesis and LNA formation.

Hydrophobic dodecanethiol-functionalized AuNPs (DDT-AuNPs) were synthesized with average core diameters of 3.0 ± 0.6 nm and 5.5 ± 1.5 nm (henceforth referred to as 3 nm AuNP and 5 nm AuNP), as determined by TEM (Figure 5.1). The AuNP diameters correspond to a size smaller and larger than the average bilayer thickness for fluid phase DPPC/DPPG bilayers (≈ 3.8 nm).
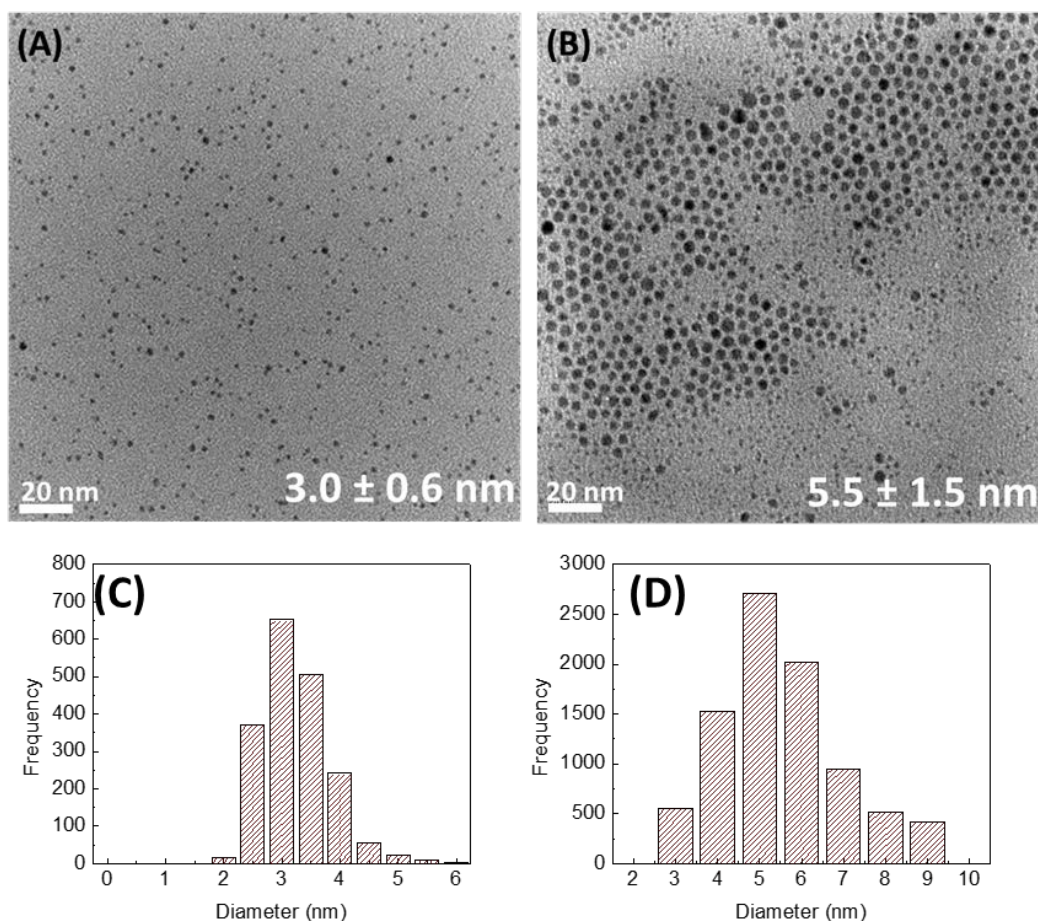
Figure 5.1. TEM images of (A) 3 nm AuNP and (B) 5.5 nm AuNP. Distribution of particle size for (C) 3 nm AuNP and (D) 5 nm AuNP. Errors represent one standard deviation from mean diameter.

LNAs were synthesized for both particle sizes at a theoretical lipid to NP (L/N) ratio of 7500:1 (low AuNP conc.) and 5000:1 (high AuNP conc.). LNAs obtained after final extrusion through 100 nm diameter pore size membrane were stable and remained dispersed for weeks without any visible sedimentation or aggregation. Pure liposomes (no AuNPs) exhibited a characteristic bluish hue after extrusion and LNA dispersions were dark brown.

A key result often excluded in prior LNA research is the AuNP inclusion efficiency based on AuNP size. This was accomplished by drying stable LNA aliquots and extracting the AuNP inclusions in toluene. A two tailed t-test (95% confidence level) of particle size distributions from TEM images demonstrates no significant difference between 3 nm diameter AuNP inclusions (3.0 ± 0.8 nm for low concentration and 3.0 ± 0.9 nm for high concentration) and actual 3 nm diameter AuNP (3.0 ± 0.6 nm). Hence, this depicts successful inclusion of the entire AuNP size range in LNA bilayers. The 5 nm AuNP (5.5 nm ± 1.6 nm) however, showed successful incorporation of smaller AuNPs only (3.8 nm ± 1.2 nm for low concentration and 3.7 nm ± 1.1 nm for high concentration) in the bilayer, which are statistically different. LNAs formed with 5 nm AuNPs are henceforth referred to as 3.8 nm AuNP LNAs and results have been summarized in Table 1. Theoretical studies previously conducted with CdSe quantum dots in DOPC bilayers showed a threshold diameter of 6.5 nm below which CdSe quantum dot bilayer inclusion is successful, and above which lipid stabilized micelle structures were formed.[58] Similarly, a threshold (AuNP + DDT) diameter was observed, above which AuNPs are preferentially stabilized by lipid monolayers or form aggregates. The post-extrusion LNA L/N ratio was determined from elemental gold and phosphorus concentrations measured by inductively coupled plasma-optical emission spectroscopy (ICP-OES). TEM and ICP-OES analysis of AuNPs inclusions and LNAs are summarized in Table 1. The AuNP concentration is lower than theoretical for all LNAs, due to AuNP aggregation and loss during hydration and extrusion. The 3 nm AuNP has a loading efficiency of 77% and 68% for the low and high concentrations respectively. The 5 nm AuNP loading efficiency was much lower (43% and

42% for high and low 5 nm AuNP concentrations respectively) due to additional large AuNP exclusion from lipid bilayers. Assuming a homogeneous AuNP distribution in all LNAs, AuNP inclusion concentration can also be estimated as AuNP per LNA as shown in Table 1. However, discussions in the following section will show that depicting AuNP inclusion concentrations in AuNP per LNA terms is a crude average.

LNAs	Diameter of AuNP inclusions, nm [a]	L/N theoretical	L/N experimental [b]	AuNP per LNA
3 nm AuNP (high)	3.0 ± 0.9	5000:1	7342:1	~ 9
3 nm AuNP (low)	3.0 ± 0.8	7500:1	9541:1	~ 6
5 nm AuNP (high)	3.7 ± 1.1	5000:1	11537:1	~ 6
5 nm AuNP (low)	3.8 ± 1.2	7500:1	17947:1	~ 3

Table 5.1. Summary of AuNP inclusions in LNAs and actual AuNP loading in lipid bilayers. [a]measured by TEM analysis of AuNPs extracted from stable LNAs. [b]measured by ICP-OES analysis of stable LNAs. Errors in diameter represent one standard deviation from the mean.

5.2.2 Cryo-TEM Characterization of LNAs.

Formation of stable SUVs with AuNP inclusions in the bilayer core was visualized by cryo-TEM imaging of LNAs (Figure 5.2). Analysis of pure liposomes (no AuNP), showed presence of unilamellar liposomes only (average diameter 85 ± 24 nm) with no multilamellar liposomes (> 1000 pure liposomes analyzed). The AuNP distribution in LNAs was not homogeneous, as similarly observed previously[30]. The LNAs were either partially loaded with isolated AuNPs (Figure 5.2C and 5.2F), partially loaded with small

AuNP clusters (Figure 5.2D and 5.2E), completely loaded with AuNPs (Figure 5.2C and 5.2E) or apparently bare (henceforth mentioned as bare liposomes, observed in the background, out of focus, in Figure 5.2B, C and E). Clusters containing a few AuNPs were observed in bilayers for all LNAs (Figure 5.2E). On statistical analysis of all LNA cryo-TEM images (> 500 liposomes counted), LNAs with AuNP clusters and apparent bare liposomes were the most prevalent liposomes at > 80%. Figure 5.2E shows an LNA completely packed with AuNPs but demonstrates a homogenous NP distribution in the bilayer. Interestingly, cryo-TEM shows that LNAs with completely packed bilayers had greater sphericity and smaller average diameter (for example, 52 ± 31 nm for 3.8 nm LNA (high) compared to the bare LNAs (87 ± 14 nm) or LNAs with small AuNP clusters (89 ± 21 nm) in the same sample. Similar observations have been made previously with iron oxide NPs in DSPC liposomes[27] and CdSe NPs in polymersomes.[59] Figure 5.2D shows the presence of larger AuNPs and possible AuNP aggregates in the lipid bilayer. Position of these aggregates/large AuNPs could not be judged with certainty through cryo-TEM. Some disc shaped/rod/worm like AuNP clusters were also observed at high AuNPs loadings (Figure 5.2B).
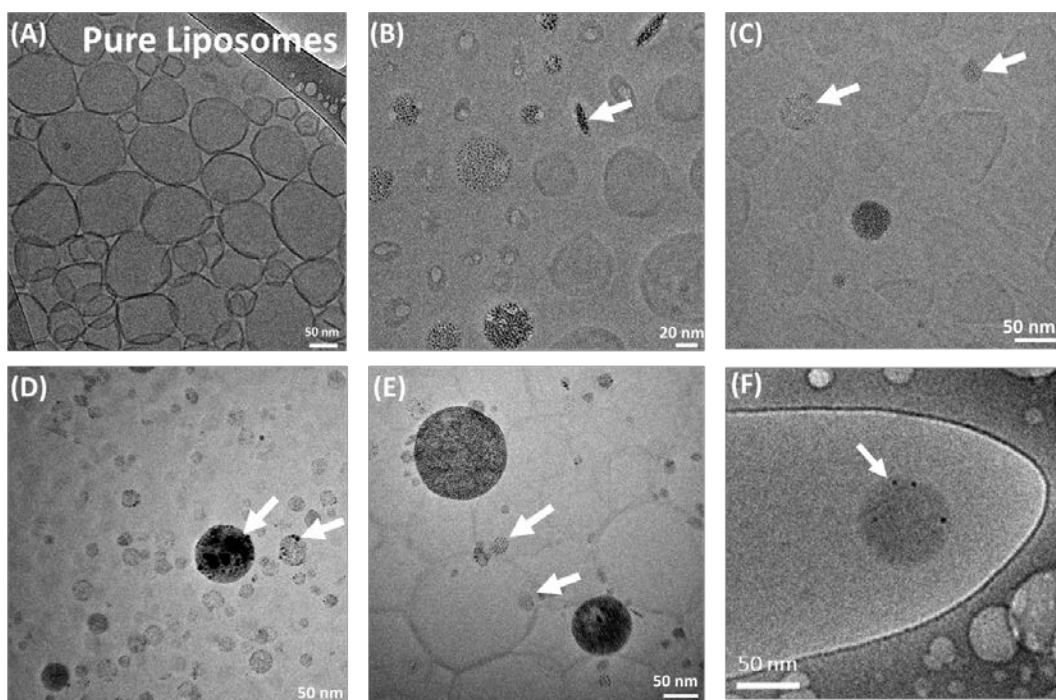
Figure 5.2. Cryo-TEM images showing (A) pure liposomes; 3 nm AuNP LNAs: (B) high (C) low; 5 nm AuNP LNAs: (D) high and (E) low; (F) shows isolated AuNP in LNAs. Arrows in (C) denote partially packed LNAs; Arrow in (B) shows existence of possible disc/rod/worm like AuNP aggregates. Arrow in (D) shows presence of large AuNP aggregates and large AuNPs. Arrow in (E) depicts small AuNP clusters in lipid bilayer.

AuNP distribution in LNAs is attributed to non-homogeneous mixing in bilayers due to cluster generation during AuNP-lipid bilayer thin film formation. Stable incorporation of hydrophobic AuNPs in lipid bilayers while maintaining structural integrity occurs by unzipping of lipid bilayers and AuNP insertion. Unzipping of bilayer by an isolated AuNP is an energy intensive process, thus AuNPs form clusters to reduce generated void spaces in the bilayers during LNA sample preparation.[30, 58, 60] We envision three distinct regions in the dry AuNP-lipid film during LNA preparation: 1) bilayer regions with large AuNP clusters, 2) bilayer regions with small AuNP clusters and 3) apparently bare lipid bilayer regions/isolated AuNPs in bilayer. LNAs with fully packed

AuNPs would be generated from region 1, where a single cluster can form a low curvature LNA itself. The detachment of bilayers containing AuNP clusters occurs at the interface with region 3 (devoid of AuNP), during hydration or the successive extrusion cycles. LNAs with small AuNP clusters are formed from region 2 (AuNP clusters are not large enough to form fully packed LNAs on their own due to high curvature limitations). Additionally, due to clustering, isolated AuNP inclusions in LNAs (Figure 5.2F) were rarely observed.

5.2.3 Bilayer Thickness from SANS.

The average bilayer thickness was determined by small angle neutron scattering (SANS) spanning temperature ranges from 40 $^{\circ}$C to 60 $^{\circ}$C for the pure liposomes and all LNAs in D_2O (solvent). SANS spectra were collected over a q range of 0.003 $Å^{-1} \leq q \leq$ 0.523 $Å^{-1}$ and bilayer thickness was determined by fitting the scattering data to a spherical vesicle model[61] over a q range of 0.02 $Å^{-1} \leq q \leq$ 0.523 $Å^{-1}$ as shown in Figure 5.3. SANS provides an ensemble averaged bilayer thickness for all liposomes and LNAs. The measured bilayer thickness should be interpreted qualitatively only due to the presence of various AuNP distributions in the bilayer. An increase in bilayer thickness was observed for all liposomes on transitioning from fluid phase to gel phase as observed previously[31, 62-64], which is attributed to greater lipid ordering below transition temperature. Pure liposome bilayer thickness increased from 3.8 nm (60°C) to 4.3 nm (40°C) across the transition temperature of 41°C (Figure 5.3B). Changes in bilayer thickness for LNAs with low and high concentrations of 3 nm AuNP was not significantly different from pure liposomes. However, 3.8 nm AuNP LNAs showed an increase in bilayer thickness compared to pure liposomes at both concentrations as evidenced by the SANS spectra shift

towards low-q for 3.8 nm AuNP LNAs. Cryo-TEM image analysis demonstrated that completely packed LNAs were smaller in size than the LNAs with AuNP clusters and bare liposomes in the same sample. In addition, statistical analysis of cryo-TEM images yielded a > 80% population of LNAs with small AuNP clusters and bare liposomes. To obtain a true statistical analysis of the sample population, SANS spectra were analyzed in the intermediate to low q regime. No distinguishing features were observed between spectra obtained from pure liposomes and LNAs in the low and intermediate q regime. The spherical vesicle model fit was extended to intermediate and low q regime and yielded similar overall diameters for pure liposomes and LNAs ($\approx$ 90 nm mean liposome diameter). Unlike statistical analysis of cryo-TEM images which is subjected to imaging biases, SANS demonstrates the prevalence of LNAs with small AuNP clusters and bare liposomes with a negligible population of completely packed smaller liposomes. However, analyzing LNA size distribution through SANS should be approached with caution due to investigation of a limited low-q region.
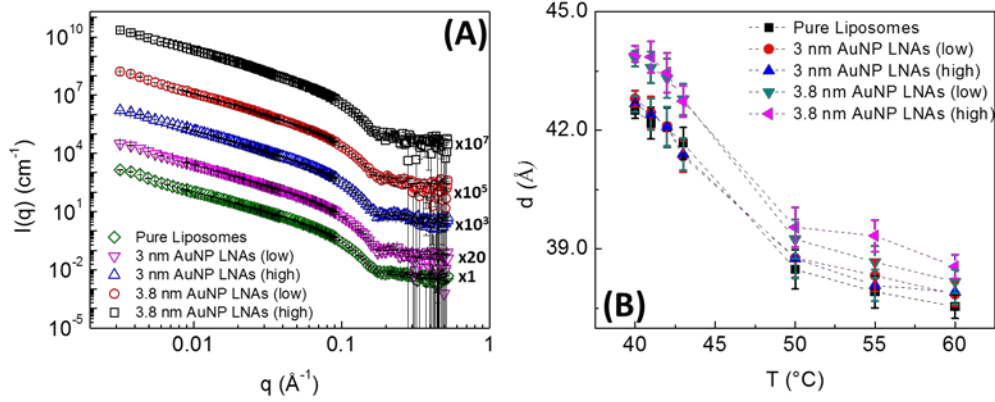
Figure 5.3. (A) SANS curves for pure liposomes and LNAs in fluid phase (60 $^{\circ}$C); curves have been offset by amounts mentioned in the plot for visual clarity. (B) Bilayer thickness calculated from SANS data at different temperatures. Error bars represent one standard deviation from the mean. Dashed lines are for visual aid only.

5.2.4 Dynamic Light Scattering.

Overall liposome motion can be classified into liposome translational motion due to diffusion and shape fluctuation motions (bending, etc.). Translational motion can be effectively measured at the appropriate q range using DLS which yields the exponentially decaying autocorrelation function g^2 (t) [65]:

$$g^2(t) = B + \beta \, exp \, (-2\Gamma_T t) \tag{1}$$

where B is the autocorrelation baseline at infinite delay, β is the correlation function amplitude and decay rate Γ_T is related to diffusion constant (D_T) as:

$$\Gamma_T = D_T q^2 \tag{2}$$

Pure liposome and LNA hydrodynamic radius (R_h) can be directly calculated from the Stokes-Einstein equation:

$$R_h = \frac{k_B T}{6\pi\eta D_T}, \tag{3}$$

where T is the temperature, k_B is the Boltzmann constant and η is the viscosity of D_2O (function of temperature). Autocorrelation curves demonstrates nearly identical decay pattern at 25 °C for pure liposomes and LNAs (Figure 5.4). Decay curve is described by a single exponential decay which confirms a narrow LNA size distribution. This further corroborates our assumption that smaller, completely-packed LNAs are a negligible population. LNAs are primarily similar in size as pure liposomes. Diffusion coefficients obtained from fitting the autocorrelation curve to Equation 1 and 2, depicts similar D_T at 25 °C (0.47 $Å^2\,ns^{-1}$ for pure liposomes vs ~0.44 $Å^2\,ns^{-1}$ and 0.43 $Å^2\,ns^{-1}$ for 3 nm AuNP LNAs and 3.8 nm AuNP LNAs respectively). D_T corresponds to a hydrodynamic radii of ~ (40, 44 and 45) nm for pure liposomes, 3 nm AuNP LNAs and 3.8 nm AuNP LNAs respectively based on Equation 3 (Figure 5.4). D_T has been measured at very dilute lipid concentrations through DLS at 25 °C. Accurate determination of D_T at NSE concentrations cannot be investigated through DLS and actual D_T lies between $0 < D_{T\,(Actual)} < D_{T\,(DLS)}$. Similarly, D_T at various temperatures have been estimated based on Equation 3 and solvent viscosity changes and does not represent diffusion coefficients accurately, existing at temperature and concentration conditions during NSE experiments.

LNA	D_T (Å^2 ns^{-1}) @ 25 °C	R_h (nm)
Pure Liposomes	0.47 ± 0.02	40.7 ± 4.0
3 nm AuNP LNAs (low)	0.45 ± 0.07	43.6 ± 2.5
3 nm AuNP LNAs (high)	0.44 ± 0.04	44.0 ± 3.1
3.8 nm AuNP LNAs (low)	0.45 ± 0.04	43.9 ± 2.1
3.8 nm AuNP LNAs (high)	0.43 ± 0.05	44.9 ± 1.9
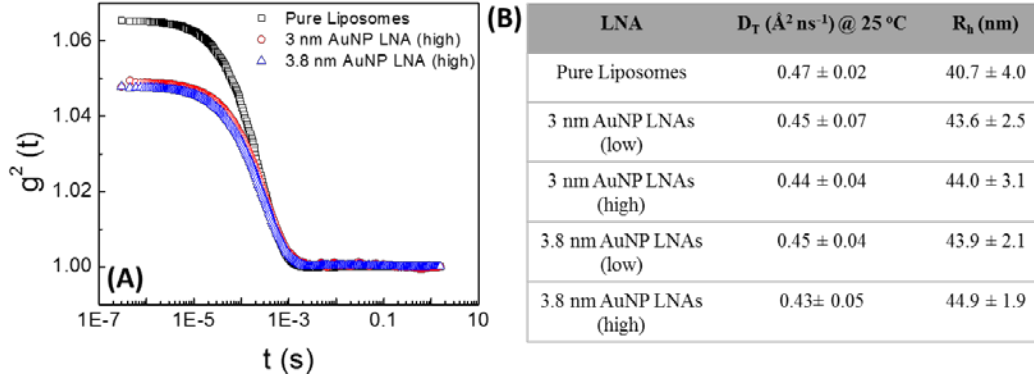
Figure 5.4. (A) Curves depict autocorrelation functions for pure liposomes (black square), 3 nm AuNP LNAs (high) (red circles) and 3.8 nm AuNP LNAs (high) (blue triangle). (B) Diffusion coefficient and hydrodynamic radius as obtained from DLS experiments at 25°C in D_2O solvent.

5.2.5 NSE Measurements of Bilayer Bending Modulus.

NSE was used to measure normalized intermediate scattering functions (ISF) $I(q, t)/I(q, 0)$ (q and t represent wave vector and Fourier time, respectively) over a q range of 0.039 Å^{-1} to 0.1 Å^{-1} and Fourier time up to 100 ns with neutron wavelengths of 8 Å and 11 Å. For pure membrane undulations (assuming no translational diffusion), Zilman-Granek (ZG) model[66] for single membrane fluctuations describes the bending fluctuations in a membrane as:

$$\frac{I(q,t)}{I(q,0)} = \exp[-(\Gamma_b t)^{\frac{2}{3}}] \tag{4}$$

where Γ_b is the bending relaxation rate given by:

$$\Gamma_b = 0.025\gamma \left(\frac{k_B T}{\tilde{\kappa}}\right)^{\frac{1}{2}} \left(\frac{k_B T}{\eta}\right) q^3 = \Gamma_{ZG} q^3 \tag{5}$$

where $\tilde{\kappa}$ is the effective bending modulus, η is the solvent viscosity (D_2O viscosity as a function of temperature in this work), k_B is the Boltzmann constant, T is the temperature

and γ approaches unity when $\tilde{\kappa} \gg k_B T$. On incorporating intermonolayer frictions[67-68] into the ZG model as proposed by Watson and Brown,[69] the effective bending modulus $\tilde{\kappa}$, can be substituted by intrinsic bending modulus κ, given by $\tilde{\kappa} = \kappa + 2h^2 k_m$ where h is the height of neutral surface from bilayer mid-plane and k_m is the monolayer area compressibility modulus. k_m is further depicted as $k_m = 12\kappa_m/h_c^2$, where κ_m is the monolayer bending modulus and monolayer hydrocarbon thickness is denoted as h_c.[70] As discussed in an earlier paper[71], monolayer bending modulus can be expressed as bilayer bending modulus as $\kappa_m = \kappa/2$, which yields $\tilde{\kappa} = \kappa(1 + 48\left(\frac{h}{2h_c}\right)^2)$, and an assumption of $h/2hc = 0.5$ to consider the neutral surface is at the hydrophobic-hydrophilic interface leads to $\tilde{\kappa} = 13\kappa$. Equation 5 has thus been used in the following form to calculate the intrinsic bending modulus:

$$\Gamma_b = 0.0069 \left(\frac{k_B T}{\kappa}\right)^{\frac{1}{2}} (\frac{k_B T}{\eta})q^3 = \Gamma_{ZG} q^3 \tag{6}$$

Figure 5.5A shows a typical NSE decay curve for 3 nm AuNP LNAs (high) when no translation diffusion is taken into account. NSE decay curves are fit to Equation 4 to yield a bending decay rate which demonstrates a q^3 dependence in the whole q range.
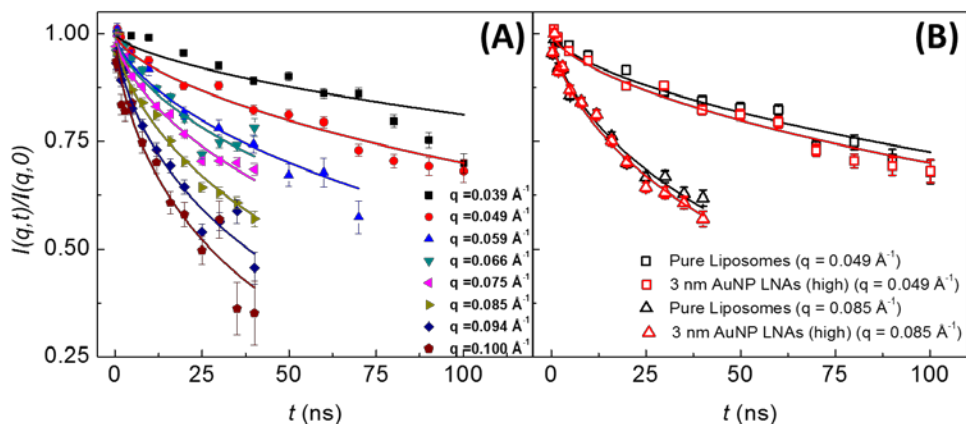
Figure 5.5. Typical normalized intermediate scattering function (ISF) at different q for 3 nm AuNP LNAs (high) at 60 ^{o}C for (A) No translational diffusion assumed; solid lines are fit to Equation 4. (B) Effect on ISF due to 3 nm AuNP inclusions (high) relative to pure liposomes at 60 ^{o}C (No diffusion, solid lines fit to Equation 4). Errors in all figures represent one standard deviation from the mean.

Figure 5.5B shows a direct comparison of AuNP inclusion effect (3 nm AuNP high conc.) on the DPPC/DPPG lipid bilayer $I(q, t)/I(q, 0)$ at two q values at 60 ^{o}C. AuNP inclusions lead to slightly larger relaxation rates (slightly faster relaxation of bilayer bending) compared to pure liposomes, which is a clear indication of membrane softening according to ZG theory. NSE yields an ensemble average bending moduli for all LNAs (fully packed LNAs, partially packed LNAs, and vacant liposomes) and should be qualitatively interpreted with respect to pure liposome bending modulus. Figure 5.6 shows the bending modulus calculated for all LNAs above the bilayer transition temperature (summarized in Table 2). The bending modulus measured for the pure lipid bilayer in the current work at 60 ^{o}C ($\approx$ 14.7 k_BT) is comparable to the bending modulus obtained for pure DPPC bilayer

($\approx 9.5\ k_BT$) at 60 °C previously by NSE[51] and low angle X-ray spectroscopy ($\approx 16.3\ k_BT$).[72] The bending modulus is an order of magnitude higher at temperatures near and below the transition temperature (Figure 5.6 inset). This is expected as bilayer stiffening occurs due to greater lipid ordering in the gel phase than in fluid phase.[51, 71, 73] 3 nm AuNP LNAs (high) show an average 15% reduction in bending modulus relative to pure liposomes in the fluid phase. Change in bending modulus was insignificant for 3 nm AuNP LNAs (low) in the fluid phase. 3.8 nm AuNP LNAs however, shows ca. 15% bending modulus reduction at both low and high AuNP loadings in the fluid phase. No bending modulus hysteresis was observed on reheating the 3 nm AuNP LNAs (high) from gel phase to fluid phase, thus ruling out any hysteresis on membrane elastic properties upon phase transition. NSE decay data must also be analyzed by taking translational diffusion into account. However, incorporating diffusion contributions as measured through DLS (at extremely dilute lipid concentrations) does not present an accurate analysis of the NSE data. This account has been presented in detail in Figure 5.7. Figure 5.7 depicts similar membrane softening as observed in Figure 5.6. On accounting for D_T, membrane softening in 3 nm AuNP LNAs (low) is also resolved. Bending moduli depicted in Table 2 (in parenthesis) demonstrates an extreme value, absolute value lies between the two extreme cases as summarized in Table 2.
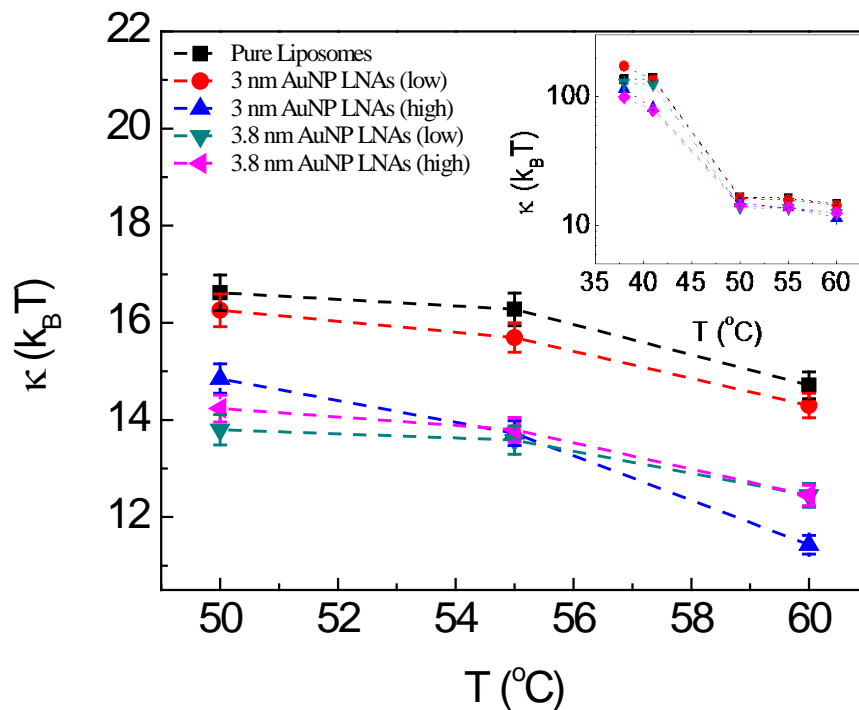
Figure 5.6. Intrinsic bending moduli κ of pure DPPC/DPPG liposomes and LNAs assuming no diffusion contribution to NSE decay. Inset shows bending moduli over fluid and gel phase. Dashed lines are for visual aid only. Error bars represent one standard deviation from the mean.
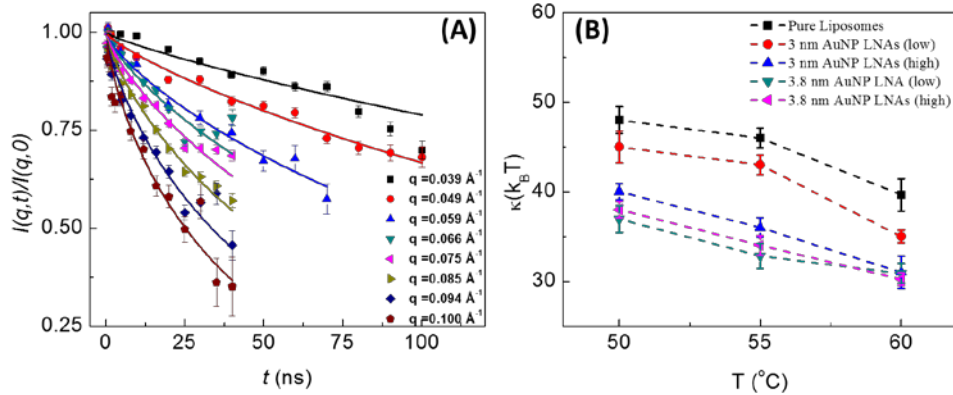
Figure 5.7. (A) Typical intermediate scattering function for 3 nm AuNP LNA (high) at 60 °C. Solid lines are fit to Equation S8 assuming D_T derived from DLS measurements. (B) Intrinsic bending moduli κ of pure DPPC/DPPG liposomes and LNAs assuming diffusion contribution (determined from DLS) to NSE decay. Dashed lines are for visual aid only. Error bars represent one standard deviation from the mean.

NSE findings demonstrate both AuNP concentration and AuNP size have a significant impact on lipid bilayer bending modulus. However, the impact of AuNP diameter in bending modulus reduction appears more prominent as seen in case of 3.8 nm AuNP LNAs. A qualitative assessment of the bilayer area compressibility modulus (K_A) with AuNP inclusions was conducted, based on SANS thickness measurements and bending modulus obtained from NSE. Bilayer bending results in compression and stretching of the lipid leaflets and can be described as a thin elastic sheet model relating κ and K_A.[74] Bending modulus κ is directly proportional to area compressibility modulus K_A as:

$$K_A = \beta\kappa/(2h_c)^2 \tag{8}$$

154

where h_c is the monolayer thickness and β is a coupling constant that depends upon the degree of coupling between the two monolayers. β ranges from 12 (strong coupling between monolayer leaflets) to 48 (no coupling and leaflets can slide freely).[75-76] Increase in hydrophobic thickness and reduction in bending modulus implies a drastic reduction in bilayer compressibility modulus K_A for LNAs from Eq. 8. Definitive quantification of K_A was not undertaken due to insufficient knowledge about the change in β in the presence of inclusions. Decrease in K_A is a clear indicator of an increase in thickness fluctuation dynamics[49] in lipid bilayer which plays a pivotal role in membrane protein functioning[77] and enzyme catalysis[78]. Thickness fluctuation dynamics measurement with AuNP inclusions in tail deuterated lipid bilayers is a potentially interesting study to quantify thickness fluctuation dynamics, amplitude and membrane visco-elastic properties.[49, 71, 79]

Table 5.2. Bilayer thickness (d) measured from SANS data and bending modulus (κ) at 60 $^\text{o}$C obtained from NSE measurements (values in parenthesis depict bending modulus when translational decay contributions are applied). Errors represent one standard deviation from mean.

Liposomes	Bilayer Thickness, d (Å)	Bending Modulus, κ ($k_B T$)
Pure Liposomes	37.5 ± 0.3	14.7 ± 0.3 (39.7 ± 1.8)
3 nm AuNP LNAs (low)	37.8 ± 0.3	14.3 ± 0.3 (35.6 ± 0.7)
3 nm AuNP LNAs (high)	37.9 ± 0.4	11.4 ± 0.2 (31.5 ± 1.8)
3.8 nm AuNP LNAs (low)	38.2 ± 0.3	12.4 ± 0.3 (30.9 ± 0.3)
3.8 nm AuNP LNAs (high)	38.6 ± 0.3	12.4 ± 0.2 (30.2 ± 0.7)

Decrease in bilayer bending modulus (decrease in area compressibility modulus) with AuNP inclusions can be explained based on contribution from multiple possible factors. It has been previously shown that bending modulus is directly related to bilayer thickness.[80-81] However, in the present case, the average bilayer thickening is a result of membrane unzipping to situate the AuNP/ AuNP cluster inclusion in the bilayer core. However, coupling between monolayers should be severely compromised on introducing isolated AuNP inclusions or cluster inclusions. Additionally, theoretical[80] and X-ray diffraction[82] studies on surfactant lamellas have demonstrated dramatic decreases in bending modulus with increasing area per molecule (bulkier head groups for surfactants). Increased area per molecule directly implies a less confined chain and smaller loss of conformational entropy during lamellar bending. Similarly, total bilayer volume in the vicinity of AuNP and AuNP cluster inclusion is greatly increased, but number of lipids in the specific volume remains constant. Thus, increase in bilayer volume can be compensated only through stretching and conformation change of lipid tails, in other words increasing the area per lipid. Previous researchers[64, 83] have well documented the phenomena of increasing area per lipid with increasing temperature (transition from gel to fluid phase). The AuNP inclusions can thus be envisioned to generate higher local fluidity compared to the bulk bilayer leading to an average bilayer softening. It has been shown previously, that small alkyl chain additives at relatively low mole fractions can cause substantial reduction in bending modulus.[80-81] AuNP inclusions in the present research is functionalized with small alkyl chain dodecanethiol, which might substantially contribute towards disrupting conformational packing, leading to membrane softening.

5.3 Conclusion

An investigation into effects of hydrophobic AuNP inclusions on lipid bilayer bending modulus was conducted through NSE spectroscopy. AuNPs with average diameters of ~ 3 nm and ~ 5.5 nm were embedded into DPPC/DPPG lipid bilayers. It was observed that AuNPs above a particular threshold diameter were not included in the DPPC/DPPG lipid bilayer, resulting in decreased loading efficiency for larger AuNPs. Non-homogeneous lipid and AuNP mixing during dry film formation leads to apparently bare, partially packed and completely packed LNAs. Average LNA bilayer thickening was observed depending on size and concentration of AuNP inclusions. On investigating LNA membrane dynamics with NSE spectroscopy, a general membrane softening was observed relative to pure liposomes which manifested in the form of reduced bending modulus. AuNP concentration and AuNP size were both factors in determining magnitude of membrane softening. On considering translational contribution to NSE decay, similar bilayer softening trends are retained. Our experimental results qualitatively point towards a decrease in area compressibility modulus and subsequently an increased thickness fluctuation dynamics. We demonstrate NSE to be a crucial tool in determining inclusion effects on membrane dynamics and mechanical properties. These studies have potential implications for membrane biophysical characterization and designing innovative drug delivery vehicles.

5.4. Experimental Methods

5.4.1 Materials.

Hydrogen tetrachloroaurate ($HAuCl_4.3H_2O$, 99.9% purity), dodecanethiol (<95%), sodium borohydride (98%), HPLC grade ethanol, chloroform and toluene, hydrochloric acid (37%, 12 mol/L, extra pure), nitric acid (69% to 71%, extra pure) and hydrogen peroxide (mass fraction of 30%) were purchased from Sigma Aldrich. Tetraoctylammoniumbromide (99.35%) was purchased from Chem-Impex Int'l Inc. Lipids were purchased from Avanti Polar Lipids as dry powder. Deuterated water (D_2O, 99.9%) was purchased from Cambridge Isotope Laboratories. Concentration standard for gold, sulfur and phosphorus were purchased from Sigma Aldrich (TraceCERT 1 g/L Au in HCl, TraceCERT, 1 g/L S in H_2O and TraceCERT 1 g/L P in H_2O). Chemicals were used without any further purifications.

5.4.2 AuNP-DDT synthesis.

Dodecanethiol (DDT) functionalized AuNPs were prepared through Brust-Schiffrin method.[84] DDT to Au precursor ratio was varied and reaction was conducted in presence of equal volumes of aqueous and organic solvent to obtain narrow diameter range. In a typical synthesis based on 50 mg total Au mass, 99 mg $HAuCl_4.3H_2O$ (49.5 mg Au) was dissolved in 400 mL double distilled water. 1.388 g phase transfer agent tetraoctylammoniumbromide (TOAB) was dissolved in 400 mL of toluene. Vigorous mixing by magnetic stirring for 30 mins transferred gold completely into toluene as evidenced by the aqueous phase becoming colorless and toluene phase becoming bright orange. Aqueous phase was not discarded. 3 nm AuNPs required addition of 51 mg dodecanethiol to the mixture and was stirred vigorously for an hour. The toluene phase at this point turns cloudy white. Similarly, 5 nm AuNPs require addition of 17 mg

158

dodecanethiol to the mixture which creates a pale orange emulsion. To both the above solutions, 96 mg of aqueous sodium borohydride (2 mL) was added rapidly and left to vigorously stir for 12 hours. Aqueous phase was discarded thereafter and volume of AuNPs in toluene was reduced to 5 mL by evaporating toluene under a nitrogen stream. 200 mL of methanol was added to AuNP dispersion in toluene to precipitate AuNPs selectively. AuNPs were centrifuged at 14500 rpm for 30 mins and supernatant containing the excess reactants were discarded. Precipitated AuNPs were redispersed in 5 mL toluene and washing step was repeated three times. Final redispersion of AuNP was in chloroform instead of toluene. Supernatant from the final wash cycle was dried and digested in presence of hydrogen peroxide and nitric acid and analyzed through ICP-OES. Supernatant contained undetectable amounts of sulfur, which shows presence of insignificant amounts of excess DDT.

5.4.3 Determination of gold and phosphorus concentration

Concentrations of gold and phosphorus in LNAs were determined using ICP-OES on a Perkin Elmer Optima 3100RL ICP-OES. An aliquot of LNA was dried and microwave digested in concentrated freshly prepared aqua regia and diluted 20 fold in deionized water post digestion. Au concentration was similarly determined for DDT-AuNP. Standards were used at similar acid concentrations.

5.4.4 Transmission electron microscopy (TEM)

TEM images of AuNPs were obtained on a Hitachi 7600 TEM with an accelerating voltage of 120 kV. 100 µL of as-prepared AuNPs in toluene was diluted 100 fold in toluene and 10 µL of this AuNP dispersion was drop cast on a 300-mesh Formvar coated copper

TEM grid (Electron Microscopy Science) and allowed to dry overnight in a dessicator. ImageJ was used to obtain a size distribution histogram by following regular size analysis protocols. Dried LNAs were redispersed in toluene and imaged similarly to measure embedded AuNP diameter.

5.4.5 Preparation of Lipid-Nanoparticle Assemblies

Liposomes comprising of 85:15 molar ratio of DPPC: DPPG was prepared by thin film hydration of lipids by D_2O and subsequent extrusion through polycarbonate membranes (pore size 400 nm, 200 nm and 100 nm). DPPC and DPPG lipids (100 mg total) were dissolved in 2 mL of HPLC grade chloroform and dried under nitrogen stream to form a dry film on a round bottom flask followed by vacuum drying for 12 hours. To generate LNAs, requisite volume of AuNPs in chloroform was added with lipids and subsequently dried. Dry lipid films were hydrated with 1 mL D_2O at 60°C for 1 hour under intermittent mechanical agitation. Resulting solution was extruded subsequently through 400 nm, 200 nm and 100 nm polycarbonate (PC) membrane 10, 10 and 41 times respectively at 60°C to obtain a dispersion of LNAs. Aggregates observed during post-hydration were removed during successive extrusion through PC membrane. LNA dispersions were stored constantly at 60 °C in a Peltier type heat box to maintain bilayer fluidity and avoid any irreversible effects on bilayer due to repeated cooling and heating induced hysteresis. Final LNAs were diluted to 5 mL in D_2O to yield ~20 mg/mL concentration of lipid.

5.4.6 Cryo-TEM Imaging of LNAs

LNA imaging was conducted by depositing 5 µL of LNA on a Quantifoil grid with 2 µm lacy carbon holes (Electron Microscopy Sciences). The grids were vitrified in liquid ethane using a Vitrobot (FEI Co.) Vitrified grids were transferred and stored in liquid nitrogen until imaging. Imaging was performed on a liquid nitrogen cooled stage (Model 915, Gatan Inc, Pleasanton, CA) at 200 kV using a JEOL JEM-2100F Transmission Electron Microscope (Peabody, MA).

5.4.7 Small Angle Neutron Scattering.

SANS experiments were conducted on NGB 10 m SANS at National Institute of Standards and Technology Center for Neutron Research (Gaithersburg, MD, USA). 1 mL of 20 mg/mL lipids in D_2O was loaded into a titanium cell with quartz windows with 1 mm path length while maintaining solution temperature above transition temperature. Measurements were carried out at temperatures of (60, 55, 50, 43, 42, 41 and 40) ^{o} C. Temperature was controlled with a circulating water bath around sample cells with an accuracy of $\pm$ 0.1 ^{o}C.

5.4.8 Neutron Spin Echo (NSE) Spectroscopy.

NSE experiments were conducted on NGA CHRNS neutron spin echo (NSE) spectrometer instrument at NIST Center for Neutron Research (NCNR, Gaithersburg, MD). Measurements were conducted at 5 different temperatures, 38 ^{o}C (gel phase), 41 ^{o}C (transition temperature), (50, 55 and 60) ^{o}C (fluid phase). Incident neutron wavelength of 0.8 nm and 1.1 nm were selected by a velocity selector having a wavelength resolution of ≈18%. Polarizers and analyzers were used to measure the polarization of the neutron before and after passing through a sample. Measurement were obtained with a wave vector range

spanning $0.039 \text{ Å}^{-1} \leq q \leq 0.1 \text{ Å}^{-1}$ and time range of $0.65 \text{ ns} \leq t \leq 100 \text{ ns}$. A titanium NCNR-standard sample cell with quartz windows with path length of 2 mm was used to load LNAs at ≈ 20 mg/mL lipid concentration in D_2O. Charcoal was used to obtain instrumental resolution and D_2O was used to collect background scattering. Temperature was controlled with a circulating water bath around sample cells with an accuracy of ± 0.1 °C. Correction for resolution and background and reduction of spin echo data was conducted on DAVE[85] software package.

5.4.9 Dynamic Light Scattering

DLS experiments were conducted on a Wyatt Dawn Helios II multi-angle light scattering instrument using 658 nm wavelength laser. LNA samples in D_2O (pure liposomes, 3 nm AuNP LNA (high) and 3.8 nm AuNP LNA (high)) used in NSE experiments at 20 mg/mL were diluted to ~0.25 mg/mL for DLS experiments. DLS data was acquired in batch mode using a 20 mL scintillation vial adapter at ambient temperatures (~25 °C). Intensity correlation functions g^2 *(t)* was regularized in the ASTRA software package.

5.5 Acknowledgement

5.6 References

1.   Al-Jamal, W. T.; Kostarelos, K., Liposomes: From a Clinically Established Drug Delivery System to a Nanoparticle Platform for Theranostic Nanomedicine. *Accounts of Chemical Research* **2011,** *44*, 1094-1104.

2.   Katagiri, K.; Imai, Y.; Koumoto, K.; Kaiden, T.; Kono, K.; Aoshima, S., Magnetoresponsive on-Demand Release of Hybrid Liposomes Formed from Fe3o4 Nanoparticles and Thermosensitive Block Copolymers. *Small* **2011,** *7*, 1683-1689.

3.   Koch, A. M.; Reynolds, F.; Kircher, M. F.; Merkle, H. P.; Weissleder, R.; Josephson, L., Uptake and Metabolism of a Dual Fluorochrome Tat-Nanoparticle in Hela Cells. *Bioconjugate Chemistry* **2003,** *14*, 1115-1121.

4.   Donaldson, K.; Stone, V.; Tran, C. L.; Kreyling, W.; Borm, P. J. A., Nanotoxicology. *Occupational and Environmental Medicine* **2004,** *61*, 727-728.

5.   Maurer-Jones, M. A.; Gunsolus, I. L.; Murphy, C. J.; Haynes, C. L., Toxicity of Engineered Nanoparticles in the Environment. *Analytical Chemistry* **2013,** *85*, 3036-3049.

6.   Ayush, V.; Francesco, S., Effect of Surface Properties on Nanoparticle–Cell Interactions. *Small* **2010,** *6*, 12-21.

7.   Catherine, C. B.; Adam, S. G. C., Functionalisation of Magnetic Nanoparticles for Applications in Biomedicine. *Journal of Physics D: Applied Physics* **2003,** *36*, R198.

8.   Chen, J.; Hessler, J. A.; Putchakayala, K.; Panama, B. K.; Khan, D. P.; Hong, S.; Mullen, D. G.; DiMaggio, S. C.; Som, A.; Tew, G. N.; Lopatin, A. N.; Baker, J. R.; Holl, M. M. B.; Orr, B. G., Cationic Nanoparticles Induce Nanoscale Disruption in Living Cell Plasma Membranes. *The Journal of Physical Chemistry B* **2009,** *113*, 11179-11185.

9.   Leroueil, P. R.; Hong, S.; Mecke, A.; Baker, J. R.; Orr, B. G.; Banaszak Holl, M. M., Nanoparticle Interaction with Biological Membranes: Does Nanotechnology Present a Janus Face? *Accounts of Chemical Research* **2007,** *40*, 335-342.

10.   Huo, S.; Jin, S.; Ma, X.; Xue, X.; Yang, K.; Kumar, A.; Wang, P. C.; Zhang, J.; Hu, Z.; Liang, X.-J., Ultrasmall Gold Nanoparticles as Carriers for Nucleus-Based Gene Therapy Due to Size-Dependent Nuclear Entry. *ACS Nano* **2014,** *8*, 5852-5862.

11.   Brown, S. D.; Nativo, P.; Smith, J. A.; Stirling, D.; Edwards, P. R.; Venugopal, B.; Flint, D. J.; Plumb, J. A.; Graham, D.; Wheate, N. J., Gold Nanoparticles for the Improved Anticancer Drug Delivery of the Active Component of Oxaliplatin. *J Am Chem Soc* **2010,** *132*, 4678-4684.

12.	Bhattacharya, R.; Patra, C. R.; Earl, A.; Wang, S.; Katarya, A.; Lu, L.; Kizhakkedathu, J. N.; Yaszemski, M. J.; Greipp, P. R.; Mukhopadhyay, D.; Mukherjee, P., Attaching Folic Acid on Gold Nanoparticles Using Noncovalent Interaction Via Different Polyethylene Glycol Backbones and Targeting of Cancer Cells. *Nanomedicine: Nanotechnology, Biology and Medicine* **2007,** *3*, 224-238.

13.	Urbina, M. C.; Zinoveva, S.; Miller, T.; Sabliov, C. M.; Monroe, W. T.; Kumar, C. S. S. R., Investigation of Magnetic Nanoparticle−Polymer Composites for Multiple-Controlled Drug Delivery. *The Journal of Physical Chemistry C* **2008,** *112*, 11102-11108.

14.	Hainfeld, J. F.; Slatkin, D. N.; Focella, T. M.; Smilowitz, H. M., Gold Nanoparticles: A New X-Ray Contrast Agent. *The British Journal of Radiology* **2006,** *79*, 248-253.

15.	Ding, H.; Yong, K. T.; Roy, I.; Pudavar, H. E.; Law, W. C.; Bergey, E. J.; Prasad, P. N., Gold Nanorods Coated with Multilayer Polyelectrolyte as Contrast Agents for Multimodal Imaging. *J Phys Chem C* **2007,** *111*, 12552-12557.

16.	Ali, M. E.; Hashim, U.; Mustafa, S.; Man, Y. B. C.; Islam, K. N., Gold Nanoparticle Sensor for the Visual Detection of Pork Adulteration in Meatball Formulation. *J Nanomater* **2012**.

17.	Stuchinskaya, T.; Moreno, M.; Cook, M. J.; Edwards, D. R.; Russell, D. A., Targeted Photodynamic Therapy of Breast Cancer Cells Using Antibody-Phthalocyanine-Gold Nanoparticle Conjugates. *Photoch Photobio Sci* **2011,** *10*, 822-831.

18.   Dickerson, E. B.; Dreaden, E. C.; Huang, X. H.; El-Sayed, I. H.; Chu, H. H.; Pushpanketh, S.; McDonald, J. F.; El-Sayed, M. A., Gold Nanorod Assisted near-Infrared Plasmonic Photothermal Therapy (Pptt) of Squamous Cell Carcinoma in Mice. *Cancer Lett* **2008,** *269*, 57-66.

19.   Rosensweig, R. E., Heating Magnetic Fluid with Alternating Magnetic Field. *J Magn Magn Mater* **2002,** *252*, 370-374.

20.   Hoffmann, I.; Michel, R.; Sharp, M.; Holderer, O.; Appavou, M.-S.; Polzer, F.; Farago, B.; Gradzielski, M., Softening of Phospholipid Membranes by the Adhesion of Silica Nanoparticles - as Seen by Neutron Spin-Echo (Nse). *Nanoscale* **2014,** *6*, 6945-6952.

21.   Li, S.; Malmstadt, N., Deformation and Poration of Lipid Bilayer Membranes by Cationic Nanoparticles. *Soft Matter* **2013,** *9*, 4969-4976.

22.   Leroueil, P. R.; Berry, S. A.; Duthie, K.; Han, G.; Rotello, V. M.; McNerny, D. Q.; Baker, J. R.; Orr, B. G.; Banaszak Holl, M. M., Wide Varieties of Cationic Nanoparticles Induce Defects in Supported Lipid Bilayers. *Nano Letters* **2008,** *8*, 420-424.

23.   Mohanraj, V. J.; Barnes, T. J.; Prestidge, C. A., Silica Nanoparticle Coated Liposomes: A New Type of Hybrid Nanocapsule for Proteins. *International Journal of Pharmaceutics* **2010,** *392*, 285-293.

24.   Alberola, A. P.; Rädler, J. O., The Defined Presentation of Nanoparticles to Cells and Their Surface Controlled Uptake. *Biomaterials* **2009,** *30*, 3766-3770.

25.   Park, S.-H.; Oh, S.-G.; Mun, J.-Y.; Han, S.-S., Loading of Gold Nanoparticles inside the Dppc Bilayers of Liposome and Their Effects on Membrane Fluidities. *Colloids and Surfaces B: Biointerfaces* **2006,** *48*, 112-118.

26.   Xia, T.; Rome, L.; Nel, A., Particles Slip Cell Security. *Nature Materials* **2008,** *7*, 519.

27.   Amstad, E.; Kohlbrecher, J.; Müller, E.; Schweizer, T.; Textor, M.; Reimhult, E., Triggered Release from Liposomes through Magnetic Actuation of Iron Oxide Nanoparticle Containing Membranes. *Nano Letters* **2011,** *11*, 1664-1670.

28.   Bothun, G. D., Hydrophobic Silver Nanoparticles Trapped in Lipid Bilayers: Size Distribution, Bilayer Phase Behavior, and Optical Properties. *Journal of Nanobiotechnology* **2008,** *6*, 13.

29.   Chen, Y.; Bose, A.; Bothun, G. D., Controlled Release from Bilayer-Decorated Magnetoliposomes Via Electromagnetic Heating. *ACS Nano* **2010,** *4*, 3215-3221.

30.   Rasch, M. R.; Rossinyol, E.; Hueso, J. L.; Goodfellow, B. W.; Arbiol, J.; Korgel, B. A., Hydrophobic Gold Nanoparticle Self-Assembly with Phosphatidylcholine Lipid: Membrane-Loaded and Janus Vesicles. *Nano Letters* **2010,** *10*, 3733-3739.

31.   Von White, G.; Chen, Y.; Roder-Hanna, J.; Bothun, G. D.; Kitchens, C. L., Structural and Thermal Analysis of Lipid Vesicles Encapsulating Hydrophobic Gold Nanoparticles. *ACS Nano* **2012,** *6*, 4678-4685.

32.   Zhou, Y.; Raphael, R. M., Effect of Salicylate on the Elasticity, Bending Stiffness, and Strength of Sopc Membranes. *Biophysical Journal 89*, 1789-1801.

33.   Lipowsky, R., Budding of Membranes Induced by Intramembrane Domains. *J. Phys. II France* **1992,** *2*, 1825-1840.

34.   Kozlovsky, Y.; Kozlov, M. M., Stalk Model of Membrane Fusion: Solution of Energy Crisis. *Biophysical Journal 82*, 882-895.

35.   Safinya, C. R., Structures of Lipid–DNA Complexes: Supramolecular Assembly and Gene Delivery. *Current Opinion in Structural Biology* **2001,** *11*, 440-448.

36.   Evans, E.; Rawicz, W., Elasticity of ``Fuzzy'' Biomembranes. *Physical Review Letters* **1997,** *79*, 2379-2382.

37.   Käs, J.; Sackmann, E., Shape Transitions and Shape Stability of Giant Phospholipid Vesicles in Pure Water Induced by Area-to-Volume Changes. *Biophysical Journal* **1991,** *60*, 825-844.

38.   Hirn, R.; Benz, R.; Bayerl, T. M., Collective Membrane Motions in the Mesoscopic Range and Their Modulation by the Binding of a Monomolecular Protein Layer of Streptavidin Studied by Dynamic Light Scattering. *Physical Review E* **1999,** *59*, 5987-5994.

39.   Hirn, R.; M. Bayerl, T.; O. Radler, J.; Sackmann, E., Collective Membrane Motions of High and Low Amplitude, Studied by Dynamic Light Scattering and Micro-Interferometry. *Faraday Discussions* **1999,** *111*, 17-30.

40.   Hildenbrand, M. F.; Bayerl, T. M., Differences in the Modulation of Collective Membrane Motions by Ergosterol, Lanosterol, and Cholesterol: A Dynamic Light Scattering Study. *Biophysical Journal* **2005,** *88*, 3360-3367.

41.   Bloom, M.; Bayerl, T. M., Membranes Studied Using Neutron Scattering and Nmr. *Canadian Journal of Physics* **1995,** *73*, 687-696.

42.   Nevzorov, A. A.; Brown, M. F., Dynamics of Lipid Bilayers from Comparative Analysis of 2h and 13c Nuclear Magnetic Resonance Relaxation Data as a Function of Frequency and Temperature. *The Journal of Chemical Physics* **1997,** *107*, 10288-10310.

43.   Dolainsky, C.; Möps, A.; Bayerl, T. M., Transverse Relaxation in Supported and Nonsupported Phospholipid Model Membranes and the Influence of Ultraslow Motions: A 31p-Nmr Study. *The Journal of Chemical Physics* **1993,** *98*, 1712-1720.

44.   Picas, L.; Rico, F.; Scheuring, S., Direct Measurement of the Mechanical Properties of Lipid Phases in Supported Bilayers. *Biophysical Journal* **2012,** *102*, L01-L03.

45.   Takeda, T.; Kawabata, Y.; Seto, H.; Komura, S.; Ghosh, S. K.; Nagao, M.; Okuhara, D., Neutron Spin-Echo Investigations of Membrane Undulations in Complex Fluids Involving Amphiphiles. *J Phys Chem Solids* **1999,** *60*, 1375-1377.

46.   Saxs, Sans and Nse Studies on "Unbound State" in Dppc/Water/Cacl2 System. *Journal of the Physical Society of Japan* **2005,** *74*, 2853-2859.

47.   Pfeiffer, W.; König, S.; Legrand, J. F.; Bayerl, T.; Richter, D.; Sackmann, E., Neutron Spin Echo Study of Membrane Undulations in Lipid Multibilayers. *EPL (Europhysics Letters)* **1993,** *23*, 457.

48.   Pan, J.; Cheng, X.; Sharp, M.; Ho, C.-S.; Khadka, N.; Katsaras, J., Structural and Mechanical Properties of Cardiolipin Lipid Bilayers Determined Using Neutron Spin

Echo, Small Angle Neutron and X-Ray Scattering, and Molecular Dynamics Simulations. *Soft Matter* **2015,** *11*, 130-138.

49.   Ashkar, R.; Nagao, M.; Butler, Paul D.; Woodka, Andrea C.; Sen, Mani K.; Koga, T., Tuning Membrane Thickness Fluctuations in Model Lipid Bilayers. *Biophysical Journal* **2015,** *109*, 106-112.

50.   Brüning, B.; Stehle, R.; Falus, P.; Farago, B., Influence of Charge Density on Bilayer Bending Rigidity in Lipid Vesicles: A Combined Dynamic Light Scattering and Neutron Spin-Echo Study. *The European Physical Journal E* **2013,** *36*, 77.

51.   Zheng, Y.; Michihiro, N.; Dobrin, P. B., Bending Elasticity of Saturated and Monounsaturated Phospholipid Membranes Studied by the Neutron Spin Echo Technique. *Journal of Physics: Condensed Matter* **2009,** *21*, 155104.

52.   Takeda, T.; Kawabata, Y.; Seto, H.; Komura, S.; Ghosh, S. K.; Nagao, M.; Okuhara, D., Neutron Spin–Echo Investigations of Membrane Undulations in Complex Fluids Involving Amphiphiles. *J Phys Chem Solids* **1999,** *60*, 1375-1377.

53.   Nickels, J. D.; Cheng, X.; Mostofian, B.; Stanley, C.; Lindner, B.; Heberle, F. A.; Perticaroli, S.; Feygenson, M.; Egami, T.; Standaert, R. F.; Smith, J. C.; Myles, D. A. A.; Ohl, M.; Katsaras, J., Mechanical Properties of Nanoscopic Lipid Domains. *J Am Chem Soc* **2015,** *137*, 15772-15780.

54.   Arriaga, L. R.; López-Montero, I.; Monroy, F.; Orts-Gil, G.; Farago, B.; Hellweg, T., Stiffening Effect of Cholesterol on Disordered Lipid Phases: A Combined Neutron Spin Echo + Dynamic Light Scattering Analysis of the Bending Elasticity of Large Unilamellar Vesicles. *Biophysical Journal* **2009,** *96*, 3629-3637.

55.   Yi, Z.; Nagao, M.; Bossev, D. P., Effect of Charged Lidocaine on Static and Dynamic Properties of Model Bio-Membranes. *Biophysical Chemistry* **2012,** *160*, 20-27.

56.   Sharma, V. K.; Mamontov, E.; Ohl, M.; Tyagi, M., Incorporation of Aspirin Modulates the Dynamical and Phase Behavior of the Phospholipid Membrane. *Physical Chemistry Chemical Physics* **2017,** *19*, 2514-2524.

57.   Boggara, M. B.; Faraone, A.; Krishnamoorti, R., Effect of Ph and Ibuprofen on the Phospholipid Bilayer Bending Modulus. *The Journal of Physical Chemistry B* **2010,** *114*, 8061-8066.

58.   Haeng Sub, W.; Kyuyong, L.; Hyuk Kyu, P., Interfacial Energy Consideration in the Organization of a Quantum Dot–Lipid Mixed System. *Journal of Physics: Condensed Matter* **2008,** *20*, 494211.

59.   Binder, W. H.; Sachsenhofer, R.; Farnik, D.; Blaas, D., Guiding the Location of Nanoparticles into Vesicular Structures: A Morphological Study. *Physical Chemistry Chemical Physics* **2007,** *9*, 6435-6441.

60.   Chandler, D., Interfaces and the Driving Force of Hydrophobic Assembly. *Nature* **2005,** *437*, 640.

61.   Kline, S., Reduction and Analysis of Sans and Usans Data Using Igor Pro. *Journal of Applied Crystallography* **2006,** *39*, 895-900.

62.   Kučerka, N.; Liu, Y.; Chu, N.; Petrache, H. I.; Tristram-Nagle, S.; Nagle, J. F., Structure of Fully Hydrated Fluid Phase Dmpc and Dlpc Lipid Bilayers Using X-Ray Scattering from Oriented Multilamellar Arrays and from Unilamellar Vesicles. *Biophysical Journal* **2005,** *88*, 2626-2637.

63.   Tristram-Nagle, S.; Liu, Y.; Legleiter, J.; Nagle, J. F., Structure of Gel Phase Dmpc Determined by X-Ray Diffraction. *Biophysical Journal* **2002,** *83*, 3324-3335.

64.   Kučerka, N.; Nieh, M.-P.; Katsaras, J., Fluid Phase Lipid Areas and Bilayer Thicknesses of Commonly Used Phosphatidylcholines as a Function of Temperature. *Biochimica et Biophysica Acta (BBA) - Biomembranes* **2011,** *1808*, 2761-2771.

65.   Chu, B., Iv - Photon Correlation Spectroscopy. In *Laser Light Scattering (Second Edition)*, Chu, B., Ed. Academic Press: 1991; pp 93-136.

66.   Zilman, A. G.; Granek, R., Undulations and Dynamic Structure Factor of Membranes. *Physical Review Letters* **1996,** *77*, 4788-4791.

67.   Seifert, U.; Langer, S. A., Viscous Modes of Fluid Bilayer Membranes. *EPL (Europhysics Letters)* **1993,** *23*, 71.

68.   Evans, E.; Yeung, A., Hidden Dynamics in Rapid Changes of Bilayer Shape. *Chemistry and Physics of Lipids* **1994,** *73*, 39-56.

69.   Watson, M. C.; Brown, Frank L., Interpreting Membrane Scattering Experiments at the Mesoscale: The Contribution of Dissipation within the Bilayer. *Biophysical Journal* **2010,** *98*, L9-L11.

70.   Boal, D., *Mechanics of the Cell*. Cambridge University Press: Cambridge, 2001.

71.   Nagao, M.; Kelley, E. G.; Ashkar, R.; Bradbury, R.; Butler, P. D., Probing Elastic and Viscous Properties of Phospholipid Bilayers Using Neutron Spin Echo Spectroscopy. *The Journal of Physical Chemistry Letters* **2017,** *8*, 4679-4684.

72.   Guler, S. D.; Ghosh, D. D.; Pan, J.; Mathai, J. C.; Zeidel, M. L.; Nagle, J. F.; Tristram-Nagle, S., Effects of Ether Vs. Ester Linkage on Lipid Bilayer Structure and Water Permeability. *Chemistry and Physics of Lipids* **2009,** *160*, 33-44.

73.   Seto, H.; Yamada, N. L.; Nagao, M.; Hishida, M.; Takeda, T., Bending Modulus of Lipid Bilayers in a Liquid-Crystalline Phase Including an Anomalous Swelling Regime Estimated by Neutron Spin Echo Experiments. *The European Physical Journal E* **2008,** *26*, 217.

74.   Boal, D., *Mechanics of the Cell*. 2 ed.; Cambridge University Press: Cambridge, 2012.

75.   Rawicz, W.; Olbrich, K. C.; McIntosh, T.; Needham, D.; Evans, E., Effect of Chain Length and Unsaturation on Elasticity of Lipid Bilayers. *Biophysical Journal* **2000,** *79*, 328-339.

76.   Goetz, R.; Gompper, G.; Lipowsky, R., Mobility and Elasticity of Self-Assembled Membranes. *Physical Review Letters* **1999,** *82*, 221-224.

77.   Henzler-Wildman, K.; Kern, D., Dynamic Personalities of Proteins. *Nature* **2007,** *450*, 964.

78.   Eisenmesser, E. Z.; Millet, O.; Labeikovsky, W.; Korzhnev, D. M.; Wolf-Watz, M.; Bosco, D. A.; Skalicky, J. J.; Kay, L. E.; Kern, D., Intrinsic Dynamics of an Enzyme Underlies Catalysis. *Nature* **2005,** *438*, 117.

79.   Woodka, A. C.; Butler, P. D.; Porcar, L.; Farago, B.; Nagao, M., Lipid Bilayers and Membrane Dynamics: Insight into Thickness Fluctuations. *Physical Review Letters* **2012,** *109*, 058102.

80.   Szleifer, I.; Kramer, D.; Ben-Shaul, A.; Roux, D.; Gelbart, W. M., Curvature Elasticity of Pure and Mixed Surfactant Films. *Physical Review Letters* **1988,** *60*, 1966-1969.

81.   Hoffmann, I.; Hoffmann, C.; Farago, B.; Prévost, S.; Gradzielski, M., Dynamics of Small Unilamellar Vesicles. *The Journal of Chemical Physics* **2018,** *148*, 104901.

82.   Paz, L.; Di Meglio, J. M.; Dvolaitzky, M.; Ober, R.; Taupin, C., Highly Curved Defects in Lyotropic (Nonionic) Lamellar Phases. Origin and Role in Hydration Process. *The Journal of Physical Chemistry* **1984,** *88*, 3415-3418.

83.   Petrache, H. I.; Dodd, S. W.; Brown, M. F., Area Per Lipid and Acyl Length Distributions in Fluid Phosphatidylcholines Determined by 2h Nmr Spectroscopy. *Biophysical Journal* **2000,** *79*, 3172-3192.

84.   Brust, M.; Walker, M.; Bethell, D.; Schiffrin, D. J.; Whyman, R., Synthesis of Thiol-Derivatised Gold Nanoparticles in a Two-Phase Liquid-Liquid System. *Journal of the Chemical Society, Chemical Communications* **1994**, 801-802.

85.   Azuah, R. T.; Kneller, L. R.; Qiu, Y. M.; Tregenna-Piggott, P. L. W.; Brown, C. M.; Copley, J. R. D.; Dimeo, R. M., Dave: A Comprehensive Software Suite for the Reduction, Visualization, and Analysis of Low Energy Neutron Spectroscopic Data. *J Res Natl Inst Stan* **2009,** *114*, 341-358.

CHAPTER SIX

CONCLUSION AND RECOMMENDATIONS

6.1 Summary and Conclusions

In this dissertation, we have successfully developed a robust colloidal AuNP catalyst platform based on pH-responsive polymers. Chapter 1 introduces the concept of gold nanoparticle based catalysis and describes a brief literature review of seminal works in this field. Primarily, we have discussed the classes of AuNP catalysts, the advantages and disadvantages of each class of catalysts and common AuNP synthesis techniques.

Chapter 2 elucidates the advantages of employing colloidal catalysts over oxide supported catalysts through the development of a technique to characterize both catalyst classes (supported and colloidal) with a common toolset. It highlights an organothiol adsorption based method in aqueous media to quantify available surface area in both

supported and colloidal catalysts. This facilitates direct comparison of catalytic activity normalized to available surface area. We show that on a per gold mass basis, colloidal catalysts demonstrate greater catalytic activity compared to supported catalysts. On the other hand, when catalytic activity is normalized to available surface area, it was found that supported catalysts show higher activity due to the synergistic support effect towards AuNP catalytic activity. Induction time phenomena arising during the model reaction was investigated in detail in this work.

After demonstrating greater catalytic activity of colloidal AuNP on a gold mass basis, Chapter 3 focusses on solving the major issue plaguing colloidal catalysts: catalyst recovery. To facilitate catalyst recovery, a robust pH-responsive small molecule functionalized AuNP catalyst platform was developed which could be recovered from reaction products through two pH triggered recovery methods. MUA functionalized colloidal AuNPs were found to be robust and pH responsive with efficient recovery through pH triggered aggregation/redispersion and pH triggered phase transfer to organic solvent mediated by a phase transfer agent octadecylamine. However, small molecules such as MUA demonstrate high packing density on AuNP surface leading to complete surface passivation, thus rendering AuNP catalytically inactive. On using partial MUA surface coverage on AuNP, catalytic activity could be retained, however colloidal stability and recovery is greatly compromised.

Consequently, Chapter 4 focusses on developing a recoverable catalyst platform which ameliorates the issues elucidated in Chapter 3. We developed a pH-responsive thiolated polymer functionalized AuNP catalysts (AuNP-SPAA), which possesses similar

pH triggered recovery properties as AuNP-MUA, while being catalytically very active due to the low packing density of long chain length polymeric ligands. AuNP-SPAA catalytic activity could be retained for up to 5 reaction cycles by manipulating the polymer functionality and altering the polymer softness. We demonstrated how conformation, packing density and polymer shell solvation affects AuNP-SPAA catalytic activity.

Chapter 5 focuses on a different field of research pertaining to gold nanoparticles. Here, we have focused on studying potential biomechanical effects of gold nanoparticle inclusions on lipid bilayers. The goal of this study was two-fold: (a) investigate membrane dynamics in presence of AuNP inclusions to elucidate potential toxic effects on cell membranes through membrane rupture, etc. (b) measure bilayer properties to characterize lipid-nanoparticle assemblies (LNAs) for application as stimuli-responsive drug-delivery vehicles. We demonstrated through neutron spin echo spectroscopy that, lipid bilayers with AuNP inclusions were significantly softer than nascent lipid bilayers. Membrane softening has direct implications on membrane functionality as various biological phenomena are controlled by membrane biomechanical properties such as membrane bending modulus, membrane viscosity and membrane thickness fluctuation dynamics.

6.2 Recommendations

6.2.1 Supported AuNP catalysts

In Chapter 2, we have demonstrated a successful technique to directly compare colloidal and supported AuNPs with a common toolset. I suggest that future work be extended to AuNP supported on other metal oxide supports and carbonaceous supports

such as charcoal, graphite, CNT, etc. We have conducted preliminary experiments with AuNPs on alumina, ceria, MgO and ZnO (Figure 6.1) where 2-MBI adsorption technique could be applied successfully (Figure 6.2). I suggest utilizing metal oxide supports of similar size range and directly comparing the AuNP catalytic activity as a means to measure support effects on catalysis. This study can easily be extended to other supports such as mesophase materials and MOFs and might present an interesting research avenue. AuNP supported on silica could not be produced by this method as the Point of Zero Charge (PZC) on silica occurs at highly acidic pH where colloidal AuNPs are not stable. However, other methods like synthesizing AuNP in presence of silica could be adopted for possible successful impregnation. MnO_2 is another potential oxide support, however MnO_2 used in this work were similar sized as AuNPs. I would suggest employing larger MnO_2 particle size as support to enhance AuNP immobilization and ease of catalyst recovery through centrifugation based separation. Surprisingly we couldn't find the PZC of Zirconia which is also a potential metal oxide support for AuNP.
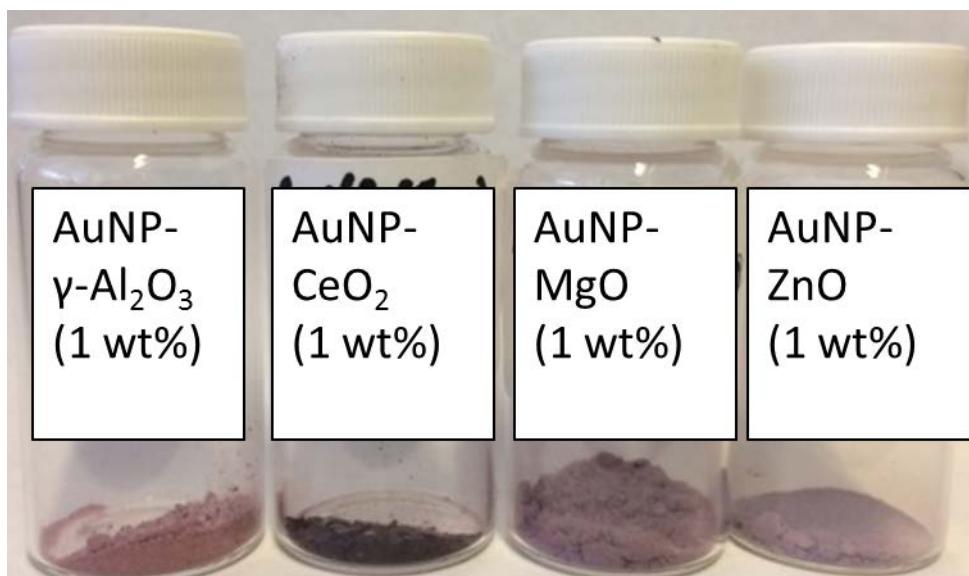
Figure 6.1. Supported catalysts formed by immobilizing 5 nm AuNP on metal oxides.
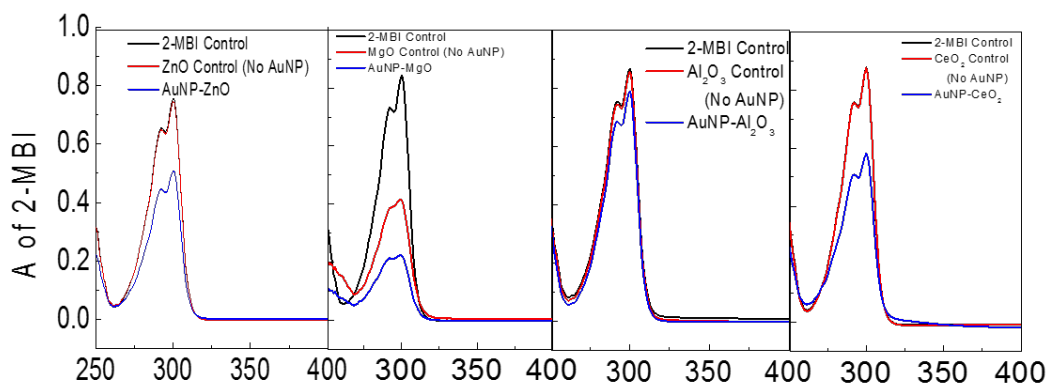
Figure 6.2. Typical 2-MBI adsorption profiles for AuNP-Metal oxide catalysts depicting preferential adsorption on AuNP (2-MBI was found to adsorb on MgO).

6.2.2 Recoverable colloidal AuNP catalysts.

In Chapter 3 and 4, we demonstrate catalysts which can be recovered via pH triggered recovery schemes. We show that PAA can be functionalized with thiol moieties

to make them suitable ligands for AuNP stabilization. However, such catalysts suffered loss of catalysis due to reducing agent induced ligand desorption and catalyst aggregation. Reducing agents are commonly required for carrying out reduction reactions such as 4-nitropenol reduction reaction which has been primarily investigated in this work. I would suggest investigating catalyst efficacy in other gold catalyzed reactions (such as CO oxidation, glycerol oxidation and carbon-carbon coupling reactions) as mentioned in this review[1] on gold nanoparticle catalysts.

We have also found that electrostatics in the AuNP polymer shell plays a vital role in controlling the catalytic activity during 4-nitrophenol reduction. We have observed catalytic activity enhancement when amine moieties are introduced into the PAA backbone in addition to thiols. This phenomena should be deeply investigated and should include a thorough investigation of EDC/NHS chemistry during the reaction. Proper polymer characterization through ATR-FTIR and H-NMR (2D if possible) should be conducted. Other methods of quantifying the amine and thiol content of the polymer can be based on colorimetric assays such as TNBS assay for primary amines and Ellman's reagent for thiol groups. Other general suggestion to harness the electrostatics would be to functionalize amine-containing polymers with thiol groups such as chitosan, polyimines, etc using similar chemical synthesis approaches. Salt concentration and interaction of charges with the polymer shell should be thoroughly investigated to normalize the reaction rates for correct comparison.

Ligand	Structure	Catalyst name	Zeta Potential (mV)
Citrate		AuNP-Citrate	-27.5 ± 9
PAA-SH		AuNP-SPAA	-36.1 ± 13.9
PAA-SH-EDA		AuNP-SPAA-EDA [+] and AuNP-SPAA-EDA [++]	-29.5 ± 9.3 & -20.7 ± 5.6
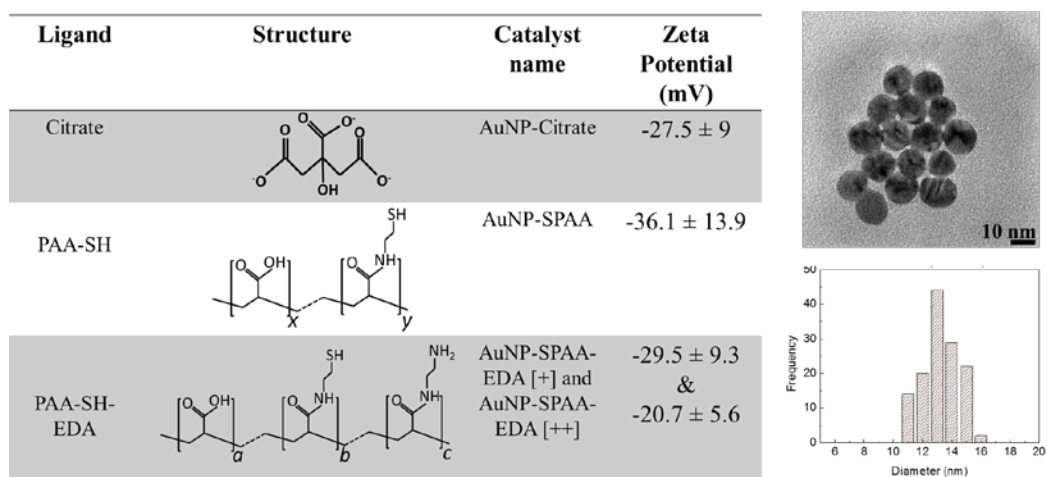
Figure 6.3. Ligand structure and Zeta Potential (ζ) of functionalized AuNPs

(A) and **(B)** Pseudo first order rate constants

Catalyst	Rate Constant (min⁻¹)	Induction time (s)
AuNP-SPAA $_{30K}$ *(50%)*	0.40	36
AuNP-SPAAEDA *(50%-25%)*	0.60	108
AuNP-SPAAEDA *(50%-50%)*	0.53	72
AuNP-Citrate	0.66	0

(C)

Catalyst	Rate Constant (min⁻¹) [Induction time (s)]		
	DDI water	*NaCl*	*PBS*
AuNPSPAA$_{30K}$(50%)	0.40 [72]	0.72 [54]	1.93 [0]
AuNPSPAA$_{30K}$-EDA (50%-25%)	0.60 [72]	0.64 [54]	1.96 [0]
AuNPSPAA$_{30K}$-EDA (50%-50%)	0.53 [72]	0.56 [72]	2.12 [0]

(E)

Catalyst	Rate Constant (min⁻¹) [Induction time (s)]
DDI water	0.40 [72]
5 mM PBS	0.53 [36]
38 mM PBS	1.18 [0]
75 mM PBS	2.12 [0]

Figure 6.4. (A) and (B) Pseudo first order rate constants depicts reaction rate enhancement on incorporating amines in the polymer backbone. (C) Depicts effect of salt and buffer on the reaction rates for 4-NP reduction due to electrostatic effects and charge screening. (D) and (E) depicts effects of buffer concentration where reaction rate enhancement is observed on increasing PBS concentration.

To investigate other approaches to recoverable catalysts, we have explored biphasic catalysts as a suitable approach. Here, hydrophobic thiolated polymer (such as polystyrene-thiol or polylactide-thiol) are used to functionalize AuNPs to render them as stable colloids in organic medium such as toluene, chloroform, etc. These organic phase catalysts can be used to conduct aqueous phase reactions as a vigorously mixed bi-phase. Catalyst

separation occurs from the aqueous product medium by phase separation after the agitation is rescinded (Figure 6.7). Reaction rate heavily depends on catalyst concentration, sodium borohydride concentration, agitation rate and organic-aqueous phase volume ratio. AuNP-Cit functionalization with SPS occurs without any aggregation or loss in AuNP (Figure 6.5 A-D). Preliminary SANS data suggests that shell thickness and shell solvation is dependent on ligand molecular weight (Figure 6.6). We have however, observed substantial aggregation during 4-NP reduction reaction (possibly due to sodium borohydride mediated ligand desorption) in addition to permanent coating of glass/Teflon reaction vessels during agitation. This renders these catalysts non-catalytic after 2-3 cycles. A thorough investigation into this phenomena can result in an efficient catalyst system for aqueous based reactions. As mentioned earlier, this system could also be utilized for other reaction systems (oxidation, carbon-carbon coupling, etc) which does not employ harsh reducing agent or sources of hydrogen. Thiol-poly-L-lactide can be potentially used as ligand to investigate stereo-selective reactions with AuNP catalysts.
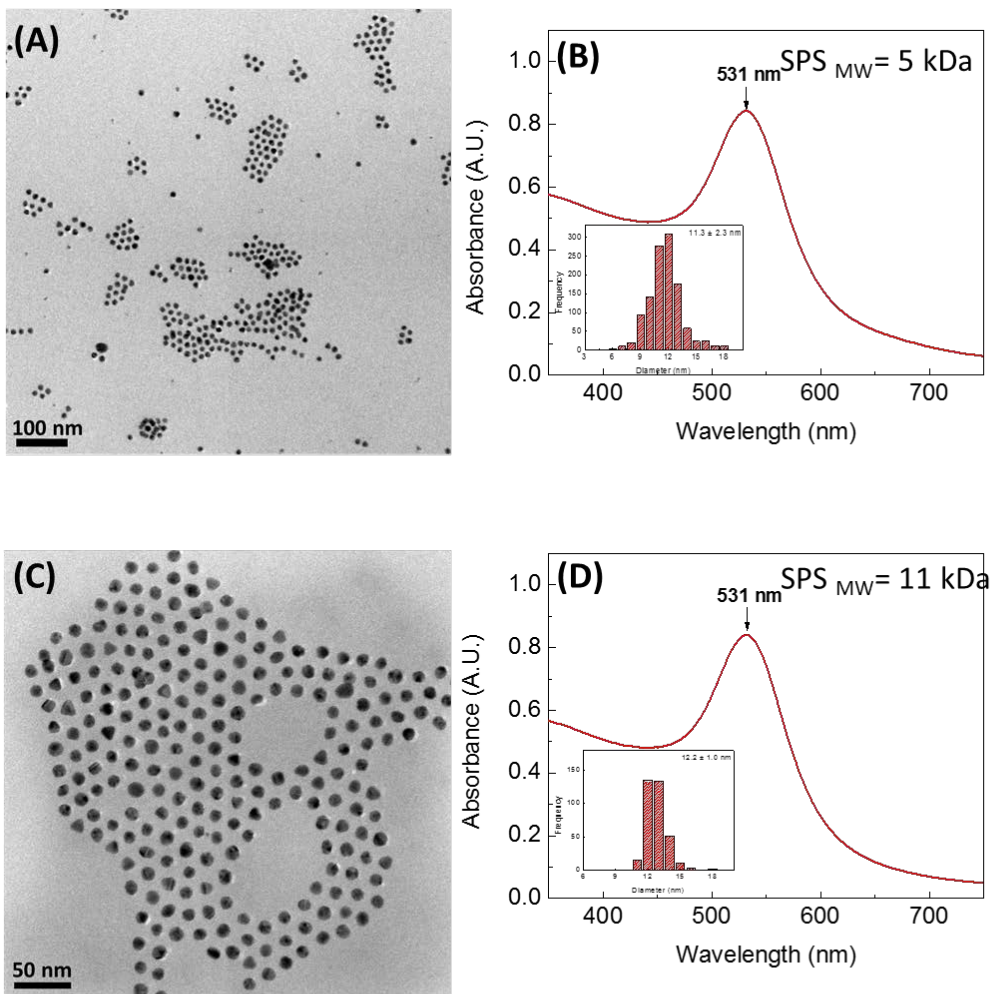
Figure 6.5. (A) and (B) depicts AuNP-SPS (5 kDa) TEM micrograph and LSPR with size distribution (inset). (C) and (D) depicts the same analysis for AuNP-SPS (11 kDa). (E) shows the summary of core diameters and inter-particle distance and ligand chain length calculated from TEM images in the non-solvated conditions.
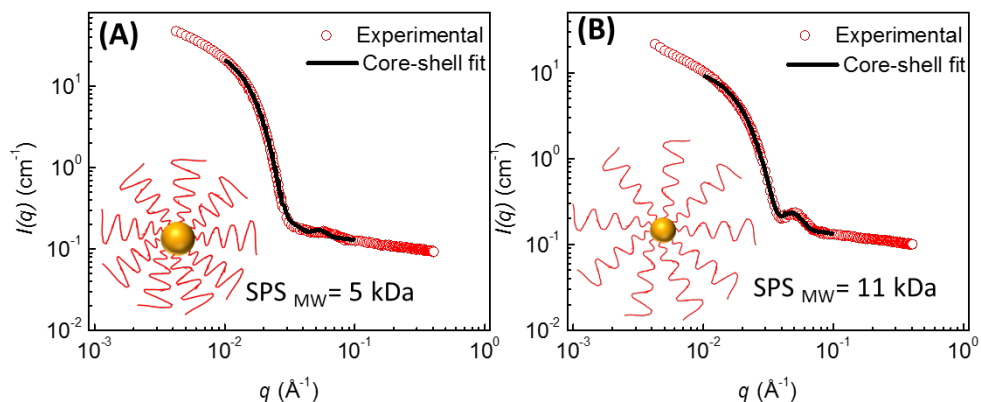
Figure 6.6. Small Angle Neutron Scattering profiles of (A) AuNP-SPS (5 kDa) and (B) AuNP-SPS (11 kDa) depicting core-shell form factor. (C) summarizes ligand chain length as determined from core-shell fitting to the SANS scattering data. Shell solvation is similarly calculated as in Chapter 4 of this dissertation.
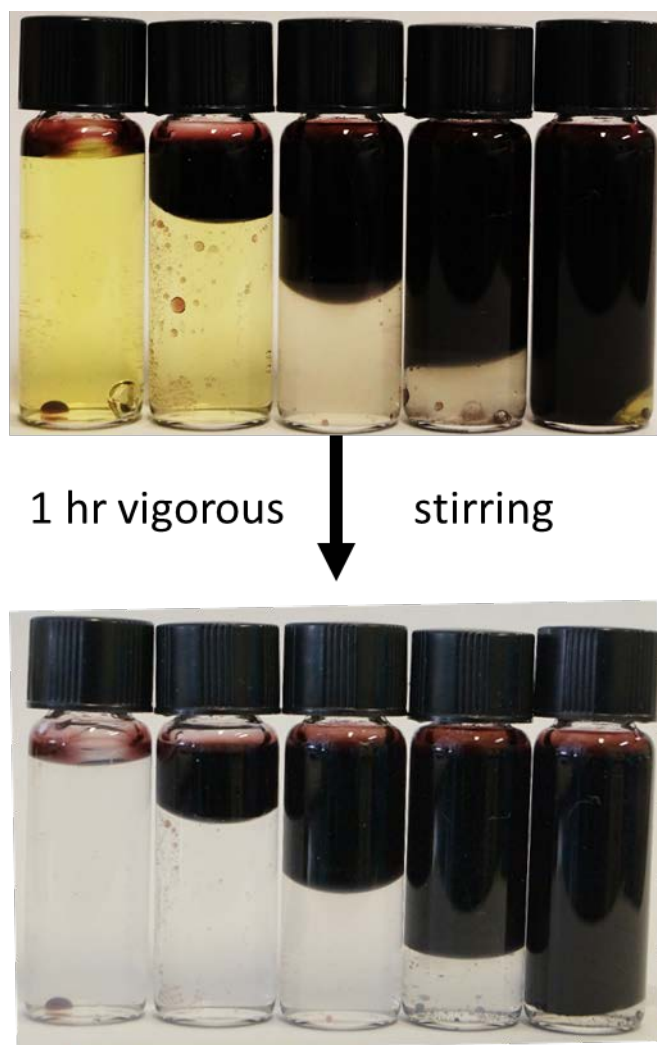
Figure 6.7. Image depicts complete 4-NP reduction using different volume ratios of catalyst phase to reactant phase.
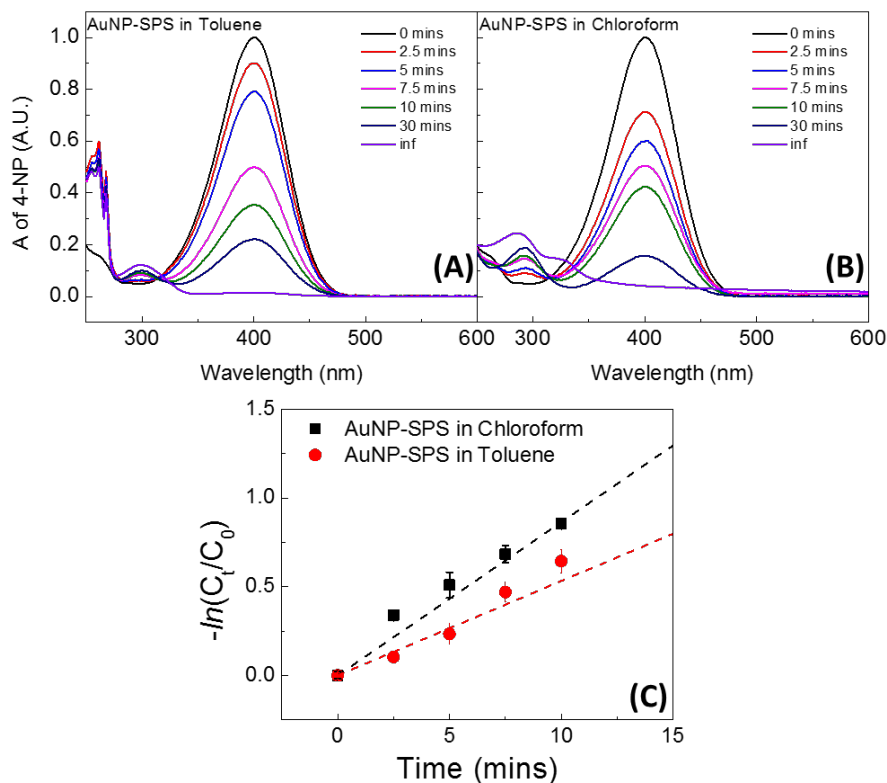
Figure 6.8. (A) and (B) shows time resolved UV-Vis spectroscopy based reaction progress tracking for 4-NP reduction reaction by $NaBH_4$. (C) Slope of the pseudo-first order reaction kinetics data fit gives the rate constant for the reactions. Error bars are standard deviation from the mean based on two individual measurements.

In chapter 5, we have successfully showed bilayer softening as a result of AuNP inclusions in lipid bilayers. This study should be extended further to study effects of AuNP inclusions on membrane properties such as membrane viscosity and thickness fluctuation dynamics through neutron spin echo spectroscopy. For these studies, hydrogenated lipids have to be replaced with tail deuterated lipids to measure the thickness fluctuation dynamics through neutron spin echo spectroscopy. In addition, we have conducted some preliminary investigation on AuNP inclusion efficiency by producing LNAs with a range

of AuNP core diameters and functionalized with ligands of different chain lengths. A through TEM (including cryo-TEM) and ICP-OES based investigation of AuNP inclusions efficiency in pure/mixed/cholesterol/PEGylated lipid bilayers needs to be carried out to understand nanoparticle inclusion and aggregation in bilayers.

REFERENCES

1.   Corma, A.; Garcia, H., Supported Gold Nanoparticles as Catalysts for Organic Reactions. *Chemical Society Reviews* **2008,** *37*, 2096-2126.

APPENDICES

Appendix A

Structural Analysis of Ultra-Pure Low-Polydispersity Lignin Fractions Derived from

Continuous Flow Hot Acid Purification Process.

[Manuscript in preparation for ACS Macro Letters]

A.1 Introduction, Results and Discussions

Lignocellulosic biomass valorization into usable chemicals, materials and fuel sources is a major focus of integrated biorefineries.[1-4] Lignin forms a major component (15-30% dry weight) of biomass in addition to cellulose and hemicellulose.[5] Biomass deconstruction to efficiently extract lignin has been a challenge, leading to lignin being considered a low value by-product of the cellulose recovery process. Currently, >99% lignin generated is used as fuel in the paper and pulp industry to recover energy required in the process.[6-7] Abundance of lignin in nature and its high aromatic content renders it as a suitable alternative precursor for fine chemical industries which currently uses petroleum sources. Lignin recovery from biomass has seen increasing advancement in recent years including commercialization of LignoForce System[TM], LignoBoost[TM] and Sequential Liquid-Lignin Recovery Process (SLRP)[TM] to name a few.[8-10] Lignin derived from these technologies are relatively clean and contains a fraction of the ash and sodium initially present in the original black liquor sources. Relatively low impurity lignin has been successfully employed in low value applications such as resins, polyurethane foams and clean biofuels.[11] However, for lignin applications for high-value products as carbon fiber precursors, lignin must be ultra-clean (< 100 ppm Na and metal content for automotive applications).[12-13] In addition to impurities, wide molecular weight distribution leads to low

strength fiber, not suitable for commercialization. Due to its natural abundance and constant output from the paper and pulp industry, lignin-based carbon fibers can be inexpensive if ultra-clean narrow molecular weight lignins can be extracted from lignin sources.

To ameliorate the issues of impurities and wide MW distribution, we have utilized a novel Aqueous Lignin Purification with Hot Acids (ALPHA) process,[14-16] where lignin was initially extracted through the SLRP[TM] process[10] from softwood black liquor and subsequently, fractionated and purified by the continuous Aqueous Lignin Purification using Hot Acids (ALPHA) process (schematic depicted in Figure A.1A). ALPHA is based on ternary phase behavior of lignin-acetic acid (AcOH)-water (H_2O) systems (Figure A.1B), which decides the appropriate process operating conditions for generating effective liquid-liquid equilibrium (LLE). Moreover, AcOH strength can be altered to yield lignin fractions of increasing MW and relatively narrower distribution in the bottom phase. In addition, ALPHA produces highly solvated lignin-rich bottom phase which leads to subsequent advantages in direct processability.
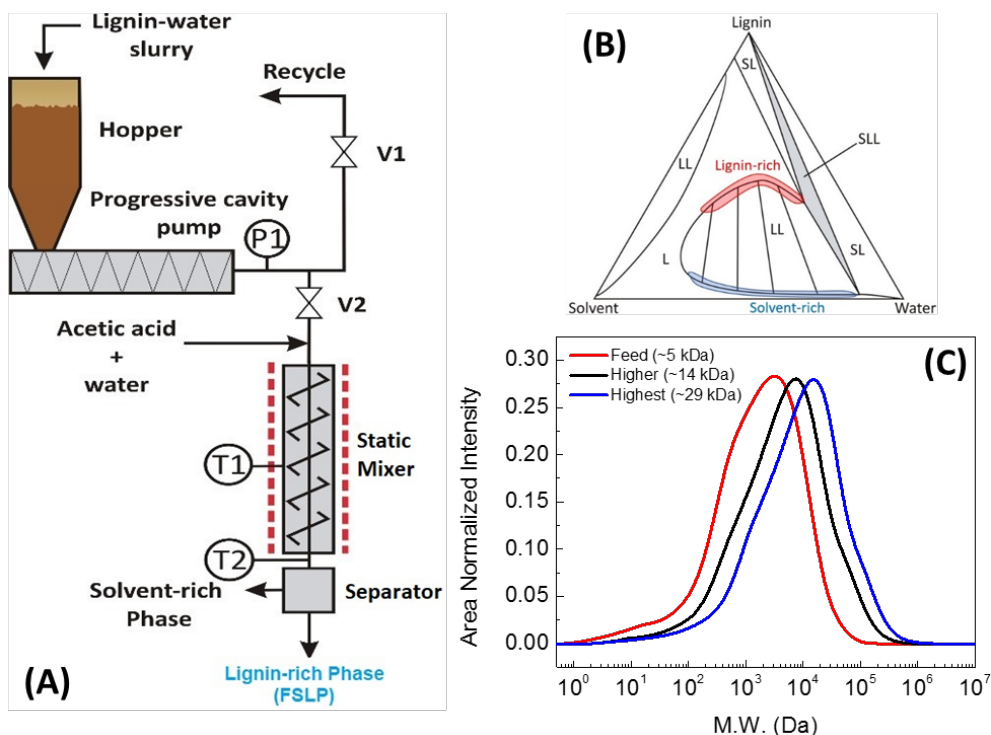
Figure A.1. (A) Schematic of continuous-flow ALPHA process. (B) Ternary phase behavior for lignin with aqueous one phase solvent. (C) Molecular weight distribution of feed and fractionated lignins.

Lignin investigated in the current work were recovered from a softwood black liquor (Kappa number 25, 42 wt% solid content), by the SLRP process described elsewhere.[10] Recovered lignin was found to be 99% via Klason method[17] and contained 1% ash (determined by combustion). Water content in the recovered lignin ranged from 30-45 % depending on ambient conditions. AcOH/H_2O ratios ranging from 15/85 to 70/30 has been previously shown to be the region of interest to generate stable liquid-liquid equilibrium in the ALPHA process.[16] AcOH concentrations outside the region leads to solid lignin (lower AcOH concentration) or single liquid phase (higher AcOH concentration). Continuous ALPHA process was operated at two AcOH/H_2O ratios to generate increasingly high molecular weight ultra-pure lignin fractions from the SLRP

recovered lignin feed. At 56/44 AcOH/H_2O ratio, 50 wt% lignin was recovered into the

solvent phase whereas the remaining lignin was extracted into the lignin rich bottom phase

(denoted as higher MW lignin fraction, MW ~ 14 kDa). Similarly, on using a stronger acid

solution at 67/33 AcOH/H_2O ratio, 90 wt% of the lignin was extracted into the solvent

phase whereas only 10 wt% lignin resided in the bottom lignin rich phase (denoted as

highest MW lignin fraction, MW ~ 29 kDa). GPC chromatograms of the ALPHA feed

lignin, higher MW and highest MW lignin fraction have been shown in Figure A.1C.

Increase in lignin MW in the lignin-rich phase can be attributed to the AcOH strength in

the solvent-rich phase, leading to dissolution of increasing MW lignin in the solvent rich

phase. Consequently, only very high MW lignin fractions remains as residue in the lignin

rich phase leading to the overall increase in number average MW, M_n. Table 1 summarizes

the lignin fraction properties generated from the ALPHA process. Metal and ash content

in the fractionated lignins were significantly lower than commercially available lignins

(ash content two order of magnitude lower than commercial softwood Kraft lignin and

cleaner than the best Organosolv lignins).

Table A1. Characterization summary of lignin feed and fractions derived from the ALPHA process. Errors are one standard deviation based on triplicate measurements.

Lignin Type	AcOH/H_2O ratio	M_n (Da)	PDI	Ash Content (wt %)	Na content (ppm)
Feed	N/A	5200	6.6	1.0	1400 ± 50
Higher M.W.	56/44	13800±150	4.44±0.03	0.068	210±46
Highest M.W.	67/33	28600±300	5.15±0.02	0.089	220±70

Recently, Ogale et al. have employed ultra-clean fractionated lignin generated from the ALPHA process by Thies et al.[18] Lignin fractions (higher and highest MW) in solution were produced continuously by the ALPHA process and were directly fed to a dry spinning apparatus. Carbon fibers spun from the highest MW lignin fractions demonstrated the highest tensile strength ever reported (~ 1.4 GPa, 40% stronger than any lignin-based carbon fibers). CF tensile modulus was also shown to increase with lignin MW (~74 GPa for clean feed and ~87 and 98 GPa for higher and highest MW fractions). Investigation by Raman spectroscopy showed that increasing lignin MW led to carbon fibers with higher graphitic content and enhanced carbon layer formation with lower disorder. In addition, X-ray diffraction demonstrated a consistent decrease in d-spacing between graphitic layer planes with increasing lignin precursor MW. This study thus indicated that in addition to lignin purity, molecular weight and lignin solution structure plays a crucial role in determining CF properties when CF processing parameters are fixed.

To elucidate the role of lignin MW and structure in solution in determining CF tensile properties, it is crucial to accurately characterize the lignin fractions generated through ALPHA. Lignin MW in solution has been conventionally studied by size exclusion chromatography (such as gel permeation chromatography, GPC).[19] However, lignin interacts through hydrogen bonding and π-π interactions leading to the presence of aggregates as well single molecules in solution.[20-23] In addition, GPC utilizes linear polystyrene/polyethylene glycol as standards for universal calibration. Neither are comparable structurally to the polydisperse, highly-branched lignin structure, which leads to lignin MW misrepresentation.[19] Standard-independent Multi-Angle Laser Light

Scattering (MALLS) is an absolute technique to determine MW. However MALLS involves issues with absorption, fluorescence and is heavily dependent on accurate refractive index increment (*dn/dc*) measurement.[21] Small angle X-ray and neutron scattering techniques (SAXS and SANS) provides a standard-independent technique to investigate structural information on a large length scale. Although intense synchrotron-based X-ray sources can provide a simple tool to characterize lignin structure, the contrast between lignin and the solvent is often insufficient to derive meaningful information from the scattering profiles, even on increasing electron densities on lignin molecules intentional (through halogenation, etc.).[24] SANS however, provides large contrast between the hydrogenated lignin molecules/aggregates and deuterated solvents, due to the large difference in neutron scattering cross sections of deuterium and hydrogen atoms. SANS has been previously used to characterize lignin from various sources and in different deuterated solvents such as DMSO, THF and D_2O.[24-27]

In the current work, SANS was conducted on lignin samples dissolved in alkaline D_2O solvent (pH modified to 12 by NaOH) which yielded good miscibility and high contrast between hydrogenated lignin molecules and background solvent. Lignin sample concentration for feed lignin and two lignin fractions ranged from 20-125 mg/mL. Scattering data was not acquired for lignin concentration below 20 mg/mL due to large counting times and poor statistics in addition to substantial incoherent scattering. Absolute molecular weights of lignin feed and lignin fractions were determined through Zimm analysis of the scattering data. In the low q region, scattering intensity from lignin solution in D_2O/NaOH can be approximated as:

$$\frac{Kc}{I(q)} = \frac{1}{M_w} * \left(1 + \frac{R_g^2 q^2}{3}\right) + 2A_2 c \tag{1}$$

where $K = \frac{\Delta\rho^2}{N_A d_{lignin}^2}$ denotes the contrast factor. $\Delta\rho$ represents the scattering length density

difference between the lignin macromolecules and the solvent, d_{lignin} is the lignin density

(1.35 g/mL), N_A is the Avogadro's number, R_g is the radius of gyration at infinite dilution

and A_2 is the second virial coefficient. Figure A.2A depicts a typical Zimm plot where

$Kc/I(q)$ has been plotted as a function of q^2 for highest MW lignin fraction at different

concentrations. Zimm plot slopes at different concentrations directly yields an approximate

radius of gyration R_g at infinite dilution (Figure A.2C). No clear dependence of R_g on lignin

concentration was observed for every sample investigated, however R_g for fractionated

lignin samples (~25 Å) were found to be marginally higher than feed lignin (~21 Å). On

extrapolating the data to the limiting condition $q{\to}0$ and infinite dilution, M_w and second

virial coefficient A_2 can be obtained from the intercept and slope of plot in Figure A.2B.

Absolute MW and A_2 has been summarized in Figure A.2D. Positive values of A_2 depicts

complete lignin miscibility in D₂O/NaOH solvent. Molecular weights estimated from

Zimm analysis are significantly higher (for example, 39 kDa for highest MW fraction) than

number average molecular weights estimated through GPC using PEG standards (~29 kDa

for highest MW). This is a common observation on characterizing highly branched and

compact lignin's molecular weight against PEG or polystyrene standards. Standards used

in GPC analysis have been shown to exist as highly coiled polymer nanoparticles, leading

to lignin MW weight underestimation.[28] However, Zimm analysis measures the standard

independent absolute MW providing a closer approximation to the actual lignin MW. It

should however be noted that Zimm analysis was conducted on a small range of concentration in the current work, thus rendering MW and A_2, approximations at best.
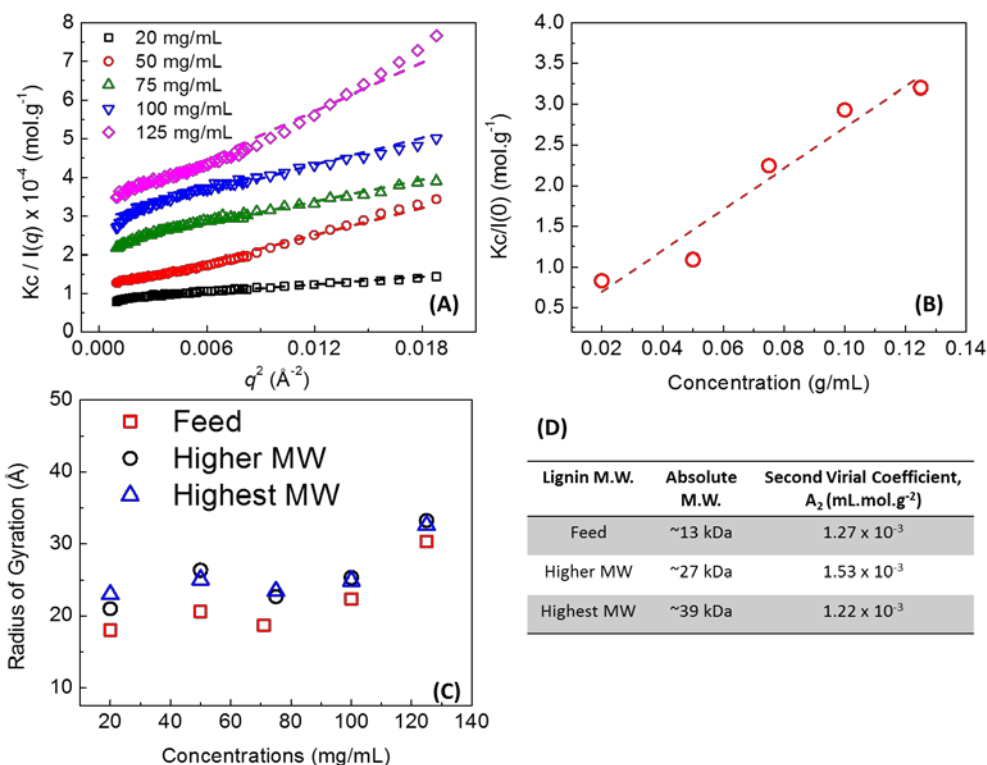
Figure A.2. (A) Typical Zimm plot of Lignin feed in $NaOH/D_2O$ in low q region $(0.03 < q < 0.14 \text{ Å}^{-1})$. Solid lines depicts linear fits to data. (B) Under $q \rightarrow 0$, MW and second virial coefficient A_2 is obtained by assuming infinitely dilute concentration. Dashed line depicts linear fit to data. (C) Radius of gyration of feed and lignin fractions obtained from Zimm plots. (D) Zimm analysis summary for feed and lignin fractions.

Typical SANS spectra for highest MW lignin fraction for concentration ranging from 20-125 mg/mL has been depicted in Figure A.3A. Low-q upturn observed in all scattering profiles suggests presence of aggregates at all concentrations. High and intermediate q region represents scattering from individual lignin macromolecules.

Standard Kratky plots were generated (Figure A.3B) from the scattering data for all lignin samples by plotting $I(q)q^2$ versus q to gauge the possible lignin macromolecular structure. Linear increase of the Kratky plots at high q is an indication of elongated rod-like structure as opposed to Gaussian-coil structures. Lignin feed and both lignin fractions demonstrate similar Kratky profile which depicts lignin macromolecules with similar structures, irrespective of lignin MW. Figure A.3B depicts a peak at the intermediate to low q region which increases with concentration, indicating association of lignin macromolecules into aggregate structures over a large length scale.
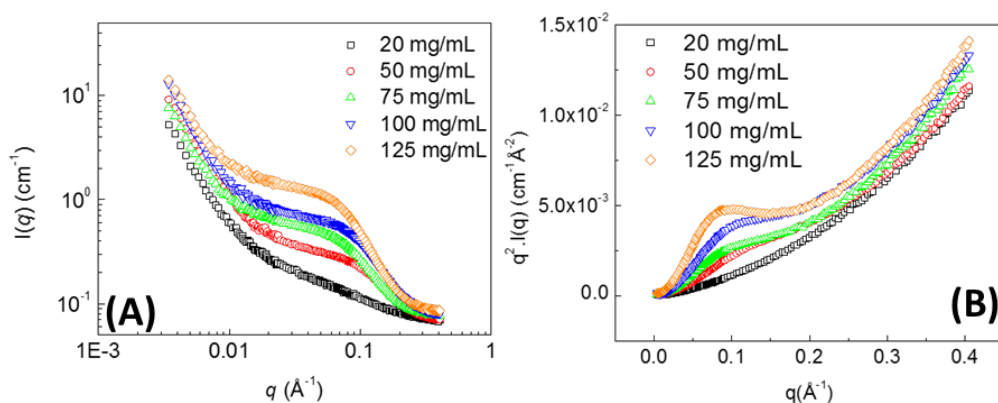
Figure A.3. (A) Scattering profile for highest MW lignin fraction. (B) Typical Kratky plots of scattering data for highest MW lignin fraction. Linearly increasing nature of the plot at high q values indicate presence of elongated structures. Error bars have been removed for optical clarity.

The low q region in the scattering profile represents scattering from large lignin aggregates in solution. Large aggregate structures was analyzed by fitting low q scattering data to a unified power law R_g model (shown with dashed black lines in Figure A.4A) which was proposed by Beaucage et al.[29-31]. Radius of gyration obtained from low q data fit is summarized in Figure A.4B. Power law exponent in the low q region ranged from ~

2.8-3.0 and demonstrates scattering from large fractal network structures formed by elongated sub-units. Aggregate structures were observed to be more compact at higher concentrations as evidenced by the decreasing R_g with concentration (Figure A.4B). The phenomenon of contracting aggregate size with concentration can be attributed to lignin aggregates being expanded at low concentration, whereas at high concentrations, inter-penetrating lignin aggregates leads to an overall size decrease. Similar observations have been made by previous researchers[27] with different lignin and polymer[32] systems. Average aggregate size in the lowest concentration regime yields the truest size. Surprisingly, no significant differences were observed in the aggregate R_g for the lignin feed and fractionated lignin demonstrating similar nature and shape of aggregates in solution.
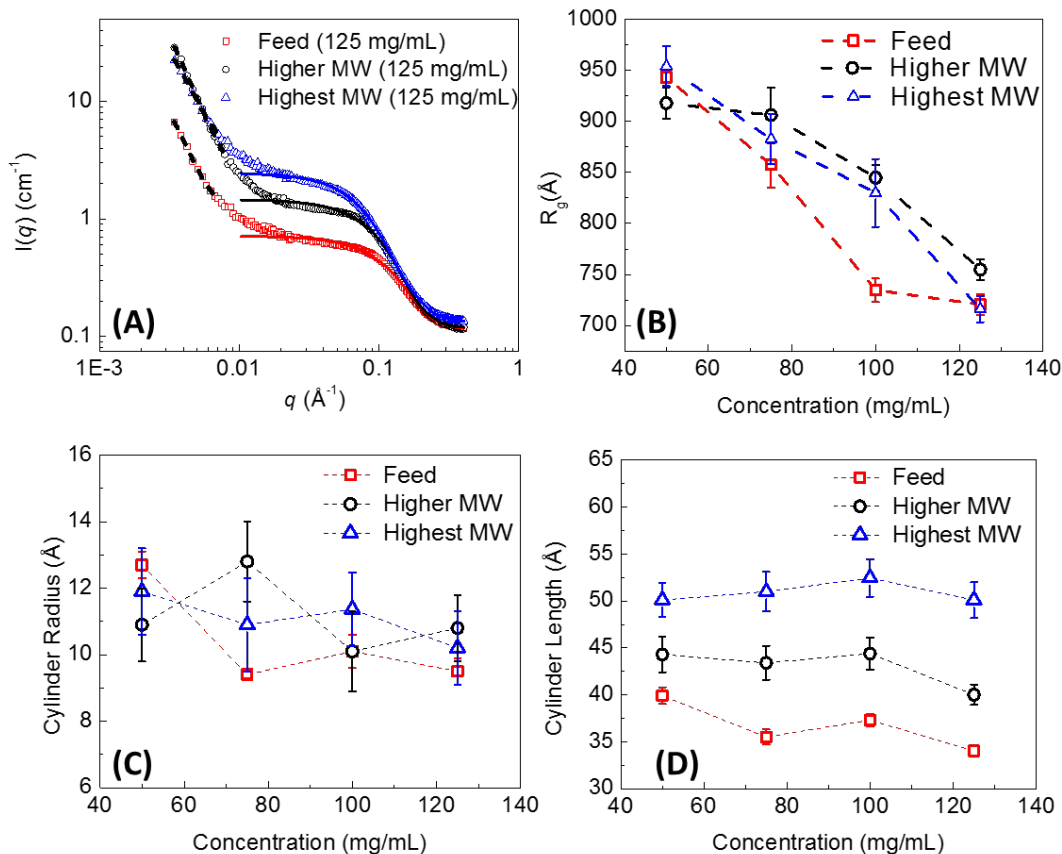
Figure A.4. (A) Scattering profile fit to cylindrical form factor (solid lines) in the intermediate to high q region and unified power law fit in the low q region (black dashed lines). (B) Depicts radius of gyration of lignin fractal aggregate structure obtained from low q unified power law fit. Dashed lines are for visual guidance only. (C) and (D) shows cylinder radius and length obtained from fitting scattering data to cylindrical form factor. Dashed lines are for visual guidance only. All errors are one standard deviation from the mean.

Due to the demonstrated elongated nature of the lignin macromolecules from Kratky analysis, high q scattering data were fit to a cylindrical ellipsoidal form factors. Cylindrical and ellipsoidal models have similar scattering profiles and were both investigated simultaneously. High q oscillations usually observed for cylindrical and ellipsoidal entities were masked by the incoherent background scattering and polydispersity for all samples. Cylindrical model fits to scattering profiles are shown in

Figure A.4A (solid lines) for lignin feed and lignin fractions yielding cylinder radius and length as structural parameters (Figure A.4C and D respectively). Surprisingly, no significant change in the lignin cylindrical radii were observed between the lignin feed, higher MW and highest MW lignin fractions. Moreover, no correlations were observed between cylinder radius and lignin concentration in solution. However, a significant increase in cylinder lengths were observed (Figure 4D) when higher MW lignin and highest MW lignin were compared to the feed lignin units. Highest MW lignin fractions demonstrated a ~51 Å average length (~43 Å higher MW lignin fraction) compared to ~37 Å for the lignin feed. Similarly, scattering data fit to ellipsoidal model yields polar radius (minor axis) and the equatorial radius (major axis) which are analogous to radius and half the length of cylinders respectively. Similar observations were made from the elliptical model fit, where no significant differences were observed in the polar radius between lignin feed and fractionated lignin. However, a significant increase in equatorial radius of ellipsoids were observed (highest MW lignin fraction depicting an average ~33 Å equatorial radius compared to ~20 Å for lignin feed). The overall decreasing trend in ellipsoid equatorial radius with concentration can be attributed to lignin molecular crowding at higher concentrations as observed by previous researchers.[25] It is noteworthy to mention, that SANS measures an ensemble average of a vast population of lignin macromolecules. Increase in average lignin macromolecule dimension with MW depicts an increase in population of high MW lignin only. The lignin population should still be treated as a polydisperse system containing all lignin MW. In addition, intermolecular lignin interaction are weaker in dilute solutions and structure parameters obtained from

dilute lignin samples (for example 50 mg/mL) describes the structure more accurately. It should be noted that lignin structure in alkaline media (pH ~12 D_2O) is highly swollen due to hydroxyl group ionization, which leads to increased lignin average size compared to lignin at neutral pH.[33]

The present study depicts simultaneous lignin purification and fractionation into higher and highest MW fractions. The solution structure of lignin feed and lignin fractions have been investigated through small angle neutron scattering. We show that lignin macromolecules are elongated rigid rod-like structures in solution and sub-unit lengths directly correlate with the lignin MW. Cylindrical and ellipsoidal form factor data fitting yields longer lignin sub-unit length for highest MW lignin fraction. Lignin, at all concentrations exists as dense fractal aggregate structures which are comprised of elongated sub-units. Lignin feed and fraction MW were determined through a Zimm analysis of scattering data. Lignin MW obtained from Zimm analysis were significantly higher than number average MW determined through GPC. Carbon fibers derived increasing lignin MW precursors depicts large increase in tensile strength and tensile modulus. We hypothesize that high MW lignin structure and elongated shape affects the lignin macromolecules alignment and packing directly during processing. Lignin solution behavior is different from lignin structure and alignment during CF processing in the presence of shear, tension and solvent choice. Further investigation of lignin macromolecules packing and alignment during various shear conditions and under tension during fiber processing should be undertaken to further explain the role of lignin MW in determining carbon fiber strength. Systematic investigation of these properties can lead to

achieving high tensile strength and modulus requirements for high value industrial applications at a fraction of the current precursor cost.

A.2 Acknowledgement

A.3 References

1.   Panagiotopoulos, I. A.; Chandra, R. P.; Saddler, J. N., A Two-Stage Pretreatment Approach to Maximise Sugar Yield and Enhance Reactive Lignin Recovery from Poplar Wood Chips. *Bioresource Technology* **2013,** *130*, 570-577.

2.   Zhang, Y.-H. P., Reviving the Carbohydrate Economy Via Multi-Product Lignocellulose Biorefineries. *Journal of Industrial Microbiology & Biotechnology* **2008,** *35*, 367-375.

3.   Himmel, M. E.; Ding, S.-Y.; Johnson, D. K.; Adney, W. S.; Nimlos, M. R.; Brady, J. W.; Foust, T. D., Biomass Recalcitrance: Engineering Plants and Enzymes for Biofuels Production. *Science* **2007,** *315*, 804-807.

4.   Ragauskas, A. J.; Williams, C. K.; Davison, B. H.; Britovsek, G.; Cairney, J.; Eckert, C. A.; Frederick, W. J.; Hallett, J. P.; Leak, D. J.; Liotta, C. L.; Mielenz, J. R.; Murphy, R.; Templer, R.; Tschaplinski, T., The Path Forward for Biofuels and Biomaterials. *Science* **2006,** *311*, 484-489.

5.   Doherty, W. O. S.; Mousavioun, P.; Fellows, C. M., Value-Adding to Cellulosic Ethanol: Lignin Polymers. *Industrial Crops and Products* **2011,** *33*, 259-276.

6.   Vainio, U.; Lauten, R. A.; Serimaa, R., Small-Angle X-Ray Scattering and Rheological Characterization of Aqueous Lignosulfonate Solutions. *Langmuir* **2008,** *24*, 7735-7743.

7.   Gosselink, R. J. A.; de Jong, E.; Guran, B.; Abächerli, A., Co-Ordination Network for Lignin—Standardisation, Production and Applications Adapted to Market Requirements (Eurolignin). *Industrial Crops and Products* **2004,** *20*, 121-129.

8.   Kouisni, L.; Holt-Hindle, P.; Maki, K.; Paleologou, M., *The Lignoforce System™: A New Process for the Production of High-Quality Lignin from Black Liquor.* 2014; Vol. 115, p 18-22.

9.   Tomani, P., *The Lignoboost Process.* 2010; Vol. 44.

10.   M. Lake and J. Blackburn Process for Recovering Lignin. 2011.

11.   Holladay, J.; White, J.; Bozell, J.; Johnson, D., *Top Value Added Chemicals from Bio-Mass: Results of Screening Potential Candidates from Biorefinery Lignin.* 2007; Vol. 2.

12.   Baker, D. A.; Rials, T. G., Recent Advances in Low-Cost Carbon Fiber Manufacture from Lignin. *Journal of Applied Polymer Science* **2013,** *130*, 713-728.

13.   Leitten, C. F.; Griffith, W. L.; Compere, A. L.; Shaffer, J. T., High-Volume, Low-Cost Precursors for Carbon Fiber Production. *SAE Transactions* **2002,** *111*, 727-734.

14.   Thies, M. C. K., A. S.; Bruce, D. A. Solvent and Recovery Process for Lignin. US20160137680A1, 2018.

15.   Klett, A. S.; Chappell, P. V.; Thies, M. C., Recovering Ultraclean Lignins of Controlled Molecular Weight from Kraft Black-Liquor Lignins. *Chemical Communications* **2015,** *51*, 12855-12858.

16.   Klett, A. S.; Payne, A. M.; Thies, M. C., Continuous-Flow Process for the Purification and Fractionation of Alkali and Organosolv Lignins. *ACS Sustainable Chemistry & Engineering* **2016,** *4*, 6689-6694.

17.   Aldaeus, F.; Schweinebarth, H.; Törngren, P.; Jacobs, A., 2011; Vol. 65, p 601.

18.   Zeng, J.; Zhang, Q.; Chen, J.; Xia, Y., A Comparison Study of the Catalytic Properties of Au-Based Nanocages, Nanoboxes, and Nanoparticles. *Nano Letters* **2010,** *10*, 30-35.

19.   Lange, H.; Rulli, F.; Crestini, C., Gel Permeation Chromatography in Determining Molecular Weights of Lignins: Critical Aspects Revisited for Improved Utility in the Development of Novel Materials. *ACS Sustainable Chemistry & Engineering* **2016,** *4*, 5167-5180.

20.   Qiu, X.; Kong, Q.; Zhou, M.; Yang, D., Aggregation Behavior of Sodium Lignosulfonate in Water Solution. *The Journal of Physical Chemistry B* **2010,** *114*, 15857-15861.

21.   Contreras, S.; Gaspar, A. R.; Guerra, A.; Lucia, L. A.; Argyropoulos, D. S., Propensity of Lignin to Associate: Light Scattering Photometry Study with Native Lignins. *Biomacromolecules* **2008,** *9*, 3362-3369.

22.   Gidh, A. V.; Decker, S. R.; See, C. H.; Himmel, M. E.; Williford, C. W., Characterization of Lignin Using Multi-Angle Laser Light Scattering and Atomic Force Microscopy. *Analytica Chimica Acta* **2006,** *555*, 250-258.

23.   Gidh, A. V.; Decker, S. R.; Vinzant, T. B.; Himmel, M. E.; Williford, C., Determination of Lignin by Size Exclusion Chromatography Using Multi Angle Laser Light Scattering. *Journal of Chromatography A* **2006,** *1114*, 102-110.

24.   Harton, S. E.; Pingali, S. V.; Nunnery, G. A.; Baker, D. A.; Walker, S. H.; Muddiman, D. C.; Koga, T.; Rials, T. G.; Urban, V. S.; Langan, P., Evidence for Complex Molecular Architectures for Solvent-Extracted Lignins. *ACS Macro Letters* **2012,** *1*, 568-573.

25.   Ratnaweera, D. R.; Saha, D.; Pingali, S. V.; Labbé, N.; Naskar, A. K.; Dadmun, M., The Impact of Lignin Source on Its Self-Assembly in Solution. *RSC Advances* **2015,** *5*, 67258-67266.

26.   Petridis, L.; Pingali, S. V.; Urban, V.; Heller, W. T.; O'Neill, H. M.; Foston, M.; Ragauskas, A.; Smith, J. C., Self-Similar Multiscale Structure of Lignin Revealed by Neutron Scattering and Molecular Dynamics Simulation. *Physical Review E* **2011,** *83*, 061911.

27.   Cheng, G.; Kent, M. S.; He, L.; Varanasi, P.; Dibble, D.; Arora, R.; Deng, K.; Hong, K.; Melnichenko, Y. B.; Simmons, B. A.; Singh, S., Effect of Ionic Liquid

Treatment on the Structures of Lignins in Solutions: Molecular Subunits Released from Lignin. *Langmuir* **2012,** *28*, 11850-11857.

28.   Harth, E.; Horn, B. V.; Lee, V. Y.; Germack, D. S.; Gonzales, C. P.; Miller, R. D.; Hawker, C. J., A Facile Approach to Architecturally Defined Nanoparticles Via Intramolecular Chain Collapse. *Journal of the American Chemical Society* **2002,** *124*, 8653-8660.

29.   Beaucage, G., Approximations Leading to a Unified Exponential/Power-Law Approach to Small-Angle Scattering. *Journal of Applied Crystallography* **1995,** *28*, 717-728.

30.   Beaucage, G., Small-Angle Scattering from Polymeric Mass Fractals of Arbitrary Mass-Fractal Dimension. *Journal of Applied Crystallography* **1996,** *29*, 134-146.

31.   Hammouda, B., Analysis of the Beaucage Model. *Journal of Applied Crystallography* **2010,** *43*, 1474-1478.

32.   Daoud, M.; Cotton, J. P., Star Shaped Polymers : A Model for the Conformation and Its Concentration Dependence. *J. Phys. France* **1982,** *43*, 531-538.

33.   Yan, M.; Yang, D.; Deng, Y.; Chen, P.; Zhou, H.; Qiu, X., Influence of Ph on the Behavior of Lignosulfonate Macromolecules in Aqueous Solution. *Colloids and Surfaces A: Physicochemical and Engineering Aspects* **2010,** *371*, 50-58.

Appendix B

Liposome-nanoparticle assembly characterization through fluorescent techniques:
Overview

208

B.1 Liposome leakage assay

Liposome leakage assay is a useful technique to study changes in lipid bilayer properties such as permeability, phase transition temperature, etc. In extension to investigating these properties, leakage assays can be utilized in quantify effects of nanoparticle, peptides, biomolecules, etc. interactions with lipid bilayer. Liposomes containing a concentrated (self-quenched) fluorophore (such as fluorescein, calcein, etc.) is allowed to release its content to the extra-liposomal fluid where it undergoes dilution. On dilution, the fluorophore regains it fluorescence which can be quantified through a fluorescence spectrometer.

We have primarily focused on investigating similar liposomes as mentioned in Chapter 5 (DPPC and DPPC/DPPG lipid bilayers) with 3 nm AuNP inclusions at different concentrations. Effect of hydrophilic AuNPs interacting with the lipid bilaer outer leaflet was investigated by adding an aliquot of AuNP colloid to the liposome dispersion and measuring the % leakage vs. time/temperature. Percent Leakage (% Leakage) was calculated based on:

$$\% \ Leakage = \frac{I(t) - I_0}{I(max) - I_0}$$

Where $I(t)$ = fluorescence intensity at time t
$I(0)$= fluorescence intensity at time t=0
$I(max)$= fluorescence intensity post liposome lysis by surfactant.

B.2 DPH Anisotropy

Isotropic samples excited by linearly polarized light emit highly polarized light. Polarized emission relaxation occurs due to fluorophore rotational diffusion leading to fluorescence

depolarization. The decay times and final anisotropies yield information about fluorophore order and steric restrictions. Diphenylhexatriene (DPH) fluorophore in aqueous solution are quenched by polar water molecules demonstrating low fluorescence. DPH fluorescence in hydrophobic environment is much greater.
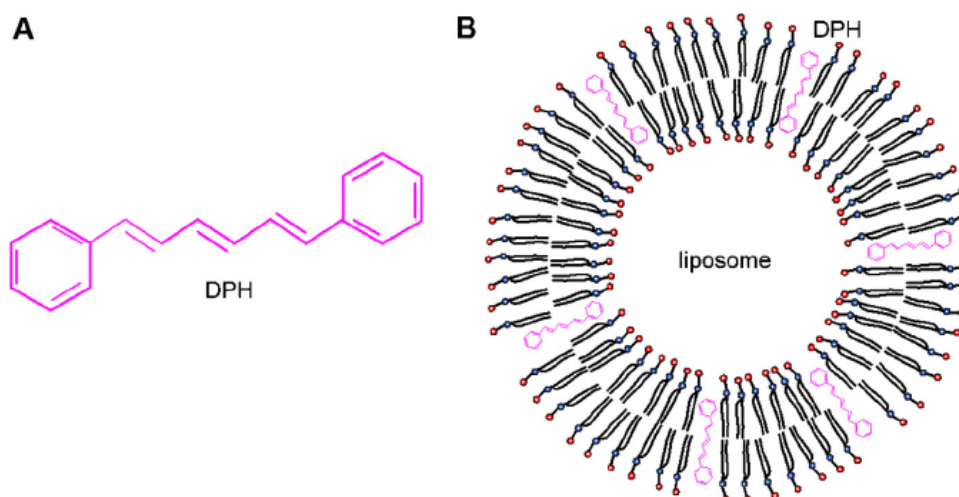
Figure B.1. (A) DPH molecule and (B) Orientation of DPH molecules in the hydrophobic lipid bilayer. Reproduced with permission from https://doi.org/10.1016/j.chemphyslip.2013.11.009

Anisotropy depends on the ratio of the polarized light to the total light intensity. I_{VV} is the intensity with excitation and emission polarizers mounted vertically, I_{HH} is for excitation and emission polarizers mounted horizontally, I_{HV} and I_{VH} also follows the same pattern of polarizers as the names suggest. This basic setup is called the L-format and is shown in Figure below.
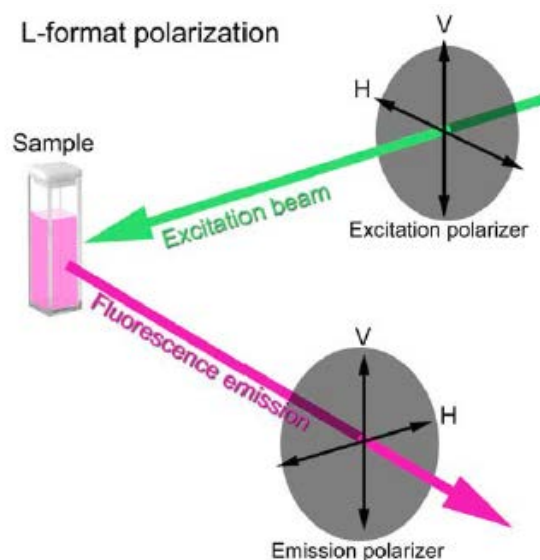
Figure B.2. L-format fluorescence polarization. Vertical (V) and Horizontal (H) orientations of each polarizer are shown.

Anisotropy <r> is defined as

$$< r > = \frac{I_{VV} - G * I_{VH}}{I_{VV} + 2 * G * I_{VH}}$$

Where g is the G factor,

$$G = \frac{I_{HV}}{I_{HH}}$$

Conversion between <r> and polarization P is,

$$P = \frac{3 < r >}{2 + < r >}$$

Anisotropy provides information on molecular size and shape and local viscosities of a fluorophore environment. A lipid membrane undergoing phase transition shows typical DPH anisotropy plots as shown in Figure. With increase in temperature and lipid bilayer

211

fluidization, rotational relaxation of DPH molecules in the bilayer leads to a sharp drop in

anisotropy.
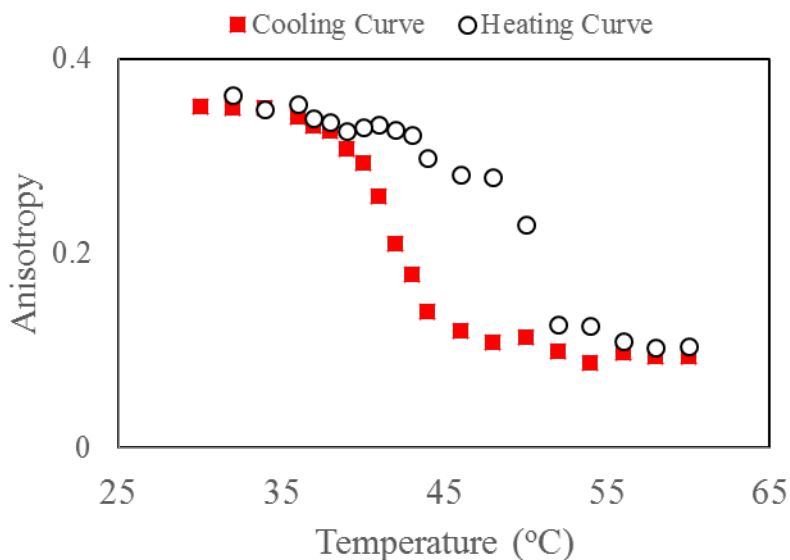
Figure B.3. Typical heating and cooling curve demonstrating
DPH anisotropy in pure DPPC liposomes.

B.3. Laurdan Dye Assay
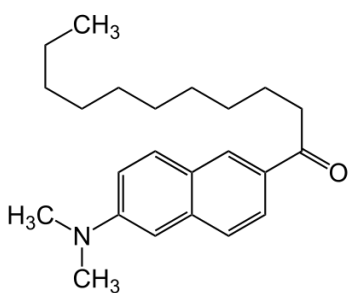
6-Dodecanoyl-2-
Dimethylaminonaphthalene

Laurdan (fluorophore) Generalized Polarization (GP) is used to study the phenomenon of

dipolar relaxation. Polarity changes are detected by shifts in Laurdan emission spectrum.

Change in GP values indicate phase behavior of lipid bilayer. The fluorescent

naphthalene moiety in the laurdan molecule possesses a dipole moment due to a partial

charge separation between the 2-dimethyl amino and 6-carbonyl residue. This dipole moment increases upon excitation and may cause reorientation of the surrounding solvent dipoles. The energy required for solvent reorientation decreases the excited state energy of the Laurdan molecule which is reflected in a continuous red shift of the probe emission spectrum. The application of the spectral shift of Laurdan is the study of the lipid bilayers. The hydrophobic tail of the fatty acid allows solubilization of the probe within the bilayer locating the fluorescent moiety towards the aqueous environment. When the lipids are in gel phase, the emission maximum of laurdan is centered at 440nm and when the lipids are in liquid crystalline phase the emission is at 490nm. This spectral shift is due to the dipolar relaxation of the laurdan in the lipidic environment. The origin of the dipolar relaxation has been attributed to a few water molecules present in the bilayer at the level of the glycerol backbone, where the laurdan naphthalene moiety resides. The concentration and MD of these water molecules is a function of the phospholipid phase state, and water reorientation along the probe excited state occurs only in the liquid crystalline state.
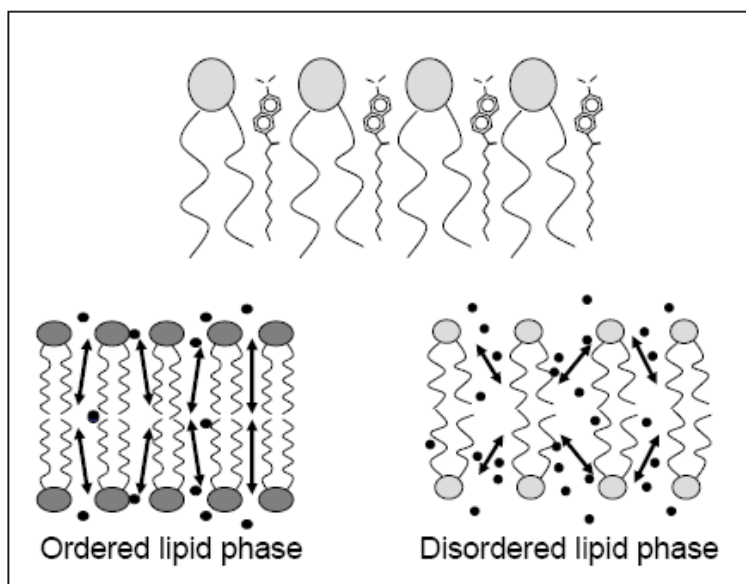
Figure B.4. Naphthalene moiety of Laurdan locates in the membrane at the level of the glycerol backbone of the phospholipids. The rearrangement of few water molecules (black dots) localized around the Laurdan dipole (arrows) will be responsible for the red shift observed in different phases.

Maximum emission wavelength shift of laurdan can be quantified by GP (Generalized polarization) which is defined as,

$$GP = \frac{I_{440} - I_{490}}{I_{440} + I_{490}}$$

Measurements are done in conventional fluorometer using excitation wavelength 340-360 nm and recording intensities at 440 nm and 490 nm. Laurdan is dissolved in either ethanol or DMSO and added to the liposomes at Laurdan: lipid molar ratio of 1:100 to 1:300. The most common lipid model systems used in this type of measurements are SUVs, LUVs and MLVs.

Appendix C

Data Analysis Resources

C.1 Small Angle Neutron Scattering (SANS) data models and analysis

All SANS data analysis and models have been discussed in Supplementary Informations of the corresponding publications. SANS raw data was reduced using NCNR macros on IgorPro. All details can be found here:

https://www.ncnr.nist.gov/programs/sans/data/red_anal.html. Fitting reduced data with models was carried out in SasView software package (http://www.sasview.org/). Details of all models used in this work can be additionally found here:

http://www.sasview.org/docs/user/index.html

C.2 Neutron Spin Echo data reduction and analysis.

NSE data was reduced using the inelastic scattering data reduction tool provided by NIST called DAVE (Data Analysis and Visualization Environment). All details can be found here: https://www.ncnr.nist.gov/dave/ and

https://www.ncnr.nist.gov/dave/documentation/nse_reduction_manual.pdf.

Appendix D

Permissions to reproduce texts and figures

Permission to reproduce Figure 1.3 A.

Permissions were received to reproduce selected figures, texts and full content for

Chapter 1, 2 and 3. All documentations are listed in this Appendix C.

218

Permission to reproduce Figure A.1A and A.1B from
DOI: 10.1021/acssuschemeng.8b02697

Permission to reproduce Figure B.1 from
https://doi.org/10.1016/j.chemphyslip.2013.11.009:

Order Completed

Thank you for your order.

Your confirmation email will contain your order number for future reference.

printable details

License Number	4442670802772
License date	Oct 05, 2018
Licensed Content Publisher	Elsevier
Licensed Content Publication	Chemistry and Physics of Lipids
Licensed Content Title	Influence of nanoparticle–membrane electrostatic interactions on membrane fluidity and bending elasticity
Licensed Content Author	Poornima Budime Santhosh,Aljaž Velikonja,Šarka Perutkova,Ekaterina Gongadze,Mukta Kulkarni,Julia Genova,Kristina Eleršič,Aleš Iglič,Veronika Kralj-Iglič,Nataša Poklar Ulrih
Licensed Content Date	Feb 1, 2014
Licensed Content Volume	178
Licensed Content Issue	n/a
Licensed Content Pages	11
Type of Use	reuse in a thesis/dissertation
Portion	figures/tables/illustrations
Number of figures/tables/illustrations	1
Format	both print and electronic
Are you the author of this Elsevier article?	No
Will you be translating?	No
Original figure numbers	Figure 3
Title of your thesis/dissertation	SURFACE FUNCTIONALIZED GOLD NANOPARTICLE APPLICATIONS IN COLLOIDAL CATALYSIS AND LIPID-NANOPARTICLE ASSEMBLIES
Expected completion date	Dec 2018
Estimated size (number of pages)	200
Requestor Location	CLEMSON UNIVERSITY 303 Crawford Court Apt 3
	CLEMSON, SC 29631 United States Attn: SAPTARSHI CHAKRABORTY
Publisher Tax ID	98-0397604
Total	0.00 USD

ORDER MORE   CLOSE WINDOW